UNIVERSIDADE FEDERAL DO PARÁ
INSTITUTO DE GEOCIÊNCIAS
PROGRAMA DE PÓS-GRADUAÇÃO EM GEOLOGIA E GEOQUÍMICA

TESE Nº 149

ESTRATIGRAFIA E EVENTOS DA TRANSIÇÃO NEOARQUEANO-PALEOPROTEROZOICO DA BACIA DE CARAJÁS, SUDESTE DO CRATON AMAZÔNICO

Tese apresentada por:

RAPHAEL NETO ARAÚJO
Orientador: Prof. Dr. Afonso Cesar R. Nogueira (UFPA)

BELÉM- PARÁ
2020

Dados Internacionais de Catalogação na Publicação (CIP) de acordo com ISBD
Sistema de Bibliotecas da Universidade Federal do Pará
Gerada automaticamente pelo módulo Ficat, mediante os dados fornecidos pelo(a) autor(a)

A658e Araújo, Raphael Neto

Estratigrafia e eventos da transição Neoarqueano-Paleoproterozoico da Bacia de Carajás, sudeste do Cráton Amazônico / Raphael Neto Araújo. — 2020.

xxvi, 187 f. : il. color.

Orientador(a): Prof. Dr. Afonso César Rodrigues Nogueira

Tese (Doutorado) - Programa de Pós-Graduação em Geologia e Geoquímica, Instituto de Geociências, Universidade Federal do Pará, Belém, 2020.

1. Estratigrafia. 2. Bacia de Carajás. 3. Glaciação Serra Sul. 4. Evolução tectono-sedimentar. 5. Neoarqueano-Paleoproterozoico. I. Título.

CDD 551.7

Universidade Federal do Pará
Instituto de Geociências
Programa de Pós-Graduação em Geologia e Geoquímica

ESTRATIGRAFIA E EVENTOS DA TRANSIÇÃO NEOARQUEANO-PALEOPROTEROZOICO DA BACIA DE CARAJÁS, SUDESTE DO CRATON AMAZÔNICO

TESE APRESENTADA POR:

RAPHAEL NETO ARAÚJO

Como requisito parcial à obtenção do Grau de Doutor em Ciências na Área de GEOLOGIA, Linha de Pesquisa ANÁLISE DE BACIAS SEDIMENTARES

Data de Aprovação: 18 / 09 / 2020

Banca Examinadora:

Prof. Dr. Afonso Cesar R. Nogueira
(Orientador - UFPA)

Prof.ª Dr.ª Lucieth Cruz Vieira
(Membro - UnB)

Prof. Dr. Ricardo Ivan Ferreira da Trindade
(Membro - USP)

Prof. Dr. Jean Michel Lafon
(Membro - UFPA)

Prof. Dr. Joelson Lima Soares
(Membro - UFPA)

À minha família:
Ofir Moraes, Edith Carvalho, Ana Barata,
Rosiane Araújo, Roberto Araújo,
Roberto Araújo Filho e Quézia Alencar.

AGRADECIMENTOS

Agradeço primeiramente à Deus e ao seu filho Jesus Cristo por todo amor, pelas bênçãos em minha vida e por ter me guiado até esse momento. Em diversos momentos da minha vida ele me mostrou que está vivo e opera milagres nas nossas vidas, acredite.

A Companhia de Pesquisa de Recursos Minerais (CPRM) ou apenas Serviço Geológico do Brasil pelo apoio material e financeiro concedido ao meu doutorado através do projeto Área de Relevante Interesse Mineral de Carajás (ARIM-Carajás) da superintendência regional de Belém (SUREG-BE). Em especial, gostaria de agradecer ao gerente de geologia César Chaves pelo apoio e auxílios prestados em diversas etapas do trabalho, principalmente nas vésperas de etapas de campo sempre prestativo aos trâmites administrativos.

À Universidade Federal do Pará (UFPA) através do Programa de Pós-graduação em Geologia e Geoquímica (PPGG) pelo apoio concedido durante o programa de doutorado. Em especial, gostaria de agradecer ao Prof. Dr. Cláudio Lamarão (coordenado do PPGG) pelo apoio e auxílios prestados principalmente durante as etapas finais da tese, bem como, a Cleida Freitas e Joanicy Lopes (secretárias do PPGG) pela ajuda nos tramites finais de entrega da tese. Aos bibliotecários do Instituto de Geociências, em especial, a sra. Lúcia Imbiriba pelas orientações e ajuda na formatação da tese de acordo com as normas do PPGG.

À mineradora Vale S.A. (Parauapebas, Pará, Brasil) por ter cedido os testemunhos de sondagem para estudo e pelo apoio dispensado durante as etapas de campo na região de Carajás. Em especial, gostaria de agradecer aos geólogos que nos acompanharam durante a descrição dos testemunhos nos galpões e nas minas desta empresa Fernando Matos, Sérgio Barcelar, Luiz Cláudio Costa, Fernando Prezotti e Cláudio Rosas. Outros geólogos e técnicos da Vale S.A. participaram destas etapas, e de igual forma, sintam-se agradecidos.

Ao meu orientador Prof. Dr. Afonso César Rodrigues Nogueira (UFPA) por todos os ensinamentos e oportunidades durante estes mais de dez anos de trabalho. Gostaria de agradecer ainda aos integrantes do grupo de Análise de Bacias Sedimentares da Amazônia (GSED), em especial, aos professores Dr. José Bandeira e Dr. Joelson Soares.

Ao Prof. Dr. Werner Truckenbrodt (UFPA) e sua esposa “Nega”, pelo carinho e apoio durante diversas etapas desse trabalho. Obrigado professor por ter lido e contribuído com o artigo sobre a glaciação Serra Sul de Carajás!

Gostaria de agradecer ainda a Dra. Lúcia Travassos da Rosa-Costa (CPRM-Belém) e a Dra. Cintia Maria Gaia da Silva (CPRM-Belém) pelo incentivo para realização desta tese de doutorado. Lúcia foi a primeira pessoa que me recebeu na CPRM em Belém, e Cintia foi a primeira pessoa a me apresentar a extensa bibliografia sobre Carajás.

Aos amigos que fiz na CPRM ao longo destes quase sete anos no serviço geológico brasileiro, Marcos Vinicius, Bruce Chiba, Pedro Cordeiro, Moacir Furtado, Marcos Quadros, Paulo Melo, Djalma Hartery e Silvio Lisboa. Em especial gostaria de agradecer ao amigo Edilberto Leão (*in memorian*), que nos deixou muito cedo, mas que tive a oportunidade de conviver e aprender com ele durante algumas etapas de campo para Carajás.

À Rosalva Coelho (CPRM-Belém) por ter me ensinado tudo sobre separação de zircão e ter me ajudado a separar os grãos de zircão das minhas amostras. Agradeço ainda aos colegas Érica, Denise, seu Avelino, Paulo Sérgio e Linaldo que me ajudaram em diferentes etapas na preparação das amostras para geocronologia, cada um com sua contribuição importante.

Ao colega de pós-graduação da UFPA Alexandre Ribeiro, atualmente doutorando da UNICAMP, que estava terminando seu mestrado e mesmo assim aceitou o convite de ir a Carajás para me ajudar durante uma das etapas de campo. Poucas são as pessoas que largam o que estão fazendo para ajudar os outros e você fez isso. Muito obrigado meu nobre colega.

Ao Prof. Dr. Pascal Philippot (IPGP/França) e os seus alunos de doutorado e pós-doutorado que estiveram em Carajás comigo durante uma das etapas de campo. Embora tenham sido dias de trabalho incessantes, muitas coisas boas nasceram das nossas discussões.

Gostaria de agradecer também ao meu sogro Joel, a minha sogra Amélia, e a minha cunhada Esther pelo carinho, apoio e torcida pelo sucesso desse trabalho. Estendo meus agradecimentos ainda a minha cunhada Luana Silva e a minha sobrinha Giovanna Araújo, que ainda não nasceu, mas que já está trazendo muita luz para esse mundo. Te desejo muitas bênçãos em sua vida e que você traga muitas coisas boas aos seus pais e a nossa família.

Agradeço ainda a todos aqueles, que embora não citados, contribuíram de alguma forma para o desenvolvimento da tese. Por fim, gostaria de pedir desculpas a minha família pela minha ausência nesses últimos anos em reuniões e dias festivos. Diversos finais de semana abdiquei do convívio da minha família devido a minha tese de doutorado. O futuro nos dará muito mais dias de alegria e amor.

"O que sabemos é uma gota; o que ignoramos é um oceano".

(Sir Isaac Newton)

RESUMO

A transição Neoarqueano-Paleoproterozoico é marcada por uma série de modificações paleoambientais, paleoclimáticas e tectônicas que resultaram em eventos dramáticos, que impuseram à Terra condições inéditas, algumas de caráter irreversível. Em termos paleoambientais, destaca-se o aumento dramático do oxigênio no sistema hidrosfera-atmosfera, a partir do *Great Oxidation Event* (GOE) por volta de 2.45 Ga. O aumento do oxigênio foi acompanhado da diminuição de *greenhouse gases* como CO_2 e CH_4, que promoveu o aparecimento de diferentes episódios glaciais por volta de *ca.* 2.45–2.22 Ga, genericamente denominados de *Huronian Glacial Event* (HGE). Embora diversos trabalhos sustentem a hipótese de que esses episódios glaciais correspondam ao primeiro evento glacial de escala global da história da Terra (*Paleoproterozoic snowball Earth*), contradições estratigráficas e geocronológicas impõem dúvidas quanto a sua extensão global. Estranhamente, ao passo que esse conjunto de eventos é amplamente reconhecido em diversas áreas cratônicas ao redor do globo, no Cráton Amazônico eles ainda permanecem pouco compreendidos e/ou ainda não reportados. Neste estudo, a investigação estratigráfica, sedimentológica e geocronológica da sucessão vulcano-sedimentar (*ca.* 5 km de espessura) da Bacia de Carajás localizada no sudeste do Cráton Amazônico, norte do Brasil, permitiu o reconhecimento e sequenciamento de alguns desses eventos registrados nessa bacia. Duas unidades litoestratigráficas estão sendo formalmente propostas para essa bacia: a Formação Serra Sul e a Formação Azul. Intervalos de diamictito glacial do Sideriano–Riaciano (*ca.* 2.58–2.06 Ga) ocorrem empilhados na Formação Serra Sul, e representam o primeiro registro de depósitos glaciais dessa idade na América do Sul. Em termos paleogeográficos, a ocorrência de depósitos glaciais Paleoproterozoicos nesta parte do globo, expande o alcance dessas glaciações para o Cráton Amazônico pela primeira vez, muito embora, o diamictito Serra Sul possa ser correlato a algumas das glaciações Paleoproterozoicas conhecidas, ou a nenhuma delas. Texturas glaciais bem preservadas como foliação glacial e *dropstone features*, indicam que a deposição da desses estratos ocorreu em um sistema subglacial costeiro, no qual sedimentos glaciogênicos foram ressedimentados em um sistema de leque submarino e através de processos de *ice rafting* em águas distais do sistema marinho. O sistema glacial Serra Sul foi desenvolvido imediatamente acima dos estratos pré-glaciais representados pelas unidades de formação ferrífera bandada e rochas vulcânicas do Neoarqueano, que não somente funcionaram como substrato principal, mas também como fonte principal de sedimentos. Adicionalmente, os dados estratigráficos indicam que imediatamente acima do diamictito Serra Sul, depósitos de ritmito da Formação Azul, localmente enriquecidos em manganês, foram depositados em um sistema marinho raso (*offshore* e *offshore*

transition/shoreface), como resultado do aumento do nível do mar durante a fase de deglaciação. Os estratos enriquecidos com manganês foram possivelmente depositados em associação com *black shale*—que levou a formação de rodocrosita durante a diagênese—nas porções mais profundas da bacia marinha. Evidências petrográficas e mineralógicas, sustentadas por observações de campo, sugerem que o manganês foi remobilizado como óxido através de falhas para zonas de baixa tensão e elevada permo-porosidade dentro de camadas de *red beds* da Formação Azul, de forma similar ao observado na migração de hidrocarbonetos. Em termos estratigráficos, a Formação Azul encerra os mesmos intervalos anteriormente inseridos no membro inferior da Formação Águas Claras. Essa formação foi redefinida para designar exclusivamente depósitos de arenito, conglomerado e conglomerado jaspilíticos depositados em um sistema tipo *fluvial braided*, que ocorrem em discordância acima da Formação Azul. Além disso, é sugerido que as formações Azul e Águas Claras representem o registro estratigráfico de uma sequência transgressiva-regressiva (T-R). Dados geocronológicos obtidos a partir da datação U-Pb de zircão detrítico separados das formações Azul e Águas Claras indicam que rochas do Mesoarqueano e Neoarqueano, possivelmente dos domínios Rio Maria e Carajás, foram as principais rochas-fonte de sedimentos. A distribuição das idades $^{207}Pb/^{206}Pb$ de 76 análises concordantes da Formação Azul indicam uma idade para população mais jovem em *ca.* 2.27 Ga, interpretada como a idade máxima de deposição dessa unidade. A ocorrência de grãos de zircão do Riaciano e Orosiriano nessa unidade sugere fortemente que o Domínio Bacajá pode ter sido fonte subordinada de sedimentos, e em termos paleogeográficos, sugere uma possível conexão entre esse domínio e o Domínio Carajás nesse período. A análise integrada dos resultados, apoiada em dados geológicos regionais anteriores, permitiu a proposição de um modelo tectono-sedimentar para a evolução da sucessão Paleoproterozoica da Bacia de Carajás. É sugerido que essa bacia provavelmente evoluiu, durante grande parte do Paleoproterozoico como uma bacia *foreland*, como resultado da colisão entre os domínios Bacajá e Carajás durante o ciclo orogenético Transamazônico por volta de *ca.* 2.2–2.0 Ga. O movimento convergente desses blocos ocasionou o soerguimento gradual do protocontinente Carajás; o fechamento do mar Azul, e a instalação de um amplo sistema fluvial-aluvial, no qual as formações Águas Claras e Gorotire foram depositadas. Esse cenário de profundas modificações esteve diretamente ligado a configuração do supercontinente Columbia, que promoveu a continentalização e amalgamação das massas de terra que posteriormente formaram o proto-Cráton Amazônico no final do Paleoproterozoico.

Palavras-chave: Estratigrafia. Bacia de Carajás. Glaciação Serra Sul. Evolução tectono-sedimentar. Neoarqueano-Paleoproterozoico.

ABSTRACT

The Neoarchean-Paleoproterozoic transition is marked by a series of paleoenvironmental, paleoclimatic and tectonic changes that resulted in dramatic events, which imposed to the Earth novel conditions, some of them with irreversible characteristics. On the paleoenvironmental aspect, it is highlighted the rise of oxygen in the hydrosphere-atmosphere system, onset the Great Oxidation Event (GOE) at around *ca.* 2.45 Ga. The rise of this gas caused consequently the decrease of the greenhouse gases such as CH_4, which promoted the emergence of glacial episodes at around *ca.* 2.45–2.22 Ga, generically termed the Huronian Glacial Event (HGE). Although several studies support the hypothesis that these glacial episodes represent the first global glaciation of the Earth's history (Paleoproterozoic snowball Earth), stratigraphic and geochronological contradictions impose doubt as to its global extension. Strangely, although this set of events is widely recognized in several cratonic areas around the globe, these events are still poorly understood and/or not yet reported in the Amazonian Craton. In this study, the stratigraphic, sedimentological and geochronological investigation of the volcano-sedimentary succession (*ca*. 5-km-thick) of the Carajás Basin, situated in the southeastern Amazonian Craton, northern Brazil, allowed the recognition and sequencing of some of these events in this basin. Two new units are being formally proposed to this basin: the Serra Sul and Azul formations. Glacial diamictite intervals of the Siderian–Rhyacian (*ca*. 2.58–2.06 Ga) occur stacked within the Serra Sul Formation, and are the first reported occurrence of glacial deposits of that age in South America. In paleogeographic terms, the occurrence of Paleoproterozoic glacial deposits in this part of the globe, expands the reach of these glaciations to the Amazonian Craton for the first time, although the Serra Sul diamictite may be correlated with any of the know Paleoproterozoic glaciations, or none of them. Well-preserved textures, such as glacial foliation and dropstone features, indicate that the deposition of the Serra Sul Formation occurred in a coastal subglacial setting, in which glaciogenic sediments were resedimented in submarine fan system, and through ice rafting process in distal waters of the marine environment. The Serra Sul glacial system was developed immediately above of pre-glacial strata represented by the Neoarchean banded iron formation and volcanic rock units, which not was the main substrate, but also was the main source of sediments to this glacial system. Additionally, the stratigraphic results indicate that the immediately above of the Serra Sul diamictite, rhythmite deposits of the Azul Formation, locally enriched in manganese, were deposited in a shallow marine environment (offshore and offshore transition/shoreface zones), as a result of the sea level rise during the deglaciation phase. The manganese-bearing strata were possibly deposited in association with black shale deposits—which allowed the formation

of rhodochrosite during diagenesis—in deep zones of the marine basin. Petrographic and mineralogical evidences, supported by field observation, indicate that manganese oxides were secondarily remobilized through faults to zones with low strain and high permo-porosity within red bed strata of the Azul Formation, similarly to that observed in hydrocarbon migration. In stratigraphic terms, the Azul Formation represents the same interval previously arranged in the lower member of the Águas Claras Formation. This formation was redefined to designate exclusively sandstone, conglomerate and jasper conglomerate strata, deposited in a braided fluvial system, which occur in unconformably immediately above of the Azul Formation. Moreover, it is suggested that the Azul and Águas Claras formations are the stratigraphic record associated with a transgressive-regressive sequence (T-R). The dating (U-Pb) of detrital zircon grains separated from the Azul and Águas Claras formations indicate that Meso- to Neoarchean rocks, possibly of the Rio Maria and Carajás domains, were the main source of sediments. The $^{207}Pb/^{206}Pb$ Age distribution of the 76 concordant analysis of the Azul Formation indicate a youngest population at *ca.* 2.27 Ga, interpreted as the maximum deposition age of this unit. The occurrence of Rhyacian to Siderian zircon grains in this unit strongly suggest that the Bacajá Domain may have been a subordinated source of sediments, and in paleogeographic terms, suggest a possible connection between this domain and the Carajás Domain at that time period. The integration of the results obtained from this study, supported by previous data on the regional geology, allowed the proposition of a tectono-sedimentary evolutive model to the Paleoproterozoic succession of the Carajás Basin. It is envisaged that this basin evolved during the greater part of the Paleoproterozoic in a foreland style, as result of the collision of the Bacajá and the Carajás domains during the Transamazonian orogenetic cycle at *ca.* 2.2–2.0 Ga. The convergent movement of these blocks caused the gradual uplift of the Carajás protocontinent; the closure of the Azul Sea, and installation of a wide fluvial-alluvial system, in which the Águas Claras and Gorotire formations were deposited. This scenario of profound changes is directly related to the Columbia supercontinent assembly at the end of the Paleoproterozoic, that promoted the continentalization and amalgamation of the ancient landmasses that later formed the proto-Amazonian Craton at the end of Paleoproterozoic.

Keywords: Stratigraphy. Carajás Basin. Serra Sul glaciation. Tectono-sedimentary evolution. Neoarchean-Paleoproterozoic.

LISTA DE ILUSTRAÇÕES

CAPÍTULO 1

Figura 1.1- Mapa de localização da área de estudo mostrando os pontos estudados na região da Serra dos Carajás, Estado do Pará (PA), Brasil.....05

CAPÍTULO 2

Figura 2.1- O Cráton Amazônico e a Província Carajás. (a) Distribuição das províncias geocronológicas do Cráton Amazônico (Tassinari & Macambira 2004). (b) Mapa geológico da Província Carajás (adaptado de Vasquez *et al.* 2008) 10

Figura 2.2- Mapa geológico da Bacia de Carajás mostrando as subáreas de estudo (modificado de Vasquez *et al.* 2008a). Os limites das novas unidades propostas para esta bacia (formações Serra Sul e Azul) descritas em Araújo & Nogueira (2019) e Araújo Filho *et al.* (2020), respectivamente, estão sendo apresentados.....11

Figura 2.3- Comparação entre as diferentes propostas estratigráficas para a região de Carajás (sudeste do Cráton Amazônico, Brasil) 13

Figura 2.4- Coluna estratigráfica da Bacia de Carajás (sudeste do Cráton Amazônico, Brasil) revisada nesta tese de doutorado. Dados estratigráficos (relações de contato, espessura de unidades e padrão de empilhamento) compilados de Docegeo (1988), Machado *et al.* (1991), Nogueira *et al.* (1995), Dias *et al.* (1996), Pinheiro (1997), Cabral *et al.* (2013), Araújo & Nogueira (2019), e Araújo Filho *et al.* (2020).....14

CAPÍTULO 3

Figura 3.1- Principais diferenças no registro sedimentar entre o Pré-Cambriano e o Fanerozóico (Catuneanu *et al*. 2005) 23

Figura 3.2- Evolução do conteúdo de oxigênio na atmosfera ao longo do tempo (Lyons *et al.* 2014) 25

Figura 3.3- Sumário de modificações paleoambientais ocorridas em *ca.* 2.3 Ga (Tang & Chen 2013).....26

Figura 3.4- Possível correlação estratigráfica entre os depósitos glaciais associados ao Evento Glacial Huroniano (HGE) de acordo com de Tang & Chen (2013) e referências nele contidas.....28

Figura 3.5- Reconstruções paleogeográficas das massas de terra que constituíram o supercontinente Columbia em: (a) aproximadamente 1,5 Ga (Rogers & Santosh 2002); (b) aproximadamente 2,0 Ga (Zhao et al. 2004); (c) e, entre 1,8-1,3 Ga (Johansson 2009).....29

CAPÍTULO 4

Figura 4.1- Síntese de metodologias e técnicas empregadas na investigação da sucessão Arqueana–Paleoproterozoica da Bacia de Carajás (Adaptado de Pufahl & Hiatt 2012).....31

CAPÍTULO 5

Figure 1- Simplified geological map of Carajás Basin (Brazil) highlighting study areas (a, b, and c) and location of drill holes (black dots), and stratigraphic framework of basin including exact stratigraphic position of Serra Sul Formation and main geochronological data available (1—Machado et al., 1991; 2—Trendall et al., 1998; 3—Tallarico et al., 2005; 4—Mougeot et al., 1996; 5—Pereira et al., 2009; 6—Teixeira et al., 2018).....39

Figure 2- Sedimentary logs in Serra Sul Formation for three distinct areas (a, b, and c) of Carajás Basin, Brazil (see Fig. 1 for location). Numbers and letters to right correspond to fotos in Figure 3.....40

Figure 3- Images of Serra Sul Formation (Carajás Basin, Brazil). (A,A′) 360° panoramic image and line interpretation of core samplerepresentative of foliated diamictite exhibiting pressure shadow (Ps) and faceted (Fc), sheared (Sh), rotated (Rt), fractured (Ft), flattened (Fl), and boudinaged (Bt) clasts of iron formation, iron chert, and volcanic to subvolcanic rock. Background color in A′ represents facies association of foliated to massive diamictite. (B,C) Thin section images of foliated diamictite showing angular clasts of chert with asymmetrical pressure shadow (B; plane polarized light, 10×) rotated in a matrix containing quartz (Qtz), magnetite (Mag), and pyrite (Py). (D) Bullet-shaped clast of porphyritic rhyolite isolated in black shale bed sandwiched by diamictite. (E) Matrix-supported conglomerate with pebble-sized iron formation clast scattered in granular matrix (F) Well-rounded clast of porphyritic rhyolite displaying disruption and puncturing of underlying laminae beneath clast. (G) Thin beds of coarse-grained mounds of chert and volcanic rock clasts surrounded by mudstone. (H) Faceted and elongated pentagonal clasts with high-angle dips randomly embedded in muddy diamictite. (I) Thin section image of diamictite (plane polarized light, 10×) showing very angular chert clasts suspended in poorly sorted and mud-rich matrix. (J) Striations on the surface of quartz grain from diamictite (scanning electron microscope image).....41

Figure 4- Model showing sedimentary mechanisms underlying diamictite-bearing succession of Serra Sul Formation (Carajás Basin, Brazil). Subglacial diamictite from coastal environment is characterized by quartz- and magnetite-rich matrix resulting from erosion and glaciotectonism on bedrock, whereas marine diamictite results from sedimentation of ice-rafted debris (IRD) and is characterized by mud-rich matrix. Glacially fed submarine fan deposits rework glaciogenic sediments and are interbedded with IRD-bearing diamictite. Neoarchean banded iron formation (BIF) and volcanic rock units were main bedrock and source of sediments. Positions of sedimentary logs (a, b, and c; see Fig. 1 for location) are indicated.....41

CAPÍTULO 6

Figure 6.1- Location map of the study area. (a) South America map showing the location of the Carajás Province in the Amazonian Craton. (b) Carajás Province map showing the location of the Carajás Basin in the Carajás domain. (c) Paleogeographic reconstruction of the Columbia supercontinent at *ca*. 2.0 Ga showing the location of the Amazonian Craton (modified from Zhao *et al.* 2002, 2004). (d) Geological map of the Carajás Basin and the surrounding areas showing the location of the studied areas (modified from Vasquez *et al.* 2008a)..... 46

Figure 6.2- Stratigraphic framework of the Carajás Basin, located in the Amazonian Craton, Brazil (modified from Araújo & Nogueira 2019). Geochronological data compiled from: 1—Machado *et al.* (1991); 2—Martins *et al.* (2017); 3—Trendall *et al.* (1998); 4—Galarza *et al.* (2008); 5—Tallarico *et al.* (2005); 6—Araújo & Nogueira (2019); 7—Justo *et al.* (2018); 8—Mougeot *et al.* (1996); 9—Araújo & Sousa (2018); 10—Pereira *et al.* (2009); 11—Teixeira *et al.* (2018); 12—Teixeira *et al.* (2019).....48

Figure 6.3- Stratigraphy of the manganese-bearing succession of the Carajás Basin (southeastern Amazonian Craton, Brazil) described in this study. a) Composite sedimentary logs in the Azul and Águas Claras formations from the studied areas. b) Simplified facies maps of the study areas.....51

Figure 6.4- Rhythmite lithofacies features. (a) Centimeter intercalation between the normal-graded sandstone and mudrock. Hummocky cross-stratified sandstone intervals occur very subordinately. (b) Fining upward cycles composed of fine-grained sandstone and mudrock. (c) Abrupt contact between the fine to medium-grained sandstone and mudrock at the base of the fining upward cycles.....52

Figure 6.5- Structural transects measured within the Azul mine. (a) SE-NW structural transect showing suave folded beds dipping slightly to the NW direction and tightly to the NE and NW direction. Fractures and faults occur mainly oriented in the NE-SW and SE-NW directions (rose diagram). (b) SW-NE structural transect showing tightly folded beds. Fractures and faults that occur are NE-SW- and SE-NW-oriented (rose diagram). Meter-scale drag folds and centimeter-scale kink-bands are largely observed. Manganese occurs hosted in the planes of fractures and stains the host rock, and subordinately forms stockwork structure..... 54

Figure 6.6- Main structural aspects observed in the Azul manganese-bearing succession of the Carajás Basin (southeastern Amazonian Craton, Brazil). (a) Manganese randomly staining rhythmite deposits. (b) Manganese concentrated on the beds located in the hinge zone of an antiformal fold. (c) Manganese enriched in the fractures and sandy laminations. (d) Manganese forming a type of stockwork structure. (e) A meter-scale fault-hosted manganese interval. (f) Micro-faults. (g) Drag fold. (h) Kink band structure.....55

Figure 6.7- Geochemical trends of some major oxides and ratios across the ST1. (a) Image of the Azul mine pit showing the locale from where the samples were collected. (b) Geochemical trend profiles of some major oxides (MnO, Fe_2O_3, and Al_2O_3,) and ratios (Mn/Fe and Mn/Al). The red line represents the Mn/Fe ratio found in typical detrital components (Maynard 2003).....56

Figure 6.8- Scanned electron-microscope (SEM) images obtained from manganese-bearing rhythmite samples of the Azul succession. (a) Cryptomelane (Cry) as needle-like crystallites and a fine-grained masse. (b) Fine-grained mass of cryptomelane concentrated in veins alongside kaolinite (Kao). (c) Fine-grained mass of cryptomelane and subhedral crystals of spessartite (Sps) concentrated in lamination. (d) Botryoid formed of cryptomelane, showing banded colloform texture and with acicular crystallites in the center intergrow latticed. (e and f) Cry as needle-like crystallites alongside Kao. Zircon (Zir) occurs subordinately. The stars represent the areas from where we obtained EDS spectra.....57

Figure 6.9- Manganese-bearing minerals identified in the Azul succession. (a) X-ray diffractogram showing todorokite (Tod), kaolinite (Kln), cryptomelane (Cry), goethite (Gt), and pyrolusite (Pyr). Energy-dispersive X-ray spectrograms of spessartite (b) and cryptomelane (c).....58

Figure 6.10- Paleoenvironmental reconstruction of the Azul marine succession that host the manganese deposits, showing a shallow-marine environment (shoreface to offshore zone) influenced by storm events. Manganese was upwelled from deep to shallow waters, where it was reduced. Downwelling currents moved the manganese to deep waters again, where it was deposited alongside black shale. Red-bed strata were deposited above in the highly oxygenated shallow waters....60

Figure 6.11- Geological section of the Azul manganese-bearing succession showing the envisaged mechanisms involved in the secondary manganese enrichment. Intervals of rhodochrosite repeatedly interbedded with black shale layers represent the protore, which acts as a “source” of manganese. The ore was remobilized through faults, such as the Carajás, for the strata immediately above (red bed) the Azul Formation, suggesting the occurrence of indigenous remobilization similar to oil migration. Ultimately, the manganese was enriched throughout the Cenozoic era through supergene processes that superposed the hypogene enrichment.....61

CAPÍTULO 7

Figure 7.1- Location map of the study area. (a) Location of the Carajás region in the southeastern Amazonian Craton, Brazil. (b) Map of the Carajás region showing the location of the Carajás Basin. (c) Geological map of the Carajás Basin showing the location of the study areas (modified from Vasquez et al. 2008b).....75

Figure 7.2- Stratigraphic column of the Carajás Basin (Amazonian Craton, Brazil) showing the main geological and geochronological data available for the volcano-sedimentary rocks that fill this basin (modified from Araújo & Nogueira, 2019). Geochronological data compiled from: 1—Machado et al. (1991); 2—Martins et al. (2017); 3—Trendall et al. (1998); 4—Galarza et al. (2008); 5—Tallarico et al. (2005); 6—Araújo & Nogueira (2019); 7—Justo et al. (2018); 8—Mougeot et al.

(1996a); 9—Araújo & Sousa (2018); 10—Pereira et al. (2009); 11—Teixeira et al. (2019a). The meaning of the ages is being discussed in the text.....76

Figure 7.3- Simplified geological map showing the location of drill cores and outcrops investigated in different areas within the Carajás Basin (southeastern Amazonian Craton, Brazil): (a) Serra Sul; (b) Tarzan; (c) Igarapé Bahia mine; (d) Bahia road; and (e) Azul mine.....80

Figure 7.4- Stratigraphic framework envisaged for the Paleoproterozoic succession of the Carajás Basin (southeastern Amazonian Craton, Brazil) based on the stratigraphic data obtained from the study and the stratigraphic data previously published by Araújo & Nogueira (2019) and Araújo Filho et al. (2020). Numbers and letters to the right correspond to images in Figs. 8.5, 8.6, and 8.7..... 83

Figure 7.5- Sedimentologic features of the Rhythmite Facies Association (RFA) of the Azul Formation. (a) Panoramic view of the Azul mine showing meter-scale succession of rhythmite in which manganese-enriched strata (arrow) is embedded. (b) Red rhythmite beds showing mudrock repeatedly interbedded with kaolinized fine-grained sandstone (arrows). Convolute laminations occur at the base of the sandy intervals. (c) Current image of a strongly altered outcrop of the Azul Formation in the Bahia road showing tilted beds of RFA conformably overlaid by RSFA deposits. (d) Cut-rock surface of the drill core showing normal-graded sandstone interlayered with black mudrock, compounding fining-upward cycles. (e) Rhythmite showing sandy dikes (square) and mud rip-up clasts in the contact between fine-grained sandstone and mudrock (arrows). The circles indicate disseminated pyrites in sandy interval. (f) Thin section photomicrograph (plane parallel light, 10×) showing a fine-grained sandstone at the base of a fining-upward cycle with a mud-rich matrix (arrow)..... 86

Figure 7.6- Sedimentological features of the Rhythmite-Sandstone Facies Association (RSFA) of the Azul Formation. (a) Outcrop on the Bahia road showing amalgamated bedset of meter-scale hummocky cross-stratified sandstone (arrow). (b) Hummocky cross-stratified sandstone (arrow) sandwiched by rhythmite strata. (c) Climbing ripple cross-laminated (arrow) and plane-parallel laminated sandstone (arrow) bedset repeatedly stacked. (d) Pyrite crystals (arrow) disseminated in sandstone. (e) Rhythmite facies showing mudrock interbedded with fine-grained sandstone with intricately interwoven cross-lamination (arrow). (f) Thin section photomicrograph (plane polarized light, 10×) of gabbro from a dike swarm, intrusive in this facies association, showing a highly altered primary mineralogy by chloritization (arrow) 87

Figure 7.7- Sedimentological features of the Sandstone-Conglomerate Facies Association (SCFA) of the Águas Claras Formation. (a) Centimeter intercalation between the massive conglomerate and the weakly stratified sandstone, constituting fining-upward cycles. (b) A bedset of trough cross-bedded and plane-parallel laminated sandstone. (c) Detail of the coarse-grained sandstone with plane-parallel lamination above a trough cross-bedded sandstone stratum. (d, e) Cut rock surface of the drill core showing jasper conglomerate with several jaspilite, banded iron formation, chert, and mafic to felsic volcanic pebbles (arrows) embedded in a granular-sandy matrix. (f) Thin section photomicrograph (cross-polarized light, 10×) of tuffaceous sandstone showing its fluidal texture, in which altered plagioclase and quartz occur embedded in a chlorite-rich matrix (arrows)..... 88

Figure 7.8- Cathodoluminescence (CL) images of some zircon grains dated (U-Pb) with their respective values of 207Pb/206Pb dates. (a) Zircon grains dated from the Azul Formation. (b–f) Zircon grains dated from the Águas Claras Formation. The yellow and red circles indicate the site of the laser spots positioned for dating using LA-ICPMS and SHRIMP, respectively.....90

Figure 7.9- U-Pb Concordia plots obtained from the dating of samples of the (a) Azul Formation and (b–f) the Águas Claras Formation (only analysis with <±10% of discordance) 93

Figure 7.10- Probability histograms showing the 207Pb/206Pb Age distribution of (a) the 76 concordant analyses of the Azul Formation, and (b) the 170 concordant analyses of the Águas Claras Formation.....94

Figure 7.11- Simple models showing the paleoenvironmental reconstruction of two distinct steps of the sedimentary evolution of the Paleoproterozoic succession of the Carajás Basin (Amazonian Craton, Brazil). (a) A shallow marine platform in which the Azul Formation was deposited immediately above the Serra Sul Formation. (b) A fluvial braided system in which the Águas Claras Formation was deposited after the deposition of the Azul Formation. It is possible that the Gorotire Formation was deposited soon after or coevally with the Águas Claras Formation. (c) Composite profile of the Paleoproterozoic succession of Carajás Basin, showing new insights on the sequence stratigraphy of this basin.....….97

Figure 7.12- (a) Simplified geological map of the Carajás region (modified from Vasquez et al. 2008a) showing potential source-rocks of the Águas Claras Formation and the inferred sediment transport pathways. The paleogeographic map shows the southern portion of the Columbia supercontinent with approximate location of the Carajás region (Modified from Zhao et al. 2004). (b) Simplified map of the Bahia road area showing the location of points where paleocurrent data were obtained by Nogueira (1995) from the fluvial strata of the Águas Claras Formation.....99

Figure 7.13- Evolutive stages envisaged for the Carajás foreland Basin during the Paleoproterozoic. (a) Underfilled stage (ca. 2.58–2.27 Ga): deposition of coarse-grained deposits (i.e., submarine fan conglomerate and sandstone) of the Serra Sul Formation. These deposits represent the basal deep marine sedimentation of the basin. (b) Filled stage (ca. 2.27–2.06 Ga): deposition of fine-grained deposits (i.e., rhythmite and sandstone) of the Azul Formation. These deposits represent the middle shallow marine sedimentation of the Carajás foreland basin. (c) Overfilled stage (ca. 2.06–1.88 Ga): deposition of coarse-grained deposits (i.e., sandstone and conglomerate) of the Águas Claras and Gorotire formations. These deposits represent the upper fluvial to alluvial sedimentation of the Carajás foreland basin 101

Figure 7.14- Paleogeographic reconstruction of the Carajás region (southeastern Amazonian Craton, Brazil) in two different evolutionary steps of the Carajás foreland basin evolution. (a) Paleogeographic scenario envisaged during the deposition of the Azul Formation, in which the Azul Sea bordered the Carajás protocontinent during its the maximum transgression. (b) Paleogeographic scenario envisaged during the deposition of the Águas Claras Formation, in which the Águas Claras fluvial system covered a large area of the Carajás protocontinent and nearby areas.....103

CAPÍTULO 8

Figure 8.1- Sumário estratigráfico e de eventos reconhecidos na Bacia de Carajás a partir dos resultados obtidos nesta tese, ocorridos na transição Neoarqueano-Paleoproterozoico. (a) Neoarqueano: deposição das dos espessas derrames de rochas vulcânicas associados ao vulcanismo Parauapebas em *ca.* 2,75 Ga. Camadas de BIF foram depositadas imediatamente acima dos estratos vulcânicos. (b) Sideriano–Riaciano: deposição de diamictito glacial, e depósitos de leque submarino associados a glaciação Serra Sul. (c) Riaciano: deposição da Formação Azul durante a fase transgressiva do mar Azul em direção ao protocontinente Carajás após *ca.* 2,27 Ga. Camadas enriquecidas com manganês foram depositadas nas partes distais marinhas em associação com depósitos de black shale. (d) Riaciano–Orosiriano: Deposição das formações Águas Claras e Gorotire em um sistema fluvial aluvial, como resultado de soerguimento tectônico causado pela movimentação convergente entre os domínios Carajás e Bacajá. (e) Orosiriano: colisão entre os domínios Carajás e Bacajá, inversão da Bacia de Carajás e colocação do Granito Carajás e enxames de diques em *ca.* 1,88 Ga. DS: discordância subaérea; SRM: superfície de regressão máxima; ZIM: zona de inundação máxima.....120

LISTA DE TABELAS

CAPÍTULO 4

Tabela 4.1- Descrição das amostras datadas nesse estudo por LA-ICP-MS e SHRIMP (U-Pb em zircão).....34

CAPÍTULO 7

Table 7.1- Summary of the main geochronological data available of the units of the Paleoproterozoic succession of the Carajás Basin (southeastern Amazonian Craton, Brazil). MDA: Maximum depositional age. LA-ICP-MS: laser ablation-inductively coupled plasma-mass spectrometry. SHRIMP: sensitive high-resolution ion microprobe. *Pb-Pb age.....78

Table 7.2- Detailed description of the samples dated (U-Pb zircon) in this study.....81

Table 7.3- Lithofacies and facies associations for the Azul and Águas Claras formations.....82

Table 7.4- Summary of U-Pb (LA-ICP-MS and SHRIMP) zircon dating results.....92

SUMÁRIO

DEDICATÓRIA ... iv
AGRADECIMENTOS ... v
EPÍGRAFE ... vii
RESUMO ... viii
ABSTRACT ... x
LISTA DE ILUSTRAÇÕES ... xii
LISTA DE TABELAS ... xxii

1 INTRODUÇÃO ... 01
1.1 APRESENTAÇÃO ... 01
1.2 ORGANIZAÇÃO DA TESE ... 03
1.3 ÁREA DE ESTUDO ... 04
1.4 OBJETIVOS ... 06
1.5 HIPÓTESES INICIAIS DE TRABALHO ... 06
1.6 JUSTIFICATIVAS ... 07
1.7 PROBLEMÁTICAS DE ESTUDO ... 07

2 CONTEXTO GEOLÓGICO ... 09
2.1 O CRÁTON AMAZÔNICO E A PROVÍNCIA CARAJÁS ... 09
2.2 A BACIA DE CARAJÁS ... 12
2.2.1 O termo "Bacia de Carajás" e as diferentes propostas estratigráficas ... 12
2.2.2 A sucessão vulcano-sedimentar ... 12
2.2.2.1 O Grupo Grão-Pará ... 12
*2.2.2.1.1 A Formação Parauapeba*s ... 15
2.2.2.1.2 A Formação Carajás ... 15
2.2.2.1.3 A Formação Igarapé Bahia ... 16
2.2.2.2 A Formação Serra Sul ... 17
2.2.2.3 A Formação Azul ... 18
2.2.2.4 A Formação Águas Claras ... 19
2.2.2.5 A Formação Gorotire ... 19
2.2.2.6 Os diques intrusivos de *ca*. 1,88 Ga e o Granito Carajás ... 20

3 OS EVENTOS NA TRANSIÇÃO NEOARQUEANO-PALEOPROTEROZOICO ... 22
3.1 PRÉ-CAMBRIANO VS. FANEROZOICO ... 22

3.2 O GRANDE EVENTO DE OXIGENAÇÃO (GOE) E O EVENTO GLACIAL HURONIANO (HGE) 23
3.3 ASPECTOS PALEOGEOGRÁFICOS 28

4 MATERIAIS E MÉTODOS 30
4.1 DESCRIÇÃO DOS TESTEMUNHOS DE SONDAGEM 30
4.2 ANÁLISE DE FÁCIES E ESTRATIGRÁFICA 31
4.3 PETROGRAFIA SEDIMENTAR E CARACTERIZAÇÃO TEXTURAL 32
4.4. GEOCRONOLOGIA U-Pb EM ZIRCÃO 32
4.4.1 Preparação geral das amostras 32
4.4.2 Datação por LA-ICP-MS 33
4.4.3 Datação por SHRIMP 35
4.5 ANÁLISE MINERALÓGICA E QUÍMICA 35
4.6 MICROSCOPIA ELETRÔNICA DE VARREDURA 35

5 SERRA SUL DIAMICTITE OF THE CARAJÁS BASIN (BRAZIL): A PALEOPROTEROZOIC GLACIATION ON THE AMAZONIAN CRATON 37

6 EVIDENCES OF AN 'OIL-LIKE' MANGANESE REMOBILIZATION IN THE PALEOPROTEROZOIC AZUL RED BEDS OF THE CARAJÁS BASIN (AMAZONIAN CRATON, BRAZIL): AN INTERPLAY AMONG SEDIMENTARY AND TECTONIC CONTROLS 43
6.1 INTRODUCTION 44
6.2 GEOLOGICAL BACKGROUND 46
6.3 MATERIALS AND METHODS 48
6.4 THE MANGANESE-BEARING SUCCESSION 50
6.4.1 Stratigraphic and sedimentological aspects 50
6.4.2 Structural setting 52
6.4.2.1 The structural transects and patterns of deformation 52
6.4.2.2 Manganese and tectonic 53
6.4.3 The identified manganese-bearing minerals 56
6.5 DISCUSSION 58
6.5.1 Sedimentary environment and model of primary manganese deposition 58
6.5.2 Model of secondary manganese enrichment 60
6.6 FINAL REMARKS 62

7 TECTONO-SEDIMENTARY EVOLUTION OF A PALEOPROTEROZOIC SUCCESSION OF THE CARAJÁS BASIN, SOUTHEASTERN AMAZONIAN CRATON, BRAZIL: INSIGHTS FROM STRATIGRAPHY, SEDIMENTOLOGY, AND U-Pb DETRITAL ZIRCON GEOCHRONOLOGY 72
7.1 INTRODUCTION 73
7.2 GEOLOGICAL SETTING 74
7.3 MATERIALS AND METHODS 79
7.4 STRATIGRAPHY AND SEDIMENTOLOGY 81
7.4.1 Stratigraphic framework of the studied succession 81
7.4.2 Facies associations 84
7.4.2.1 Azul Formation 84
7.4.2.1.1 Rhythmite Facies Association (RFA) 84
7.4.2.1.2 Rhythmite-Sandstone Facies Association (RSFA) 84
7.4.2.2 Águas Claras Formation 85
7.4.2.2.1 Sandstone-Conglomerate Facies Association (SCFA) 85
7.5 U-Pb ZIRCON GEOCHRONOLOGY 89
7.5.1 General zircon morphological features 89
7.5.2 Dating results 89
7.5.2.1 Azul Formation sample 89
7.5.2.2 Águas Claras Formation samples 90
7.6 DISCUSSION 94
7.6.1 Reconstructing the sedimentary environment 94
7.6.2 New insights on the sequence stratigraphy of the Carajás Basin 96
7.6.3 Provenance of studied succession: A proof of a connection between the Carajás and Bacajá domains during the Paleoproterozoic? 98
7.6.4 Unraveling the Carajás foreland basin 100
7.6.5 Implications on the Columbia supercontinent configuration and glimpses on the Paleogeographic scenario 102
7.7 CONCLUSIONS 104

8 CONSIDERAÇÕES FINAIS 117

REFERÊNCIAS 121

ANEXO A – ARTIGO: NEW STRATIGRAPHIC PROPOSAL OF A PALEOPROTEROZOIC SILICICLASTIC SUCCESSION: IMPLICATIONS FOR THE EVOLUTION OF THE CARAJÁS BASIN, AMAZONIAN CRATON, BRAZIL 139

ANEXO B – MATERIAL SUPLEMENTAR DO ARTIGO SERRA SUL DIAMICTITE OF THE CARAJÁS BASIN (BRAZIL): A PALEOPROTEROZOIC GLACIATION ON THE AMAZONIAN CRATON..... 157

ANEXO C – MATERIAL SUPLEMENTAR DO ARTIGO EVIDENCES OF AN "OIL-LIKE" MANGANESE REMOBILIZATION IN THE PALEOPROTEROZOIC AZUL RED BEDS OF THE CARAJÁS BASIN (AMAZONIAN CRATON, BRAZIL): AN INTERPLAY AMONG SEDIMENTARY AND TECTONIC CONTROLS..... 171

ANEXO D – MATERIAL SUPLEMENTAR DO ARTIGO TECTONO-SEDIMENTARY EVOLUTION OF A PALEOPROTEROZOIC SUCCESSION OF THE CARAJÁS BASIN, SOUTHEASTERN AMAZONIAN CRATON, BRAZIL: INSIGHTS FROM STRATIGRAPHY, SEDIMENTOLOGY, AND U-Pb DETRITAL ZIRCON GEOCHRONOLOGY 172

1 INTRODUÇÃO

1.1 APRESENTAÇÃO

Na borda sudeste do Cráton Amazônico, na região da Serra dos Carajás (Estado do Pará, norte do Brasil), uma sucessão vulcano-sedimentar com cerca de 5 km de espessura ocorre bem preservada em uma faixa sigmoidal de direção E-W com 90 x 40 km de dimensão, designada como Bacia de Carajás, estruturada a partir de uma tectônica transcorrente transamazônica por volta de 2,2–2,0 Ga (Cordani *et al*. 1984, Machado *et al.* 1991, Dall'Agnol *et al.* 1997, 2006, Macambira *et al.* 2009, Tavares *et al.* 2018). Devido a complexidade no entendimento estrutural e estratigráfico dessa área, a sucessão dessa bacia já foi organizada em diferentes propostas estratigráficas (Araújo *et al.* 1988, Docegeo 1988, Araújo & Maia 1991, Machado *et al.* 1991, Nogueira *et al.* 1995, Pinheiro & Holdsworth 1997a, 1997b, Pinheiro 1997, Macambira 2003, Tavares 2015, Tavares *et al.* 2018, Araújo & Nogueira 2019). De modo geral, a base da Bacia de Carajás é preenchida por espessos pacotes de rochas vulcânicas e estratos de formação ferrífera bandada depositados durante o Neoarqueano (Wirth *et al.* 1986, Gibbs *et al.* 1986, Olszewski *et al.* 1989, Lindenmayer *et al.* 2001, Meirelles & Dardenne 1991, Trendall *et al.* 1998, Macambira 2003, Cabral *et al.* 2013, 2017, Martins *et al.* 2017). Acima desses intervalos, depósitos predominantemente siliciclásticos com mais de 1,5 km de espessura, depositados durante o Paleoproterozoico, ocorrem empilhados em diferentes unidades litoestratigráficas (Araújo & Nogueira 2019, Araújo Filho *et al.* 2020).

As rochas vulcânicas e as unidades de formação ferrífera bandada já foram alvo de vários estudos, e são relativamente bem compreendidas do ponto de vista paleoambiental, tectônico, geoquímico, e geocronológico (Trendall *et al.* 1998, Tallarico *et al.* 2000, 2005, Dreher 2004, Dreher *et al*. 2005, Galarza *et al*. 2008, Martins *et al.* 2017, Melo *et al.* 2019, Lacasse *et al.* 2020). Por outro lado, ainda é restrito o conhecimento sobre o cenário geológico envolvido durante a sedimentação da sucessão siliciclástica dessa bacia, os ambientes deposicionais registrados, a sua evolução tectono-sedimentar, bem como, os seus padrões geocronológicos. Com base no estudo das rochas vulcânicas da base, diversos autores propuseram diferentes configurações geotectônicas para a instalação da Bacia de Carajás durante o Neoarqueano, como por exemplo: ambiente rifte associado a um sistema extensional pós-colisional, ambiente associado a subducção e bacia intracratônica (Docegeo 1988, Olszewski *et al.* 1989, Martins *et al.* 2017, Dardenne *et al.* 1988, Meirelles & Dardenne 1991, Machado *et al.* 1991). Entretanto, a evolução dessa bacia ao longo do Paleoproterozoico ainda é desconhecida.

A passagem entre o Neoarqueano e o Paleoproterozoico é marcada por uma série de modificações paleoambientais, e paleoclimáticas que propiciaram as condições ideais para o

surgimento, manutenção e proliferação da vida em larga escala na Terra. Entre estes eventos, o mais impressionante foi o surgimento de um sistema atmosfera-hidrosfera oxigenado por volta de 2.45 Ga, a partir do evento conhecido como "Grande Evento de Oxigenação" ou GOE (Bekker *et al.* 2004, Holland 2002). O GOE tem sido objeto de estudo de inúmeros trabalhos com relação a sua origem (fotossíntese e/ou vulcanismo), duração, extensão e seus efeitos para a origem da vida multicelular primitiva (Karhu & Holland 1996, Rye & Holland 1998, Aspler & Chiarenzelli 1998, Canfield *et al*. 2000, 2013, Kasting 2001, Kasting & Siefert 2002, Holland 2002, 2006, 2009, Bekker *et al*. 2004, 2010, Canfield 2005, Anbar *et al*. 2007, Bekker & Kaufman 2007, Lyons & Reinhard 2009, Frei *et al*. 2009, Konhauser *et al*. 2009, 2011, Farquhar *et al*. 2010, Tang *et al*. 2011, 2012, Young 2012, 2013a, 2013b, Lyons *et al*. 2014, Ciborowski & Kerr 2016, Bellefroid *et al.* 2018, Philippot *et al.* 2018, Eguchi *et al.* 2020).

O aumento de oxigênio na atmosfera terrestre durante o GOE, com consequente remoção de *greenshouse gases* (CH_4, CO_2, H_2S, H_2, etc.) da atmosfera tem sido postulado como responsável pela diminuição da temperatura global durante o início do Paleoproterozoico e instalação de diversos episódios glaciais ocorridos entre cerca de 2.45–2.2 Ga, denominados genericamente como "Evento Glacial Huroniano" ou HGE (Young *et al.* 2001, Hoffman 2013, Tang & Chen 2013, Young 2013a, 2013b, 2014, 2019, Somelar *et al.* 2020). O HGE foi iniciado de forma sincrônica ao GOE em cerca de 2.45 Ga (Bekker *et al.* 2004, Hoffman 2013). Alguns autores suportam a hipótese de que o HGE represente o primeiro episódio glacial de escala global (*snowball Earth*) da história da Terra (Evans *et al.* 1997, Kirschvink *et al.* 2000, Kopp *et al.* 2005, Hoffman 2013), enquanto outros, baseado nas contradições estratigráficas e geocronológicas desses intervalos glaciais, sugerem que o HGE pode ter sido controlado por fatores tipicamente locais/regionais ao invés de controles necessariamente globais (Young *et al.* 2014, Young 2019).

Estratos enriquecidos com manganês posicionados acima dos intervalos glaciais do Paleoproterozoico têm sido interpretados como evidência do aparecimento de uma biosfera aeróbica altamente produtiva como resultado da recuperação climática após o HGE (Kirschvink *et al* 2000, Sekine *et al.* 2011a). Em sucessões do Paleoproterozoico, esses estratos ocorrem geralmente empilhados com depósitos de *black shale*, e registram a sedimentação em uma bacia marinha rasa estratificada, onde o manganês foi depositado durante fases transgressivas associadas a saturação de águas rasas com oxigênio (Force & Cannon 1988, Roy 1997, 2006). Evidências de remobilização ou múltiplas remobilizações de óxidos de manganês através de sistemas de falhas e dobras, sob condições hidrotermais (*hypogene Mn-enrichment*) são

comumente reportadas em depósitos do Pré-Cambriano como resultado de uma tectônica regional (Ghosh *et al.* 2015, Jones 2011, Jones *et al.* 2013, Ossa Ossa *et al.* 2016).

Em termos paleogeográficos, durante o Arqueano, é geralmente especulado que dois supercontinentes existiram, um à norte, denominado de Kenorland, e outro a sul, denominado de Zimvaalbara. A quebra desses supercontinentes é geralmente sugerida como responsável pela geração de volumosos derrames vulcânicos no final do Neoarqueano e início do Paleoproterozoico, acima dos quais, estratos de formação ferrífera bandada tipo Lago Superior foram amplamente depositadas. É também sugerido que esse vulcanismo pode ter sido responsável pelo aumento no conteúdo de O_2 na atmosfera, que resultou no GOE e HGE (Kasting *et al.* 1993, Holland 2002, Aspler & Chiarenzelli 1998, Ciborowski & Kerr 2016). É sugerido ainda que outro supercontinente foi formado na transição entre o Paleoproterozoico e o Mesoproterozoico, conhecido como Columbia ou Nuna (Rogers & Santosh 2002, Zhao *et al*. 2002, 2004). Embora a influencia no registro sedimentar associado a formação do Columbia seja bem compreendida em diversos crátons ao redor do mundo, ainda são desconhecidos os efeitos tectono-sedimentares produzidos pela emergência desse supercontinente nas bacias marginais do proto-Cráton Amazônico durante o final do Paleoproterozoico.

Neste estudo, a investigação de parte da sucessão siliciclástica da Bacia de Carajás através de análise de fácies e estratigráfica, bem como, a análise de proveniência, suportado por trabalhos regionais prévios, permitiu o reconhecimento e sequenciamento de importantes eventos ocorridos na transição entre o Neoarqueano e o Paleoproterozoico dessa bacia. Alguns eventos reportados neste estudo constituem descobertas importantes para o Cráton Amazônico, e o inserem em um contexto global de inovações paleoambientais, paleoclimáticas e geotectônicas ocorridas na transição Neoarqueano-Paleoproterozoico.

1.2 ORGANIZAÇÃO DA TESE

Esta tese de doutorado está organizada em oito capítulos, e os seus resultados estão apresentados em forma de artigos científicos. O Capítulo 1 aborda os aspectos introdutórios do trabalho, que inclui a apresentação, organização da tese, a área de estudo, objetivos, hipóteses iniciais de trabalho, justificativa, e as problemáticas de estudo. O Capítulo 2 apresenta os materiais e métodos utilizados, que engloba os procedimentos empregados na descrição dos testemunhos de sondagem e as análises realizadas. O capítulo 3 aborda o contexto geológico regional, que inclui os aspectos geológicos do Cráton Amazônico e da Bacia de Carajás. O Capítulo 4 apresenta de forma sucinta os principais aspectos relacionados aos eventos

paleoclimáticos e paleoambientais ocorridos na transição Neoarqueano-Paleoproterozoico, como o GOE e o HGE. O Capítulo 5 apresenta o artigo científico intitulado *Serra Sul diamictite of the Carajás Basin (Brazil): A Paleoproterozoic glaciation on the Amazonian craton*. O artigo está publicado no periódico internacional *Geology* (Qualis A1 CAPES, na área de geociências), Volume 47, Número 12, 2019 (p. 1166–1170), e tem o autor desta tese como primeiro autor.

O Capítulo 6 apresenta o artigo científico intitulado *Evidences of an oil-like manganese migration in the azul red beds of the Carajás Basin (Amazonian craton, Brazil): An interplay among sedimentary and tectonic controls*. O manusccrito está em preparação, e tem o autor desta tese como primeiro autor. O Capítulo 7 apresenta o artigo científico intitulado *Tectono-sedimentary evolution of a Paleoproterozoic succession of the Carajás Basin, southeastern Amazonian Craton, Brazil: Insights from stratigraphy, sedimentology, and U-Pb detrital zircon geochronology*. O manuscrito está submetido ao periódico internacional *Precambrian Reseacrh* (Qualis A1 CAPES, na área de geociências), e tem o autor desta tese como primeiro autor. O Capítulo 8 apresenta as considerações finais desta tese de doutorado. As referências e os anexos encontram-se no final da tese. Os anexos compreendem majoritariamente o material suplementar dos artigos que compõem essa tese de doutorado. Por sua vez, o anexo A apresenta o artigo intitulado *New stratigraphic proposal of a Paleoproterozoic siliciclastic succession: Implications for the evolution of the Carajás Basin, Amazonian craton, Brazil*. O artigo está publicado no periódico internacional *Journal of South American Earth Sciences* (Qualis B1 CAPES, na área de geociências), no Volume 102, Ano 2020 (102665), e tem o autor desta tese como co-autor do artigo.

1.3 ÁREA DE ESTUDO

A área de estudo está localizada na região da Serra dos Carajás, à oeste da cidade de Parauapebas no sudeste do estado do Pará (PA), norte do Brasil. O município de Parauapebas (PA) foi a sede logística para os trabalhos de campo realizados entre os anos de 2015 a 2018. A área encontra-se limitada pelas longitudes 50°0'00"O e 50°45'00"O e latitudes 5°50'00"S e 6°20'00"S, nos domínios da folhas Serra dos Carajás (SB-22-Z-A-II) e Rio Itacaiúnas (SB-22-Z-A-I). Os pontos estudados, que incluem majoritariamente testemunhos de sondagem, e subordinadamente afloramentos em cortes de estrada e cava de mina a céu aberto, estão distribuídos em seis diferentes subáreas dentro da área de estudo: Mina do Azul; Estrada do Igarapé Bahia; Mina do Igarapé Bahia; Serra do Tarzan; e Serra Sul (Figura 1.1).

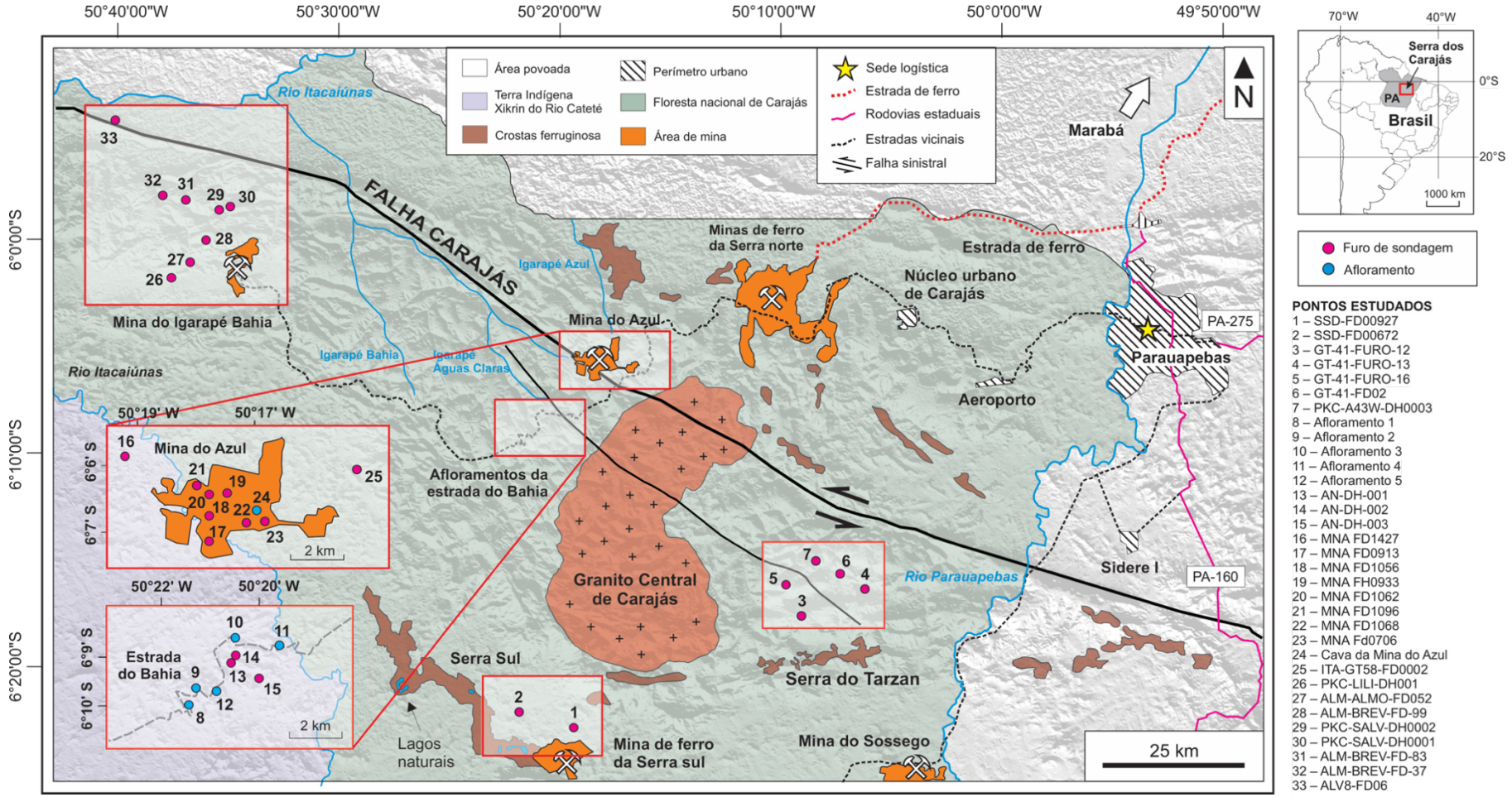

PONTOS ESTUDADOS

1 – SSD-FD00927
2 – SSD-FD00672
3 – GT-41-FURO-12
4 – GT-41-FURO-13
5 – GT-41-FURO-16
6 – GT-41-FD02
7 – PKC-A43W-DH0003
8 – Afloramento 1
9 – Afloramento 2
10 – Afloramento 3
11 – Afloramento 4
12 – Afloramento 5
13 – AN-DH-001
14 – AN-DH-002
15 – AN-DH-003
16 – MNA FD1427
17 – MNA FD0913
18 – MNA FD1056
19 – MNA FH0933
20 – MNA FD1062
21 – MNA FD1096
22 – MNA FD1068
23 – MNA Fd0706
24 – Cava da Mina do Azul
25 – ITA-GT58-FD0002
26 – PKC-LILI-DH001
27 – ALM-ALMO-FD052
28 – ALM-BREV-FD-99
29 – PKC-SALV-DH0002
30 – PKC-SALV-DH0001
31 – ALM-BREV-FD-83
32 – ALM-BREV-FD-37
33 – ALV8-FD06

Figura 1.1: Mapa de localização da área de estudo mostrando os pontos estudados na região da Serra dos Carajás, Estado do Pará (PA), Brasil.

1.4 OBJETIVOS

Esta tese de doutorado tem como objetivo geral caracterizar a estratigrafia e os eventos registrados na sucessão do Neoarqueano-Paleoproterozoico da Bacia de Carajás, no sudeste do Cráton Amazônico (Brasil). Para alcançar este objetivo geral, foram cumpridos os seguintes objetivos específicos:

1) Construção de um arcabouço estratigráfico da sucessão siliciclástica que preenche a Bacia de Carajás, a partir da compilação de dados estratigráficos publicados em trabalhos anteriores, e caracterização e proposição formal de novas unidades para esta bacia;

2) Interpretação das fácies e associação de fácies para reconstruções paleoambientais e inferências sobre mudanças nos regimes paleoclimáticos;

3) Reconhecimento de superfícies estratigráficas, para servirem como base para correlações estratigráficas e definição de sequencias deposicionais, bem como, para servirem de subsídios para interpretações evolutivas;

4) Definição das fases minerais e reconhecimento do arranjo estrutural da sucessão hospedeira da mineralização de manganês para compreensão da história evolutiva desses depósitos;

5) Caracterização da proveniência sedimentar de algumas unidades da Bacia de Carajás, como indicadores paleogeográficos e de mudanças tectônicas, relacionadas à emergência do supercontinente Columbia no final do Paleoproterozoico;

1.5 HIPÓTESES INICIAIS DE TRABALHO

Os questionamentos científicos que serviram como base para elaboração desta tese, e hipóteses iniciais de trabalho foram:

1) Os depósitos siliciclásticos do Grupo Igarapé-Bahia (ou outra unidade?) são de origem glacial ou estritamente relacionado a um sistema de leque submarino? Existe alguma correlação desses depósitos com eventos de escala global?

2) A sucessão que hospeda o manganês foi depositada em um sistema marinho? Qual seria o melhor modelo de deposição do manganês hospedado na Formação Águas Claras (ou outra unidade?)? O manganês é de origem primária ou secundária? Qual o modelo de enriquecimento do minério? Qual a idade máxima de deposição para estes depósitos?

3) É possível que os dados sedimentológicos e estratigráficos sirvam para reconstruções paleoambientais, paleoclimáticas e paleogeográficas ocorridas na transição Neoarqueano-Paleoproterozoico, como o GOE e o HGE? E ainda, existe implicação desses dados para a evolução geodinâmica do Craton Amazônico nesse período?

1.6 JUSTIFICATIVAS

As principais justificativas que motivaram o estudo da sucessão do Neoarqueano-Paleoproterozoico da Bacia de Carajás foram:

1) Apesar dos inúmeros trabalhos na região de Carajás, motivados principalmente pelo gigantesco potencial mineral da área, a Bacia de Carajás ainda carece de estudos estratigráficos e sedimentológicos de detalhe, que permitam uma compreensão precisa do seu arcabouço estratigráfico;

2) A hipótese de uma bacia originada e desenvolvida em um curto intervalo de tempo, estritamente durante o Neoarqueano, ainda persiste em muitas publicações especializadas sobre a região de Carajás;

3) Pouco se conhece a respeito da evolução da Bacia de Carajás após a sua origem provavelmente como um rifte em cerca de 2.75 Ga. A história evolutiva dessa bacia durante o Paleoproterozoico ainda é incerta;

4) A reconstrução paleoambiental, paleogeográfica e paleoclimática de unidades siliciclásticas da Bacia de Carajás é importante para traçar os eventos ocorridos no Cráton Amazônico durante o Neoarqueano-Paleoproterozoico, que podem estar relacionados a eventos de escala global, ainda não reconhecidos neste cráton.

1.7 PROBLEMÁTICAS DE ESTUDO

As principais problemáticas no estudo da sucessão do Neoarqueano-Paleoproterozoico da Bacia de Carajás são:

1) Ausência de afloramentos. A densa cobertura vegetal da região amazônica juntamente com o intenso intemperismo físico e químico impedem a visualização completa das unidades em campo. Além disso, raros são os afloramentos conhecidos dentro da Bacia de Carajás (e.g., os afloramentos ao longo da estrada do Igarapé Bahia). Essa problemática faz com que a maioria das informações estratigráficas dessa bacia estejam restritas a furos de sondagem. Apesar da investigação de testemunhos de sondagem ser uma ferramenta importante para o estudo desses depósitos, dados sedimentológicos e estratigráficos cruciais para interpretações paleoambientais (e.g., dados de paleocorrente, geometria de camadas, reconhecimento de superfícies e geometria de estruturas sedimentares) muitas vezes são impedidos de serem obtidos pela própria limitação física imposta pelo material de estudo. Além disso, o estudo a partir de testemunhos de sondagem impede uma visualização precisa do arranjo geométrico e extensão lateral do depósito, da distribuição lateral das fácies e associação de fácies, bem como, o padrão de empilhamento registrado;

2) Alteração secundária dos litotipos. Processos como intemperismo, hidrotermalismo e metamorfismo que tendem a modificar a mineralogia e as texturas originais das rochas são recorrentemente observados na sucessão da Bacia de Carajás. O intenso intemperismo químico tende a modificar grãos instáveis do arcabouço, geralmente transformando-os em argilominerais (e.g., caulinitização). O metamorfismo, mesmo que de baixo grau metamórfico, em intervalos específicos, tende a modificar a mineralogia e textura original dos litotipos. Similarmente, a percolação de fluídos hidrotermais modifica a mineralogia primária (e.g., cloritização, silicificação);

3) Baixa resolução estratigráfica das unidades. Os testemunhos de sondagem embora permitam o estudo de sucessões sedimentares em subsuperfície, são pouco profundos em relação a espessura das unidades. As unidades são geralmente muito mais espessas do que a profundidade dos furos de sondagem. Algumas unidades atingem até quase 1 km de espessura (e.g., Formação Águas Claras), enquanto que os furos de sondagem são geralmente da ordem de 300-500 m de profundidade. O empilhamento preciso dos depósitos só pode ser feito quando se estuda um conjunto de furos de sondagem, e se reconhecem padrões de empilhamento e superfícies estratigráficas. Adicionalmente, a descontinuidade lateral dos estratos como resultado de erosão e deformação, muitas vezes impedem a correlação entre as unidades.

2 CONTEXTO GEOLÓGICO

2.1 O CRÁTON AMAZÔNICO E A PROVÍNCIA CARAJÁS

O Cráton Amazônico, encerra dois escudos de idade pré-cambriana, o Escudo das Guianas, à norte, e o Escudo Brasil Central, à sul (Figura 2.1a). Esses dois escudos são separados por uma faixa de direção E-W representada pela sucessão dominantemente paleozoica da Bacia do Amazonas-Solimões (Tassinari & Macambira 2004). Esses autores subdividiram o Cráton Amazônico em seis províncias geocronológicas: Amazônia Central (>2,5 Ga); Maroni-Itacaiúnas (2,2–1,95 Ga); Ventuari-Tapajós (1,95–1,8 Ga); Rio Negro-Juruena (1,8–1,55 Ga); Rondoniana-São Ignácio (1,5–1,3 Ga); e Sunsás (1,25–1,0 Ga). A Província Carajás está localizada no Escudo Brasil Central, na Província Geocronológica Amazônia Central. Essa província é limitada a norte pelo Domínio Bacajá, a sul pelo Domínio Santana do Araguaia, a leste pelo Domínio Iriri-Xingu e a oeste pelo Cinturão Araguaia (Vasquez *et al.* 2008a, 2008b).

A Província Carajás é dividida à norte pelo Domínio Carajás (DC), e à sul pelo Domínio Rio Maria (DRM), também denominado de Terreno Granito-Greenstone de Rio Maria (Figura 2.1b, Dall'Agnol *et al.* 2013). O DC é constituído a norte pela Bacia de Carajás (Figura 2.2) e a sul pelo Subdomínio de Transição (Souza *et al.* 1996, Dall'Agnol *et al.* 1997, 2006, 2013). O embasamento da Bacia de Carajás, também denominada sigmoide central de Carajás (Araújo *et al.* 1988, Araújo & Maia 1991, Pinheiro 1997, Pinheiro & Holdsworth 1997a, 1997b, Holdsworth & Pinheiro 2000) é constituído por rochas ígneas e metamórficas, que inclui associações de tonalito–trondhjemito–granodiorito (TTG), com idade de metamorfismo em torno de 2,85 Ga atribuídos ao denominado Complexo Xingu (Machado *et al.* 1991).

Durante o Ciclo Orogenético Transamazônico ocorrido em torno de 2,2–2,0 Ga (Cordani *et al.* 1984, Machado *et al.* 1991, Macambira *et al.* 2009, Tavares 2015, Tavares *et al.* 2018), grande parte da Bacia de Carajás foi deformada em diferentes segmentos, com diferentes graus de deformação. Esse ciclo orogenético foi o último grande evento tectônico que afetou a bacia, e provavelmente foi responsável por moldar a Bacia de Carajás em uma geometria sigmoidal. Outras coberturas da região da Província Carajás e circunvizinhanças, embora apresentem deformações e graus de metamorfismo diferentes, apresentam arranjos geométricos semelhantes (e.g, Bacia de Buritirama, Bacia do Aquiri, Serra Pelada, etc.), o que sugere que tenham sido deformadas sincronicamente durante este evento.

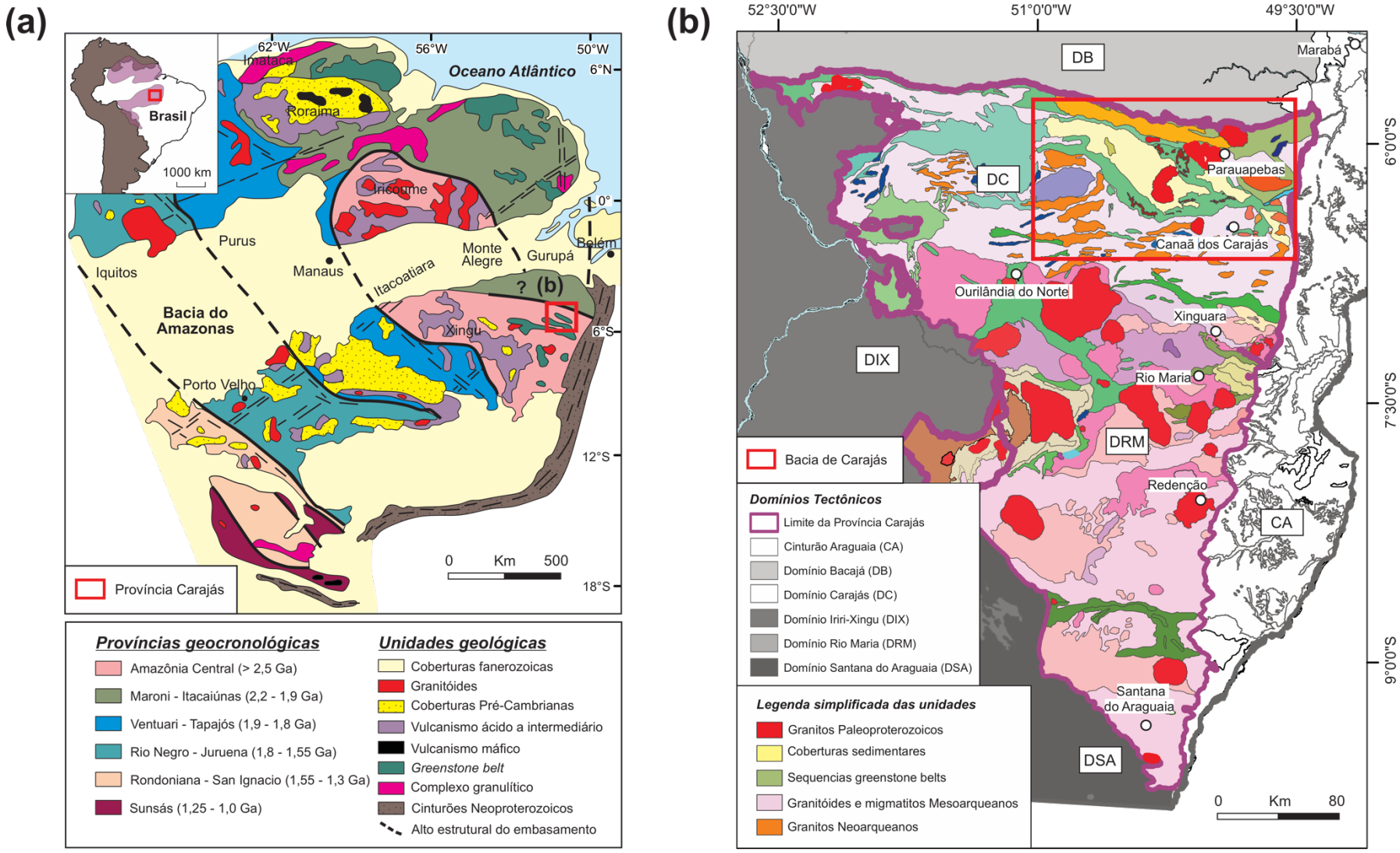

Figura 2.1: O Cráton Amazônico e a Província Carajás. (a) Distribuição das províncias geocronológicas do Cráton Amazônico (Tassinari & Macambira, 2004). (b) Mapa geológico da Província Carajás (adaptado de Vasquez *et al.* 2008a).

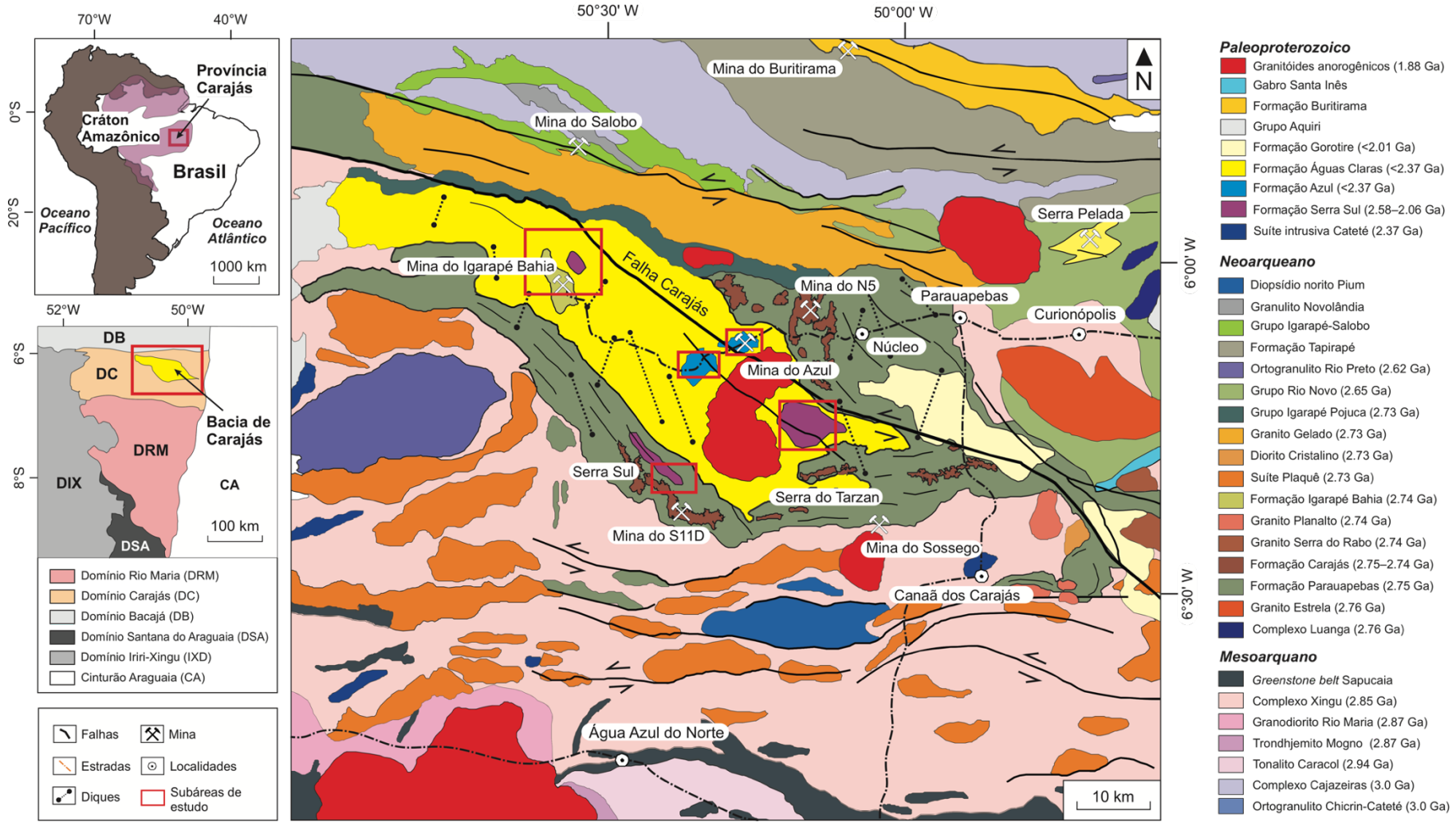

Figura 2.2: Mapa geológico da Bacia de Carajás mostrando as subáreas de estudo (modificado de Vasquez *et al.* 2008a). Os limites das novas unidades propostas para esta bacia (formações Serra Sul e Azul) descritas em Araújo & Nogueira (2019) e Araújo Filho *et al.* (2020), respectivamente, estão sendo apresentados.

2.2 A BACIA DE CARAJÁS

2.2.1 O termo “Bacia de Carajás” e as diferentes propostas estratigráficas

A utilização do termo “Bacia de Carajás” na bibliografia especializada ainda é controversa. Muitos autores utilizam esse termo para se referir a área geográfica ocupada pelo sigmoide da Serra dos Carajás, enquanto outros, não utilizam este termo por considerarem o sigmoide central de Carajás apenas um relicto de uma bacia antiga muito mais ampla do que os seus limites atuais. Aqui neste estudo, nós recomendamos fortemente o uso do termo “Bacia de Carajás” tanto do ponto de vista descritivo, para se referir a área geográfica em formato sigmoidal que aflora na região da Serra dos Carajás, bem como do ponto de vista genético, para se referir a bacia precursora na qual foi depositado a sucessão vulcano-sedimentar durante o final do Neoarqueano e início do Paleoproterozoico.

Diferentes propostas estratigráficas foram apresentadas para a região de Carajás nas últimas décadas (Figura 2.3; Docegeo 1988, Araújo *et al.* 1988, Araújo & Maia 1991, Nogueira *et al.* 1995, Pinheiro & Holdsworth 1997a, 1997b, Macambira 2003, Tavares *et al.* 2018). Os resultados desta tese de doutorado permitiram que fosse realizada uma revisão da coluna estratigráfica da Bacia de Carajás (Figura 2.4). Os principais resultados são apresentados em Araújo & Nogueira (2019), Araújo Filho *et al.* (2020), e Araújo *et al.* (submetido). Nesses estudos, duas novas unidades foram formalmente propostas: a Formação Serra Sul e a Formação Azul. Além disso, vários aspectos relacionados a estratigrafia desta bacia foram revistos, como a redefinição de unidades e a mudanças de categorias litoestratigráficas. As unidades que preenchem a Bacia de Carajás, de acordo com a revisão estratigráfica realizada neste estudo, estão sendo sucintamente descritas a seguir.

2.2.2 A sucessão vulcano-sedimentar

2.2.2.1 O Grupo Grão-Pará

O Grupo Grão-Pará (Docegeo 1988) encerra dominantemente um espesso pacote de rochas vulcânicas e formação ferrífera bandada (BIF) do Neoarqueano, cortados por diques e soleiras de gabro tardios (Beisiegel *et al.* 1973). O Grupo Grão-Pará ocorre na base da estrutura sinformal da Serra do Carajás (Docegeo 1988), em não conformidade com rochas do embasamento associadas ao Complexo Xingu (Trendall *et al.* 1998). A presença de feições sedimentares e de texturas ígneas preservadas apontam para condições de baixo grau metamórfico, apesar de apresentarem evidências de hidrotermalismo em diversos estratos (Pinheiro 1997, Macambira 2003, Dreher 2004). Esse grupo é subdivido, da base para o topo, nas formações Parauapebas, Carajás e Igarapé Bahia.

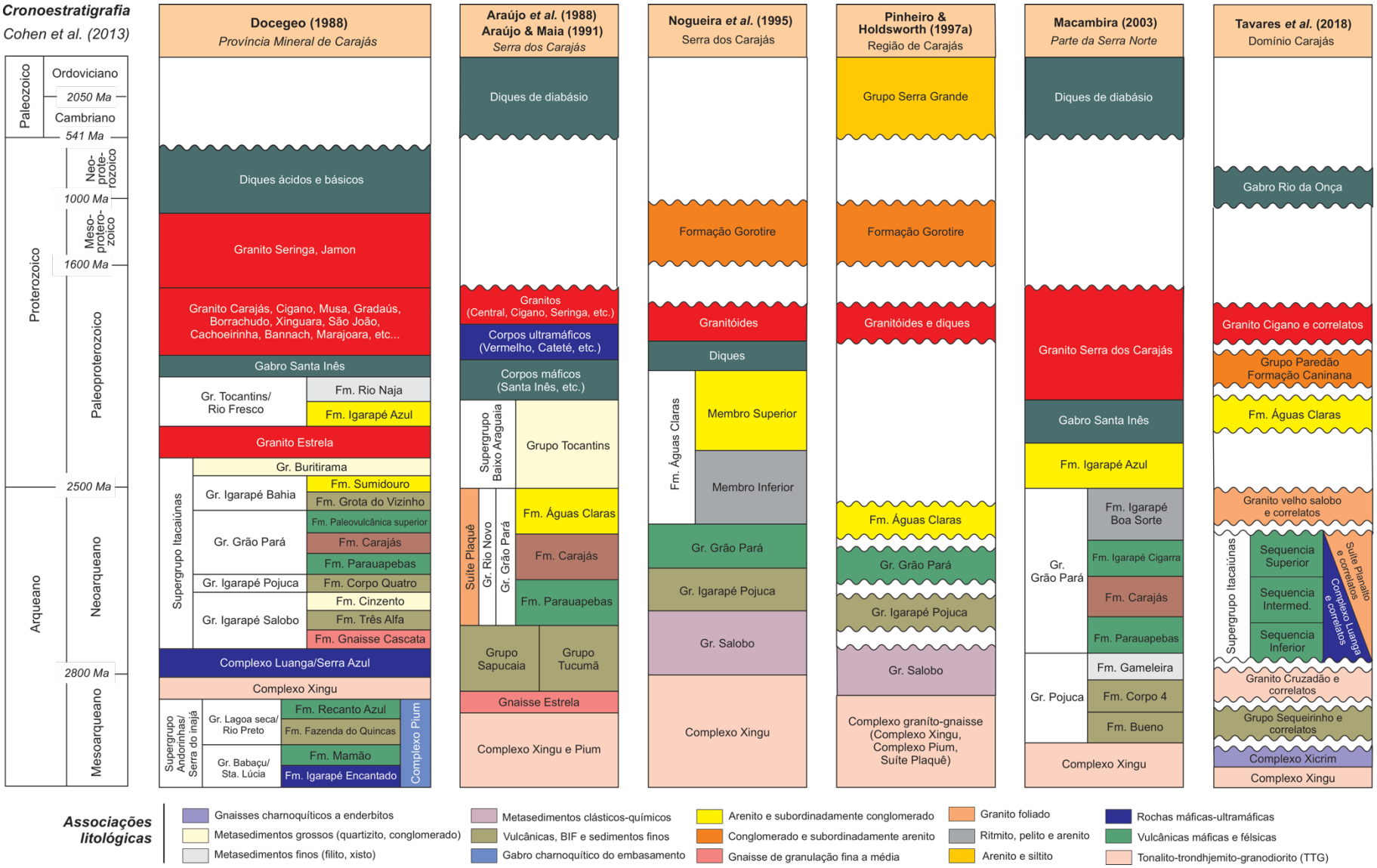

Figura 2.3: Comparação entre as diferentes propostas estratigráficas para a região de Carajás (sudeste do Cráton Amazônico, Brasil).

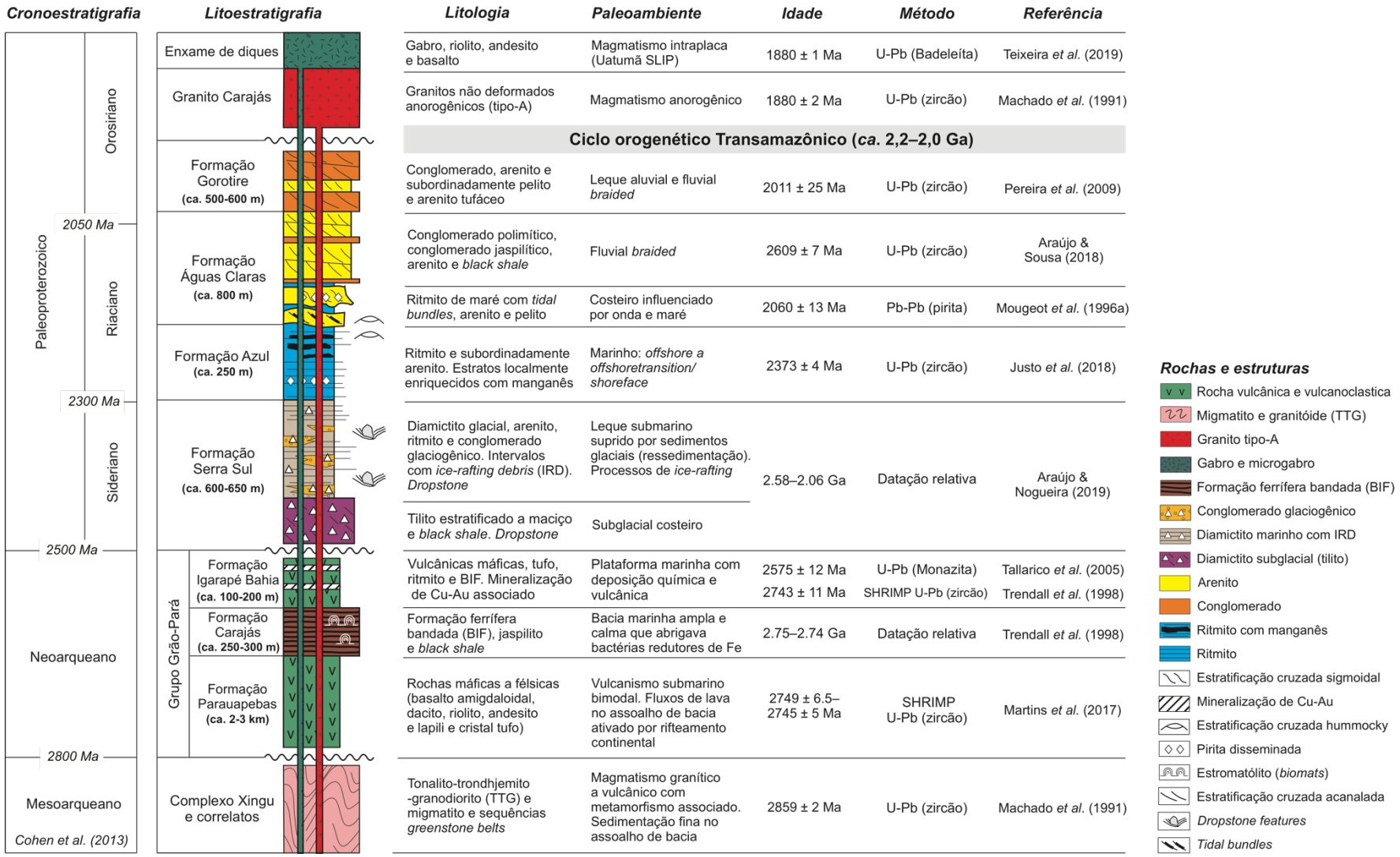

Figura 2.4: Coluna estratigráfica da Bacia de Carajás (sudeste do Cráton Amazônico, Brasil) revisada nesta tese de doutorado. Dados estratigráficos (relações de contato, espessura de unidades e padrão de empilhamento) compilados de Docegeo (1988), Machado *et al.* (1991), Nogueira *et al.* (1995), Dias *et al.* (1996), Pinheiro (1997), Cabral *et al.* (2013), Araújo & Nogueira (2019), e Araújo Filho *et al.* (2020).

2.2.2.1.1 A Formação Parauapebas

A Formação Parauapebas é constituída dominantemente por basalto e basalto andesítico que variam de acinzentado a esverdeado, amigdaloidal, porfirítico, afanítico ou de granulação fina, e hipocristalinos (Martins *et al.* 2017). Estas rochas constituem uma sucessão originada a partir de fluxos de lava, que atinge até 2–3 km de espessura (Cabral *et al.* 2013). A assembleia mineral primária é constituída dominantemente por clinopiroxênio e plagioclásio. A ocorrência de riolito, lapilli tufo e cristal tufo sugere vulcanismo bimodal máfico a félsico (Gibbs *et al.* 1986). O magmatismo máfico foi interpretado como gerado em um ambiente extensional de rifte continental (Gibbs *et al.* 1986, Olszewski *et al.* 1989, Macambira, 2003) ou em arco de ilha associado a zona de subducção (Meirelles 1986, Meirelles & Dardene 1991, Teixeira 1994, Lindenmayer *et al.* 2001). Idades U-Pb em zircão extraídos de rochas vulcânicas ácidas de 2760 ± 11 Ma (Trendall *et al.* 1998), 2759 ± 2 Ma (Machado *et al.* 1991) e 2758 ± 39 Ma (Wirth *et al.* 1986, Olszewski *et al.* 1989) indicam um extenso vulcanismo Neoarqueano, no estágio inicial de preenchimento da Bacia de Carajás. De acordo com Martins *et al*. (2017), embora a assinatura geoquímica não descarte um ambiente de *back-arc*, os fluxos de lava associados a deposição da Formação Parauapebas, é resultado de uma configuração extensional através de um rifte continental originado a partir de uma configuração pós-orogênica na passagem do Mesoarqueano para o Neoarqueano.

2.2.2.1.2 A Formação Carajás

A Formação Carajás (Beisiegel *et al.* 1973) compreende dominantemente estratos de formação ferrífera bandada (BIF), que ocorrem intercalados com depósitos de *black shale* e jaspilito, os quais ocorrem de forma subordinada (Machado *et al*. 1991, Trendall *et al.* 1998). Hematita ocorre como óxido de ferro principal (Lindenmayer *et al.* 2001). A espessura da unidade é estimada em aproximadamente 250–300 m (Cabral *et al.* 2017), embora alguns autores estimem que essa unidade atinja em subsuperfície até 400 m (Trendall *et al.* 1998). É sugerido que as formações ferríferas tenham se depositado em uma plataforma marinha rasa, ampla e tectonicamente estável, provavelmente na zona fótica sob influência de organismos fotossintéticos, durante a transgressão do mar Carajás (Macambira 2003, Lindenmayer *et al.* 2001, Macambira & Schrank 2002). A datação de tufo concordante com as camadas de jaspilito fornece uma idade mínima de 2743 ± 11 Ma (Trendall *et al.* 1998) e 2757± 18 Ma (Macambira *et al.* 1996) para a Formação Carajás.

Trendall *et al.* (1998) utilizou a idade de cerca de 2,74 Ga e a idade do basalto subjacente da Formação Parauapebas de cerca de 2,75 Ga, para sugerir que as unidades de BIF da

Formação Carajás foram depositadas entre 2,75–2,74 Ga, enquanto que dados de Sm-Nd indicam idades de 2593 ± 260 Ma e 1701 ± 97 Ma para eventos hidrotermais (Macambira *et al.* 1990). Evidências biogênicas associadas ao carbono presente em camadas de *black shale*, sugerem que as camadas de BIF da Formação Carajás podem ter sido originadas através de esteiras microbianas que habitavam o mar Carajás, no qual bactérias redutoras de ferro foram responsáveis pela deposição das camadas de BIF. É sugerido que esses organismos eram formados por uma ou mais espécies que produziram provavelmente grandes colônias de estromatólitos durante o Neoarqueano (Luz & Crowley 2012).

2.2.2.1.3 A Formação Igarapé Bahia

Sobrejacente a Formação Carajás ocorre uma unidade vulcânica superior com sedimentação clástica associada, a qual contem expressivos depósitos de Cu-Au (Tallarico *et al.* 2000, 2005, Galarza *et al.* 2003, 2008, Dreher 2004, Dreher *et al.* 2008). Docegeo (1988) descreveu essa unidade originalmente como Grupo Igarapé Bahia, considerada como uma sequência vulcanossedimentar, de baixo grau metamórfico pertencente ao Supergrupo Itacaiúnas, que aflora em uma janela erosiva dentro da Formação Águas Claras (Galarza *et al.* 2003, 2008). De acordo com Macambira (2010), o Grupo Igarapé Bahia corresponderia a denominada Formação Igarapé Cigarra proposta em Macambira *et al.* (1990) e Macambira (2003). De acordo com Docegeo (1988) esse grupo poderia ser dividido em duas formações: Formação Grota do Vizinho (metabasalto hidrotermalizado, metapelito, *wacke*, ritmito, formação ferrífera com magnetita, carbonato e sulfetos, rochas metapiroclasticas ácidas e intermediárias e brechas mineralizadas com Cu-Au, com fragmentos de formação ferrífera bandada, chert, púmice e rochas básicas) e Formação Sumidouro (metarenito, em parte arcoseano e ferruginoso, com intercalações de metabasalto).

Dreher (2004) descreveu estas mesmas rochas em testemunhos de sondagem, atribuindo rochas vulcânicas e piroclásticas na sua porção inferior à Formação Grota do Vizinho, e o conjunto de rochas piroclásticas e clásticas finas na sua porção superior à Formação Sumidouro. Araújo Filho *et al.* (2020), sugeriram que a Formação Sumidouro do Grupo Igarapé Bahia representa, na realidade, parte da Formação Águas claras, e concluiu que dessa forma é injustificada a classificação da unidade Igarapé Bahia como grupo e optou por designar essa unidade como Formação Igarapé Bahia, anteriormente já designada como formação em Araújo & Nogueira (2019). Nesse contexto, a Formação Igarapé Bahia designaria um conjunto de rochas vulcânicas intercaladas subordinadamente com rochas siliciclásticas finas (ritmitos) que ocorrem logo acima da Formação Carajás e na parte basal da mina do Igarapé Bahia.

As rochas metavulcânicas encaixantes da mineralização de Cu-Au apresentam idades U-Pb em zircão da ordem de 2,74–2,75 Ga (Galarza *et al.* 2002, Santos 2002, Tallarico *et al.* 2002) e idades Pb-Pb em zircão de 2748 ± 34 Ma (Tallarico *et al.* 2005). A datação Pb-Pb em calcopirita de brechas hidrotermais e metavulcânica, metapiroclástica, e diques revelaram idades de 2772 ± 46, 2756 ± 24, 2754 ± 36, e 2777 ± 22 Ma, respectivamente (Galarza *et al.* 2008). De forma similar, a datação de ouro revelou idade de 2744 ± 12 Ma. Esse conjunto de idades foi interpretada como sugestivas de um vulcanismo Neoarqueano contemporâneo a mineralização de Cu-Au por volta de 2,74–2,75 Ga. Por outro lado, idades de 2385 ± 122 e 2417 ± 120 Ma também em calcopirita sugerem remobilização da mineralização de Cu-Au (Galarza *et al.* 2008). De forma similar, a datação U-Pb (SHRIMP) em monazita, proveniente da matriz de brechas ricas em magnetita, revelou idade de 2575 ± 12 Ma para a mineralização, confirmando a sua natureza epigenética (Tallarico *et al.* 2005).

2.2.2.2 A Formação Serra Sul

Cabral *et al.* (2013) investigando isótopos de enxofre (*mass-independent S-isotope fractionation*—MIF-S) a partir de piritas associadas a camadas de *black shale*, que ocorrem intercaladas a camadas de BIF na área de Serra Sul, descreveram brechas com matriz rica em magnetita e clastos de formação ferrífera, as quais eles interpretaram como relacionadas a processos hidrotermais. Araújo & Nogueira (2019) reavaliaram esses estratos e propuseram que eles pertenceriam a uma nova unidade, ainda não reconhecida na Bacia de Carajás. Com base na designação original de Cabral *et al.* (2013) que denominaram esses estratos como sucessão Serra Sul, Araújo & Nogueira (2019) propuseram uma nova formação para a Bacia de Carajás, denominada de Formação Serra Sul.

Segundo Araújo & Nogueira (2019), essa unidade ocorre em discordância acima das camadas de BIF da Formação Carajás, bem como, acima de camadas de rochas vulcânicas do Neoarqueano. A Formação Serra Sul compreende, da base para o topo, diamictitos glaciais foliados a maciços que ocorrem intercalados com camadas de *black shale*, conglomerados polimíticos de origem glacial, que ocorrem intercalados com camadas de ritmito, e camadas espessas de ritmito no topo. Os clastos são constituídos predominantemente por fragmentos de BIF, vulcânicas máficas e félsicas, jaspilito e chert, o que sugere que os estratos pré-glaciais (unidades de BIF e rochas vulcânicas) funcionaram não somente como substrato principal para o sistema glacial Serra Sul, mas também como fonte principal de sedimentos. Diamictitos foliados apresentam matriz rica em quartzo e magnetita e foram interpretados como produtos de erosão subglacial (i.e., tilito). Por outro lado, diamictitos com matriz rica em lama e com

dropstone features foram interpretados como diamictitos marinhos produzidos por processos de ressedimentação através de sistema de leque submarino e *ice-rafting*.

Ainda de acordo com Araújo & Nogueira (2019), o topo da unidade é constituído dominantemente por camadas espessas de ritmito (>60 m de espessura), enquanto que o seu contato superior foi observado apenas com Formação Águas Claras. Esses autores com base em datação relativa propuseram que a Formação Serra Sul foi depositada provavelmente durante o Sideriano–Riaciano (cerca de 2,58–2,06 Ga). O diamictito Serra Sul representa o primeiro registro de rochas glaciais do Paleoproterozoico reportado na América do Sul. Em termos paleogeográficos, a ocorrência desses estratos no Cráton Amazônico expande o alcance das glaciações do Paleoproterozoico para esta parte do globo. Por outro lado, ainda de acordo com Araújo & Nogueira (2019), a Glaciação Serra Sul, que pode ser correlata com qualquer uma das glaciações ocorridas durante o Paleoproterozoico ligadas ao HGE, ou a nenhuma delas.

2.2.2.3 A Formação Azul

A Formação Azul foi definida formalmente no trabalho de Araújo Filho *et al.* (2020), como resultado da elevação de categoria do Membro Inferior da Formação Águas Claras, originalmente definida por Nogueira *et al.* (1995). Essa unidade corresponde ainda a denominada Formação Igarapé Boa Sorte proposta em Macambira *et al.* (1990) e Macambira (2003). A Formação Azul encerra estratos de ritmito, localmente enriquecidos em manganês, depositados em ambiente marinho plataformal. De acordo com Araújo Filho *et al.* (2020) a unidade Formação Azul foi designada com este nome por referência a sua área-tipo, a mina de manganês do azul, que por sua vez foi denominada dessa forma como referência ao Igarapé Azul que ocorre próximo a mina de manganês.

Segundo Araújo *et al.* (submetido), essa unidade compreende depósitos de *offshore* e *offshore transition/shoreface*, que gradam para depósitos costeiros a fluviais da Formação Águas Claras, como previamente sugerido em Nogueira (1995), Nogueira *et al.* (1995) e Araújo Filho *et al.* (2020). A datação U-Pb de grãos de zircão detrítico dessa unidade indicam uma população mais jovem entre 2,37–2,27 Ga (Justo *et al.* 2018, Araújo *et al.* submetido). Dados de isótopos de enxofre ($\Delta^{33}S$) obtidos por Fabre *et al.* (2011), a partir de piritas diagenéticas disseminadas em laminações de arenito de ritmitos da Formação Azul, indicam valores de MIF-S próximos de zero (0.013±0.003‰) o que sugere sedimentação em uma atmosfera rica em oxigênio, pós-GOE.

2.2.2.4 A Formação Águas Claras

A Formação Águas Claras foi inicialmente designada com este nome por Araújo *et al.* (1988) para designar rochas vulcano-sedimentares metamorfizadas em baixo grau metamórfico que flora na poção central do sigmoide de Carajás. A Formação Águas Claras foi redefinida no trabalho de Nogueira *et al.* (1995), como constituída por dois membros: Membro Inferior, que compreenderiam ritmito, pelito e subordinadamente arenito finos depositados em ambiente marinho; e o Membro Superior, que encerrariam dominantemente arenito grosso e conglomerado, e subordinadamente ritmito depositados em ambiente costeiro a fluvial, influenciados por processos de maré e tempestade.

Recentemente, no trabalho de Araújo Filho *et al.* (2020), a Formação Águas Claras foi novamente redefinida. Esses autores propuseram que essa unidade encerraria apenas estratos de arenito e conglomerado, depositados em um sistema fluvial tipo *braided*, que ocorrem em uma passagem gradacional a abrupta imediatamente acima da Formação Azul. Por sua vez, essas unidades seriam os correspondentes estratigráficos associados a uma sequencia transgressiva-regressiva, depositada nos estágios finais de sedimentação da Bacia de Carajás. Esses mesmos autores descreveram intervalos de tufos intercalados as camadas de arenitos, os quais interpretaram como produto de um vulcanismo subaéreo adjacente ao sistema fluvial Águas Claras. A área-tipo da unidade foi estabelecida na estrada que dá acesso a mina do Igarapé Bahia por Nogueira *et al.* (1995).

Na área da estrada do Igarapé Bahia, a Formação Águas Claras é cortada por enxames de diques de diferentes direções e com espessura superior a 150 metros, constituídos dominantemente por metagabros médios a grossos, com textura subofítica (Barros *et al.* 1992). A datação U-Pb de grãos de zircão detrítico indicam uma população mais jovem em torno de 2,6–2,7 Ga (Dias *et al.* 1996, Mougeot *et al.* 1996b, Trendall *et al.* 1998, Justo *et al.* 2018, Araújo & Sousa 2018). Embora Dias *et al.* (1996) tenham obtido uma idade de 2645 ± 12 Ma para os diques que cortam a Formação Águas Claras na sua área-tipo, essas idades tem sido consideradas como idades de grão de zircão detrítico herdados da rocha encaixante Araújo Filho *et al.* (2020). Dados de paleocorrente de estratos cruzados de origem fluviais e costeiro indicam paleofluxo principal para SW e SE (Nogueira 1995).

2.2.2.5 A Formação Gorotire

A Formação Gorotire foi inicialmente proposta por Barbosa *et al.* (1966) para se referir a uma unidade estritamente siliclástica que ocorre na região próximo à Serra dos Gradaús, em Redenção (PA). Docegeo (1988) utilizou este mesmo nome para designar rochas que ocorrem

acima de intervalos pelíticos na região de Rio Fresco. Pinheiro (1997) descreveu a ocorrências de arcósio e grauvaca arcosiana na região da Serra do Rabo (próximo a vila Cedere I, sudoeste da cidade de Parauapebas), sudeste da Bacia de Carajás, o qual correlacionou a Formação Gorotire. Para esse autor, a Formação Gorotire nessa região ocorre em associação com a Formação Águas Claras. Ele interpreta essa unidade como uma sucessão sedimentar imatura, recobrindo diretamente o Grupo Grão-Pará, embora o contato não tenha sido observado.

A Formação Gorotire compreende paraconglomerados polimíticos com seixos arredondados constituídos dominantemente por quartzo, arenito, BIF, gnaisse, granito e rochas vulcânicas, dispersos em uma matriz arenosa (Pinheiro 1997, Nascimento & Oliveira 2015). Lima & Pinheiro (2001) interpretaram que a Formação Gorotire foi depositada durante o Mesoproterozoico, a partir de uma sedimentação clástica grossa preencheu um *graben* a norte da Falha Carajás. Nascimento & Oliveira (2015) descreveram em detalhe as fácies sedimentares dessa unidade, atribuindo à sua deposição um sistema de leque aluvial a fluvial entrelaçado, com paleofluxo principal para NE e N, também controlado pelo sistema da Falha Carajás.

Dados geocronológicos obtidos da datação de grãos de zircão detrítico pelo método U-Pb indicam idade máxima de deposição para essa unidade em torno de 2011 ± 25 Ma (Pereira *et al.* 2009) e 2055 ± 54 Ma (Justo *et al.* 2018). Embora dúvidas ainda cerquem o real posicionamento estratigráfico da Formação Gorotire, com base nos dados disponíveis é plausível supor que essa unidade tenha se depositado em associação com a Formação Águas Claras nos estágios finais da sedimentação da Bacia de Carajás durante o Orosiriano. Pereira *et al.* (2009) estudando a Formação Gorotire na região da Serra Norte renomeou esta unidade informalmente como Formação Caninana atribuindo uma idade de sedimentação entre 2011-1880 Ma, como resultado da reativação da Falha Carajás.

2.2.2.6 Os diques intrusivos de *ca*. 1,88 Ga e o Granito Carajás

A região de Carajás e Rio Maria é cortada por enxames de diques datados em cerca de 1880 Ma, 1110 Ma, 535 Ma e 200 Ma (U-Pb em monazita, Teixeira *et al.* 2019). Os diques com cerca de 1,88 Ga são associados ao *Uatamã Silicic Large Igneous Province* (SLIP), como resultado a assembleia do supercontinente Columbia (Teixeira *et al.* 2019, Giovanardi *et al.* 2019). Valores isotópicos e de elementos traço sugerem que esta geração de diques está diretamente associada a uma configuração de supra-subducção ou pós-colisional (Giovanardi *et al.* 2019). Próximo também a idade de 1,88 Ga, ocorrem granitos anorogênicos truncando a região de Carajás e Rio Maria. Entre eles, o Granito Carajás, que aflora na porção central da Bacia de Carajás, datado em cerca de 1880 ± 2 Ma (U-Pb em zircão, Machado *et al.* 1991) e

1882 ± 10 Ma (SHRIMP U-Pb em zircão, Teixeira *et al.* 2018). Esse conjunto de granitos anorogênicos tem sido interpretado como produtos derivados essencialmente de fusão da base da crosta (Teixeira *et al.* 2019), enquanto outros autores, sugerem que esses granitos são pós-tectônicos em relação ao ciclo orogenético Transamazônico (Machado *et al.* 1991). Tanto os diques quanto o Granito Carajás, pós-datam a sucessão que preenche a Bacia de Carajás.

3 OS EVENTOS NA TRANSIÇÃO NEOARQUEANO–PALEOPROTEROZOICO

3.1 PRÉ-CAMBRIANO VS. FANEROZOICO

O pré-Cambriano corresponde a aproximadamente 88% da história geológica da Terra, e apresenta características particulares em relação ao Fanerozóico (Figura 3.1). Esse período engloba os estágios inicias de evolução da Terra, que inclui a formação das primeiras massas de terra, aparecimento dos primeiros organismos multicelulares fotossintetizantes, glaciações de escala global (*Paleoproterozoic and Neoproterozoic snowball Earth*) e o surgimento de uma atmosfera oxigenada a partir do Grande Evento de Oxigenação (GOE).

De acordo com Catuneanu *et al.* (2005), as principais diferenças no registro sedimentar entre os depósitos do Pré-Cambriano em relação ao Fanerozoico incluem:

1) As sucessões do Pré-cambriano geralmente apresentam um baixo potencial de preservação. Devido esses depósitos serem mais antigos, eles apresentam uma história geológica muito mais complexa, que envolve diversos episódios de tectonismo, metamorfismo e diagênese;
2) A escassez ou até mesmo ausência de fósseis impedem datações precisas. Métodos de datação radiométrica são amplamente empregados nesses depósitos, mas muitas vezes não permitem uma datação precisa dos estratos;
3) Os mecanismos de formação de bacias sedimentares durante o Pré-Cambriano são diferentes daqueles que operaram durante todo o Fanerozoico. Durante o Arqueano um regime concorrente de plumas e placas tectônicas foram responsáveis pelo crescimento e diferenciação crustal nesse período. É sugerido que somente a partir do final do Neoarqueano (ou Neoproterozoico) a tectônica de placas “moderna” começou a operar na Terra;
4) A intensidade e a duração dos processos parecem ter sido muito maiores durante o Pré-Cambriano. É sugerido que os ciclos eram muito mais prolongados. Grande quantidade de sedimentos foram produzidas em um longo intervalo de tempo, e depositados em bacias sedimentares com amplos espaços de acomodação;
5) A ausência de uma atmosfera rica em oxigênio e ausência de vegetação proporcionavam condições diferenciadas de intemperismo físico e químico.

Eventos	Pré-cambriano	Fanerozoico
Intervalo de tempo	ca. 88% da história da Terra	ca. 12% da história da Terra
Preservação das fácies sedimentares	Relativamente baixa (modificada por tectonismo, diagênese e metamorfismo)	Relativamente alta
Controle do tempo	Relativamente baixo (baseado em camadas-guia e baixa resolução geocronológica)	Relativamente alto (camadas-guia, bioestratigrafia, magneto-estratigrafia e radiocronologia)
Mecanismos de formação de bacias	Regime concorrentes de plumas tectônicas e placas tectônicas. Regimes erráticos	Regime de placas tectônicas. Regimes estáveis
Intensidade e duração dos processos	Relativamente alta (ciclos longos, altas taxas de intemperismo, erosão, transporte, deposição, litificação e diagênese)	Relativamente baixa. Duração e intensidade dos processos bem conhecida e estabelecida
Padrão de sedimentação	O Arqueano é caracterizado por sedimentação química-exalativa (BIF) com vulcanismo. No Proterozoico formam-se espessas sucessões siliciclásticas	Sedimentação bem conhecida. Eventos reconhecidos e correlacionáveis

Figura 3.1: Principais diferenças no registro sedimentar entre o Pré-Cambriano e o Fanerozóico (Catuneanu *et al.* 2005).

3.2 O GRANDE EVENTO DE OXIGENAÇÃO (GOE) E O EVENTO GLACIAL HURONIANO (HGE)

Duas escolas divergem quanto as causas para origem do Grande Evento de Oxigenação (*Great Oxidation Event*—GOE). A primeira escola, defende que o aparecimento de oxigênio em grande quantidade na atmosfera da Terra foi engatilhado por atividades vulcânicas ocorridas no final do Neoarqueano, como resultado da quebra dos primeiros supercontinentes Kenorland e Zimvaalbara nesse período (Aspler & Chiarenzelli 1998, Holland 2002, Ciborowski & Kerr 2016, Kump & Barley 2007). A segunda escola, defende que a oxigenação da atmosfera é resultado direto do aparecimento e estabelecimento da fotossíntese em larga escala, processada por cianobactérias em ambiente submarino (Kopp *et al.* 2005). Embora essas duas correntes teóricas divirjam sobre a origem e a evolução do oxigênio na atmosfera, ambos os mecanismos são atualmente sugeridos como responsáveis pela oxigenação da superfície da Terra. Embora o GOE seja datado por volta de 2,45–2,22 Ga (Bekker *et al.* 2004), dados de biomarcadores indicam que o surgimento de cianobactérias fotossintetizantes ocorreu por volta de 2,7 Ga

(Hedges & Kumar 2009, Brocks *et al.* 1999, 2003). Esses primeiros estágios de oxigenação antecederam em aproximadamente 250 milhões de anos o GOE, e são geralmente conhecidos como "borrifadas" (*whiffs*) de oxigênio. Apesar da magnitude e duração ainda permanecerem sem definição, é sugerido que esses eventos, foram responsáveis pelos primeiros estágios de oxigenação da atmosfera ainda no Neoarqueano (Anbar *et al.* 2007, Lyons *et al.* 2014).

É sugerido ainda que o aumento do oxigênio na superfície da Terra ocorreu em duas etapas: a primeira no Paleoproterozoico durante o GOE, no qual o oxigênio pode ser acumulado em níveis que puderam sustentar as primeiras formas de vida, e a segunda no Neoproterozoico, ocorrido por volta de 800–500 Ma (Och & Shields-Shou 2012) em um evento conhecido como *Neoproterozoic Oxidation Event* (NOE), associado às mudanças paleoambientais pós-glaciais (*snowball Earth*) nesse período (Figura 3.2). Durante o GOE, o aumento de O_2 na atmosfera ocasionou a diminuição de *greenhouse gases* (CH_4, CO_2, H_2S, H_2, etc.) responsáveis pela manutenção de um clima quente na Terra (Pavlov *et al*. 2000, Kump *et al.* 2013, Hoffman 2013). Por sua vez, a diminuição da temperatura global culminou na instalação de diversos episódios glaciais durante o Sideriano-Riaciano, conhecidos genericamente como Evento Glacial Huroniano (*Huronian Glacial Event*—HGE), em referência ao Supergrupo Huronian no Canadá, onde esses depósitos ocorrem mais bem preservados e de forma mais completa com quatro intervalos glaciais reconhecidos datados entre 2.45–2.2 Ga (Young 1970, 1991, 2014, 2019, Miall 1983, Young *et al.* 2001).

As causas e o tempo de duração do HGE ainda permanecem discutíveis, assim como, a sua extensão. A ocorrência de diamictitos em baixas latitudes suportam a hipótese de que essa glaciação represente o primeiro episódio *snowball Earth* da Terra (Evans *et al.* 1997, Hoffman 2013, Gumsley *et al.* 2017), enquanto outros trabalhos, sugerem que esses eventos glaciais podem ter sido controlados e terem tido uma extensão muito mais local/regional do que necessariamente global (Young 2014, 2019). O HGE foi seguido de intensa deposição de carbonato marinho, caracterizados por uma excursão positiva de $\delta^{13}C_{carb}$, conhecida como Evento Lomagundi–Jatuli, iniciado por volta de 2.22 Ga (Karhu & Holland 1996, Bekker *et al*. 2003). Martin *et al.* (2013), assumindo que o Evento Lomagundi–Jatuli tenha ocorrido de forma sincrônica globalmente, estimou que esse evento tenha durado entre 249 ± 9 Ma (2306 ± 9 Ma a 2057 ± 1 Ma) e 128 ± 9.4 Ma (2221 ± 5 Ma a 2106 ± 8 Ma). O fim do Evento Lomagundi–Jatuli é geralmente considerado coincidente com o final do GOE, em cerca de 2.1–2.0 Ga, muito embora o tempo e as relações entre esses eventos sejam discutíveis (Gumsley *et al.* 2017).

Diversos isótopos tem sido utilizados para traçar os caminhos da oxigenação da atmosfera terrestre (e.g., $\delta^{56}Fe$, $\delta^{53}Cr$, $\delta^{97/95}Mo$, $\delta^{98/95}Mo$, $\delta^{34}S$, $\Delta^{33}S$, Pufahl & Hiatt 2012). Entre esses, o mais utilizado é o *mass-independent fractionation of sulphur isotopes* (MIF-S), que persistiu em condições anóxicas até o estabelecimento do GOE por volta de 2,45 Ga. O desaparecimento do MIF-S do registro sedimentar é considerado uma das evidências mais consistentes para o aumento do oxigênio na atmosfera (Pavlov & Kasting 2002, Farquhar & Wing 2003, Bekker *et al.* 2004, Papineau *et al.* 2007, Kump 2008, Guo *et al.* 2009, Farquhar *et al*. 2010, Reinhard *et al.* 2013, Luo *et al.* 2016). Adicionalmente, outros indícios sedimentológicos, como o aparecimento de *red beds*, formação de paleosolos lateríticos, e o desaparecimento de pirita, siderita e uraninita detríticas, são considerados evidências robustas para a oxigenação da atmosfera a partir de 2,45 Ga (Figura 3.3, Pufahl & Hiatt 2012, Bekker & Holland 2012). A ocorrência de expressivos depósitos de manganês no Paleoproterozoico tem sido associada ao aumento da oxigenação da atmosfera, como consequência da recuperação climática após as glaciações paleoproterozoicas, que possivelmente ocasionou a aceleração do GOE (Sekine *et al.* 2011a, 2011b).

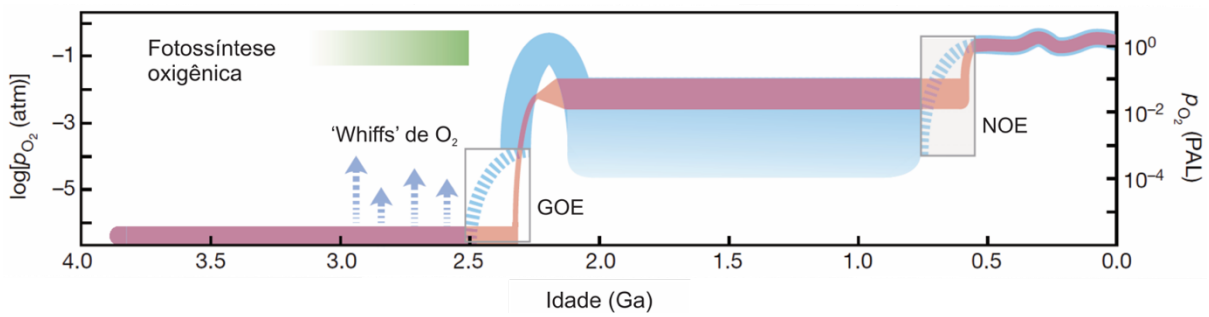

Figura 3.2: Evolução do conteúdo de oxigênio na atmosfera ao longo do tempo (Lyons *et al.* 2014).

Durante o GOE, é provável que as partes mais rasas dos oceanos devem ter sido progressivamente oxigenadas, enquanto que a formação de grandes depósitos de manganês indica que as partes mais profundas dos oceanos continuaram sendo anóxicas (Holland 2006). O aumento no conteúdo de O_2 na atmosfera-hidrosfera terrestre acima de cerca de 10^{-2} vezes em relação ao *present atmospheric level* (PAL), permitiu a deposição de manganês em larga escala em bacias marinhas estratificadas. Dados isotópicos de ósmio (*redox-sensitive element*), indicam sincronicidade entre o aumento de conteúdo de oxigênio na atmosfera e a deglaciação Paleoproterozoica (Sekine *et al.* 2011a, 2011b). Diamictitos glaciais associados ao HGE já foram reportados em diversos crátons ao redor do mundo, e em quase todos os continentes: América do Norte, África, Austrália, Antártica, Ásia e Europa (Figura 3.4, Tang & Chen 2013).

Na América do Sul, a primeira ocorrência de depósitos glaciais do Paleoproterozoico foi descrita recentemente por Araújo & Nogueira (2019), na região da Serra Sul da Bacia de Carajás. O diamictito Serra Sul apresenta idade relativa de 2,58–2,06 Ga. Esses autores consideram que a Glaciação Serra Sul pode ser correlata a qualquer uma das glaciações do Paleoproterozoico, ou a nenhuma delas. Trabalhos futuros devem ter como objetivo estabelecer a possível correlação dessa glaciação registrada para o Cráton Amazônico com o HGE.

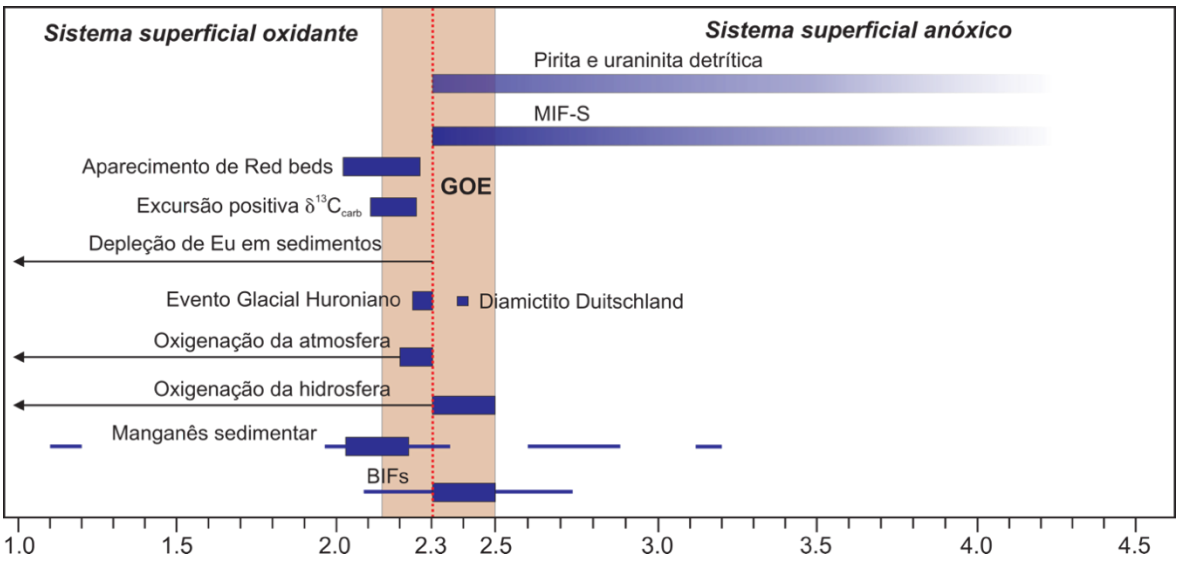

Figura 3.3: Sumário de modificações paleoambientais ocorridas em *ca.* 2.3 Ga (Tang & Chen 2013).

3.3 ASPECTOS PALEOGEOGRÁFICOS

Durante o Arqueano é sugerido que dois supercontinentes existiram, o supercontinente Kenorland a norte e o supercontinente Zimvaalbara a sul. O Kenorland, encerrava as massas continentais registradas atualmente na América do Norte, enquanto que o supercontinente Zimvaalbara incluía os crátons do Zimbábue, Kaapvaal e Pilbara. A quebra do desse supercontinente foi acompanhada do aumento do nível do mar e intensa deposição de formação ferrífera bandada tipo Lago Superior em torno de 2.75 Ga (Aspler & Chiarenzelli 1998). No final do Paleoproterozoico é sugerido que outro supercontinente foi formado, denominado supercontinente Columbia ou Nuna (Figura 3.5; Hoffman 1997, Rogers & Santosh 2002). Esse supercontinente teria se formado entre cerca 2,1–1,8 Ga e permaneceu amalgamado até o início do Mesoproterozoico, quando a quebra desse supercontinente promoveu a geração de intenso magmatismo em cerca de 1,3–1,2 Ga (Zhao *et al*. 2004). A formação do supercontinente Columbia na América do Sul é registrada principalmente na borda oeste do Cráton Amazônico, nos cinturões Rio negro, Juruena e Rondoniano. Durante a formação desse supercontinente é

sugerido que o Cráton Amazônico e o Cráton São Francisco colidiram respectivamente com o Cráton Oeste Africano e o Cráton do Congo em cerca de 2.1–2.0 Ga, durante o ciclo orogenético Transamazônico e Eburneano (Zhao *et al.* 2004, e referências nele contidas).

Enquanto a reconstrução paleogeográfica desse supercontinente ao redor do mundo é relativamente bem compreendida, o entendimento sobre a participação do Cráton Amazônico nesse contexto de modificações paleogeográficas tem sido ampliado nas últimas décadas como resultado do acúmulo de dados paleomagnéticos desse período (D'Agrella-Filho *et al.* 2016). Os dados paleomagnéticos sugerem que o Cráton Amazônico se juntou ao supercontinente Columbia em aproximadamente 1780 Ma (D'Agrella-Filho *et al.* 2016), em um cenário que se assemelhava à configuração "South AMerica and BAltica" ou SAMBA (Johansson 2009). De acordo com Rogers (1996), a formação desse supercontinente no final do Paleoproterozoico é marcada pela sedimentação flúvio-deltáico no topo das bacias formadas durante esse período. Na Bacia de Carajás os efeitos tectônicos relacionados a formação desse supercontinente estão relacionados provavelmente relacionado a colisão entre o Domínio Bacajá e o Domínio Carajás, ocorrido provavelmente por volta de 2,2–2,0 Ga durante o ciclo orogenético Transamazônico (Cordani *et al.* 1984, Macambira *et al.* 2009, Tavares *et al.* 2018).

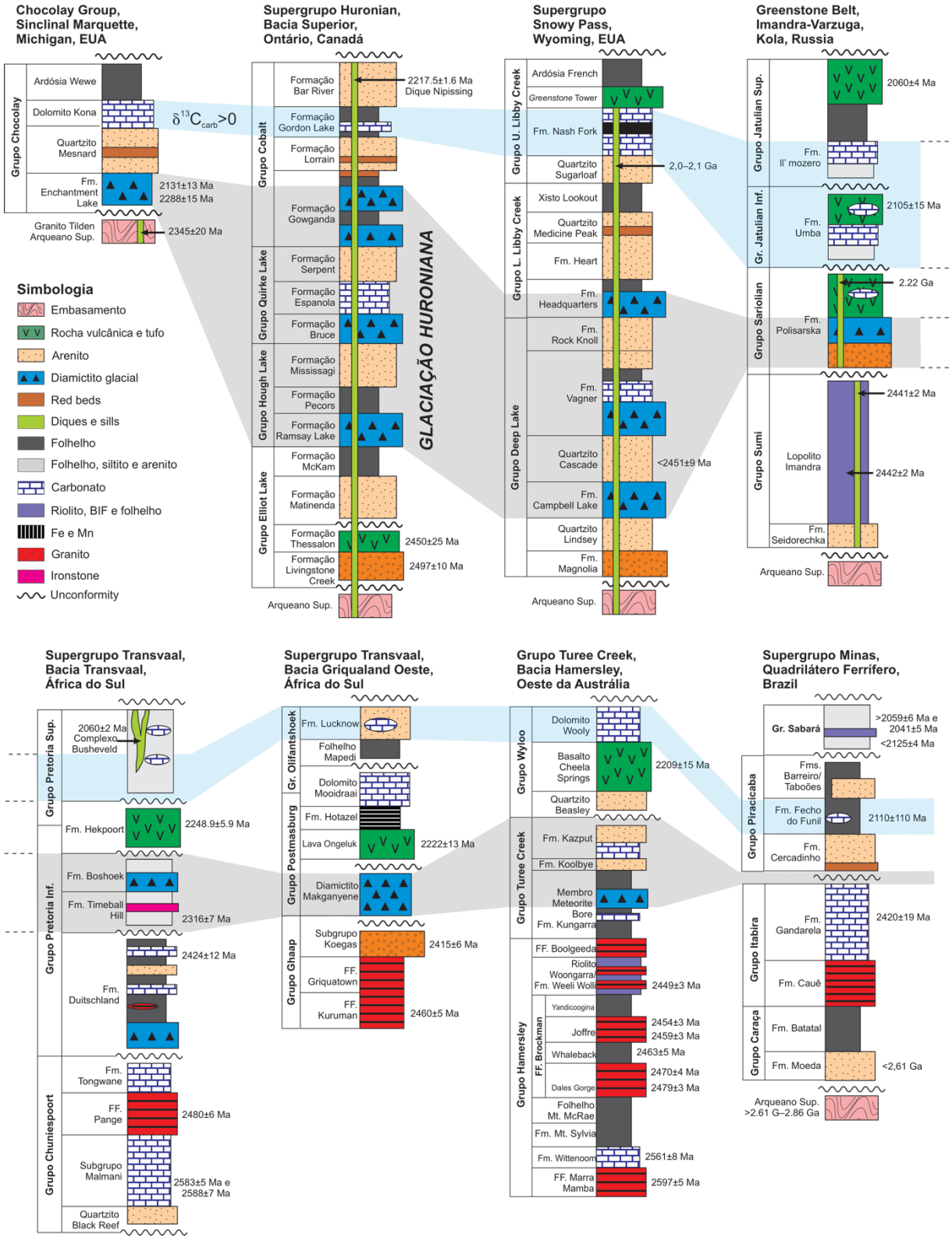

Figura 3.4: Possível correlação estratigráfica entre os depósitos glaciais associados ao Evento Glacial Huroniano (HGE) de acordo com Tang & Chen (2013) e referências nele contida.

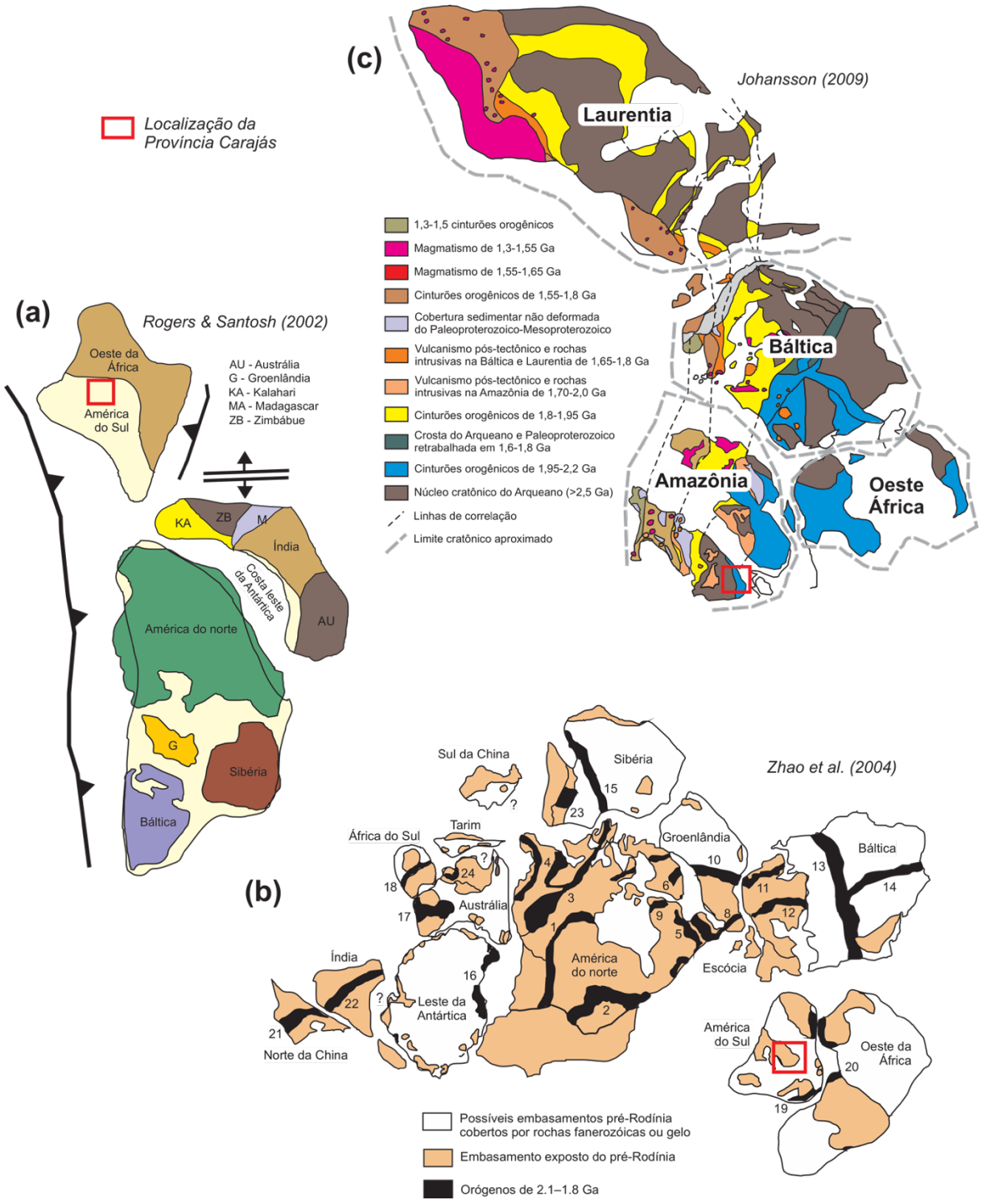

Figura 3.5: Reconstruções paleogeográficas das massas de terra que constituíam o supercontinente Columbia em: (a) aproximadamente 1,5 Ga (Rogers & Santosh 2002); (b) aproximadamente 2,0 Ga (Zhao *et al.* 2004); (c) e, entre 1,8-1,3 Ga (Johansson 2009).

4 MATERIAIS E MÉTODOS

A investigação da sucessão Arqueana–Paleoproterozoica da Bacia de Carajás seguiu uma metodologia similar a descrita em Pufahl & Hiatt (2012), os quais descrevem em detalhe as metodologias para investigação sedimentológica e geoquímica de sucessões do Pré-cambriano. Foram feitas descrições integradas de afloramentos e testemunhos de sondagem, nos quais foram empregadas análise de fácies sedimentares e estratigráfica, e foram realizadas coletas para análises petrográficas, geoquímicas, microscopia eletrônica de varredura e análise geocronológica. Os resultados foram integrados para reconstituição paleoambiental, inferências paleoclimáticas, e construção de modelos geodinâmicos e paleogeográficos (Figura 4.1). A seguir estão sendo detalhadas cada uma das metodologias e os materiais utilizados nesse estudo.

4.1 DESCRIÇÃO DOS TESTEMUNHOS DE SONDAGEM

A descrição de afloramentos seguiu o procedimento habitual de campo, com anotações em caderneta, coleta de amostras e registros fotográficos. Para localizar os diferentes pontos estudados foi utilizado o aparelho GPS (*Global Positioning System*), que determina com precisão as coordenadas geográficas. Já a descrição de testemunhos seguiu uma metodologia um pouco diferente. Inicialmente foi realizada uma seleção detalhada dos melhores testemunhos de sondagem para descrição, a partir de uma descrição geral e sintética de um grupo de testemunhos, isso incluiu descartar aqueles intensamente deformados por tectônica, fortemente alterados por intemperismo, próximos de zonas hidrotermais, ou ainda que eram truncados por múltiplas intrusões de diques de composição gabróica. Priorizou-se a seleção de testemunhos que apresentavam a maior diversidade litológica e superfícies de contato, que pudessem ser utilizadas para correlações estratigráficas.

De modo geral, os testemunhos localizados em profundidades rasas ocorrem fortemente intemperizados e intervalos com brecha ocorrem próximos a zonas de falha e geralmente próximos à corpos intrusivos. A descrição dos testemunhos seguiu na ordem da última (maior profundidade) para a primeira caixa (menor profundidade), no intuito de se realizar o empilhamento estratigráfico e a visualização de estruturas de forma mais precisa possível. Os perfis estratigráficos foram organizados em fichas de descrição padrão, e em mesma escala vertical e granulométrica. Priorizou-se a descrição de testemunhos cortados ao meio, no intuito de facilitar a visualização das estruturas sedimentares e garantir as interpretações dos processos.

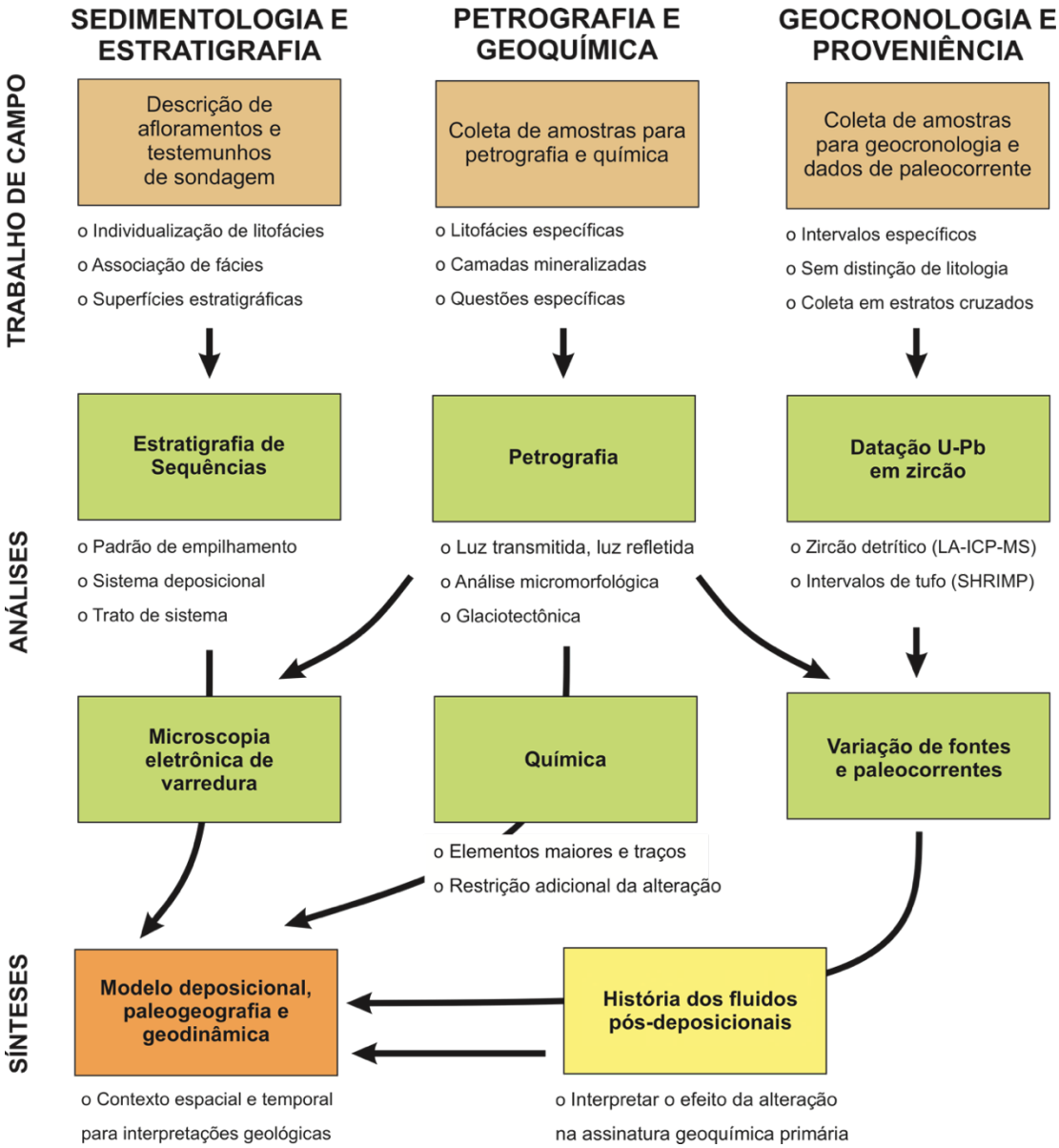

Figura 4.1: Síntese de metodologias e técnicas empregadas na investigação da sucessão do Neoarqueano-Paleoproterozoico da Bacia de Carajás (Adaptado de Pufahl & Hiatt 2012).

4.2 ANÁLISE DE FÁCIES E ESTRATIGRÁFICA

Neste estudo foram empregadas as metodologias clássicas utilizadas em análise de fácies sedimentares, que compreende a individualização das fácies de acordo com os litotipos e posteriormente, a organização arranjo das fácies em associações de fácies, que definem os ambientes deposicionais (Walker 1990, 1992). Para definição das sequencias deposicionais foram utilizadas as propostas apresentadas em Embry & Johannessen (1992), Embry (2002), e Embry (2009), que organizam as sequencias deposicionais dentro de sequencias transgressiva-regressiva (T-R). A utilização dessa proposta é justificada devido ao nível de observação e informação obtidos a partir da descrição dos testemunhos de sondagem.

4.3 PETROGRAFIA SEDIMENTAR E CARACTERIZAÇÃO TEXTURAL

Pequenos pedaços de amostras dos testemunhos de sondagem, que não excediam muito mais do que 10 cm de comprimento, bem como amostras-de-mão de afloramentos, foram coletados para preparação de lâminas delgadas no Laboratório de laminação da Universidade Federal do Pará (UFPA). Os litotipos foram classificados texturalmente e composicionalmente através da contagem de pelo menos 300 pontos, seguindo a metodologia Gazzi-Dickinson (Zuffa 1985). De modo geral, a caracterização textural seguiram as seguintes etapas: (1) reconhecimento da distribuição granulométrica baseado na escala granulométrica de Wentworth (1922), o grau de arredondamento e esfericidade dos grãos; (2) classificação dos arenitos com base na proposição de Pettijohn *et al.* (1987); e, (3) determinação da composição de possível cimento carbonático (calcita e/ou dolomita), através de tingimento de metade da lâmina com uma solução de alizarina vermelha-S e ferrocianeto de potássio utilizando a metodologia descrita em Adams *et al.* (1984).

Em conglomerados, seções delgadas foram preparadas com intuito de investigar a composição dos clastos e da matriz, importantes para interpretação de processos sedimentares, e inferências sobre prováveis áreas-fontes, tempo de transporte e dinâmica sedimentar. A descrição de diamictito de origem glacial seguiu as metodologias descritas em Busfield & Le Heron (2013, 2018). De acordo com esses autores, a análise micromorfológica—técnica bem estabelecida para estudos no quaternário—de diamictitos glaciais, que inclui o reconhecimento de elementos texturais diagnósticos da ação glacial (e.g., *sedimentary boudins*, *load structures*, e *galaxy structures*), podem trazer informações importantes sobre a dinâmica glacial antiga, e auxiliam na investigação de eventos glaciais e interpretações sobre a dinâmica glacial na criosfera do Pré-Cambriano, geralmente sujeito a efeitos tectônicos e metamórficos. Esses autores advogam que a descrição micromorfológica dos litotipos é crucial para identificação e separação de texturas glaciais e efeitos tectônicos secundários.

4.4 GEOCRONOLOGIA U-Pb EM ZIRCÃO

4.4.1 Preparação geral das amostras

Amostras de rocha, com aproximadamente 10 kg, foram coletadas de afloramentos e testemunhos de sondagem para datação pelo método U-Pb em zircão (Tabela 4.1). Amostras de ritmito da Formação Azul, e amostras de arenito e conglomerado da Formação Águas Claras foram coletadas para datação por *laser ablation inductively coupled plasma mass spectrometry* (LA-ICP-MS). Amostras de arenito tufáceo da Formação Águas Claras foram coletadas para datação por *sensitive high-resolution ion microprobe* (SHRIMP). A preparação das amostras

para separação dos grãos de zircão envolveu procedimentos similares aos descritos em Fedo *et al.* (2003). As amostras foram inicialmente pesadas, lavadas e britadas. Posteriormente seguiu os procedimentos de pulverização, deslame, bateamento em tanque de água e peneiramento, em jogo de peneiras em intervalos de 80 e 200 mesh. Duas frações foram separadas, uma na fração areia fina (0,250–0,125 mm), e outra na fração areia muito fina (0,125–0,0625 mm). Cada fração foi submetida inicialmente a separação magnética através de ímã de mão para remoção dos minerais magnéticos, e posteriormente processadas no separador magnético Frantz, em diferentes correntes (0,5, 1,0 e 1,5 A). Posteriormente, a fração de minerais pesados foi separada da fração leve utilizando-se o líquido denso bromofórmio.

Em algumas amostras do concentrado foi utilizada a técnica de microbateamento em Placa de Petri com álcool para concentração dos minerais pesados. Os grãos de zircão foram catados em lupa petrográfica e colados em fita dupla face. Cerca de 80-100 grãos foram catados de cada fração e organizados em *mounts* diferentes. Cada *mount* foi organizado numericamente e alfabeticamente para nomeação dos grãos. A catação foi realizada desconsiderando-se os aspectos como cor, tamanho e morfologia. Todos esses procedimentos foram realizados no Laboratório de Análise Mineral (LAMIN-BE) do Serviço Geológico do Brasil (CPRM), da Superintendência regional de Belém. Os cristais foram embutidos então em resina epóxi (a frio), desgastados para a exposição do interior dos grãos e polidos em pasta de diamante 0,25 μm, no Laboratório de laminação da Universidade Federal do Pará (UFPA). Subsequentemente, cada *mount* foi coberto com uma película de ouro de aproximadamente 20 μm, em alto vácuo, e posteriormente imageados por catoluminescência, acoplada ao microscópio eletrônico de varredura (MEV), modelo LS15 da Zeiss pertencente ao LAMIN-BE. Uma das amostras, foi imageada por catodoluminescência no microscópio de varredura da CPRM em consórcio com a Universidade de Brasília (UnB), FEI QUANTA 450, e outras três foram imageadas no laboratório de Microscopia Eletrônica de Varredura da Universidade de São Paulo (USP). Para a limpeza do mount foi utilizado banho com ácido nítrico diluído (3%), água Nanopure® em ultrassom e por último em acetona para extração de qualquer resíduo de umidade.

4.4.2 Datação por LA-ICP-MS

As análises por LA-ICP-MS foram conduzidas no Laboratório de Geologia Isotópica da UFPA (Pará-Iso/UFPA), e no laboratório de isótopos da Universidade Federal de Ouro Preto (UFOP). No laboratório Pará-Iso/UFPA as análises foram realizadas através do espectrômetro de massa por termo ionização modelo Finnigan MAT262. Detalhes sobre a instrumentação e procedimentos analíticos estão descritos em Milhomem Neto & Lafon (2019). A ablação

ocorreu em *spots* de 10, 20 e 25 μm, através do equipamento Neptune laser. De modo geral, os *spots* foram posicionados evitando-se zonas metamíticas e fraturadas, e foram posicionados preferencialmente na borda dos grãos. As análises dos sinais isotópicos foram executadas em ciclos de 10 leituras, seguida de branco, e análise do material de referência principal, zircão GJ-1 (Jackson *et al.* 2004), enquanto que o zircão 91500 foi utilizado como material de referência secundário. No laboratório de isótopos da UFOP, a ablação ocorreu em *spots* de 20 μm, com frequência de 6 Hz e fluência de 10%. O material pulverizado foi carreado por um fluxo de He (0,1 l/min), Ar (0,5 l/min) e N (0,09 l/min) onde foi utilizado o padrão internacional GJ-1 para a correção da deriva do equipamento, assim como o fracionamento entre os isótopos de U e Pb.

Para a verificação da acurácia foram realizadas análises no padrão internacional Plešovice. Os dados foram adquiridos em 460 ciclos de 0,1 segundo, seguindo a sequência de aquisição de 3 GJ-1, 2 Plešovice e 15 amostras e em cada leitura foram determinadas as intensidades das massas ^{202}Hg, ^{204}(Pb+Hg), ^{206}Pb, ^{207}Pb, ^{208}Pb e ^{238}U. A redução dos dados brutos incluiu as correções para branco, deriva do equipamento e chumbo comum utilizando-se a planilha de Excel de Gerdes & Zeh (2006). As idades foram calculadas e os gráficos construídos com os recursos do ISOPLOT 3.0 (Ludwig 2003). Para cada amostra datada, idades médias foram calculadas para cada grupo de pontos, similarmente ao apresentado em Caquineau *et al.* (2018). Os resultados foram plotados em diagramas Concórdia e histogramas de frequência das idades ^{207}Pb/^{206}Pb. Somente pontos com ≥ 90% de concordância foram considerados para o cálculo das idades.

Tabela 4.1: Descrição das amostras datadas nesse estudo por LA-ICP-MS e SHRIMP (U-Pb em zircão).

Amostra	**Litologia**	**Formação**	**Local**	**Método**	**Instituição**	**Redução dos dados**
DEQ-387	Ritmito	Formação Azul	Furo AN-DH-001	LA-ICP-MS	UFPA	Planilha Excel (Gerdes & Zeh 2006)
DEQ-388	Arenito	Formação Águas Claras	Furo AN-DH-002	LA-ICP-MS	UFPA	
DEO-066	Conglomerado	Formação Águas Claras	Mina do Azul	LA-ICP-MS	UFOP	
DEQ-581	Arenito tufáceo	Formação Águas Claras	Furo ALV8-FD06	SHRIMP	USP	*Software* SQUID 1.6 (Ludwig 2009)
DEQ-582	Arenito tufáceo	Formação Águas Claras	Furo ALV8-FD06	SHRIMP	USP	
DEQ-583	Arenito tufáceo	Formação Águas Claras	Furo ALV8-FD06	SHRIMP	USP	

4.4.3 Datação por SHRIMP

As análises realizadas por SHRIMP foram executadas através do espectrômetro de massa de íons secundários acoplado com uma Microssonda Iônica de Alta Resolução, do tipo SHRIMP IIe/MC, instalada no Instituto de Geociências da Universidade de São Paulo (IGc-USP). A concentrações de U-Th-Pb foram calibradas em relação ao conteúdo certificado do material de referência Temora 2 com idade de 416,8 ± 3,8 Ma. Detalhes sobre a instrumentação e procedimentos analíticos estão descritos em Sato *et al.* (2014). As análises ocorreram com spot fixado em 30 µm. Os resultados analíticos foram reduzidos utilizando-se o *software* SQUID 1.6 (Ludwig 2009) e os diagramas Concordia foram construídos utilizando-se o *software* Isoplot/Ex v. 4.15 (Ludwig 2003).

4.5 ANÁLISE MINERALÓGICA E QUÍMICA

Amostras enriquecidas com manganês foram analisadas através de difração de raios-X (DRX) no laboratório de análises minerais do Serviço Geológico do Brasil da Superintendência regional de Manaus (LAMIN-MA). As análises foram realizadas em Difratômetro de raios-x modelo X´PERT PRO MPD (PW 3040/60), da PANalytical, com Goniômetro PW3050/60 (Theta/Theta) e com tubo de raios-x cerâmico de anodo de Cu (Kα1 1,5406 Å), modelo PW3373/00, foco fino longo, 2200W, 60kv. O detector utilizado é do tipo RTMS, X'Celerator. A aquisição de dados foi feita com o *software* X'Pert Data Collector, versão 2.1a, e o tratamento dos dados com o *software* X´Pert HighScore versão 3.0d, também da PANalytical. Foram utilizadas as seguintes condições de análise: Voltagem (kV): 40; Corrente (mA): 40; *Scan range* (° 2θ): 5-70; *Step size* (° 2θ): 0,02; *Scan mode*: *Continuous*; *Counting time* (s): 50; *Divergence slit*: *Slit Fixed* 1/4°; *Mask Fixed* 10 mm; *Anti-scatter slit Name*: 5,7mm. A identificação dos minerais foi feita através da comparação do difratograma obtido com padrões (fichas) do banco de dados do ICDD-PDF (*International Center dor Diffraction Data – Powder Diffraction File*). Amostras, também enriquecidas em manganês, coletadas na mina de manganês do Azul foram analisadas por ICP-AES (*Inductively Coupled Plasma – Atomic Emission Spectrometry*) e ICP-MS no laboratório *French National Centre for Scientific Research* (CNRS), na França, para determinação dos óxidos maiores e elementos traços, respectivamente.

4.6 MICROSCOPIA ELETRÔNICA DE VARREDURA

A análise por microscopia eletrônica de varredura (MEV) foi realizada em um microscópio modelo LS15 da Zeiss no laboratório de análise mineral (LAMIN-BE) da Superintendência Regional de Belém do Serviço Geológico do Brasil—CPRM. Lâminas

polidas, fragmentos de rocha e grãos de quartzo foram cobertos a alto vácuo por uma fina película de 20 μm de espessura, de carbono (C) ou ouro (Au), de acordo com o material analisado. O filamento de emissão utilizado é de tungstênio e foi usado o modo de alto vácuo (3,0–1,5 10–5 mPa) para a obtenção de imagens eletrônicas e realização de análises químicas. As imagens de elétron retroespalhado (*Backscattering Electron*—BSE) dos minerais e texturas foram obtidas com voltagem de 20 kV, corrente de chegada de 45 a 60 pA, distância de trabalho de 8,5 mm e ampliação entre 55 e 3000 vezes. As análises da composição química dos minerais foram por espectrometria por dispersão de energia (*Energy Dispersive Spectrometry*—EDS) de raios-X em um detector X-Act SSD 10 mm^2 da Oxford Instruments.

Os resultados analíticos também foram adquiridos a uma distância de trabalho de 8,5 mm e com voltagem de 20 kV, mas com corrente de chegada entre 170 e 250 pA para manter uma taxa de contagem de saída de cerca de 2000 cps. Foram feitas análises pontuais e perfis de centro-borda dos cristais. Os resultados obtidos foram padronizados por espectros de energia de padrões do programa AZTec da Oxford Instruments. Resultados com desvio padrão acima de 10% da concentração do elemento foram descartados do cálculo da composição dos minerais, podendo esses estar presentes nos minerais em baixas concentrações como impurezas aprisionadas no retículo cristalino ou marcar incipiente alteração secundária dos minerais analisados. As imagens obtidas através do modo de elétrons secundários (*secondary electrons*) foram executadas em grãos de quartzo e pequenos fragmentos de rocha. Os materiais analisados foram previamente catados em lupa petrográfica e fixados através de fita dupla face de carbono em *stubs* do microscópio eletrônico de varredura.

5 SERRA SUL DIAMICTITE OF THE CARAJÁS BASIN (BRAZIL): A PALEOPROTEROZOIC GLACIATION ON THE AMAZONIAN CRATON

Raphael Araújo[1,2*] and Afonso Nogueira[1]

[1] Management of Geology and Mineral Resources, Geological Survey of Brazil, 66095-904, Belém, Brazil

[2] Institute of Geoscience, Federal University of Pará, 66075-110, Belém, Brazil

*Corresponding author e-mail address: raphaelneto@ufpa.br

Artigo publicado no periódico internacional *Geology*.

GEOLOGY | THE GEOLOGICAL SOCIETY OF AMERICA®

https://doi.org/10.1130/G46923.1

Manuscript received 10 June 2019
Revised manuscript received 28 August 2019
Manuscript accepted 3 September 2019

Published online 15 October 2019

Serra Sul diamictite of the Carajás Basin (Brazil): A Paleoproterozoic glaciation on the Amazonian craton

Raphael Araújo[1,2]* and Afonso Nogueira[2]

[1]Management of Geology and Mineral Resources, Geological Survey of Brazil, Av. Perimetral 3645, Belém 66095-904, Brazil
[2]Institute of Geoscience, Federal University of Pará, R. Augusto Corrêa 01, Belém 66075-110, Brazil

ABSTRACT

This paper reports the discovery of glacial deposits of likely Siderian–Rhyacian age (2.58–2.06 Ga) in South America (Carajás Basin, Brazil), thereby expanding the potential reach of Paleoproterozoic glaciations to the Amazonian craton for the first time. Glacially derived diamictites are stacked within a hitherto unrecognized ~600-m-thick siliciclastic succession, here named the Serra Sul Formation. Well-preserved textures, with evidence of glaciotectonism and ice rafting, indicate deposition in a coastal subglacial to glacial-fed submarine fan system, in which the immediately underlying units (banded iron formation and volcanic rock) were the main source and bedrock. The Serra Sul diamictite may be correlated with any of the known Paleoproterozoic glaciations, or with none of them.

INTRODUCTION

Paleoproterozoic glaciations (ca. 2.45–2.22 Ga; Rasmussen et al., 2013) are recorded in almost every continent, but they have not yet been reported in South America. These glaciations, also called the Huronian Glaciation Event (Tang and Chen, 2013), occurred at the time of the Great Oxidation Event (GOE), and it is suggested that they were triggered by the supercontinent breakups at the end of the Archean (Aspler and Chiarenzelli, 1998; Bleeker, 2003; Strand, 2012). While some studies have argued that they may represent an early snowball Earth episode (e.g., Evans et al., 1997; Hoffman, 2013), others have suggested that there may have been a series of more typical glaciations occurring at different times and in different places (e.g., Young, 2014).

In the Carajás Basin, Amazonian craton (Brazil), intervals of matrix-supported breccia were previously reported as a particular rock of the Serra Sul succession, and considered a Neoarchean magnetite-rich breccia of the lowermost banded iron formation (BIF) unit (Cabral et al., 2013). Strangely, these rocks were never described in the Neoarchean succession (Grão-Pará Group), which is generally documented as a set of ca. 2.75 Ga BIF and mafic to felsic volcanic rock (Trendall et al., 1998) affected by Cu-Au mineralization at ca. 2.57 Ga (Tallarico et al., 2005). This was partially due to the lack of an accurate stratigraphic framework for the Carajás Basin that has caused several units to be neglected, misinterpreted, or even overestimated.

The initial investigation of structures and textures from drill cores revealed that the strata of the Serra Sul succession are inverted. This is generally observed on the borders of the Carajás Basin that were deformed by regional folds associated with the latest tectonic event that affected the area, the Transamazonian cycle at ca. 2.0 Ga (Machado et al., 1991). In fact, the breccia intervals occur within a siliciclastic succession hitherto unrecognized in the basin, hereafter formally named the Serra Sul Formation. This formation unconformably overlies the Neoarchean units and unconformably underlies the siliciclastic deposits of the Águas Claras Formation of ca. 2.06 Ga (Mougeot et al., 1996), suggesting Paleoproterozoic (2.58–2.06 Ga) age constraints (Fig. 1).

In this study, based on a detailed description of well-preserved delicate primary textures throughout the Serra Sul Formation (see Items DR1 and DR2 in the GSA Data Repository[1]), we attempted to resolve this issue by producing sedimentological and stratigraphic evidence that helps to identify the origin of these breccia. The results provide important evidence of the paleoenvironmental conditions on the Amazonian craton in the early Paleoproterozoic.

MATERIALS AND METHODS

A sedimentological and stratigraphic study based on detailed descriptions of drill cores from throughout the Serra Sul Formation was undertaken. To cover as much of the lateral stratigraphic information as possible, detailed measured sections were taken throughout an ~600-m-thick succession from drill cores located in three different areas of the Carajás Basin (*a*, *b*, and *c* in Fig. 1; see Items DR3, DR4, and DR5). For each of these areas, a simplified sedimentary log was created and organized in the north-south section toward the basin depocenter (Fig. 2). Small samples (up to 10 cm long) were collected from the drill cores, and polished thin sections were made in order to verify the microstructures and compositions of the diamictite matrices and clasts. Scanning electron microscope (SEM) analyses were performed to investigate the microtextures on quartz grain surfaces. For this analysis, small pieces of core ($n = 2$) were gradually broken and quartz grains ($n = 100$) were randomly selected, then fixed in an electrically conductive carbon double-stick tape, coated with gold, and imaged using secondary electrons at the Geological Survey of Brazil (Belém).

RESULTS

Foliated to Massive Diamictite Facies Association

The association of foliated to massive diamictite facies comprises diamictite

*E-mail: raphaelneto@ufpa.br

[1]GSA Data Repository item 2019397, complete set of core-based sedimentary logs, borehole locations, table of lithofacies, and supplementary figures, is available online at http://www.geosociety.org/datarepository/2019/, or on request from editing@geosociety.org.

CITATION: Araújo, R., and Nogueira, A., 2019, Serra Sul diamictite of the Carajás Basin (Brazil): A Paleoproterozoic glaciation on the Amazonian craton: Geology, v. 47, p. 1166–1170, https://doi.org/10.1130/G46923.1

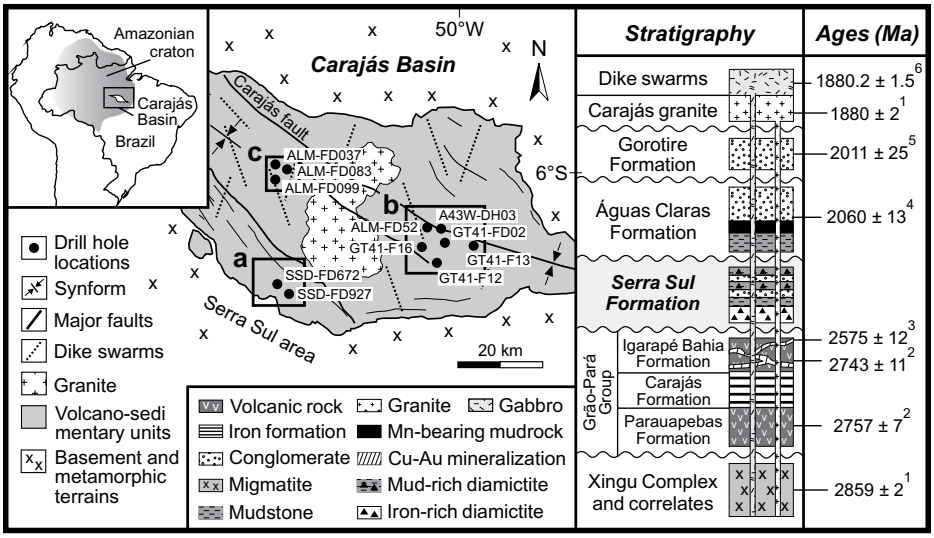

Figure 1. Simplified geological map of Carajás Basin (Brazil) highlighting study areas (*a*, *b*, and *c*) and location of drill holes (black dots), and stratigraphic framework of basin including exact stratigraphic position of Serra Sul Formation and main geochronological data available (1—Machado et al., 1991; 2—Trendall et al., 1998; 3—Tallarico et al., 2005; 4—Mougeot et al., 1996; 5—Pereira et al., 2009; 6—Teixeira et al., 2018).

interbedded with thin beds of black shale (as much as 3 m thick). There are uninterrupted intervals of diamictite, 150 m thick, in the stratigraphic section (Fig. 2, log *a*; see Item DR1). The diamictite has a foliated matrix that tends toward a massive aspect. The BIF and mafic to felsic volcanic-subvolcanic rock clasts vary in size from pebbles to boulders, and vary in shape from angular to well rounded. Faceted, flattened, rotated, boudinaged, sheared, and lens-shaped clasts are widespread (Figs. 3A and 3B; see Item DR6). Fractures occur preferentially along the borders of clasts and rarely cross-cut them; they are even found perpendicular to the foliation and filled with quartz and dolomite. In some clasts, the inflection of the foliation resulted in the development of asymmetrical and symmetrical pressure shadows. The fine-grained and dark-colored matrix is composed of micrometer-scale fragments (up to 100 µm) of quartz and magnetite, and the alignment of these two minerals defines the foliation (Fig. 3C). Isolated bullet-shaped and boulder-sized clasts occur in black shale beds, sandwiched by diamictite intervals (Fig. 3D).

Rhythmite Facies Association

Another facies association found within the Serra Sul Formation is composed of only rhythmite that constitutes a monotonous succession as much as 300 m thick at the base of the stratigraphic section (Fig. 2, logs *b* and *c*; see Items DR2 and DR7). The rhythmite is composed of intercalated normally graded, fine-grained sandstone and mudstone stacked into fining-upward cycles as much as 10 cm thick; the lithological contact is generally marked by soft-sediment deformation structures and rip-up clasts.

Conglomerate-Sandstone-Rhythmite-Diamictite Facies Association

Conglomerate and sandstone interbedded multiple times with rhythmite and diamictite compose the final facies association observed in this study (Fig. 2, log *b*; see Item DR2). Normally graded to massive conglomerate and sandstone are stacked into 0.30–30-m-thick fining-upward cycles. In the stratigraphic section, they reach uninterrupted intervals of as much as 150 m thick. In sandstone, the grains are mainly composed of iron chert. Conglomerate clasts are angular to well-rounded fragments of BIF, iron chert, and volcanic rock ranging from pebble to cobble size, with cross-laminae and planar laminae weakly developed. Clast- to matrix-supported conglomerate has a sandy to granular matrix (Fig. 3E; see Item DR8). Rhythmite and diamictite occur interbedded with one another. The massive diamictite reaches as much as 10 m thick and consists of a mud-rich matrix in which pebble- to cobble-sized and angular to well-rounded BIF, iron chert, and volcanic rock clasts occur scattered. Isolated pebble-sized clasts occur with high dip angles and deformed underlying laminae (Fig. 3F), and coarse-grained clasts are mound forming in concave-down beds (Fig. 3G). Faceted clasts, including elongated pentagonal ones, also occur scattered within the muddy matrix (Figs. 3H and 3I; see Item DR9). Fractures, steps, and grooves occur on quartz grain surfaces (Fig. 3J; see Item DR10).

DISCUSSION

Diamictite Textures: Tectonic versus Sedimentary

The observation that foliated diamictite is restricted to certain beds and that it occurs interlayered with massive diamictite and black shale beds indicates an intrastratal deformation at the time of deposition, and the coeval occurrence of deformed and preserved clasts in the same interval suggests a highly heterogeneous deformational setting (e.g., Menzies, 2012; Busfield and Le Heron, 2013, 2018). The observation that fractures are restricted to the borders of the clasts and rarely cutting them, are preferentially oriented perpendicular to foliation, and are filled with quartz and dolomite that replaced the original matrix minerals indicates that these structures were formed during sedimentation and subsequently infilled by secondary minerals.

Similar to the interpretation of Cabral et al. (2013), our observations indicate that the pervasive deformation fabric present in some diamictite intervals is derived from synsedimentary deformation, certainly linked to subglacial mechanisms, rather than tectonic deformations. The observation in drill cores that the succession is only tilted and that no shear bands are present strengthens this hypothesis, as does the fact that no evidence of metamorphism was recorded in the thin section. Ultimately, the occurrence of well-preserved delicate microtextures such as steps, striations, and fractures on the surfaces of quartz sand grains confirms that the Serra Sul diamictite is unmetamorphosed or was metamorphosed to a very low grade (cf. Machado et al., 1991; Pinheiro and Holdsworth, 1997).

Data Interpretation and Model

The occurrence of foliated to massive diamictite with faceted, fractured, flattened, sheared, boudinaged, and rotated clasts with pressure shadows suggests that these rocks were formed in subglacial environments and recorded primary ice-contact sedimentation (i.e., tillite), where high strain rates led to progressive deformation (Menzies et al., 2006; Busfield and Le Heron, 2013, 2018; Le Heron et al., 2017). The quartz- and magnetite-rich matrices of these diamictites suggest that they were derived from a rock flour produced by intense abrasion of the bedrock. The observation that volcanic rock and BIF clasts penetrate, puncture, and deform the underlying laminae of mudstone suggests that these clasts are dropstones. The occurrence of beds composed of coarse-grained clast mounds surrounded by fine-grained sediments further suggests that these beds are dumpstone (i.e., rock formed from the melt-out of debris contained in floating dirt-laden icebergs; Thomas and Connell, 1985).

The large number of faceted clasts embedded in mudstone beds, some of which have elongated pentagonal shapes and high dip angles, indicates that they were dropped over a muddy substrate and associated with rapid burial by fine sediments without subsequent reworking. Similarly, the fairly common occurrence of faceted

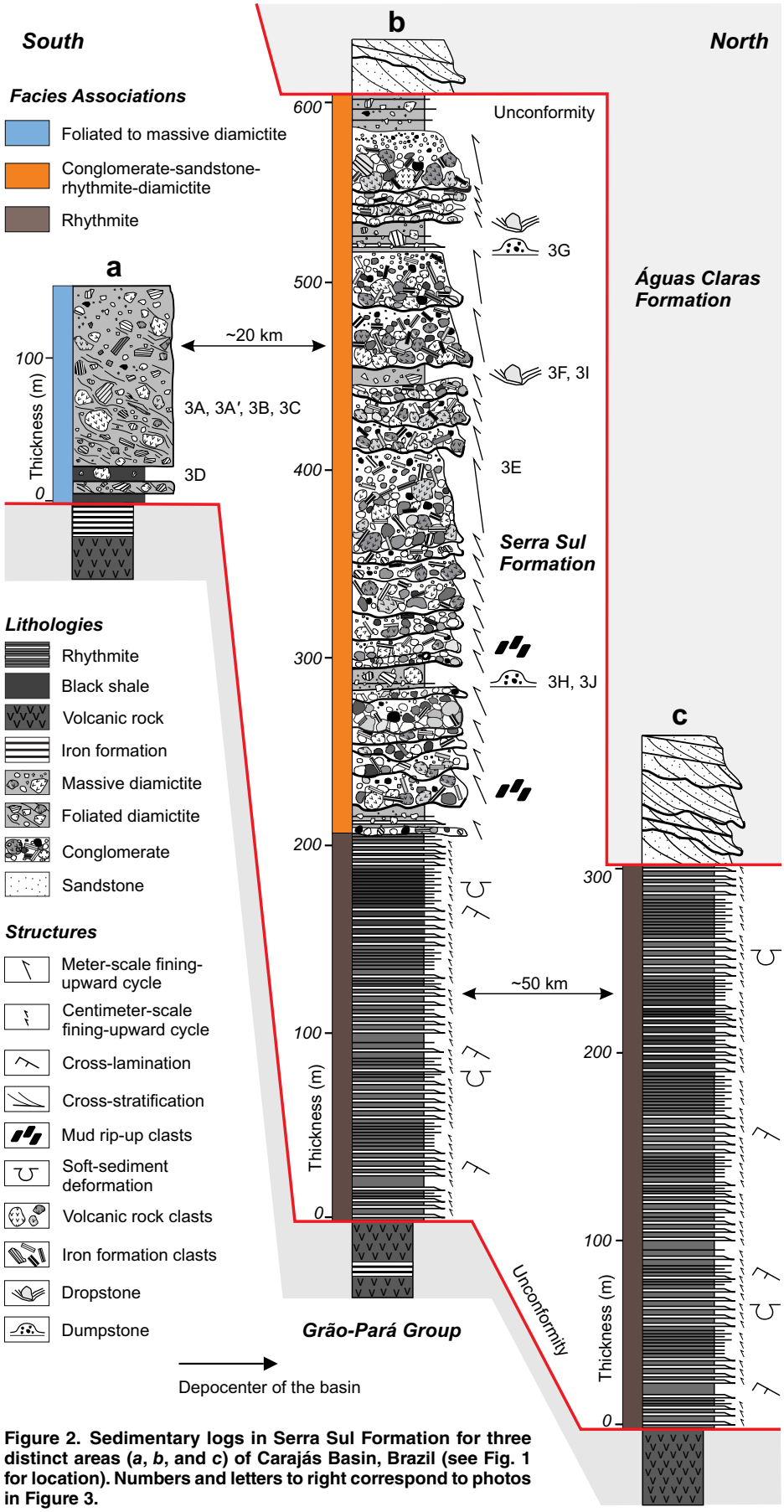

Figure 2. Sedimentary logs in Serra Sul Formation for three distinct areas (*a*, *b*, and *c*) of Carajás Basin, Brazil (see Fig. 1 for location). Numbers and letters to right correspond to photos in Figure 3.

clasts sandwiched by mudstone indicates a hydrodynamically incongruent sedimentary setting (Le Heron, 2015; Le Heron et al., 2017). The grooves observed on the surfaces of the quartz grains are straight, parallel, and V-shaped, suggesting that they are striations produced by glacial erosion (Whalley and Krinsley, 1974; Mahaney et al., 1996; Immonen, 2013). On the other hand, the rhythmic centimeter-scale intercalation between fine-grained sandstone with normal gradation and mudstone suggests deposition by low-density turbidity currents, and the meter-scale intercalations of massive to normally graded conglomerate and sandstone suggests deposition by the types of high-density turbidity currents associated with submarine fan systems (Pickering et al., 2015).

A glacially influenced coastal to marine system is envisaged as the depositional environment that accommodated the sediments of the Serra Sul Formation (Fig. 4). This system was developed over and supplied by bedrock mainly composed of Neoarchean BIF and volcanic rock belonging to the Grão-Pará Group. This hypothesis is strongly supported by the observation that quartz and magnetite compose the matrices of subglacial diamictite, and by the fact that BIF, iron chert, and volcanic rock are the main constituents of the clasts. The surface that separates the Serra Sul deposits from the Neoarchean strata represents a great unconformity that may be used for correlation inside and outside the basin. Ice overloading on the continent, combined with the lateral expansion of glaciers, promoted high rates of deformation of the bedrock. This was likely strengthened by the presence of a previously formed regolith cover that greatly favored the glaciotectonic deformation and had a composition similar to that of the bedrock. Short-lived marine transgressions into the continent associated with the retreat of glaciers may explain the occurrence of black shale beds repeatedly interbedded with subglacial diamictite at the base of coastal deposits.

In the marine setting, submarine fan systems were washed and supplied by glacial meltwater, which promoted the resedimentation of glaciogenic debris in deep waters. The simultaneous release of ice-rafted debris (IRD) from icebergs in distal waters and deposition of fine-grained particles generated massive diamictite beds with dropstones and dump structures. The alternation of sedimentation by submarine fan systems and ice rafting explains the multiple intercalations of IRD-bearing diamictite and sandy and/or conglomeratic facies that is observed throughout the succession (Fig. 2, log *b*). Although gravity-flow deposits constitute a greater part of the succession, IRD-bearing intervals of glaciogenic diamictite are sharply distinct. The interbedding of these deposits testifies to subaqueous sedimentation within the basin. The similar

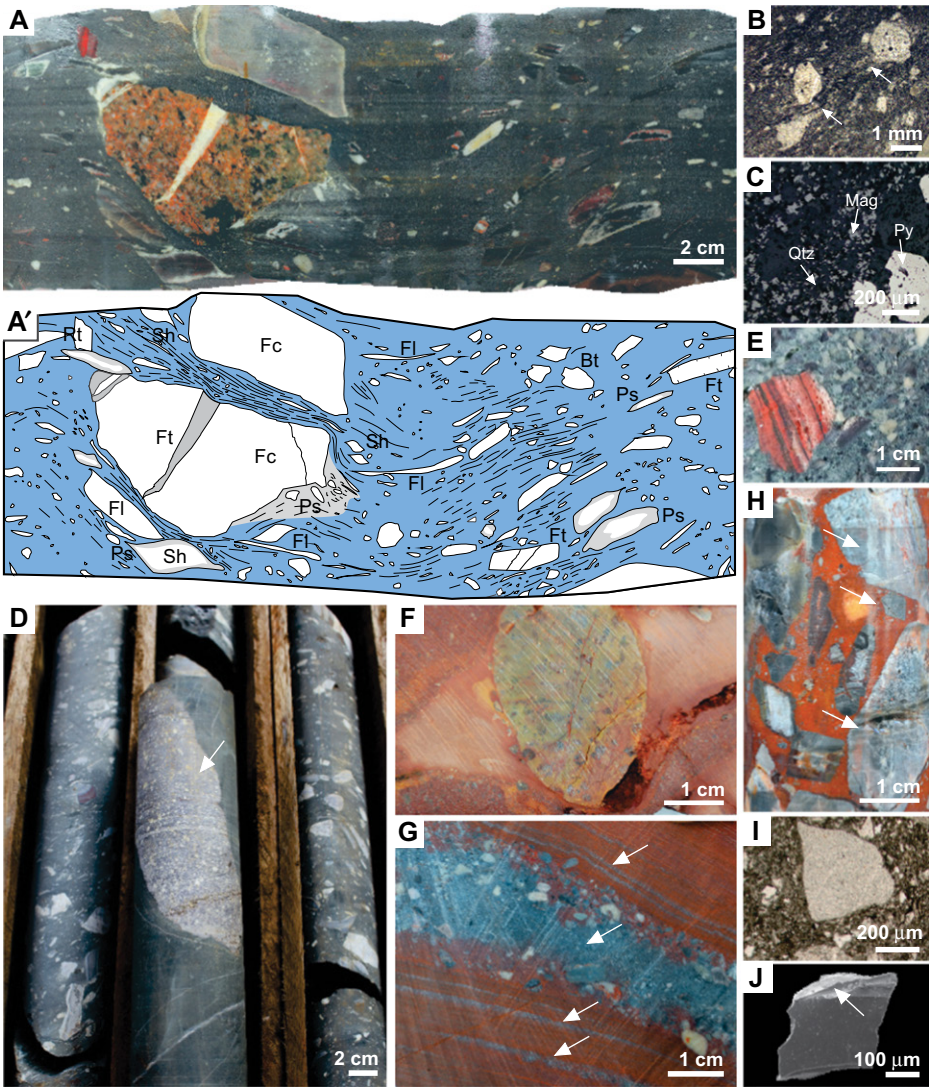

Figure 3. Images of Serra Sul Formation (Carajás Basin, Brazil). (A,A′) 360° panoramic image and line interpretation of core sample representative of foliated diamictite exhibiting pressure shadow (Ps) and faceted (Fc), sheared (Sh), rotated (Rt), fractured (Ft), flattened (Fl), and boudinaged (Bt) clasts of iron formation, iron chert, and volcanic to subvolcanic rock. Background color in A′ represents facies association of foliated to massive diamictite. (B,C) Thin section images of foliated diamictite showing angular clasts of chert with asymmetrical pressure shadow (B; plane polarized light, 10×) rotated in a matrix containing quartz (Qtz), magnetite (Mag), and pyrite (Py). (D) Bullet-shaped clast of porphyritic rhyolite isolated in black shale bed sandwiched by diamictite. (E) Matrix-supported conglomerate with pebble-sized iron formation clast scattered in granular matrix. (F) Well-rounded clast of porphyritic rhyolite displaying disruption and puncturing of underlying laminae beneath clast. (G) Thin beds of coarse-grained mounds of chert and volcanic rock clasts surrounded by mudstone. (H) Faceted and elongated pentagonal clasts with high-angle dips randomly embedded in muddy diamictite. (I) Thin section image of diamictite (plane polarized light, 10×) showing very angular chert clasts suspended in poorly sorted and mud-rich matrix. (J) Striations on the surface of quartz grain from diamictite (scanning electron microscope image).

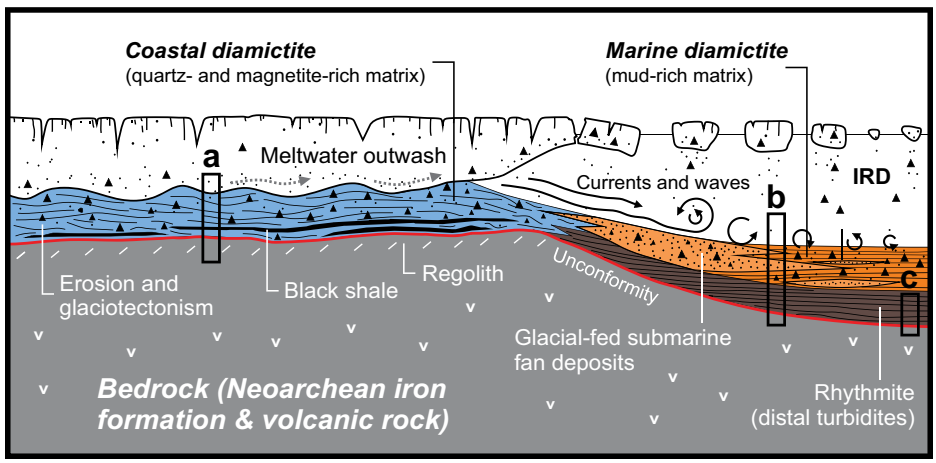

Figure 4. Model showing sedimentary mechanisms underlying diamictite-bearing succession of Serra Sul Formation (Carajás Basin, Brazil). Subglacial diamictite from coastal environment is characterized by quartz- and magnetite-rich matrix resulting from erosion and glaciotectonism on bedrock, whereas marine diamictite results from sedimentation of ice-rafted debris (IRD) and is characterized by mud-rich matrix. Glacially fed submarine fan deposits rework glaciogenic sediments and are interbedded with IRD-bearing diamictite. Neoarchean banded iron formation (BIF) and volcanic rock units were main bedrock and source of sediments. Positions of sedimentary logs (*a*, *b*, and c; see Fig. 1 for location) are indicated.

composition of clasts in the subglacial (Fig. 2, log *a*) and debris-flow diamictite (Fig. 2, logs *b* and *c*) suggests a genetic correlation between these environments and that the debris-flow deposits are glaciogenic (e.g., Le Heron et al., 2017). The thick beds of rhythmite at the base of the succession (Fig. 2, logs *b* and *c*) suggest a prolonged sedimentation by low-density turbidity currents in the deepest parts of the basin, although the absence of IRD-bearing intervals in these deposits does not necessarily indicate ice-free conditions (e.g., Le Heron, 2015).

Ultimately, the depositional system hypothesized for the Serra Sul Formation is similar to those interpreted for Paleoproterozoic glaciations worldwide (e.g., Miall, 1985; Chen et al., 2019). The Serra Sul succession represents the first large-scale siliciclastic sedimentation after the predominantly chemical sedimentation that characterized the Neoarchean of the Carajás Basin. Compared to the Neoproterozoic Sturtian glaciation, in which iron formation was deposited simultaneously with diamictite in sub–ice shelf settings (Lechte and Wallace, 2016), the deposition of diamictite in the Serra Sul system was completely decoupled from the deposition of the BIF. Although the expressive rift-related volcanism of the Carajás Basin represented by the Grão-Pará Group (Olszewski et al., 1989; Martins et al., 2017) may be related to the breakup of the southern supercontinent at the end of the Archean, and may have also been one of the triggers of Serra Sul glaciation, this volcanic

event predates by nearly 200 m.y. (2.75–2.58 Ga) the onset of this cooling episode.

CONCLUSIONS

A core-based sedimentological and stratigraphic investigation in the Carajás Basin (Brazil) revealed the occurrence of likely Siderian–Rhyacian (2.58–2.06 Ga) glacial strata within a succession hitherto unrecognized, newly named the Serra Sul Formation. We suggest that Amazonia underwent glaciation in the early Paleoproterozoic, which may or may not be correlated with any of the known Paleoproterozoic glaciations. The Serra Sul diamictite represents the first reported occurrence of Paleoproterozoic glacial deposits in South America, expanding the potential reach of glaciations of this time period to the Amazonian craton for the first time.

ACKNOWLEDGMENTS

We thank Sérgio Huhn, Fernando Matos, and Luiz Costa of Vale S.A. (Parauapebas, Brazil) for making the drill cores available for the research; the Geological Survey of Brazil (Belém, Brazil) and the PROPESP/UFPA for supporting this work; Werner Truckenbrodt for his constructive comments on an earlier version of the manuscript; and Roberto Araújo Filho and Alexandre Ribeiro for fieldwork assistance. We are also very grateful to Daniel Le Heron, Paul Hoffman, Kari Strand, and an anonymous reviewer for reviewing our manuscript; and to James Schmitt for his editorial work.

REFERENCES CITED

Aspler, L.B., and Chiarenzelli, J.R., 1998, Two Neoarchean supercontinents? Evidence from the Paleoproterozoic: Sedimentary Geology, v. 120, p. 75–104, https://doi.org/10.1016/S0037-0738(98)00028-1.

Bleeker, W., 2003, The late Archean record: A puzzle in ca. 35 pieces: Lithos, v. 71, p. 99–134, https://doi.org/10.1016/j.lithos.2003.07.003.

Busfield, M.E., and Le Heron, D.P., 2013, Glacitectonic deformation in the Chuos Formation of northern Namibia: Implications for Neoproterozoic ice dynamics: Proceedings of the Geologists' Association, v. 124, p. 778–789, https://doi.org/10.1016/j.pgeola.2012.10.005.

Busfield, M.E., and Le Heron, D.P., 2018, Snowball Earth under the microscope: Journal of Sedimentary Research, v. 88, p. 659–677, https://doi.org/10.2110/jsr.2018.34.

Cabral, A.R., et al., 2013, Trace-element and multi-isotope geochemistry of Late-Archean black shales in the Carajás iron-ore district, Brazil: Chemical Geology, v. 362, p. 91–104, https://doi.org/10.1016/j.chemgeo.2013.08.041.

Chen, Y., Chen, W., Li, Q., Santosh, M., and Li, J., 2019, Discovery of the Huronian Glaciation Event in China: Evidence from glacigenic diamictites in the Hutuo Group in Wutai Shan: Precambrian Research, v. 320, p. 1–12, https://doi.org/10.1016/j.precamres.2018.10.009.

Evans, D.A., Beukes, N.J., and Kirschvink, J.L., 1997, Low-latitude glaciation in the Paleoproterozoic era: Nature, v. 386, p. 262–266, https://doi.org/10.1038/386262a0.

Hoffman, P.F., 2013, The Great Oxidation and a Siderian snowball Earth: MIF-S based correlation of Paleoproterozoic glacial epochs: Chemical Geology, v. 362, p. 143–156, https://doi.org/10.1016/j.chemgeo.2013.04.018.

Immonen, N., 2013, Surface microtextures of ice-rafted quartz grains revealing glacial ice in the Cenozoic Arctic: Palaeogeography, Palaeoclimatology, Palaeoecology, v. 374, p. 293–302, https://doi.org/10.1016/j.palaeo.2013.02.003.

Lechte, M., and Wallace, M., 2016, Sub–ice shelf ironstone deposition during the Neoproterozoic Sturtian glaciation: Geology, v. 44, p. 891–894, https://doi.org/10.1130/G38495.1.

Le Heron, D.P., 2015, The significance of ice-rafted debris in Sturtian glacial successions: Sedimentary Geology, v. 322, p. 19–33, https://doi.org/10.1016/j.sedgeo.2015.04.001.

Le Heron, D.P., Tofaif, S., Vandyk, T., and Ali, D.O., 2017, A diamictite dichotomy: Glacial conveyor belts and olistostromes in the Neoproterozoic of Death Valley, California, USA: Geology, v. 45, p. 31–34, https://doi.org/10.1130/G38460.1.

Machado, N., Lindenmayer, Z., Krogh, T.E., and Lindenmayer, D., 1991, U-Pb geochronology of Archean magmatism and basement reactivation in the Carajás area, Amazon shield, Brazil: Precambrian Research, v. 49, p. 329–354, https://doi.org/10.1016/0301-9268(91)90040-H.

Mahaney, W.C., Claridge, G., and Campbell, I., 1996, Microtextures on quartz grains in tills from Antarctica: Palaeogeography, Palaeoclimatology, Palaeoecology, v. 121, p. 89–103, https://doi.org/10.1016/0031-0182(95)00069-0.

Martins, P.L.G., Toledo, C.L.B., Silva, A.M., Chemale, F., Jr., Santos, J.O.S., and Assis, L.M., 2017, Neoarchean magmatism in the southeastern Amazonian Craton, Brazil: Petrography, geochemistry and tectonic significance of basalts from the Carajás Basin: Precambrian Research, v. 302, p. 340–357, https://doi.org/10.1016/j.precamres.2017.10.013.

Menzies, J., 2012, Strain pathways, till internal architecture and microstructures—Perspectives on a general kinematic model—A 'blueprint' for till development: Quaternary Science Reviews, v. 50, p. 105–124, https://doi.org/10.1016/j.quascirev.2012.07.012.

Menzies, J., van der Meer, J.J.M., and Rose, J., 2006, Till—As a glacial "tectomict", its internal architecture, and the development of a "typing" method for till differentiation: Geomorphology, v. 75, p. 172–200, https://doi.org/10.1016/j.geomorph.2004.02.017.

Miall, A.D., 1985, Sedimentation on an early Proterozoic continental margin under glacial influence: The Gowganda Formation (Huronian), Elliot Lake area, Ontario, Canada: Sedimentology, v. 32, p. 763–788, https://doi.org/10.1111/j.1365-3091.1985.tb00733.x.

Mougeot, R., Respaut, J.P., Briqueu, L., Ledru, P., Milesi, J.P., Lerouge, C., Marcoux, E., Huhn, S.B., and Macambira, M.J.B., 1996, Isotope geochemistry constraints for Cu, Au mineralizations and evolution of the Carajás Province (Pará, Brazil), *in* Proceedings, Congresso Brasileiro de Geologia 39, Salvador: Abstracts: Salvador, Sociedade Brasileira de Geologia, v. 7, p. 321–324.

Olszewski, W.J., Wirth, K.R., Gibbs, A.K., and Gaudette, H.E., 1989, The age, origin, and tectonics of the Grão Pará Group and associated rocks, Serra dos Carajás, Brazil: Archean continental volcanism and rifting: Precambrian Research, v. 42, p. 229–254, https://doi.org/10.1016/0301-9268(89)90013-2.

Pereira, R.M.P., Rosiere, C.A., Santos, J.O.S., Lobato, L.M., Silva, R.C.F., and McNaughton, N.J., 2009, Unidade Caninana: Sequência clástica Paleoproterozóica revelada por datação U-Pb em zircões detríticos da Província Mineral Carajás: Abstract presented at XI Simpósio de Geologia da Amazônia, Manaus, Brazil, 2–5 August.

Pickering, K.T., Corregidor, J., and Clark, J.D., 2015, Architecture and stacking patterns of lower-slope and proximal basin-floor channelized submarine fans, Middle Eocene Ainsa System, Spanish Pyrenees: An integrated outcrop–subsurface study: Earth-Science Reviews, v. 144, p. 47–81, https://doi.org/10.1016/j.earscirev.2014.11.017.

Pinheiro, R.V.L., and Holdsworth, R.E., 1997, Reactivation of Archaean strike-slip fault systems, Amazon region, Brazil: Journal of the Geological Society, v. 154, p. 99–103, https://doi.org/10.1144/gsjgs.154.1.0099.

Rasmussen, B., Bekker, A., and Fletcher, I.R., 2013, Correlation of Paleoproterozoic glaciations based on U-Pb zircon ages for tuff beds in the Transvaal and Huronian Supergroups: Earth and Planetary Science Letters, v. 382, p. 173–180, https://doi.org/10.1016/j.epsl.2013.08.037.

Strand, K., 2012, Global and continental-scale glaciations on the Precambrian earth: Marine and Petroleum Geology, v. 33, p. 69–79, https://doi.org/10.1016/j.marpetgeo.2012.01.011.

Tallarico, F.H.B., Figueiredo, B.R., Groves, D.I., Kositcin, N., McNaughton, N.J., Fletcher, I.R., and Rego, J.L., 2005, Geology and SHRIMP U-Pb geochronology of the Igarapé Bahia deposit, Carajás copper-gold belt, Brazil: An Archean (2.57 Ga) example of iron-oxide Cu-Au-(U-REE) mineralization: Economic Geology and the Bulletin of the Society of Economic Geologists, v. 100, p. 7–28, https://doi.org/10.2113/100.1.0007.

Tang, H., and Chen, Y., 2013, Global glaciations and atmospheric change at ca. 2.3 Ga: Geoscience Frontiers, v. 4, p. 583–596, https://doi.org/10.1016/j.gsf.2013.02.003.

Teixeira, W., Hamilton, M.A., Girardi, V.A.V., Faleiros, F.M., and Ernst, R.E., 2018, U-Pb baddeleyite ages of key dyke swarms in the Amazonian Craton (Carajás/Rio Maria and Rio Apa areas): Tectonic implications for events at 1880, 1110 Ma, 535 Ma and 200 Ma: Precambrian Research, v. 329, p. 138–155, https://doi.org/10.1016/j.precamres.2018.02.008.

Thomas, G.S.P., and Connell, R.J., 1985, Iceberg drop, dump, and grounding structures from Pleistocene glacio-lacustrine sediments, Scotland: Journal of Sedimentary Petrology, v. 55, p. 243–249, https://doi.org/10.1306/212F8689-2B24-11D7-8648000102C1865D.

Trendall, A.F., Basei, M.A.S., Laeter, J.R., and Nelson, D.R., 1998, SHRIMP zircon U-Pb constraints on the age of the Carajás Formation, Grão Pará Group, Amazon Craton: Journal of South American Earth Sciences, v. 11, p. 265–277, https://doi.org/10.1016/S0895-9811(98)00015-7.

Whalley, W.B., and Krinsley, D.H., 1974, A scanning electron microscope study of surface textures of quartz grains from glacial environments: Sedimentology, v. 21, p. 87–105, https://doi.org/10.1111/j.1365-3091.1974.tb01783.x.

Young, G.M., 2014, Contradictory correlations of Paleoproterozoic glacial deposits: Local, regional or global controls?: Precambrian Research, v. 247, p. 33–44, https://doi.org/10.1016/j.precamres.2014.03.023.

Printed in USA

6 EVIDENCES OF AN "OIL-LIKE" MANGANESE REMOBILIZATION IN THE PALEOPROTEROZOIC AZUL RED BEDS OF THE CARAJÁS BASIN (AMAZONIAN CRATON, BRAZIL): AN INTERPLAY AMONG SEDIMENTARY AND TECTONIC CONTROLS

Raphael N. Araújo[1,2]*, Afonso C.R. Nogueira[2,3], Marcelo J. Sousa[4], Roberto V.L. Pinheiro[3], Rômulo S. Angélica[2,3], Luiz C. Costa[5], F. Gauthier-Lafaye[6]

[1] Management of Geology and Mineral Resources, Geological Survey of Brazil, 66095-904, Belém, Brazil

[2] Post-graduate Program in Geology and Geochemistry, Federal University of Pará, 66075-110, Belém, Brazil

[3] Faculty of Geology, Federal University of Pará, 66075-110, Belém, Brazil

[4] Mineral Economics and Exploratory Geology Division, Geological Survey of Brazil, 70040-904, Brasília, Brazil

[5] Management of Geology and Drilling of Iron Deposits, N-4 mine, Vale S.A., 68516-000, Parauapebas, Brazil

[6] Laboratoire D'hydrologie et de Géochimie de Strasbourg, CNRS-UDS, France

*Corresponding author e-mail address: raphael.araujo@cprm.gov.br

ABSTRACT

Manganese is a redox-sensitive element that was widely deposited during the early Paleoproterozoic era due to the raised oxygen level in the hydrosphere-atmosphere system as a result of oxygen catastrophe caused by the Great Oxidation Event (GOE) and as an aftermath of Paleoproterozoic glaciations. In addition, manganese was widely remobilized during orogens, which affected most of the Precambrian successions worldwide. In this study, we investigated the manganese-bearing deposits of the Azul Formation of the Carajás Basin in southeastern Amazonian Craton, Brazil. Facies analysis indicates that manganese is hosted in the offshore strata of a shallow marine basin, interpreted as red beds deposits, which are unconformably overlain by thick fluvial beds of the Águas Claras Formation. The structural analysis of these deposits shows that the manganese-bearing succession is tightly deformed. Moreover, the chemical and mineralogical analysis demonstrate that manganese oxides are enriched near the fault zones. Besides, the deposit is characterized by a diversity of manganese-bearing minerals, including cryptomelane, pyrolusite, spessartite and todorokite. Based on the findings achieved in this study, we envisage an accumulation model for the Azul manganese-bearing succession, where sedimentary and tectonic controls are crucial tools for the large-scale manganese accumulation. We predict that manganese was reduced in highly oxygenated shallow waters and afterward downwelling moved to the deepest parts of the basin, in which it deposited in association with the black shale strata. Subsequently, the remobilization of

manganese from rhodochrosite-enriched strata, which formed during diagenesis, under hydrothermal conditions allowed for the re-precipitation of this metal as oxides in the discontinuities within the succession. The manganese migrated through faults and accumulated in low strain zones and also through intervals with high porosity and permeability within the host rock, such as sandy laminations and beds, as observed in the migration of hydrocarbons. We believe that the primary accumulation of manganese was only possible due to favorable conditions that allowed this metal to precipitate in subaqueous conditions. This involves a highly oxygenated environment during the transgression of the Azul Sea onto the protocontinent. It is important to note that we are not disputing that supergenic processes actuated to enrich the manganese ore, instead, we propose that the hypogene mechanism also contributed toward the enrichment of this ore in the Azul Formation. However, the deformation and remobilization of the manganese ore from the enriched strata to red beds of the Azul Formation was crucial for the final stage of manganese accumulation at the end of the Paleoproterozoic era.

Keywords: Paleoproterozoic. Hypogene Mn-enrichment. Like-oil migration. Fault-hosted manganese. Sedimentary controls.

6.1 INTRODUCTION

The accumulation of manganese in the Precambrian sedimentary successions is associated with, in many cases, multiple factors from specific paleoenvironmental conditions to post-depositional processes (Roy 1997, 2006, Tsikos *et al.* 2003, Sekine *et al.* 2011, Jones 2011, Jones *et al.* 2013, Johnson *et al.* 2016). Although peaks of deposition of this metal occurred during the Neoarchean and Neoproterozoic eras, manganese deposits were mainly deposited in the early Paleoproterozoic era (Roy 2006, Maynard, 2010). The widespread deposition of manganese in this era is generally associated with the emergence of oxygenated earth onset of the Great Oxidation Event (GOE) at *ca.* 2.45 Ga (Laznicka 1992, Glasby 1997, Roy 1997, 2006, Bekker *et al.* 2004, Maynard 2010, Sekine *et al.* 2011, Johnson *et al.* 2013). Importantly, manganese, a redox-sensitive element, is commonly used as a proxy to indicate the amount of oxygen in the atmosphere-hydrosphere system (Sekine *et al.* 2011, Johnson *et al.* 2013). The primary deposition of manganese was triggered when the atmospheric O_2 became higher than *ca.* 10^{-2} times the present atmospheric level (PAL) (Sekine *et al.* 2011). Broadly, the manganese was deposited in highly oxidized shallow marine zones, whereas the deep waters with euxinic conditions allowed for the deposition of thick deposits of black shale (Force &

Cannon 1988, Sekine *et al*. 2011). Furthermore, manganese-bearing successions are generally enriched and controlled by secondary processes such as tectonic mechanisms, which frequently cause the distinction between these processes to become very difficult (Jones *et al.* 2013, Gosh *et al.* 2015).

In the Carajás Basin, which is considered as a relic sedimentary basin, situated in southeastern Amazonian Craton in Brazil (Fig. 6.1), expressive deposits of manganese are hosted in a dominantly siliciclastic succession named the Azul Formation (Araújo Filho *et al*. 2020), anteriorly considered as a part of the Águas Claras Formation (Nogueira *et al*. 1995, Araújo & Nogueira 2019). Although manganese ore has been extensively explored in the past 50 years, the stratigraphic setting and the sedimentary mechanisms involved in the deposition of this metal are still uncertain. While some studies suggest that the origin of these deposits is linked to predominantly supergenic processes through episodic precipitation occurring throughout the Cenozoic era (Vasconcelos *et al.* 1994, Ruffet *et al.* 1996), authors of other studies have indicated the presence of some structural controls on the manganese deposits (Pinheiro 1997, Silva 2006). However, an integrative model that unravels the role of each of these processes and the mechanisms involved in manganese deposition in the succession of the Azul Formation has not been conceived yet.

Moreover, the relationship between the Azul manganese deposits and the events occurring during the early Paleoproterozoic era has not been discussed yet, and its exact controls on manganese deposition and enrichment still remain uncertain. Partially, this problem results due to imprecise stratigraphic settings and poor age constraints that hindered accurate paleoenvironmental reconstructions. Importantly, the Azul succession may be a significant archive of events occurring at that time period, mainly regarded as the evolution of the primitive atmosphere-hydrosphere system. The discovery of the Paleoproterozoic glacial diamictite strata of the Serra Sul Formation revived the possibility that these units can record a geological history more complex than presumed (Araújo & Nogueira 2019).

In this study, we carried out a combination of sedimentological, stratigraphical, tectonic, chemical, and mineralogical investigations on the Azul manganese-bearing succession of the Carajás Basin (southeastern Amazonian Craton, Brazil) to address the origin of and the mechanisms involved in the enrichment of manganese in this unit. Our results throw more light on the evolution of this part of the Amazonian Craton in the early Paleoproterozoic era and allowed to insert the Carajás manganese deposit within a context of regional and global scale events, including paleoclimatic, tectonic and paleoenvironmental changes intrinsically related to that time period.

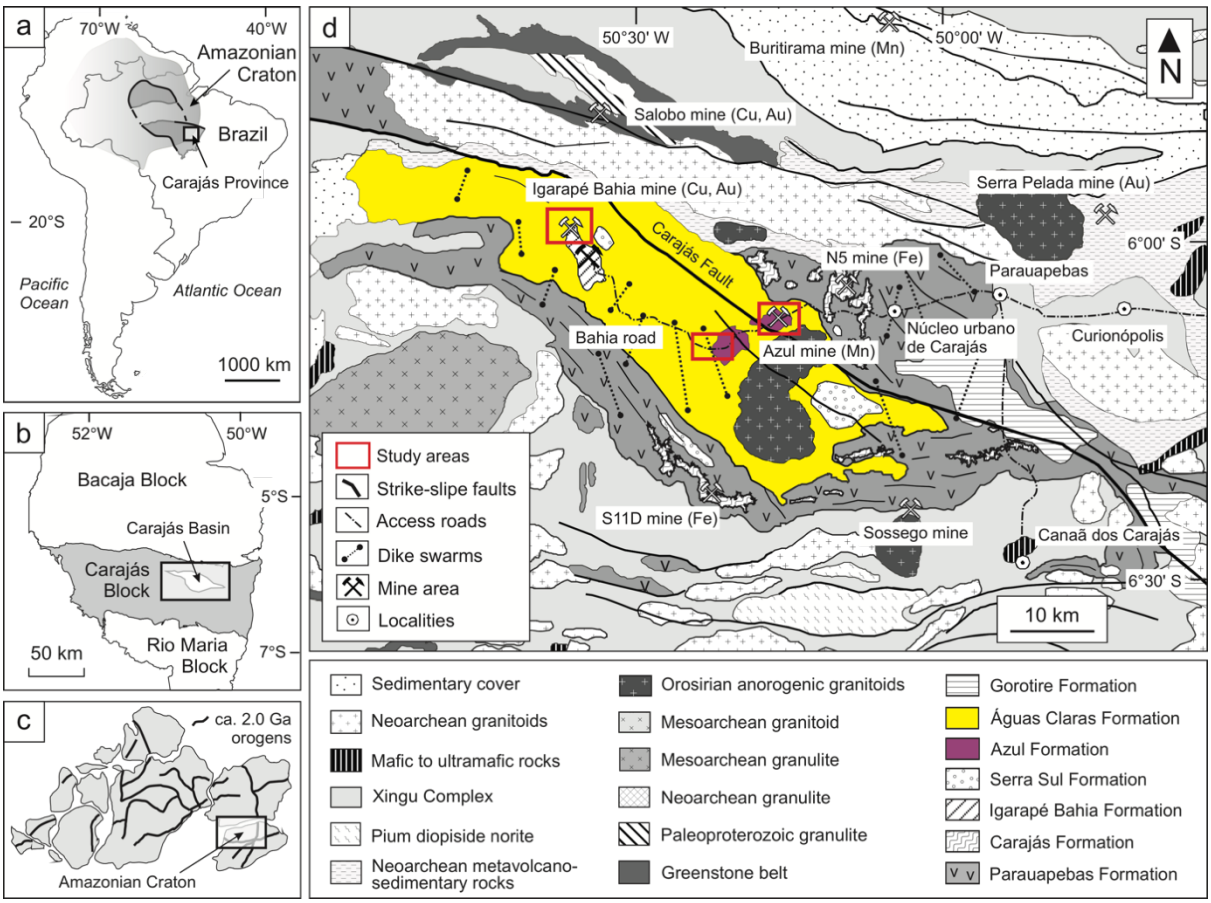

Figure 6.1: Location map of the study area. (a) South America map showing the location of the Carajás Province in the Amazonian Craton. (b) Carajás Province map showing the location of the Carajás Basin in the Carajás domain. (c) Paleogeographic reconstruction of the Columbia supercontinent at *ca*. 2.0 Ga showing the location of the Amazonian Craton (modified from Zhao *et al.* 2002, 2004). (d) Geological map of the Carajás Basin and the surrounding areas showing the location of the studied areas (modified from Vasquez *et al.* 2008a).

6.2 GEOLOGICAL BACKGROUND

The Carajás Province is one of the most important Archean domains of the Amazonian Craton, where several world-class mineral deposits are located (Dall'Agnol *et al.* 2013). Located in the southeastern part of this craton, this province has been inserted into the Amazonia Central Geochronological Province and is surrounded by the youngest rocks from the Statherian to the Neoproterozoic ages (Tassinari & Macambira 2004). The Carajás Province is compartmented in two distinct segments called the Rio Maria Domain and Carajás Domain (Vasquez *et al.* 2008a, 2008b). While the Rio Maria Domain predominantly encompasses Mesoarchean rocks, the Carajás Domain dominantly encompasses rocks formed during the Neoarchean (Dall'Agnol *et al.* 1997, 2006, Vasquez *et al.* 2008b, Feio *et al*. 2013). The Carajás Basin is located in the northern portion of the Carajás Domain and filled with a volcano-

sedimentary succession deposited throughout the Neoarchean to the Paleoproterozoic era (Tavares *et al.* 2018, Araújo & Nogueira, 2019, Araújo *et al.* 2020).

This Carajás Basin is considered a synclinal basin filled by unmetamorphosed to a very low-grade metamorphosed rocks, limited by strike-slip faults and surrounded by highly deformed and metamorphosed igneous and sedimentary units (Pinheiro 1997, Pinheiro & Holdsworth 1997, Holdsworth & Pinheiro 2000). The basin has a basement constituted by granite and gneiss rocks attributed to the Xingu Complex, which presents a migmatization age of *ca.* 2.85 Ga (Machado *et al.* 1991). The basin is truncated by several dike swarms and by the Carajás Granite in its central portion, which presents a crystallization age of *ca.* 1.88 Ga (Machado *et al.* 1991, Teixeira *et al.* 2018, Teixeira *et al.* 2019). According to Araújo & Nogueira (2019), the Carajás Basin-filling rocks may be stratigraphically stacked into the Grão-Pará Group, Serra Sul, Águas Claras, and Gorotire formations (Fig. 6.2).

The Grão-Pará Group occur at the base of the Carajás Basin and comprises a thick pile (2–3 km in thickness) of mafic to felsic volcanic rocks (Cabral *et al.* 2017) that can be attributed to the Parauapebas Formation, deposited in a rift setting at *ca.* 2.75 Ga, above which banded iron formation strata designed as the Carajás Formation lies (Olszewski *et al.* 1989, Trendall *et al.* 1998, Martins *et al.* 2017). Above these strata, pelitic, tuffaceous and volcanic rocks of the Igarapé Bahia Formation, anteriorly considered as a group, were deposited at *ca.* 2.74 Ga (Trendall *et al.* 1998, Galarza *et al.* 2008) and affected by a *ca.* 2.58 Ga Cu-Au mineralization (Tallarico *et al.* 2005). On the other hand, the Serra Sul, Azul, Águas Claras, and Gorotire formations comprise mudstones, sandstones, and conglomerates, which were likely deposited through the Siderian to the Rhyacian periods (Araújo & Nogueira 2019, Araújo Filho *et al.* 2020, Araújo *et al.* submitted). The Serra Sul Formation was recently established in the Carajás Basin and encompasses mainly diamictite, sandstone, and conglomerate strata deposited during a Paleoproterozoic glaciation event that occurred in the Amazonian Craton known as the Serra Sul glaciation (Araújo & Nogueira 2019).

Similarly, the Azul Formation was formally proposed as a new lithostratigraphic unit of the Carajás Basin in a recent study presented by Araujo Filho *et al.* (2020). The recognition of the presence of an important stratigraphic surface in this basin allowed them to propose this new formation, historically considered the lowermost part (lower member) of the Águas Claras Formation (Nogueira *et al.* 1995). The Azul Formation occurred outcropping mainly in the Azul mine and dominantly encompasses the rhythmite strata deposited in a marine setting (Araujo Filho *et al.* 2020) and is unconformably overlaid by the Águas Claras Formation, which mainly comprises sandstone and conglomerate stacked in fining upward cycles deposited in a fluvial

braided setting (Araújo & Maia 1991, Nogueira 1995, Nogueira et al. 1995, Pinheiro 1997, Costa 2017, Araujo & Sousa 2018, Araujo Filho *et al.* 2020, Araújo *et al.* submitted). The Águas Claras Formation is better exposed in the roadcut outcrops along the access road to the Igarapé Bahia mine, where Nogueira *et al.* (1995) established a type-section of this unit.

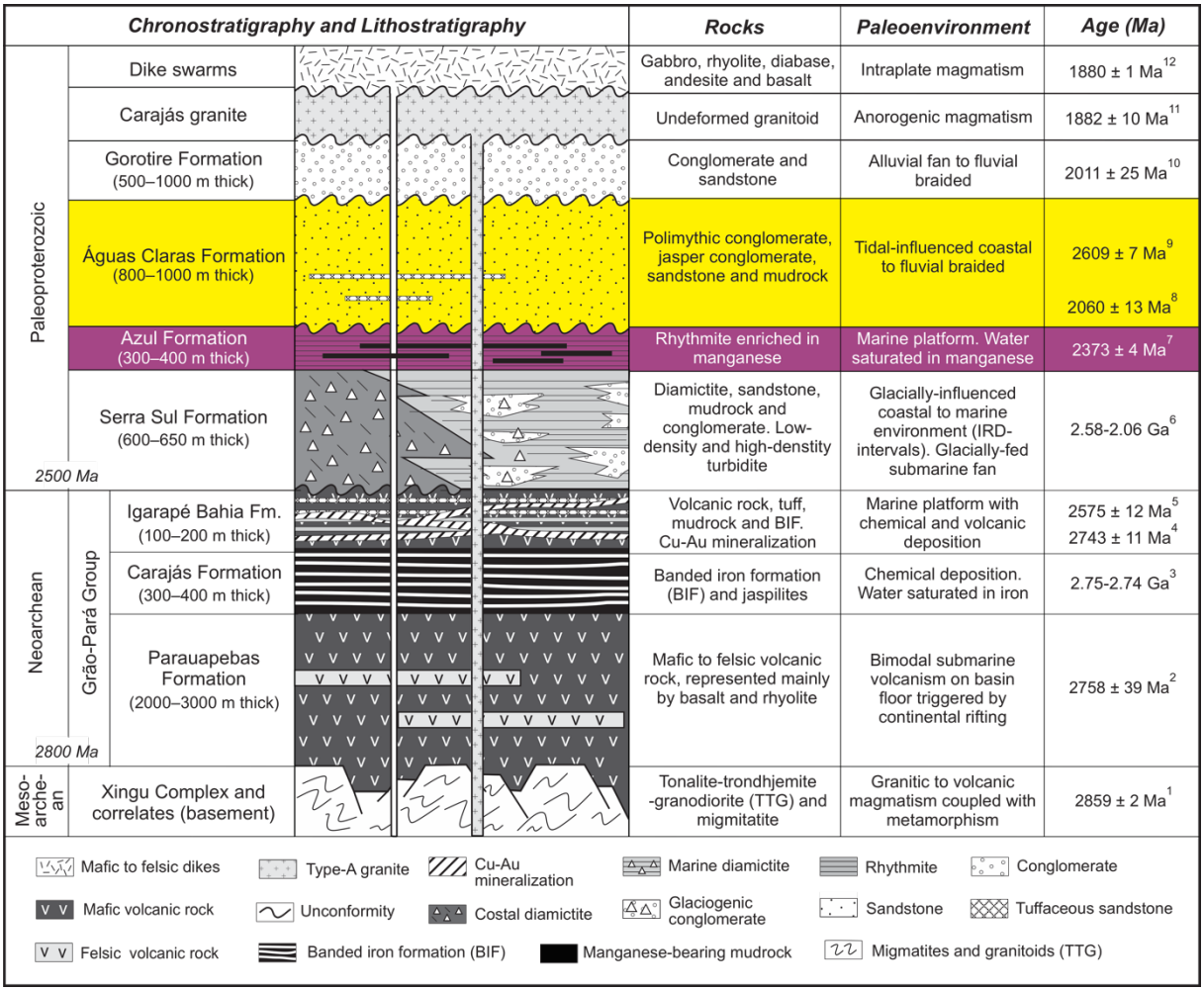

Figure 6.2: Stratigraphic framework of the Carajás Basin, located in the Amazonian Craton, Brazil (modified from Araújo & Nogueira 2019). Geochronological data compiled from: 1—Machado *et al.* (1991); 2—Martins *et al.* (2017); 3—Trendall *et al.* (1998); 4—Galarza *et al.* (2008); 5—Tallarico *et al.* (2005); 6—Araújo & Nogueira (2019); 7—Justo *et al.* (2018); 8—Mougeot *et al.* (1996); 9—Araújo & Sousa (2018); 10—Pereira *et al.* (2009); 11—Teixeira *et al.* (2018); 12— Teixeira *et al.* (2019).

6.3 MATERIALS AND METHODS

Sedimentological and stratigraphic analysis in the drill cores and outcrops that cross the Azul Formation was undertaken. They are located in three different areas of the Carajás Basin: i) the Igarapé Bahia mine, ii) the Bahia road, and iii) the Azul mine. A composite sedimentary log of each studied area, organized in an oriented section, was constructed in addition to a

simplified facies map for each area. Classical procedures of facies analysis, including the recognition of stratigraphic surfaces and lithofacies, and the subsequent arrangement of these in different facies associations, which record particular paleoenvironmental settings, were carried out. Structural data was collected from two representative structural transects, in NW-SE and NE-SW directions, located within the Azul mine. The attitudes of the beds, fractures, and faults were systematically measured along the structural transects and subsequently plotted in stereograms (equal area) and rose diagrams. For the construction of the diagrams, Stereonet3D software was used.

Small pieces of samples (*ca.* 5 cm length) were collected from the mineralized strata to identify the manganese-bearing minerals present in the succession. These samples were analyzed using an X-ray diffractometer (XRD) and scanning electron microscope (SEM). For the DRX analysis, the samples were prepared using the classical procedures generally applied to this kind of analysis—grounding the sample in an agate mortar and subsequently preparing a tablet to be analyzed in the equipment model X´PERT PRO MPD (PW 3040/60) of PANalytical at the Geological Survey of Brazil (CPRM, Manaus, Brazil). The data was handled using the software X´Pert HighScore of PANalytical. Minerals were identified by making a comparison with the pattern files of each mineral achieved in the ICDD-PDF (International Center for Diffraction Data – Powder Diffraction File) database. For an SEM analysis, polished thin sections were fixed in SEM stubs using a double-sized tape. The samples were analyzed in the SEM model, LS15 of Zeiss at CPRM (Belém, Brazil), in which mainly the microtextural aspects of minerals were observed.

To assist in the mineral identification with SEM analysis, Energy-dispersive X-ray spectroscopy (EDS) analysis was performed in specific areas of the thin sections of the sample. The EDS detector model X-Act SSD 10mm^2 of Oxford Instruments is coupled with the SEM equipment and the results of the EDS analysis were presented in the spectrograms of each analyzed area. Additionally, to evaluate the content of manganese oxide and other-related oxides throughout the major structures that cross the succession, controlled sampling was performed across the NW-SE structural transect (Supplementary Material, Table S-1). The samples were analyzed using ICP-AES (Inductively Coupled Plasma – Atomic Emission Spectrometry) at the French National Centre for Scientific Research (CNRS), France.

6.4 THE MANGANESE-BEARING SUCCESSION

6.4.1 Stratigraphic and sedimentological aspects

The manganese-bearing succession, described in this study, constitutes a dominantly siliciclastic succession with a thickness of approximately 300 m, which encompasses a major part of the Azul Formation (Fig. 6.3). In this succession, six lithofacies were described and subsequently arranged in three distinct facies associations—Rhythmite Facies Association (RFA), Rhythmite-Sandstone Facies Association (RSFA), and Conglomerate-Sandstone Facies Association (SCFA). The former two belong to the Azul Formation and are stacked at the base of the succession, while the other belongs to the Águas Claras Formation. The stratigraphic stacking pattern observed in the manganese-bearing succession strongly suggests that the RFA deposits occur laterally interbedded with the RSFA ones. These facies associations are unconformably overlaid by the CSFA. Importantly, the manganese-enriched intervals are found strictly positioned in the RFA strata.

The surface that separates the underlying Azul from the overlying Águas Claras Formation may be mapped in several areas of the Carajás Basin (Araújo Filho *et al.* 2020). Near the southwestern border of the Carajás Basin, this surface occurs unconformably overlaid on the glaciogenic deposits of the Serra Sul Formation and the Grão-Pará Group (Araújo & Nogueira 2019). Regarding the stratigraphic architecture of the Carajás Basin, the manganese-enriched mudrock strata of the Azul Formation occur dominantly outcropped toward the NE direction of this basin. The primary textures and structures are well-preserved and can be easily recognized throughout the succession. The dominant facies in the manganese-bearing succession is the rhythmite lithofacies, which is constituted by millimeter to centimeter intercalations between the normal-graded sandstone and mudrock. Hummocky cross-stratified sandstone intervals occur very subordinately (Fig. 6.4).

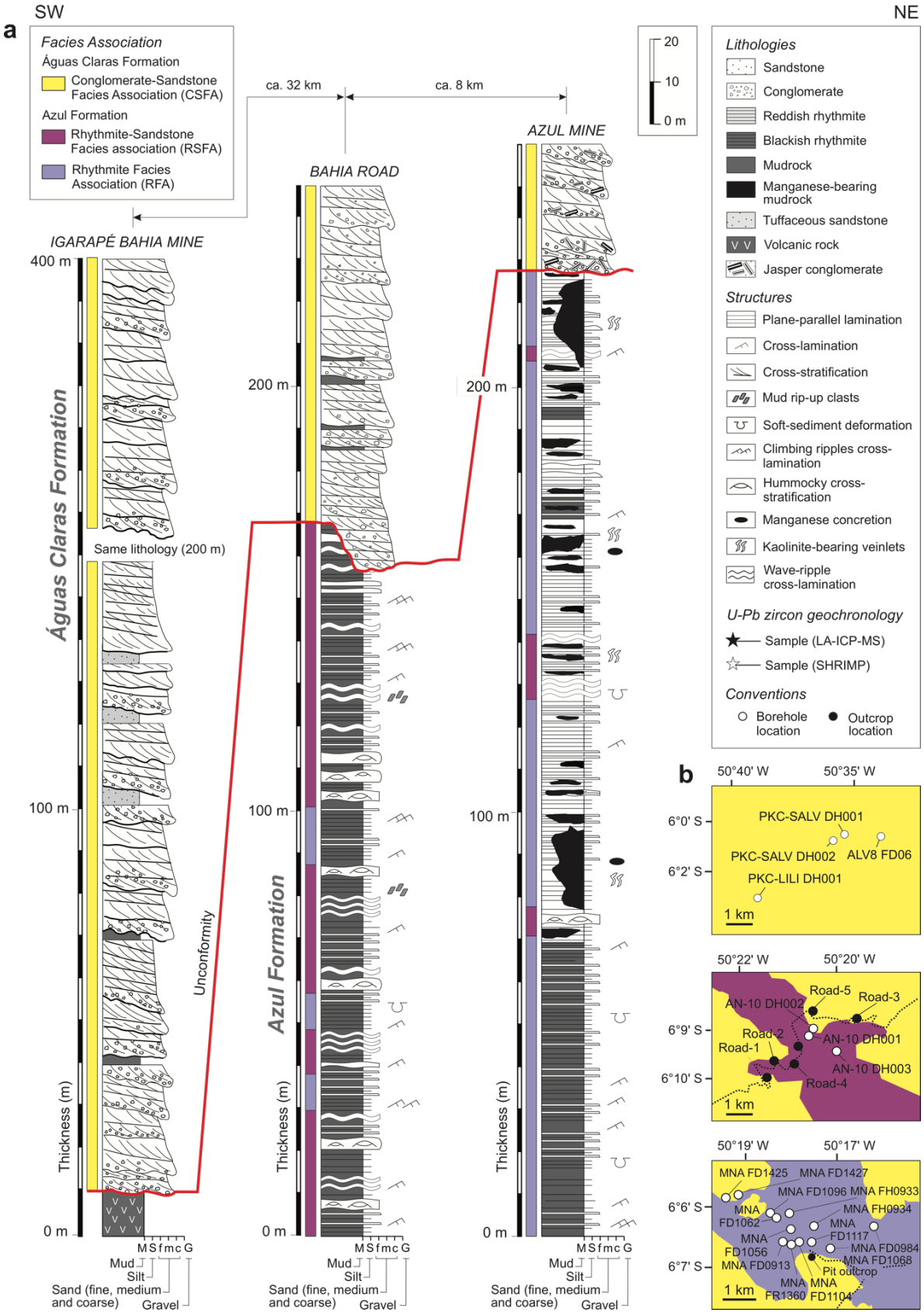

Figure 6.3: Stratigraphy of the manganese-bearing succession of the Carajás Basin (southeastern Amazonian Cráton, Brazil) described in this study. a) Composite sedimentary logs in the Azul and Águas Claras formations from the studied areas. b) Simplified facies maps of the study areas.

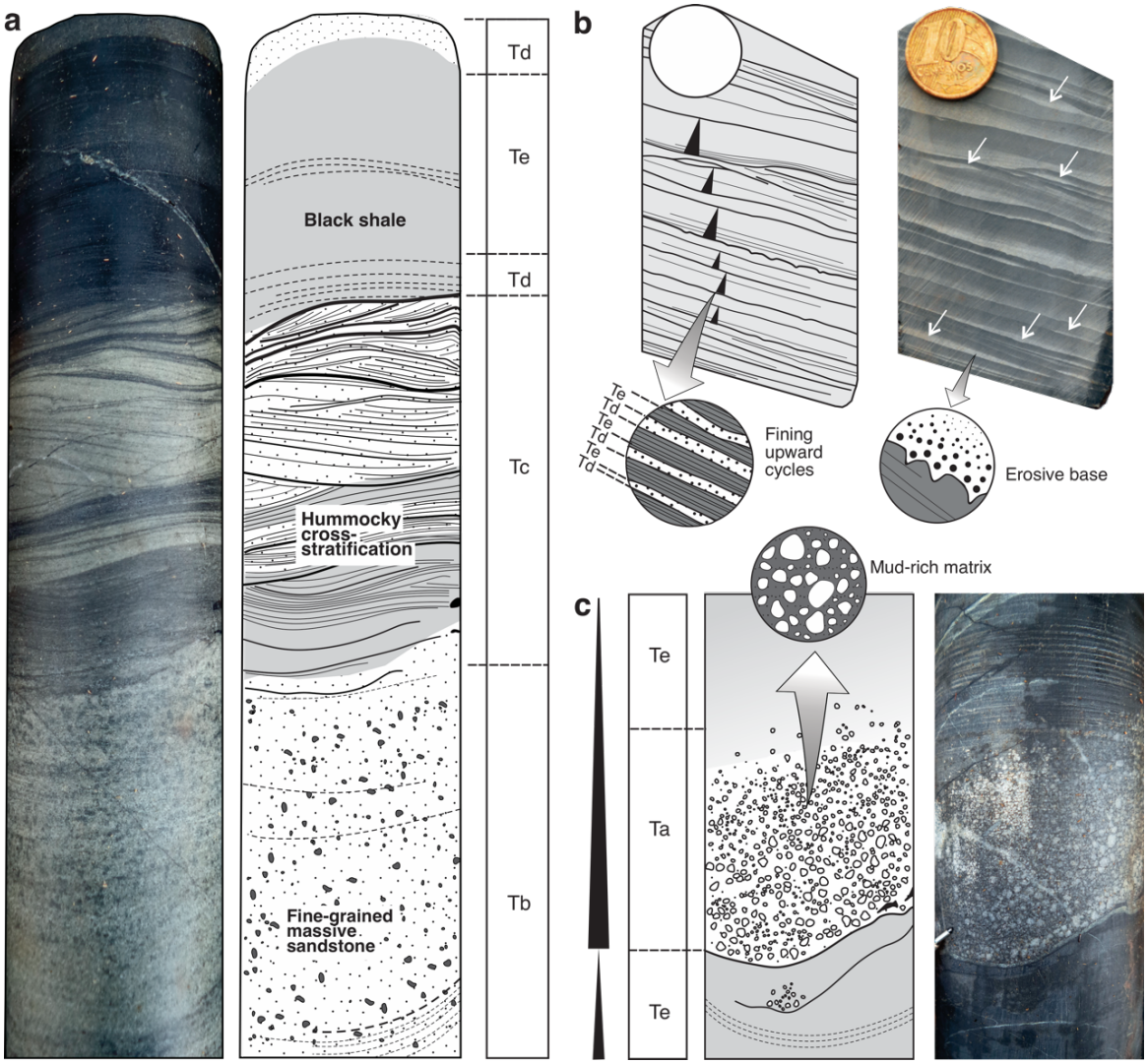

Figure 6.4: Rhythmite lithofacies features. (a) Centimeter intercalation between the normal-graded sandstone and mudrock. Hummocky cross-stratified sandstone intervals occur very subordinately. (b) Fining upward cycles composed of fine-grained sandstone and mudrock. (c) Abrupt contact between the fine to medium-grained sandstone and mudrock at the base of the fining upward cycles.

6.4.2 Structural setting

6.4.2.1 The structural transects and patterns of deformation

In the structural transect 1 (ST1), the bedding (Sn = S_0) is preferentially oriented in the NE-SW (60° to 70°) and NW-SE (100° to 110°) directions, dipping to 60° to 80° toward NW and 10° to 80° toward NE, respectively. In the structural transect 2 (ST2), the bedding (Sn = S_0) is preferentially oriented in the NW-SE (100° to 110°) direction, dipping to 70° to 80° toward SW and NE directions and subordinately oriented in NE-SW (70° to 80°) direction, dipping 30° to 40° to SE. Regarding fractures and faults, in the ST1, they are closely oriented in the NW-SE direction and near the E-W direction, while in the ST2, they are oriented in the

NW-SE and NE-SW directions (Fig. 6.5). The fold vergences are preferentially oriented toward SW and SE directions. The deformation is partitioned in different strain domains following the main direction with 110º to 280º of azimuth, where faults delimit the blocks with different deformation domains.

The geometric boundary between the strain domains is represented by oblique faults following the main direction of the Carajás Fault. Inverse faults, drag folds, and kink bands with deformation planes, preferentially oriented in the NW-SE direction with vergence to the SW direction, are the main structural features observed and may occur in several scales and styles. Generally, the meter- to centimeter-scale folds, which occur preferentially oriented along the close E-W direction, show an axis plunging of 30º to 50º toward the NW direction. Reclined folds show axis plunging with shallow angles (10º) toward the SE direction. They vary from gentle folds to tight folds, mostly asymmetric, and with slightly divergent isogon patterns. Fracturing and faulting are responsible for less important kinking, which affects the flanks of drag folds and bedding. These kink bands are plunging toward the south, in most cases, related to sets of non-pervasive N-S and NW-SE fractures.

6.4.2.2 Manganese and tectonic

In intense deformation zones, manganese occurs frequently in association with kaolinite, which either occurs structurally controlled. In some cases, the manganese simply stains the host rock irrespective of its structural arrangement. In other cases, the manganese occurs enriched in meter-, centimeter- to millimeter-scale plans of fractures and faults, preferentially those in the NW-SE direction. Moreover, the manganese occurs in concentrated amounts in hinge zones of antiformal folds, including drag folds. In certain intervals, the manganese occurs in halos-like shapes, forming, in some cases, even centimeter-scale manganesiferous concretions of strictly secondary origin. Near the plans of discontinuity, the manganese also occurs in concentrated amounts in the bedding of the host rock (Fig. 6.6).

The geochemical results obtained from across the SE-NW structural transect supported the observation that manganese occurs in abundance in the damage fault zones. In contrast, between these zones, the manganese decreases abruptly. Similarly, iron and aluminum decrease in the damage fault zones and increase between them. The content of manganese oxide reaches up to *ca.* 75%, while that of iron oxide and aluminum oxide reaches up to *ca.* 15% and 25%, respectively. Regarding the ratios between these metals, both the ratios Mn/Fe and Mn/Al increases in the damage fault zones, while they decrease in the zones between them. The trend of these ratios accompanies that of manganese oxide (Fig. 6.7).

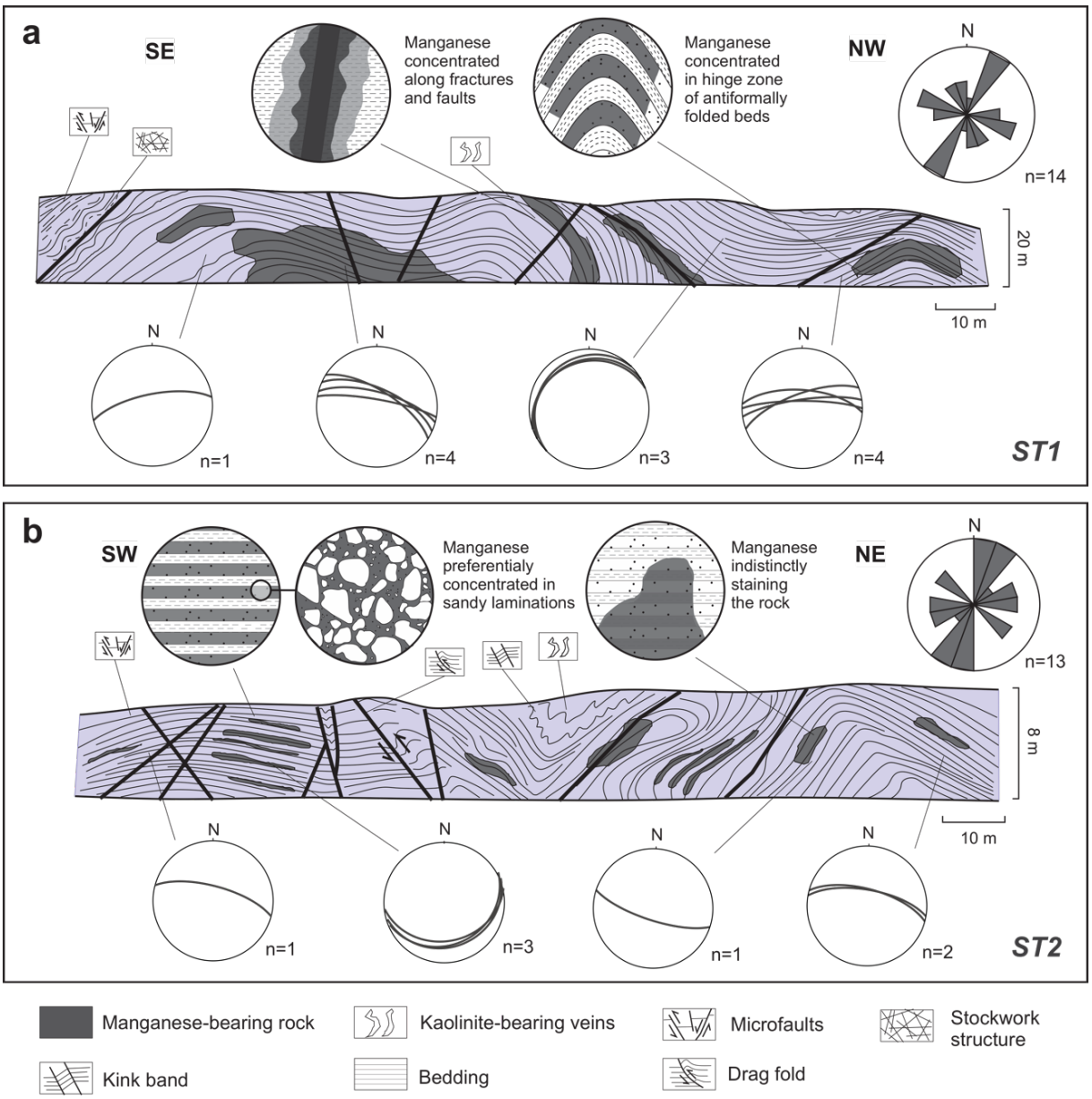

Figure 6.5: Structural transects measured within the Azul mine. (a) SE-NW structural transect showing suave folded beds dipping slightly to the NW direction and tightly to the NE and NW direction. Fractures and faults occur mainly oriented in the NE-SW and SE-NW directions (rose diagram). (b) SW-NE structural transect showing tightly folded beds. Fractures and faults that occur are NE-SW- and SE-NW-oriented (rose diagram). Meter-scale drag folds and centimeter-scale kink-bands are largely observed. Manganese occurs hosted in the planes of fractures and stains the host rock, and subordinately forms stockwork structures.

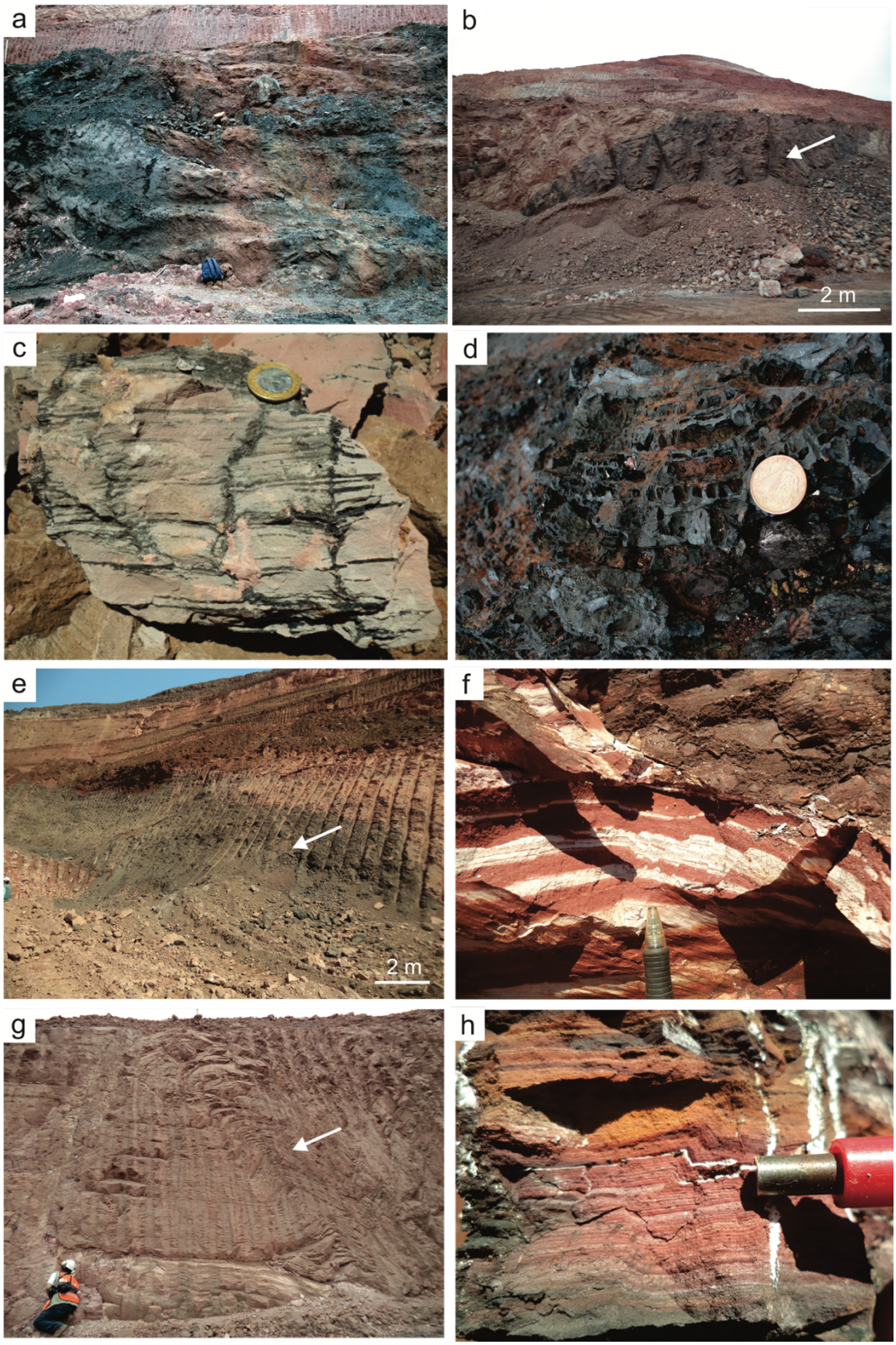

Figure 6.6: Main structural aspects observed in the Azul manganese-bearing succession of the Carajás Basin (southeastern Amazonian Craton, Brazil). (a) Manganese randomly staining rhythmite deposits. (b) Manganese concentrated on the beds located in the hinge zone of an antiformal fold. (c) Manganese enriched in the fractures and sandy laminations. (d) Manganese forming a type of stockwork structure. (e) A meter-scale fault-hosted manganese interval. (f) Micro-faults. (g) Drag fold. (h) Kink band structure.

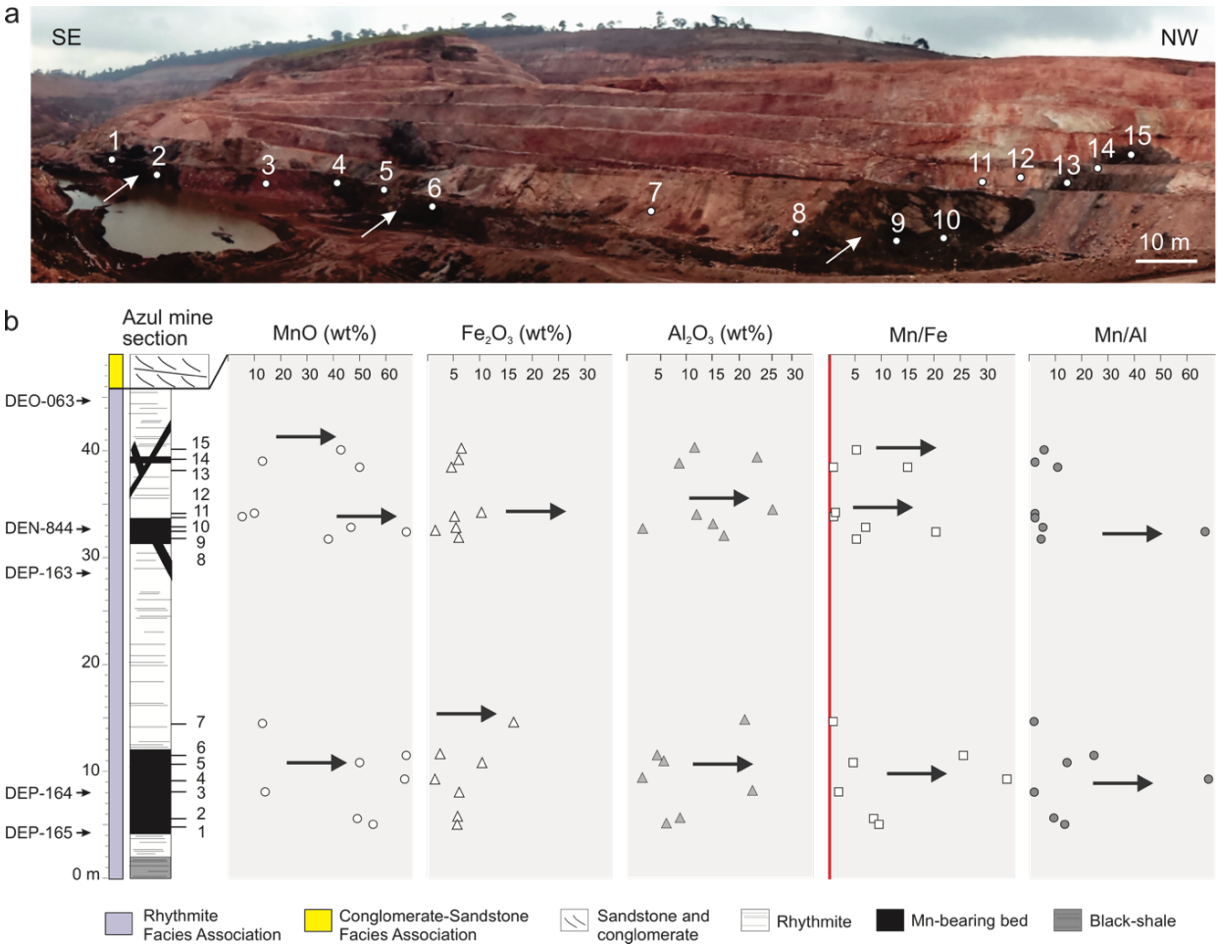

Figure 6.7: Geochemical trends of some major oxides and ratios across the ST1. (a) Image of the Azul mine pit showing the locale from where the samples were collected. (b) Geochemical trend profiles of some major oxides (MnO, Fe_2O_3, and Al_2O_3,) and ratios (Mn/Fe and Mn/Al). The red line represents the Mn/Fe ratio found in typical detrital components (Maynard 2003).

6.4.3 The identified manganese-bearing minerals

The SEM, DRX, and EDS analyses revealed that the main mineral-bearing minerals in the Azul succession are the cryptomelane and pyrolusite (Figs. 6.8 and 6.9). Additionally, todorokite, hollandite, and spessartite occur quite subordinately. Cryptomelane occurs as needle-like crystallites, as a fine-grained masse or yet with botryoidal and acicular habits. Moreover, cryptomelane fills the micrometer-scale veins. Pyrolusite was identified in the DRX analysis, and no information about the habit and the form of occurrence of this mineral may be presented. Todorokite is the main manganese-bearing mineral that forms the finely laminated manganese ore. This mineral occurs almost alongside kaolinite, which occurs while exhibiting its typical thin hexagonal platelets habit, stacked in the form of booklets. Pyrolusite and cryptomelane are commons manganese-bearing minerals that constitute the massive ore, and

the pisolitic ore is dominantly formed by cryptomelane. Subhedral crystals of spessartite occur very subordinately as grains finely scattered in laminations of rhythmite.

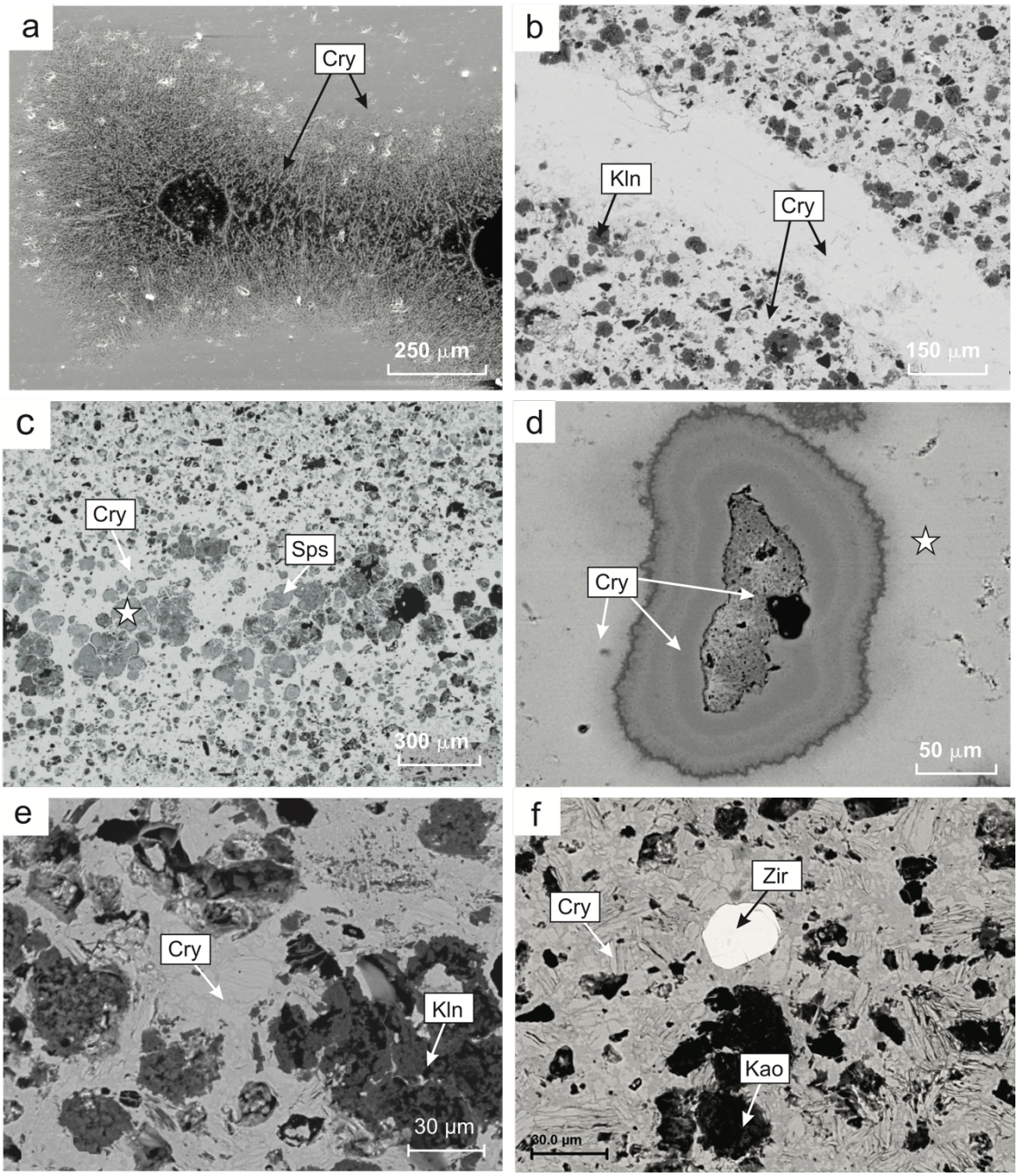

Figure 6.8: Scanned electron-microscope (SEM) images obtained from manganese-bearing rhythmite samples of the Azul succession. (a) Cryptomelane (Cry) as needle-like crystallites and a fine-grained masse. (b) Fine-grained mass of cryptomelane concentrated in veins alongside kaolinite (Kao). (c) Fine-grained mass of cryptomelane and subhedral crystals of spessartite (Sps) concentrated in lamination. (d) Botryoid formed of cryptomelane, showing banded colloform texture and with acicular crystallites in the center intergrow latticed. (e and f) Cry as needle-like crystallites alongside Kao. Zircon (Zir) occurs subordinately. The stars represent the areas from where we obtained EDS spectra.

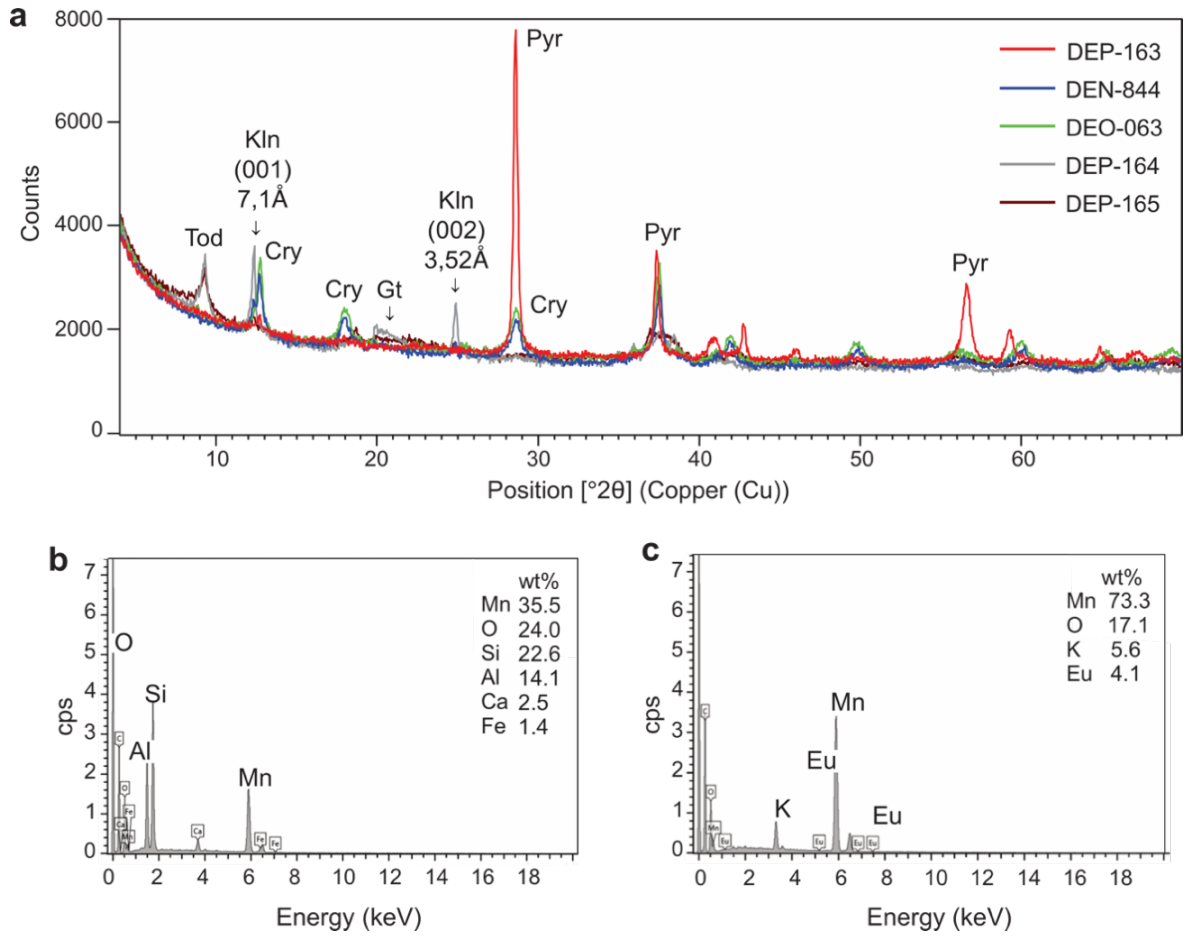

Figure 6.9: Manganese-bearing minerals identified in the Azul succession. (a) X-ray diffractogram showing todorokite (Tod), kaolinite (Kln), cryptomelane (Cry), goethite (Gt), and pyrolusite (Pyr). Energy-dispersive X-ray spectrograms of spessartite (b) and cryptomelane (c).

6.5 DISCUSSION

6.5.1 Sedimentary environment and model of primary manganese deposition

The observation that normally graded sandstone occurs repeatedly interlayered with structureless to even laminated mudrock in fining-upward cycles suggests that it comprises low-density turbidity deposits lodged within the basin in subaqueous conditions (Bouma 1962, Mutti & Ricci Lucchi 1975, Stow & Piper 1984, Mutti 1992, Stow *et al*. 1996, Pickering *et al.* 2015). Additionally, the observation that these deposits constitute a monotonous thick and laterally extensive succession spanning kilometers suggests a deposition in a marine environment. Moreover, the fact that rhythmite belongs to the RSFA, dominated by wave-generated structures, including hummocky cross-stratification, evidences storm events in the Azul marine system and suggests that these deposits were settled in the offshore transition zone (c.f. De Raff *et al*. 1977, Cheel & Leckie 1993, Dumas & Arnott 2006). Moreover, the occurrence of thick

intervals of rhythmite facies, interpreted as turbidites, in the RFA deposits suggest that they were deposited in the offshore zone of the Azul marine system (Coe *et al.* 2003, Nichols 2009).

As previously suggested by Araújo Filho *et al.* (2020) and Araújo *et al.* (submitted), possibly, the manganese in the Azul succession was deposited during the transgression of the Azul Sea into the protocontinent, which was followed by an abrupt fall of the sea level and the deposition of the Águas Claras Formation. The manganese was precipitated in shallow and highly oxygenated waters, and afterwards, downwelling led to its deposition in the deepest parts of the marine basin alongside black shale deposits (Roy 1997, 2006, Force & Cannon 1988, Dasgupta *et al.* 1992). Rhodochrosite was possibly formed from the reaction between organic matter and manganese oxides/hydroxides ($HCO3^{-} + Mn^{2+} \rightarrow MnCO_3 + H_2$) during diagenesis (Roy 1997, 2006). The reddish siltstone strata, where the Azul manganese deposits are hosted, are interpreted as red-bed strata. The occurrence of this deposit suggests an increase in the oxygenation of waters (Song *et al.* 2018). Alternatively, these deposits could represent a ferruginous paleosol resulting from the existence of a highly oxygenated atmosphere, although no evidence of subaerial exposure (e.g., mud cracks) has been recorded. This paleosol would have originated from the exposition of the Azul marine deposits at the time of the installation of the Águas Claras fluvial system (Fig. 6.10).

The possible rhodochrosite is interpreted as the only primary manganese-bearing mineral to be recorded in the Azul succession, although some authors suggested that the manganese was deposited as oxides in the oxygenated waters of the Azul basin as well (Dardenne *et al.* 2009). Bacterial activity may have helped reduce manganese in the deepest and most anoxic parts of the marine basin. The occurrence of metal-reducing bacteria already pointed to iron precipitation in the Neoarchean Carajás banded iron formation (Luz & Crowley 2012). If the Azul succession are, in fact, connected with the Serra Sul glaciation in a continuous evolution, it may represent the immediate marine deposits sedimented in the aftermath of this cooling episode, as result of the sea-level rise. The occurrence of wave-generated structures in the Azul deposits strongly suggests an ice-free condition (e.g., Le Heron *et al.* 2011). Ultimately, the manganese requires a highly oxidizing sedimentary environment to precipitate (Koop *et al*. 2005). Carbon isotopic compositions of organic matters show extremely depleted values of δC^{13}, reflecting high organic activities before and during the very early diagenesis, in which carbon was extensively consumed for the precipitation of rhodochrosite (Dardenne *et al.* 2009). Moreover, near-zero values for the sulfur isotope mass-independent fractionation (MIF) obtained from the Serra Sul and Azul formations strongly suggest deposition in an oxygenated environment. Additionally, the Azul manganese deposits is constantly correlated

to the manganese deposits of the Francevilian series of Gabon, suggesting a similar age for the two series (Gauthier-Lafaye *et al.* 2010).

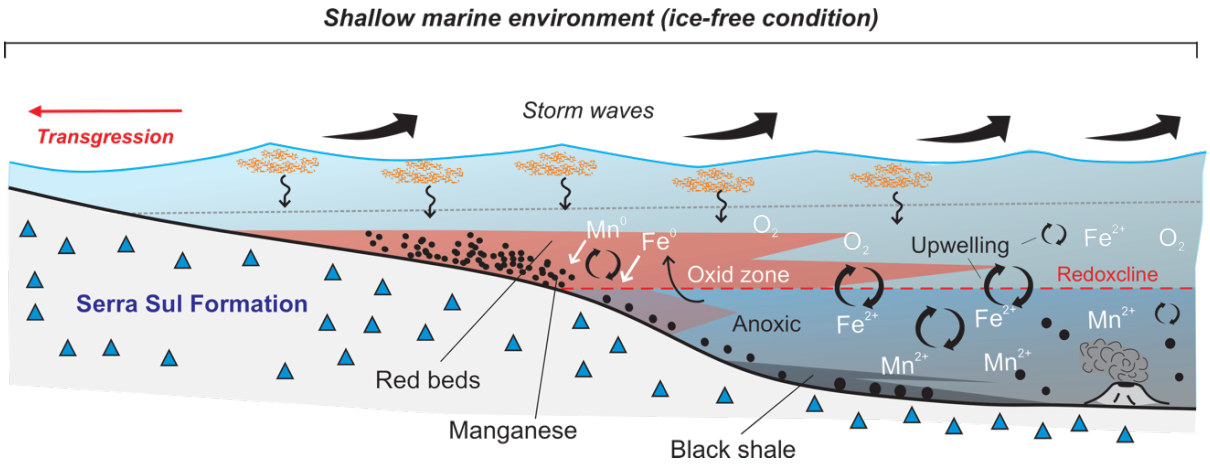

Figure 6.10: Paleoenvironmental reconstruction of the Azul marine succession that host the manganese deposits, showing a shallow-marine environment (shoreface to offshore zone) influenced by storm events. Manganese was upwelled from deep to shallow waters, where it was reduced. Downwelling currents moved the manganese to deep waters again, where it was deposited alongside black shale. Red-bed strata were deposited above in the highly oxygenated shallow waters.

6.5.2 Model of secondary manganese enrichment

During the tectonic deformation of the Azul manganese-bearing succession, it might be supposed that manganese was remobilized and migrated preferentially to places favorable for ore precipitation, possibly in those with low strain and a relatively larger available space. Based on this assumption, we have predicted a model of secondary manganese enrichment in the Azul succession, where the manganese was deposited by means of secondary mechanisms related to the tectonic process and supergene ones in the last stages. In this model, the rhodochrosite functioned as a "source" of manganese, which remobilized and migrated through discontinuity planes of faults and fractures to favorable zones. The manganese was mainly concentrated in the hinge zones of folds and along the planes of discontinuity. Moreover, after migration across the discontinuity planes, the manganese was concentrated in sandy laminations within the rhythmite due to the higher permeability and porosity of these rocks, compared to mudrock intervals. The broad migration of manganese crosses the rocks, occurring in certain locales, for the ore to be somewhat randomly distributed (Fig. 6.11).

We envisage that the Carajás Fault Domain was the main driver for manganese remobilization within the Azul red bed succession. Additionally, the occurrence of the secondary enrichment due to supergenic process is suggested by the occurrence of an in-situ

manganesiferous crust and pisolitic and boulder deposits discontinuously positioned above the succession, which is interpreted to be formed as a result of the dismantling of the supergene crust. In contrast, the primary manganese was deposited, and rhodochrosite was formed during diagenesis at *ca.* 2.27 Ga (Araújo *et al.* submitted), and the hypogene enrichment possibly occurred during regional tectonic deformation at *ca.* 2.0, which occurred during the so-called Transamazonian orogenetic cycle (Cordani et al. 1984, Macambira et al. 2009, Tavares et al. 2018). On the other hand, multiple generations of manganese oxides had already been recognized and its $^{40}Ar/^{39}Ar$ and K-Ar cryptomelane dating revealed ages between 69 and 0.2 Ma ago, which can be interpreted as a result of changing weather conditions in the Amazon during the Cenozoic era (Vasconcelos *et al.* 1994).

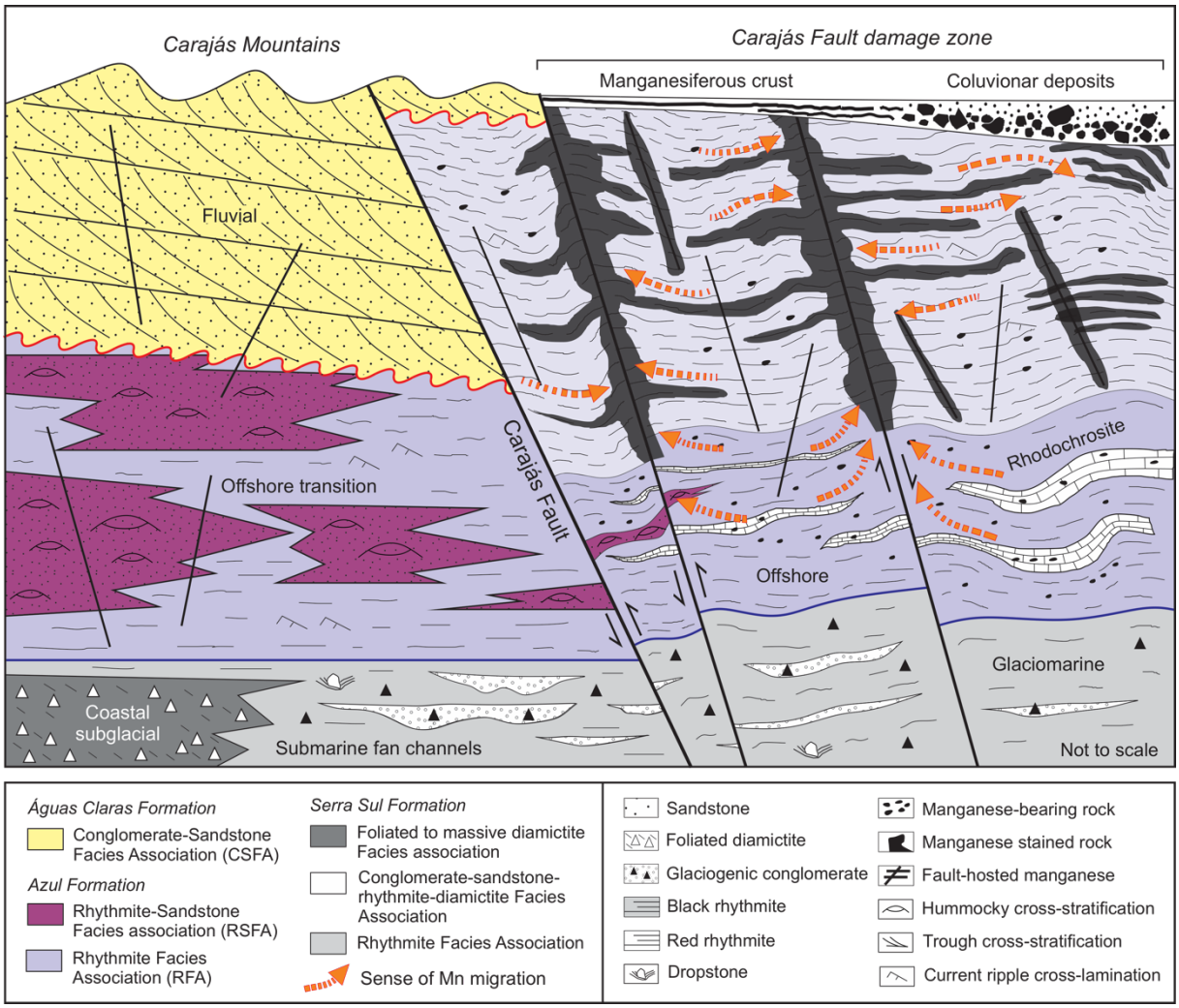

Figure 6.11: Geological section of the Azul manganese-bearing succession showing the envisaged mechanisms involved in the secondary manganese enrichment. Intervals of rhodochrosite repeatedly interbedded with black shale layers represent the protore, which acts as a "source" of manganese. The ore was remobilized through faults, such as the Carajás, for the strata immediately above (red bed) the Azul Formation, suggesting the occurrence of

indigenous remobilization similar to oil migration. Ultimately, the manganese was enriched throughout the Cenozoic era through supergene processes that superposed the hypogene enrichment.

6.6 FINAL REMARKS

This envisaged model of the Azul manganese-bearing succession, which involves a miscellaneous process, is considered for the first time here. Although rhodochrosite has been considered by some authors as the protore of the Azul deposits and secondary manganese enrichment with the supergene process being recurrently debated and studied (e.g., Valarelli *et al.* 1978, Bernardelli *et al.* 1978, Beauvais *et al.* 1987, Vasconcelos *et al.* 1994, Ruffet *et al.* 1996, Costa *et al.* 2005), minor attention was given to the tectonic influences on this deposit. The manganese remobilization hypothesized herein may be roughly compared with oil migration. Importantly, similar mechanisms are recurrently described for other manganese-bearing deposits worldwide that are similar in terms of age (e.g., Jones 2011, Jones *et al.* 2013, Ghosh *et al.* 2015, Ossa Ossa *et al.* 2016).

Ultimately, the occurrence and the mineralogical diversities observed in the Azul manganese deposit, represented by cryptomelane, pyrolusite, todorokite, and spessartite, were caused by the different mechanisms involved in the process from the formation to the enrichment of the manganese, in which supergenic and metamorphic/tectonic effects were mixed and/or superimposed. The occurrence of spessartite in these deposits is indicative of the metamorphism of the primary rhodochrosite to a low grade, whereas the occurrence of todorokite may be related to the oxidation and leaching of primary manganese carbonate (Johnson *et al.* 2016). The enrichment in rare earth elements, such as Europium (Eu), in pisolitic deposits strongly suggests a supergene enrichment, while the high Mn/Fe ratio suggests a hydrothermal enrichment of the Azul manganese deposit (Jones *et al.* 2013). Moreover, these sedimentary and tectonic mechanisms might have been operated during the end of the Paleoproterozoic era at *ca.* 2.2–2.0 Ga, and both, along with supergene processes, contributed to the enrichment of the manganese in the Azul red beds.

ACKNOWLEDGMENTS

The authors are very grateful to the Vale S.A. for making the drill cores available to study; the Geological Survey of Brazil for providing support through the Área de Relevante Interesse mineral de Carajás (ARIM-Carajás) project; and the PROPESP/UFPA for providing financial support for the language proofreading service (Edital 01/2020–PAPQ). This paper is a part of

the PhD thesis of the first author, who is grateful to the Post-graduate Program in Geology and Geochemistry (PPGG/UFPA).

REFERENCES

Araújo Filho, R.C., Nogueira, A.C., Araújo, R N., 2020. New stratigraphic proposal of a Paleoproterozoic siliciclastic succession: Implications for the evolution of the Carajás Basin, Amazonian craton, Brazil. J. S. Am. Earth Sci., (102), 102665.

Araújo R.N., Milhomem Neto J.M., Macambira M.J.B., Nogueira A.C.R. (submitted). Tectono-sedimentary evolution of a Paleoproterozoic succession of the Carajás Basin, southeastern Amazonian Craton, Brazil: Insights from stratigraphy, sedimentology, and U-Pb detrital zircon geochronology.

Araújo, R.N, Nogueira, A.C.R, 2019. Serra Sul diamictite of the Carajás Basin (Brazil): A Paleoproterozoic glaciation on the Amazonian craton. Geology 12 (47), pp. 1166–1170.

Araújo, R.N., Sousa M.J., 2018. Geologia, estratigrafia e análise do minério dos depósitos de manganês de Carajás: regiões do Azul, Sereno Buritirama e Antônio Vicente. Belém, CPRM-Companhia de Pesquisa de Recursos Minerais, 198 p. (in Portuguese).

Beauvais A., Melfi A., Nahon D., Trescases J. J., 1987. Pétrologie du gisement latérique manganésifêre d'Azu1 (Brésil). Mineral. Deposita 22, pp. 124-134.

Bekker, A., Holland, H.D., Wang, P.L., Rumble, III D., Stein, H.J., Hannah, J.L., Coetzee, L.L., Beukes, N.J., 2004. Dating the rise of atmospheric oxygen. Nature (427), pp. 117–120.

Bernardelli, A.L., Beisiegel, V.R., 1978. Geologia economica da jazida de manganes do Azul. An. XXX Congr. Bras. Geol. 4: 1431-1444.

Bouma, A.H., 1962. Sedimentology of some flysch deposits: a graphic approach to facies interpretation. Amsterdam, Elsevier, 168 pp.

Cabral, A.R., Bühn, B., Gomes Jr, A.A.S., Galbiatti, H.F., Lehmann, B., Halder, S., 2017. Multiple sulfur isotopes from the Neoarchaean Serra Sul black shale, Carajás mineral province, northern Brazil. Journal of South American Earth Sciences (79), pp. 377–383.

Cheel, R.J., Leckie, D.A., 1993. Hummocky Cross-Stratification: Sedimentology Review. Oxford, U.K., Blackwell Scientific Publications, pp. 103–122.

Coe A.L., Bosence D., Church K.D., Flint S.S., Howell J.A., Wilson R.C.L., 2003. The Sedimentary Record of Sea-Level Change (edited by: Angela L. Coe). Cambridge University Press and The Open University, 288p.

Cordani, U.G., Tassinari, C.C.G., Kawashita, K.A., 1984. A Serra dos Carajás como região limítrofe entre províncias tectônicas. Ciências da Terra (9), pp. 6–11 (in Portuguese).

Costa F.F.O. 2017. A Sucessão Siliciclástica paleoproterozoica associada ao depósito de manganês do Azul da Serra dos Carajás. MS Dissertation. Instituto de Geociências, Universidade Federal do Pará, Belém, 62 p.

Costa M.L., Fernandez O.J.C., Requelme M.E.R. 2005. Depósito de manganês do Azul, Carajás: estratigrafia, mineralogia, geoquímica e evolução geológica. In: Marini O.J., Queiroz E.T., Ramos B.W. (ed.). Caracterização de depósitos minerais em distritos mineiros da Amazônia. Brasília, DNPM, FINEP. ADIMB, p. 231-333.

Dall'Agnol R., Oliveira D.C., Lamarão C.N. 2013. Magmatismo granitoide arqueano e evolução geológica do Subdomínio de Transição da Província Carajás, sudeste do Cráton Amazônico, Brasil. Bol. Mus. Para. Emílio Goeldi. Cienc. Nat., 8 (3) pp. 251-256.

Dall'Agnol R., Oliveira M.A., Almeida J.A.C., Althoff F.J., Leite A.A.S., Oliveira D.C., Barros C.E.M. 2006. Archean and Paleoproterozoic granitoids of the Carajás Metallogenetic Province, eastern Amazonian craton. Abstracts of Symposium on magmatism, crustal evolution, and metallogenesis of the Amazonian craton, 1:99-150.

Dall'Agnol R., Souza Z.S., Althoff F.J., Barros C.E.M., Leite A.A.S., Jorge João X.S. 1997. General aspects of the granitogenesis of the Carajás metallogenic province. Extended Abstracts of the International Symposium on Granites and Associated Mineralizations, 1:135-161.

Dardenne M.A., Brod T.C.J., Guimarães E.M., Santos R.V. 2009. Modelo metalogenético da mineralização primária do depósito de manganês do Azul (Carajás). XI Simpósio de Geologia da Amazônia, Manaus. Resumo expandido.

Dasgupta, S., Roy, S., Fukuoka, M., 1992. Depositional Models for manganese oxide and carbonate deposits of the Precambrian Sausar Group, India. Economic Geology (87), pp. 1412–1418.

Dumas, S., Arnott, R.W.C., 2006. Origin of hummocky and swaley cross-stratification—The controlling influence of unidirectional current strength and aggradation rate. Geology (34), pp. 1073–1076.

Feio, G.R.L., Dall'Agnol, R., Dantas, E.L., Macambira, M.J.B., Santos, J.O.S., Althoff, F.J., Soares, J.E.B., 2013. Archean granitoid magmatism in the Canaã dos Carajás area: implications for crustal evolution of the Carajás province, Amazonian craton, Brazil. Precambrian Res. (227), pp. 157–185.

Force, E.R., Cannon, W.F. 1988. Depositional Model for Shallow-Marine Manganese Deposits around Black Shale Basins. Economic Geology (83), pp. 93–117.

Galarza, M.A., Macambira, M.J.B., Villas, R.N.N., 2008. Dating and isotopic characteristics (Pb and S) of the Fe oxide-Cu-Au-U-REE Igarapé Bahia ore deposit, Carajás mineral province, Pará state, Brazil. Journal of South American Earth Sciences (25), pp. 377–397.

Gauthier-Lafaye F., Nogueira A.C.R., Pinheiro R.V.L., Albani A.E. 2010. The Paleoproterozoic Francevilian Series: witness of a geochemical and biological upheaval. In: 45º Congresso Brasileiro de Geologia, Belém. Abstract.

Ghosh R., Chakraborty D., Halder M., Baidya T.K. 2015. Manganese mineralization in Archean greenstone belt, Joda-Noamundi sector, Noamundi basin, East Indian Shield. Ore Geology Reviews, 70:96-109.

Glasby G.P. 1997. Fractionation of manganese from iron in Archaean and Proterozoic sedimentary ores. In: Nicholson K., Hein J.R., Buhn B. & Dasgupta S. (ed.). Manganese Mineralization: Geochemistry and Mineralogy of Terrestrial and Marine Deposits. Geological Society Special Publication, 199:29-42.

Holdsworth, R.E., Pinheiro, R.V.L., 2000. The anatomy of shallow-crustal transpressional structures: insights from the Archaean Carajás fault zone, Amazon, Brazil. Journal of Structural Geology (22), pp. 1105–1023.

Johnson J.E., Webb S.M., Chi Ma, Fischer W.W. 2016. Manganese mineralogy and diagenesis in the sedimentary rock record. Geochimica et Cosmochimica Acta, 173:210-231.

Johnson J.E., Webb S.M., Thomas K., Ono S., Kirschvink J.L., Fischer W.W. 2013. Manganese-oxidizing photosynthesis before the rise of cyanobacteria. Proceedings of the National Academy of Sciences of the United States of America, 110(28):11238-11243.

Jones S. 2011. Proterozoic deformation in the East Pilbara and tectonic setting of fault-hosted manganese at Woodie Woodie mine. Australian Journal of Earth Sciences, 58:639-673.

Jones S., McNaughton N. J., Grguric B. 2013. Structural controls and timing of fault-hosted manganese at Woodie Woodie, East Pilbara, Western Australia. Ore Geology Reviews, 50:52-82.

Justo, A.P., Dantas, E.L., Freitas-Silva, F.H., Rodrigues, J.B., 2018. Detrital zircon populations in the Neoarchean to Paleoproterozoic sedimentary coverage of Carajás, Amazon Cráton, Brazil. Congresso Brasileiro de Geologia, 49, Rio de Janeiro, SBG (in Portuguese).

Kopp, R.E., Kirschvink, J.L., Hilburn, I.A., Nash, C.Z., 2005. The Paleoproterozoic snowball Earth: A climate disaster triggered by the evolution of oxygenic photosynthesis. Proceedings of the National Academy of Sciences (102), pp. 11131–11136.

Laznicka P. 1992. Manganese deposits in the global lithogenic system: quantitative approach. Ore Geology Reviews, 7:279-356.

Le Heron, D. P., Cox, G., Trundley, A., Collins, A., 2011. Sea ice−free conditions during the Sturtian glaciation (early Cryogenian), South Australia. Geology (39), pp. 31-34.

Luz, B.R., Crowley, J.K., 2012. Morphological and chemical evidence of stromatolitic deposits in the 2.75 Ga Carajás banded iron formation, Brazil. Earth and Planetary Science Letters (355), pp. 60–72.

Macambira, M.J.B, Vasquez, M.L., Silva, D.C.C., Galarza, M.A., Barros, C.E.M., Camelo, J.F., 2009. Crustal growth of the central-eastern Paleoproterozoic domain, SE Amazonian craton: Juvenile accretion vs. reworking. Journal of South American Earth Sciences (27), pp. 235–246.

Machado, N., Lindenmayer, Z., Krogh, T. E., Lindenmayer, D., 1991. U-Pb geochronology of Archaean magmatism and basement reactivation in the Carajás area, Amazon shield, Brazil. Precambrian Research (49), pp. 329–354.

Martins, P.L.G., Toledo, C.L.B., Silva, A.M., Chemale Jr, F., Santos, J.O.S., Assis, L.M., 2017. Neoarchean magmatism in the southeastern Amazonian Craton, Brazil: Petrography, geochemistry and tectonic significance of basalts from the Carajás Basin. Precambrian Research (302), pp. 340–357.

Maynard J.B. 2010. The chemistry of manganese ores through time: A signal of increasing diversity of earth-surface environments. Economic Geology, 105(3):535-552.

Maynard J.B., 2003. Manganiferous sediments, rocks, and ores. In: Mackenzie, F.T., Holland, H.D., Turekion, K.K. (Eds.), Treatise on Geochemistry, Vol. 7 Sediments, Diagenesis, and Sedimentary Rocks, pp. 289–308.

Mougeot, R., Respaut, J.P., Briqueu, L., Ledru, P., Milesi, J.P., Lerouge, C., Marcoux, E., Huhn, S.B., Macambira, M.J.B., 1996. Isotope geochemistry constraints for Cu, Au mineralization and evolution of the Carajás 763 province (Pará, Brazil). In: Congresso Brasileiro de Geologia, 39, Salvador, SBG. 7:321–324.

Mutti E. 1992. (ed.). Turbidite Sandstone. Agip Intituto di Geologia Università di Parma, Milano, 277 p.

Mutti E. & Ricci Lucchi F. 1975. Turbidite facies and facies associations. *In*: E. Mutti et al. (ed.). Examples of Turbidite facies and Facies Associations from Selected Formations of the Northern Apennines. Field Trip Guidebook A-11. IX International Sedimentological Congress, Nice, pp. 21-36.

Nichols G., 2009. Sedimentology and stratigraphy (2nd ed.). Chichester, UK; Hoboken, NJ: Wiley-Blackwell, 432 p.

Nogueira, A.C.R., Truckenbrodt, W., Pinheiro, R.V.L., 1995. Formação Águas Claras, Pré-Cambriano da Serra dos Carajás, redescrição e redefinição litoestratigráfica. Boletim do Museu Paraense Emílio Goeldi, Série Ciências da Terra 7, pp. 177–197 (in Portuguese).

Olszewski, W.J., Wirth, K.R., Gibbs, A.K., Gaudette, H.E., 1989. The age, origin, and tectonics of the Grão Pará Group and associated rocks, Serra dos Carajás, Brazil: Archean continental volcanism and rifting. Precambrian Res. (42), pp. 229–254.

Ossa Ossa F., Hofmann A., Vidal O., Kramers J.D., Belyanin G., Cavalazzi B. 2016. Unusual manganese enrichment in the Mesoarchean Mozaan Group, Pongola Supergroup, South Africa. Precambrian Research, (281), pp. 414-433.

Pereira, R.M.P., Rosiere, C.A., Santos, J.O.S., Lobato, L.M., Silva, R.C.F., McNaughton, N.J., 2009. Unidade Caninana: sequência clástica Paleoproterozoica revelada por datação U-Pb em zircões detríticos da Província Mineral Carajás. Simpósio de Geologia da Amazônia, 11, SBG (in Portuguese).

Pinheiro R. V. L. 1997. Reactivation history of the Carajás and Cizento strike-slip systems, Amazon, Brazil. PhD Thesis, Departament of Geological Sciences, University of Durham, England, 408 p.

Pinheiro, R.V.L., Holdsworth, R.E., 1997. The structure of the Carajás N-4 ironstone deposit and associated rocks: relationship to Archaean strike-slip tectonics and basement reactivation in the Amazon region, Brazil. Journal of South American Earth Sciences (10), pp. 305–319.

Roy, S., 1997. Genetic diversity of manganese deposition in the terrestrial geological record. In: Nicholson, K., Hein, J.R., Buhn, B., Dasgupta, S. (Eds). Manganese Mineralization: Geochemistry and Mineralogy of Terrestrial and Marine Deposits, Geological Society Special Publication (199), pp. 5–27.

Roy, S., 2006. Late Archean initiation of manganese metallogenesis: its significance and environmental controls. Ore Geology Reviews (17), pp. 179–198.

Ruffet G., Innocent C., Michard A., Féraud G., Beauvais A., Nahon D., Hamelin B., 1996. A geochronological $^{40}Ar/^{39}Ar$ and $^{87}Rb/^{87}Sr$ study of K-Mn oxides from the weathering sequence of Azul, Brazil. Geochim. Cosmochim. Acta, 60 (12), pp. 2219-2232.

Sekine, Y., Tajika, E., Tada, R., Hirai, T., Goto, K.T., Kuwatani, T., Goto, K., Yamamoto, S., Tachibana, S., Isozaki, Y.m Kirschvink, J.L., 2011. Manganese enrichment in the Gowganda Formation of the Huronian Supergroup: A highly oxidizing shallow-marine environment after the last Huronian glaciation. Earth and Planetary Science Letters (307), pp. 201–210.

Silva D.C.C., 2006. Estudo da geometria e cinemática das rochas sedimentares arqueanas da Mina do Igarapé Azul – Carajás-PA. Dissertação de mestrado. Universidade Federal do Pará.

Song, H., Jiang, G., Poulton, S.W., Wignall, P.B., Tong, J., Song, H., An, Z., Chu, D., Tian, L., She, Z., & Wang, C. (2017). The onset of widespread marine red beds and the evolution of ferruginous oceans. Nature Communications, 8, 399.

Stow D.A.V. & Piper D.W. (ed.). 1984. Fine-grained Sediments: Deep-water Processes and Facies. Geot. Soc. Lond., Bristol, 659 p. (Special Publication, 15).

Stow D.A., Reading H.G., Collinson J.D. 1996. Deep seas. *In*: Reading, H.G. (ed.). *Sedimentary Environments: Process, Facies and Stratigraphy*. Blachwell, Oxford, p. 395-483.

Tallarico, F.H.B., Figueiredo, B.R., Groves, D.I., Kositcin, N., McNaughton, N.J., Fletcher, I.R., Rego, J.L., 2005. Geology and SHRIMP U-Pb geochronology of the Igarapé Bahia deposit, Carajás copper-gold belt, Brazil: an Archean (2.57 Ga) example of iron-oxide Cu-Au-(U-REE) mineralization. Economic Geology (100), pp. 7–28.

Tassinari C.C.G. & Macambira M.J.B. 2004. A evolução tectônica do Cráton Amazônico. In: Mantesso-Neto V., Bartorelli A., Carneiro C.D.R., Brito Neves B.B. (ed.). Geologia do Continente Sul-Americano: Evolução da Obra de Fernando Flávio Marques de Almeida, p. 471-485.

Tavares, F.M., Trouw, R.A.J., da Silva, C.M.G., Justo, A.P., Oliveira, J.K.M., 2018. The multistage tectonic evolution of the northeastern Carajás Province, Amazonian Craton, Brazil: Revealing complex structural patterns. Journal of South American Earth Sciences (88), pp. 238–252.

Teixeira, M.F.B., Dall'Agnol, R., Santos, J.O.S., Oliveira, D.C., Lamarão, C.N., McNaughton, N.J., 2018. Crystallization ages of Paleoproterozoic A-type granites of Carajás Province, Amazon Craton: Constraints from U-Pb geochronology of zircon and titanite. Journal of South American Earth Sciences (88), pp. 312–331.

Teixeira, W., Hamilton, M.A., Girardi, V.A.V., Faleiros, F.M., Ernst, R.E., 2019. U-Pb baddeleyite ages of key dyke swarms in the Amazonian Craton (Carajás/Rio Maria and Rio Apa areas): Tectonic implications for events at 1880, 1110 Ma, 535 Ma and 200 Ma. Precambrian Research (329), pp. 138–155.

Trendall, A.F., Basei, M.A.S., De Laeter, J.R., Nelson, D.R., 1998. SHRIMP U-Pb constraints on the age of the Carajás Formation, Grão Pará Group, Amazon Craton. Journal of South American Earth Sciences (11), pp. 265–277.

Tsikos H., Beukes N.J., Moore J.M., Harris C. 2003. Deposition, diagenesis, and secondary enrichment of metals in the Paleoproterozoic Hotazel iron formation, Kalahari manganese field, South Africa. Economic Geology, 98:1449-1462.

Valarelli, J.V., Bernardelli, A.L., Beisiegel, V.R., 1978. Aspectos genéticos do minerio de mangan~s do Azul. An. XXX Congr. Bras. geol. 4:1670-1679.

Vasconcelos P. M., Renne P. R., Brimhall G. H., Becker T. A., 1994. Direct dating of weathering phenomena by $^{40}Ar/^{39}Ar$ and K-Ar analysis of supergene K-Mn oxides. Geochim. Cosmochim. Acta (58), pp. 1635-1665.

Vasquez, M.L., Sousa, C.S., Carvalho, J.M.A., 2008a. Mapa Geológico e de Recursos Minerais do Estado do Pará. Escala 1:1.000.000. Geological Survey of Brazil – CPRM (in Portuguese).

Vasquez, M.L., Rosa-Costa, L.T., Silva, C.G., Ricci, P.F., Barbosa, J.O., Klein, E.L., Lopes, E.S., Macambira, E.B., Chaves, C.L., Carvalho, J.M., Oliveira, J.G., Anjos, G.C., Silva, H.R., 2008b. Geologia e Recursos Minerais do Estado do Pará: Sistema de Informações Geográficas-SIG: Texto Explicativo dos Mapas Geológico e Tectônico e de Recursos Minerais do Estado do Pará. Escala 1:1.000.000. In: Vasquez M.L., Rosa-Costa L.T. (Eds.). Belém, Geological Survey of Brazil - CPRM, 329 pp (in Portuguese).

Zhao G.C., Cawood P.A., Wilde S.A., Sun M. 2002. Review of global 2.1–1.8 orogens: implications for a pre-Rodinia supercontinent. Earth-Science Reviews, 59:125-162.

Zhao, G., Sun, M., Wilde, S.A., Li, S., 2004. A Paleo-Mesoproterozoic supercontinent: assembly, growth and breakup. Earth-Science Reviews (67), 91–123.

WEBMAIL
SERVIÇO GEOLÓGICO DO BRASIL - CPRM

Raphael Araújo Neto <raphael.araujo@cprm.gov.br>

Confirming submission to Precambrian Research

1 mensagem

Precambrian Research <em@editorialmanager.com> 7 de agosto de 2020 11:08
Responder a: Precambrian Research <precam-eo@elsevier.com>
Para: Raphael Araújo <raphael.araujo@cprm.gov.br>

"This is an automated message."

Tectono-sedimentary evolution of a Paleoproterozoic succession of the Carajás Basin, southeastern Amazonian Craton, Brazil: Insights from stratigraphy, sedimentology, and U-Pb detrital zircon geochronology

Dear Mr. Araújo,

We have received the above referenced manuscript you submitted to Precambrian Research.

To track the status of your manuscript, please log in as an author at https://www.editorialmanager.com/precam/, and navigate to the "Submissions Being Processed" folder.

Thank you for submitting your work to this journal.

Kind regards,
Precambrian Research

More information and support

You will find information relevant for you as an author on Elsevier's Author Hub: https://www.elsevier.com/authors

FAQ: How can I reset a forgotten password?
https://service.elsevier.com/app/answers/detail/a_id/28452/supporthub/publishing/kw/editorial+manager/

For further assistance, please visit our customer service site: https://service.elsevier.com/app/home/supporthub/publishing/. Here you can search for solutions on a range of topics, find answers to frequently asked questions, and learn more about Editorial Manager via interactive tutorials. You can also talk 24/7 to our customer support team by phone and 24/7 by live chat and email.

In compliance with data protection regulations, you may request that we remove your personal registration details at any time. (Use the following URL: https://www.editorialmanager.com/precam/login.asp?a=r). Please contact the publication office if you have any questions.

7 TECTONO-SEDIMENTARY EVOLUTION OF A PALEOPROTEROZOIC SUCCESSION OF THE CARAJÁS BASIN, SOUTHEASTERN AMAZONIAN CRATON, BRAZIL: INSIGHTS FROM STRATIGRAPHY, SEDIMENTOLOGY, AND U-PB DETRITAL ZIRCON GEOCHRONOLOGY

R.N. Araújo[1,2]*, J.M. Milhomem Neto[3], M.J.B. Macambira[1], A.C.R Nogueira[1,3]

[1] Post-graduate Program in Geology and Geochemistry, Federal University of Pará, 66075-110, Belém, Brazil

[1] Management of Geology and Mineral Resources, Geological Survey of Brazil, 66095-904, Belém, Brazil

[3] Faculty of Geology, Federal University of Pará, 66075-110, Belém, Brazil

*Corresponding author e-mail address: raphael.araujo@cprm.gov.br

Artigo submetido ao periódico internacional *Precambrian Research.*

ABSTRACT

The Carajás Basin, southeastern Amazonian Craton in northern Brazil, hosts a *ca.* 6 km thick pile of volcano-sedimentary rocks. It is generally claimed that this basin started as a rift configuration in which thick volcanics and banded iron formation strata were deposited during the Neoarchean (*ca.* 2.75 Ga). Conversely, the tectono-sedimentary evolution of this basin through the Paleoproterozoic remains unraveled. In this study, based on a stratigraphic, sedimentological, and U-Pb detrital zircon geochronological investigation of a marine to fluvial succession of this basin, we suggest that the Carajás Basin evolved in a foreland setting during the greater part of the Paleoproterozoic era. We envisage that the Carajás foreland basin was sedimented in the underfilled stage by deep-marine strata (i.e., glaciogenic submarine fan deposits), likely of the Siderian-Rhyacian (*ca*. 2.58–2.06) Serra Sul Formation. Subsequently, shallow-marine deposits of the Azul formation were deposited in the filled stage, followed by deposition of fluvial to alluvial deposits of the Águas Claras and Gorotire formations during the overfilled stage. The geochronological results revealed that the Azul and Águas Claras formations were supplied mainly by Meso- to Neoarchean source-rocks, whereas Paleoproterozoic and Paleoarchean rocks played the role of a subordinate source of sediments. The occurrence of Paleoproterozoic zircon grains (youngest cluster of age at *ca.* 2.27 Ga) in the Azul Formation may be interpreted as its maximum depositional age, as well as, for that of Águas Claras Formation. Besides, the occurrence of Rhyacian zircon grains suggest, at least in part, a connection with the Carajás protocontinent with the Bacajá Domain, a Transamazonian terrane (*ca.* 2.2–2.0 Ga) located to the north of the Carajás area in the present-day configuration.

The integration of sedimentological, stratigraphic, and geochronological data strongly suggest that the Carajás foreland basin was formed as a result of the collision between the Bacajá Domain and the Carajás protocontinent that took place during the Transamazonian cycle. Ultimately, we suggest that this scenario of dramatic upheavals is directly related to the configuration of the Columbia supercontinent, which initially led to the emergence of the Carajás foreland basin, and soon after, the cratonization of the proto-Amazonia.

Keywords: Paleoproterozoic; Tectono-sedimentary evolution; Carajás foreland basin; proto-Amazonia cratonization; Columbia supercontinent.

7.1 INTRODUCTION

The emergence and attenuation of supercontinents caused profound changes in the landmasses that constituted them. The recognition of the detailed stratigraphic, sedimentologic, and geochronologic framework of the Archean-Paleoproterozoic successions preserved in these ancient landmasses is crucial to understand the paleoenvironmental, paleoclimatic, paleogeographic, and tectonic changes that took place in that time period. Moreover, this time period is marked by several paleoenvironmental modifications, which includes the appearance of an oxygenated atmosphere-hydrosphere system and onset of the so-called Great Oxidation Event (GOE) at *ca*. 2.45 Ga (Holland 2002, Bekker *et al.* 2004). The GOE was accompanied by the installation of a series of protracted cooling episodes that culminated in several glaciations generally termed as the Huronian Glacial Event at *ca*. 2.45–2.2 Ga (Tang & Chen 2013, Young 2014).

Regarding the paleogeographic setting, it is generally argued that ancient landmasses were amalgamated between the Paleo and Mesoproterozoic periods to form the so-called Columbia supercontinent (Rogers & Santosh 2002, Zhao *et al.* 2004). However, little is known about the participation of the Amazonian Craton in this continent with regard to the paleoenvironmental changes that occurred due to its formation. Besides, the age and provenance of Paleoproterozoic successions registered in these ancient landmasses are constantly investigated and the difficulty of dating these strata are commonly reported, hindering the precise correlation between the successions and the events globally (Rasmussen *et al.* 2013, Gumsley *et al.* 2017).

In the Carajás Basin, the recent discovery of possible Siderian-Rhyacian (2.58–2.06 Ga) glaciogenic strata on the Amazonian Craton linked to the Serra Sul glaciation (Araújo & Nogueira 2019) opened new perspectives on the evolution of the Amazonian Craton and its role

within the global context of paleoenvironmental changes that occurred during the Paleoproterozoic. It also suggested that the Carajás Basin was filled by a transgressive-regressive sequence after this cooling episode, which culminated in the closure and inversion of the Carajás Basin (Araújo Filho *et al.* 2020). However, the Paleoproterozoic succession of the Carajás Basin should be re-evaluated, mainly because there are still many gaps in its tectono-sedimentary evolutionary history, and because the causes, effects, and global context of these changes registered in this basin still need to be resolved.

In this study, the Paleoproterozoic succession of the Carajás Basin was investigated using stratigraphy, sedimentology, and zircon U–Pb geochronology. The results allowed us to propose a comprehensive tectono-sedimentary evolution for the Carajás Basin during the Paleoproterozoic. Importantly, our model is supported by previously published data on the region (e.g., Cordani *et al.* 1984, Machado *et al.* 1991, Macambira *et al.* 2009, Tavares *et al.* 2018), although more work is needed to improve it. Additionally, attempts were made to better constrain the events recorded in the Paleoproterozoic succession of the Carajás Basin within the context of global changes that occurred in that period. It is unequivocal that the southeastern Amazonian Craton underwent paleoenvironmental and tectonic modifications relevant to the emergence of the Columbia supercontinent during the end of Paleoproterozoic.

7.2 GEOLOGICAL SETTING

The Carajás Basin (southeastern Amazonian Craton, Brazil) is located in the northern part of the Carajás Domain, which, along with the Rio Maria Domain, constitutes the Carajás Province (Machado *et al.* 1991, Vasquez *et al.* 2008a, Macambira *et al.* 2009). This province is limited by the Bacajá Domain to the North, by the Neoproterozoic Araguaia Belt to the East, the Iriri-Xingu Domain to the West, and the Santana do Araguaia Domain to the South. While the Rio Maria Domain comprises predominantly Mesoarchean rocks, the Carajás Domain consists of rocks predominantly formed during the Neoarchean (Vasquez *et al.* 2008a). Conversely, a majority of the Bacajá Domain comprises a set of granitic and metamorphic rocks formed mainly during the Paleoproterozoic, although the basement comprises Mesoarchean orthogneisses of the Cajazeiras Complex (Macambira *et al.* 2009).

The Carajás Basin (Fig. 7.1) has a sigmoidal shape and is considered a synclinal basin filled with unmetamorphosed to very low-grade metamorphosed rocks (Pinheiro & Holdsworth 1997, Holdsworth & Pinheiro 2000). It has a basement constituted by granite and gneiss rocks, which includes granite and gneiss of the tonalite-trondhjemite-granodiorite (TTG) type, attributed to the Xingu Complex that presents a migmatization age of *ca*. 2.85 Ga (Machado *et*

al. 1991). The basin is truncated in the central portion by the Carajás Granite, which presents a U-Pb zircon age of 1880 ± 2 Ma (Machado *et al.* 1991). Similarly, the basin and the Carajás-Rio Maria region are cross-cut by dike swarms with different U-Pb monazite ages of 1880, 1110, 535, and 200 Ma (Teixeira *et al.* 2019a).

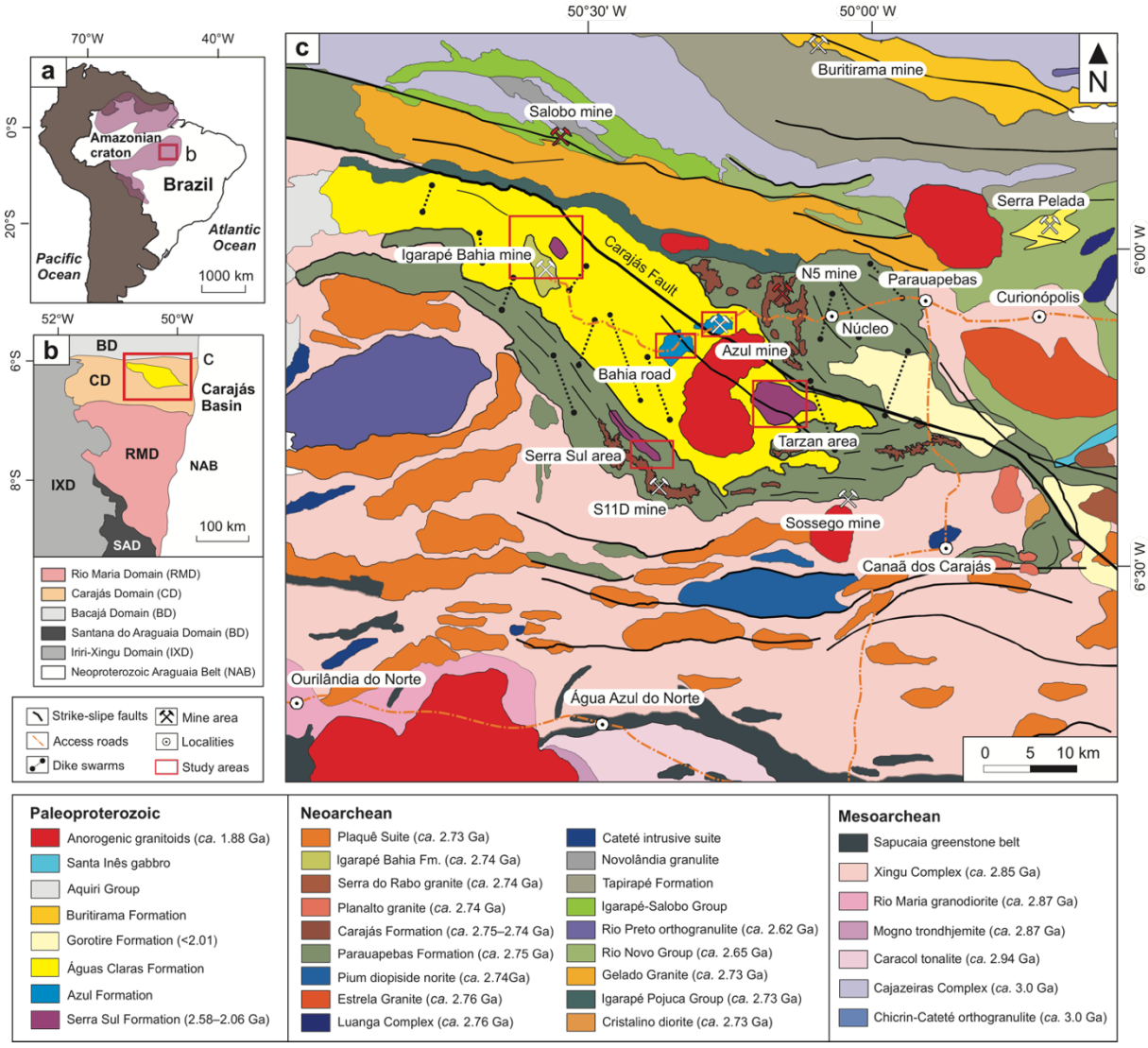

Figure 7.1: Location map of the study area. (a) Location of the Carajás region in the southeastern Amazonian Craton, Brazil. (b) Map of the Carajás region showing the location of the Carajás Basin. (c) Geological map of the Carajás Basin showing the location of the study areas (modified from Vasquez *et al.* 2008b).

The succession of the Carajás Basin is constituted by Neoarchean volcanic and banded-iron formation strata, which are overlaid by coarse to fine-grained sedimentary rocks deposited during the Paleoproterozoic (Olszewski *et al.* 1989, Machado *et al.* 1991, Nogueira *et al.* 1995,

Trendall *et al.* 1998, Martins *et al.* 2017, Tavares *et al.* 2018, Araújo & Nogueira 2019, Araújo Filho *et al.* 2020). The succession is stacked upsection into the following units: Grão Pará Group (Parauapebas, Carajás and Igarapé Bahia formations), Serra Sul, Azul, Águas Claras, and Gorotire formations (Fig. 7.2).

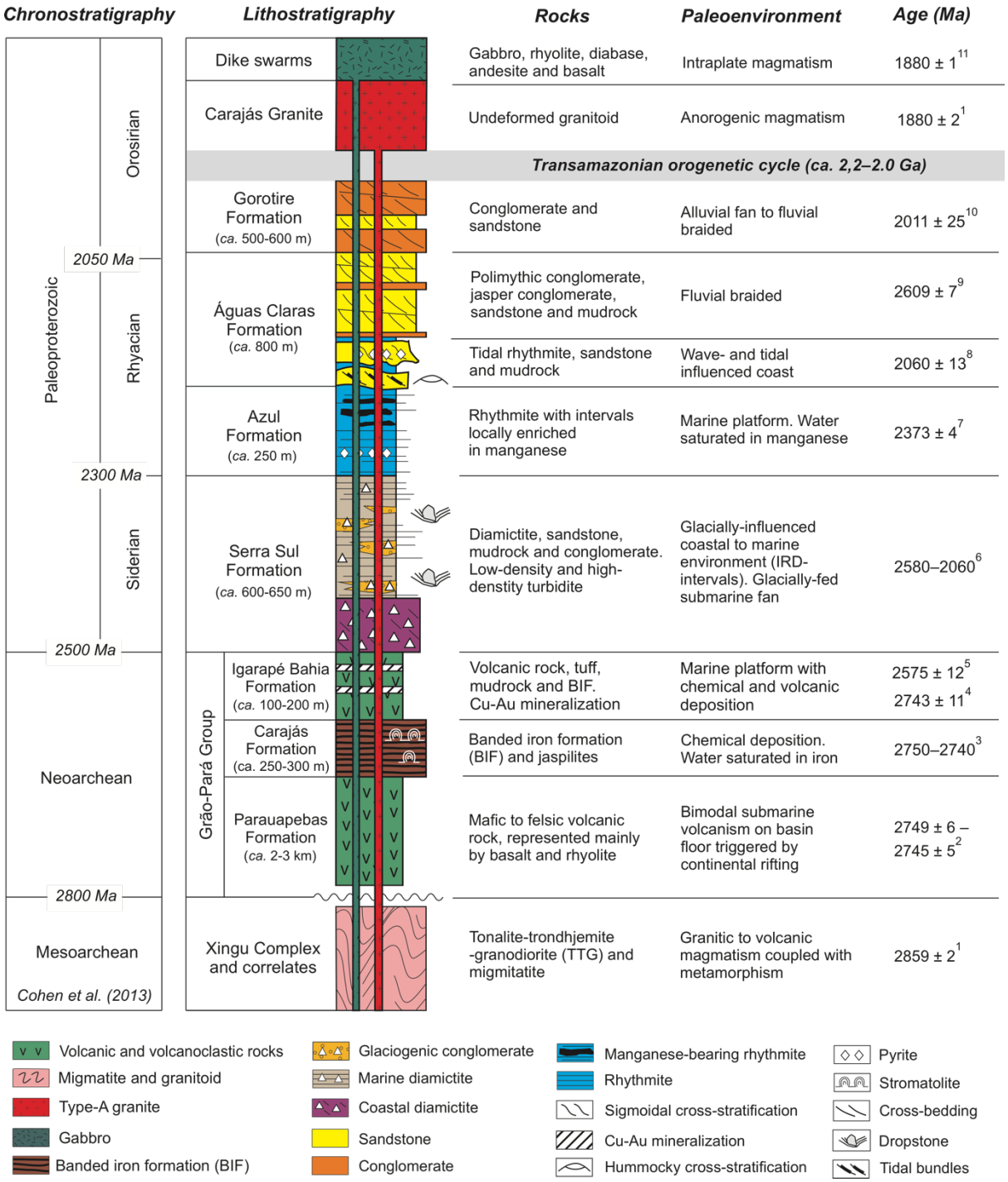

Figure 7.2: Stratigraphic column of the Carajás Basin (Amazonian Craton, Brazil) showing the main geological and geochronological data available for the volcano-sedimentary rocks that fill this basin (modified from Araújo & Nogueira, 2019). Geochronological data compiled from: 1—Machado *et al.*

(1991); 2—Martins *et al*. (2017); 3—Trendall *et al*. (1998); 4—Galarza *et al*. (2008); 5—Tallarico *et al*. (2005); 6—Araújo & Nogueira (2019); 7—Justo *et al*. (2018); 8—Mougeot *et al*. (1996a); 9—Araújo & Sousa (2018); 10—Pereira *et al*. (2009); 11—Teixeira *et al*. (2019a). The meaning of the ages is being discussed in the text.

The Parauapebas Formation comprises a set of *ca*. 2–3 km thick mafic to felsic volcanic rocks which lie immediately above a *ca.* 250–300 m thick banded iron formation (BIF) strata of the Carajás Formation. It is generally claimed that both units were deposited coevally at *ca*. 2.75–2.74 Ga (Olszewski *et al.* 1989, Trendall *et al.* 1998, Cabral *et al.* 2013, Martins *et al.* 2017), although, the stratigraphic and temporal correlations between these deposits need to be reassessed. Volcanics, pyroclastic, and rhythmite strata deposited at *ca*. 2.74 Ga (Galarza *et al.* 2008) were arranged into the Igarapé Bahia Formation overlying the banded iron formation units. In these strata, a primary Cu-Au mineralization was coeval and presented a remobilization age of *ca*. 2.58 Ga (Tallarico *et al.* 2005).

Araújo & Nogueira (2019) used the age of *ca*. 2.58 Ga (Tallarico *et al.* 2005), and the age of *ca.* 2.06 Ga–obtained from the disseminated pyrite crystals in the Águas Claras Formation (Mougeot *et al.* 1996a)–to relatively date the Serra Sul Formation (diamictite, rhythmite, and conglomerate), which unconformably overlaid the Grão Pará Group. The Serra Sul Formation encompassed the glacially derived diamictite deposited in a coastal subglacial to submarine fan system. The Serra Sul diamictite is the only reported occurrence of Paleoproterozoic glacial deposits in South America (Araújo & Nogueira, 2019).

Recently, the Azul Formation was proposed to encompass a set of rhythmite strata locally enriched in manganese, occurring beneath the Águas Claras Formation (Araújo Filho *et al*. 2020). According to these authors, the Azul and the Águas Claras formations were deposited in marine and fluvial settings, respectively, and are the stratigraphic records associated a transgressive-regressive sequence. The Gorotire Formation was interpreted as being positioned in the uppermost part of the Paleoproterozoic succession of the Carajás Basin (Araújo & Nogueira 2019). This Formation comprises a set of polimythic and clast-supported conglomerate and sandstone stacked in fining upward cycles deposited in an alluvial to fluvial system (Nascimento & Oliveira 2015).

The accurate age of the putative Paleoproterozoic Azul, Águas Claras and Gorotire formations of the Carajás Basin is hotly debated as there is little geochronological data available on these units (Tab. 7.1). As discussed by Araújo Filho *et al.* (2020), several dates in these units were obtained without the required stratigraphic support, which led to innumerous

misinterpretations about the true age of these strata. While the geochronological data available indicated that the Azul and Águas Claras formations presented a maximum depositional age (MDA) of *ca*. 2.37 Ga (Justo *et al.* 2018), the Gorotire Formation presented an MDA of *ca*. 2.01 Ga (Pereira *et al.* 2009).

To a great extent, several studies have proposed different tectonic settings such as rift-related (e.g., Docegeo 1988, Olszewski *et al.* 1989, Martins *et al.* 2017), subduction-related (e.g., Dardenne *et al.* 1988, Meirelles & Dardenne 1991), intracratonic basin (e.g., Machado *et al.* 1991), and pull-apart (e.g., Araújo *et al.* 1988, Araújo & Maia 1991) for the evolution of the Carajás Basin over time. A rift-related setting for the Carajás Basin is assumed to be due to the collision between the Rio Maria and Carajás domains that took place in the Mesoarchean and the Neoarchean eras (Feio *et al.* 2013). However, all these proposals considered the evolution of the Carajás Basin to have taken place during the Neoarchean, whereas the tectonic-sedimentary evolution of this basin during the Paleoproterozoic still remains unknown.

Table 7.1: Summary of the main geochronological data available of the units of the Paleoproterozoic succession of the Carajás Basin (southeastern Amazonian Craton, Brazil). MDA: Maximum depositional age. LA-ICP-MS: laser ablation-inductively coupled plasma-mass spectrometry. SHRIMP: sensitive high-resolution ion microprobe. *Pb-Pb age.

Formation	**Lithology**	**U-Pb Age**	**Method**	**Mineral**	**Interpretation**	**Reference**
Gorotire Formation	Conglomerate	2011 ± 25 Ma	LA-ICP-MS			Pereira *et al.* (2009)
		2055 ± 54 Ma				Justo *et al.* (2018)
Águas Claras Formation	Sandstone	2778 ± ?		Zircon	MDA	Mougeot *et al.* (1996b)
		2681 ± 5 Ma	SHRIMP			Trendall *et al.* (1998)
		2796 ± 36 Ma	LA-ICP-MS			Justo *et al.* (2018)
		2060 ± ? Ma*	–	Pyrite	Diagenesis or hydrothermalism	Mougeot *et al.* (1996a)
Azul Formation	Rhythmite	2373 ± 4 Ma	LA-ICP-MS	Zircon	MDA	Justo *et al.* (2018)

7.3 MATERIALS AND METHODS

Sedimentological and stratigraphic investigations were carried out in the drill cores (n=17) and outcrops (n=6) of the Paleoproterozoic succession situated in different areas of the Carajás Basin (Fig. 7.3; Serra Sul, Tarzan, Igarapé Bahia mine, Bahia road, and Azul mine). In total, 14 new descriptions among the drill cores and outcrops of the Azul and Águas Claras formations were obtained. For each of these occurrences, a stratigraphic profile was constructed and correlated with previously published stratigraphic profiles presented by Araújo & Nogueira (2019) and Araújo Filho *et al.* (2020) in order to construct an accurate stratigraphic framework for the Paleoproterozoic succession.

A summary, with details on the drill cores and outcrops investigated in this study, is presented in the Supplementary Material (Table S-1). A facies analysis was undertaken in the new occurrences of the Azul and Águas Claras formations, which included the recognition of lithofacies arranged in different facies associations and recorded particular paleoenvironmental settings. More importantly, even though the succession was faulted, tilted, and folded, the delicate sedimentary structures and textures are well-preserved and enable a reliable interpretation of structures and textures. The methodology applied in the stratigraphic and sedimentological investigation is given in Appendix A.

A total of six samples of the Azul (n=1) and Águas Claras (n=5) formations were collected for the U-Pb zircon geochronological investigation (Tab. 7.2). The detailed methodology carried out for the preparation of samples is given in Appendix B. In general, the samples were prepared following the classical procedures prescribed in Fedo *et al.* (2003), which included crushing, pulverization, and sieving. The heavy mineral fraction was separated using dense liquids and the Frantz magnetic separator. From each sample, approximately 80–100 zircon grains were randomly handpicked regardless of size, color, or morphology. Subsequently, the grains were mounted and the cathodoluminescence (CL) images were individually obtained for each zircon grain at the Laboratório de Análises Minerais headquartered at the Geological Survey of Brazil (LAMIN-BE/CPRM, Belém, Brazil).

The CL images were obtained to check the morphology, internal structure, cracks, damage zones, the possible presence of inclusions in the zircon grains, and identify the metamitic zircon grains. While two samples were dated using the LA-ICP-MS (laser ablation-inductively coupled plasma-mass spectrometry) method at the Isotope Geology Laboratory housed at the Federal University of Pará (Pará-Iso/UFPA, Belém, Brazil), one sample was dated with the same method at the Isotope Geology Laboratory housed at the Federal University of Ouro Preto (DEGEO/UFOP, Ouro Preto, Brazil). Three other samples were dated using the

SHRIMP (sensitive high-resolution ion microprobe) method at the Laboratory of High Resolution Geochronology headquartered at the University of São Paulo (GeoLab/USP, São Paulo, Brazil). Details on the methodology and data processing applied in the LA-ICP-MS and SHRIMP analyses are available in Appendices C and D, respectively.

As the studied zircon grains were older than 1.5 Ga, the individual dates and weighted average ages were calculated using the $^{207}Pb/^{206}Pb$ ratios, as recommended by Spencer *et al.* (2016). The validity of the mean square weighted deviation (MSWD) was evaluated in accordance with the rule formulated by Wendt & Carl (1991). Only points with $\leq \pm 10\%$ of discordance and $\leq 5\%$ of analytical uncertainties were considered and plotted in Concordia diagrams and frequency histograms. A total of 362 zircon grains were analyzed from the Azul and Águas Claras formations, of which, a little more than half (*ca.* 60%) proved to be robust enough to support all the interpretations. The maximum depositional ages (MDA) were calculated using the conservative method of youngest grain cluster at 2σ uncertainty (YGC 2σ), following the recommendations of Coutts *et al.* (2019). The ages were calculated and the Concordia plots were constructed using the Isoplot 4.15 software (Ludwig 2008).

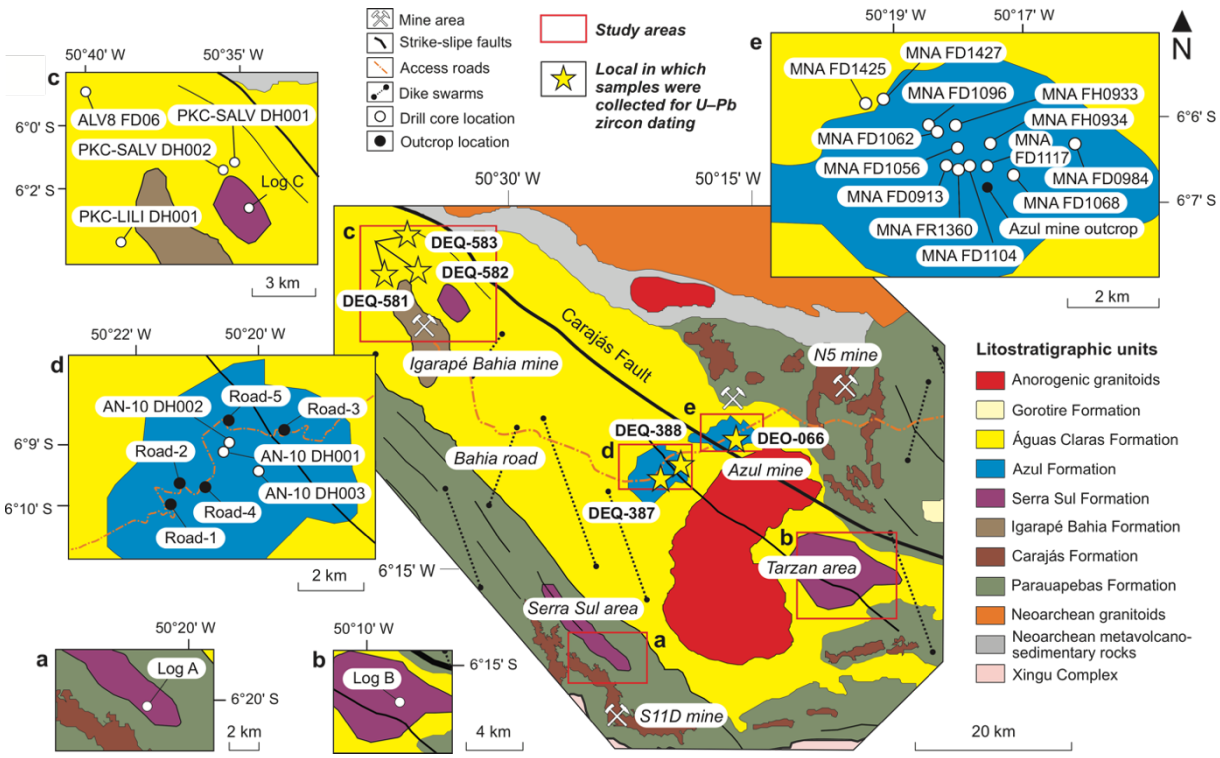

Figure 7.3: Simplified geological map showing the location of drill cores and outcrops investigated in different areas within the Carajás Basin (southeastern Amazonian Craton, Brazil): (a) Serra Sul; (b) Tarzan; (c) Igarapé Bahia mine; (d) Bahia road; and (e) Azul mine.

Table 7.2: Detailed description of the samples dated (U-Pb zircon) in this study.

Sample	Lithology	Formation	Location	Interval (m)	Method	Laboratory
DEQ-387	Rhythmite	Azul Formation	Drill core AN-DH-001	176.67–184.25	LA-ICP-MS	Pará-Iso/UFPA
DEQ-388	Sandstone	Águas Claras Formation	Drill core AN-DH-002	73.74–77.53		
DEO-066	Conglomerate		Azul mine Outcrop	48.10–48.23		DEGEO/UFOP
DEQ-581	Tuffaceous sandstone		Drill core ALV8-FD06	659.29–666.94	SHRIMP	GeoLab/USP
DEQ-582	Tuffaceous sandstone			670.74–674.53	SHRIMP	
DEQ-583	Tuffaceous sandstone			754.53–762.03	SHRIMP	

7.4 STRATIGRAPHY AND SEDIMENTOLOGY

7.4.1. Stratigraphic framework of the studied succession

The stratigraphic framework envisaged in this study constituted an uninterrupted *ca.* 1500 m thick package of strictly siliciclastic succession (rhythmite, sandstone, diamictite and conglomerate) of the Serra Sul, Azul, and Águas Claras formations, occurring above the volcanic and BIF strata of the Grão-Pará Group. The basal contact of the Azul Formation with the Serra Sul Formation was not observed. However, the observations that the Serra Sul deposits immediately overlaid the Neoarchean iron formation units and volcanic rock strata, as well as the Águas Claras Formation immediately overlaid the Azul Formation, strongly suggests that the Azul Formation are stacked above the Serra Sul Formation.

Three facies associations are reported in the Azul and Águas Claras formations, where six different lithofacies are arranged (Tab. 7.3). The two facies associations in the Azul Formation were defined as Rhythmite Facies Association (RFA) and Rhythmite-Sandstone Facies Association (RSFA), whereas the one in the Águas Claras Formation was defined as the Sandstone-Conglomerate Facies Association (SCFA). Although the RFA and RSFA occur laterally interbedded, stratigraphic observations suggests that the RSFA occur above the RFA, and both are unconformably overlaid by the SCFA deposits. Random gabbroic dike swarms occur truncating the succession (Fig. 7.4).

Table 7.3: Lithofacies and facies associations for the Azul and Águas Claras formations.

Formation	Facies Association	Lithofacies	Description
Azul Formation	Rhythmite Facies Association (RFA)	Rhythmite	Beds as thick as hundred meters (up to *ca*. 150 m thick). Millimeter to centimeter scale intercalation between fine-grained sandstone and mudrock stacked in fining-upward cycles. Red to black colored. Plane-parallel laminated and cross-laminated
	Rhythmite-Sandstone Facies Association (RSFA)	Rhythmite	Beds up to *ca*. 80 m thick. Millimeter to centimeter scale intercalation between normal graded sandstone and finely laminated mudrock stacked in fining-upward cycles
		Sandstone	Beds up to *ca*. 10 m thick. Fine- to medium-grained. Interbedded with rhythmite. Hummocky cross-stratification, cross-lamination, and wave-ripple cross-lamination. Wave-generated structures
Águas Claras Formation	Sandstone-Conglomerate Facies Association (SCFA)	Sandstone	Beds thicker than dozens of meters (up to *ca*. 30 m thick). Medium- to coarse-grained. Occur at the top of centimeter- to meter-scale fining-upward cycles interbedded with conglomerate. Plane-parallel laminated, tabular, and trough cross-stratified
		Conglomerate	Beds varying from *ca*. 0.3 to 3 m thickness. Constitute concave-up beds that pass up section to medium- to coarse-grained sandstone in fining upward cycles. Weakly stratified. Matrix- to clast- supported
		Jasper conglomerate	Beds up to *ca*. 3 m in thickness. Occur at the base of fining upward cycles. Weakly stratified. Jaspilite, chert, banded iron formation, and volcanic clasts occur widely embedded in a granular-to sandy matrix
		Tuffaceous sandstone	Beds up to *ca*. 8 m thickness. Subordinately interbedded with sandstone and conglomerate. Lightly welded. Lapillus occur sparsely embedded. Chlorotic matrix. Altered feldspars
		Mudrock	Beds up to *ca*. 0.3 m thickness. Occur at the top of fining-upward cycles, sandwiched by sandstone. Finely laminated. Disseminated pyrite

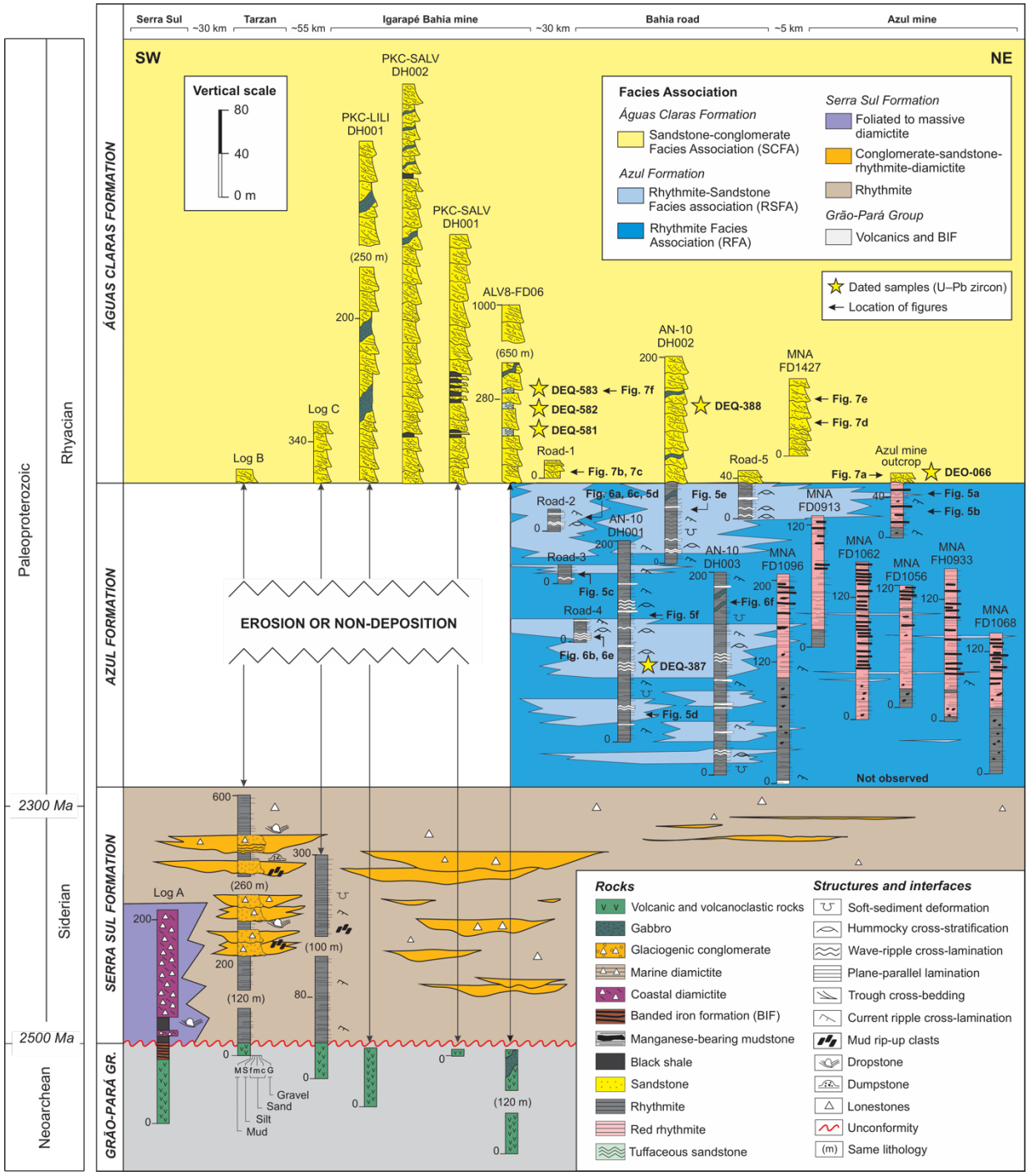

Figure 7.4: Stratigraphic framework envisaged for the Paleoproterozoic succession of the Carajás Basin (southeastern Amazonian Craton, Brazil) based on the stratigraphic data obtained from the study and the stratigraphic data previously published by Araújo & Nogueira (2019) and Araújo Filho *et al.* (2020). Numbers and letters to the right correspond to images in Figs. 7.5, 7.6, and 7.7.

7.4.2 Facies associations

7.4.2.1. Azul Formation

7.4.2.1.1. Rhythmite Facies Association (RFA)

The Rhythmite Facies Association (RFA) consists of rhythmite lithofacies by themselves (Fig. 7.5). In the stratigraphic succession, this facies association constitutes a package of approximately 200 m thickness. The rhythmite lithofacies comprises a millimeter-centimeter scale intercalation between the normally graded sandstone and the laminated mudrock stacked in fining-upward cycles. In general, the base of the sandstone beds presents erosive features. In the zone of contact between the mudrock and sandstone, soft-sediment deformation structures (e.g., convolute laminations and ball-and-pillow structures) are commonly observed. The fine-grained sandstone varies from moderate to poorly sorted and presents a mud-rich matrix, in which quartz grains are embedded. While the sandy beds are generally plane-parallel laminated, the current-generated cross-laminations occur subordinately and wave-generated structures are rarely observed. The manganese-bearing strata constitute intervals up to *ca.* 8 m thickness. Fine-grained pyrite crystals occur sparsely disseminated in the sandy laminations. The rocks display typical colors ranging from black to red.

7.4.2.1.2. Rhythmite-Sandstone Facies Association (RSFA)

The Rhythmite-Sandstone Facies Association (RSFA) comprises sandstone, rhythmite, and mudrock lithofacies (Fig. 7.6). The most striking sedimentological feature of this facies association is the occurrence of several intervals of hummocky cross-stratified sandstone. In the stratigraphic succession, this facies association constitutes uninterrupted intervals of up to 80 m thickness. The rhythmite facies is composed by a millimeter- to centimeter intercalation between the normally graded sandstone and the laminated mudrock. The sandstone lithofacies constitute beds up to 10 m thickness. Structures produced by currents and waves such as climbing ripple cross-laminations, hummocky cross-stratifications, planar to low-angle cross-laminations, quasi-planar laminations, and pinch-and-swell structures are generally observed. The hummocky cross-stratification structure varies from centimeter- to meter-scale in size (up to 3 m in length). Conversely, the hummocky cross-stratified sandstone intervals constitute beds generally amalgamated and sandwiched by rhythmite lithofacies, which laterally reach dozens of meters in extension. The sandstone lithofacies vary from fine- to medium-grained and is mainly composed by quartz clasts. Chert, volcanic rock, jaspilite, and BIF sandy clasts occur very subordinately. Ripple marks are frequently observed at the top of sandstone beds and finely disseminated pyrite crystals occur both in rhythmite and sandstone layers.

7.4.2.2. Águas Claras Formation

7.4.2.2.1. Sandstone-Conglomerate Facies Association (SCFA)

The Sandstone-Conglomerate Facies Association (SCFA) comprises sandstone, conglomerate, jasper conglomerate, tuffaceous sandstone, and mudrock lithofacies (Fig. 7.7). In the stratigraphic succession, the SCFA reaches up to *ca.* 800 m in thickness, and unconformably overlies the RFA and the RSFA deposits. The SCFA also unconformably overlies the volcanic rocks of the Grão-Pará Group and the glaciogenic strata of the Serra Sul Formation. The sandstone is medium-to coarse-grained. The trough cross-bedding structure is the most observed structure in this lithofacies, while plane-parallel and tabular-cross bedding is less observed. The conglomerate occurs weakly stratified and grade upward to sandstone lithofacies, constituting fining-upward cycles that vary from 0.3 to 3 m in thickness. Jasper conglomerate lithofacies occurs at the base of the fining-upward cycle and pass upward to sandstone lithofacies as well. The clasts are composed of jaspilite, banded iron formation, chert, and volcanic rock fragments. The pebble clasts vary from rounded to well-rounded and occur embedded in a granular-sandy matrix. The lithofacies of jasper conglomerate occurs very subordinately in the SCFA deposits and is reported for the first time to the Águas Claras Formation. The tuffaceous sandstone and mudrock lithofacies are repeatedly sandwiched by the sandstone lithofacies, constituting beds up to *ca.* 8 and *ca.* 0.3 m in thickness, respectively. Various lapilli are locally observed in the tuffaceous sandstone lithofacies, whereas finely disseminated pyrite crystals occur in the mudrock strata.

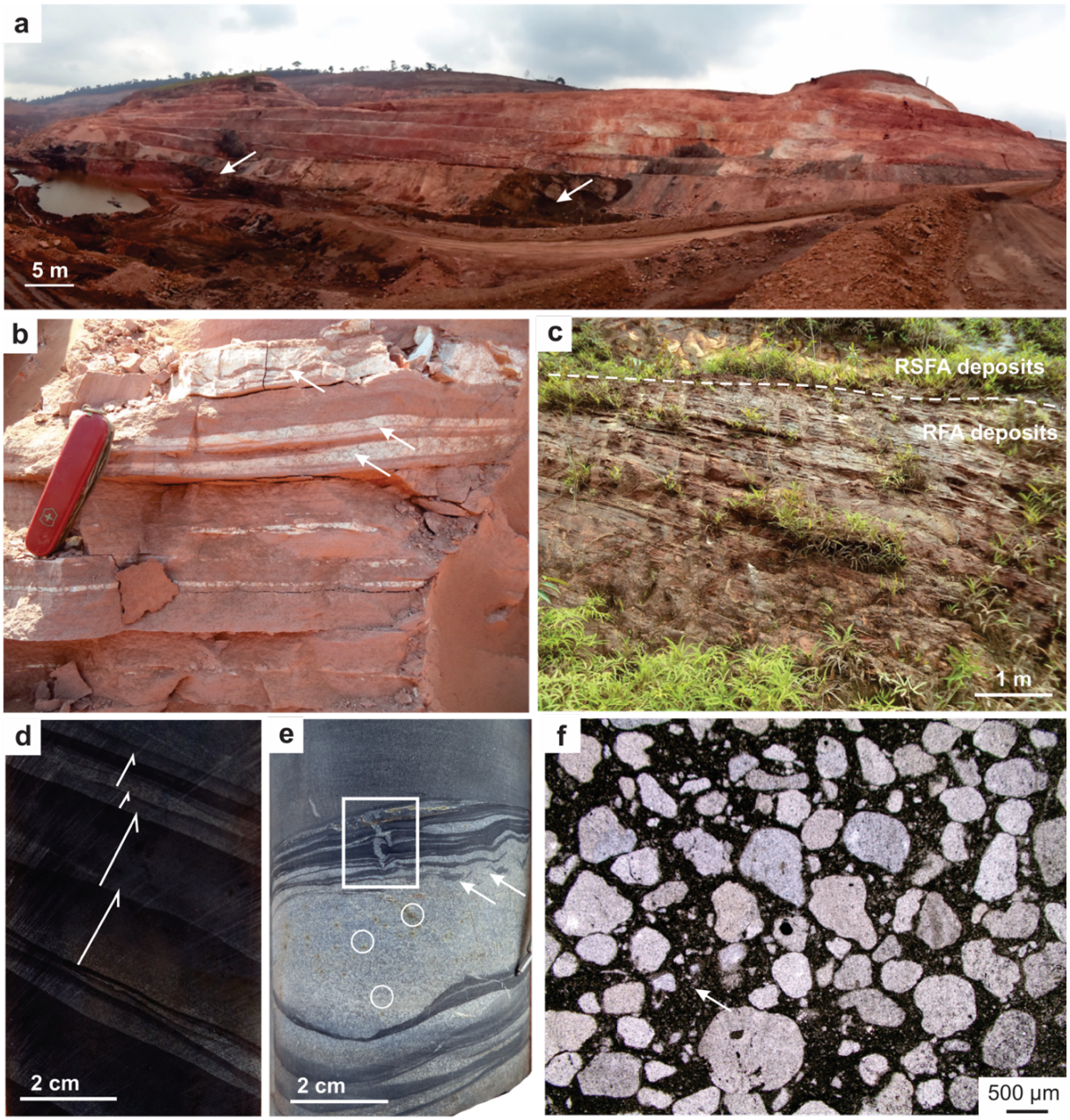

Figure 7.5: Sedimentologic features of the Rhythmite Facies Association (RFA) of the Azul Formation. (a) Panoramic view of the Azul mine showing meter-scale succession of rhythmite in which manganese-enriched strata (arrow) is embedded. (b) Red rhythmite beds showing mudrock repeatedly interbedded with kaolinized fine-grained sandstone (arrows). Convolute laminations occur at the base of the sandy intervals. (c) Current image of a strongly altered outcrop of the Azul Formation in the Bahia road showing tilted beds of RFA conformably overlaid by RSFA deposits. (d) Cut-rock surface of the drill core showing normal-graded sandstone interlayered with black mudrock, compounding fining-upward cycles. (e) Rhythmite showing sandy dikes (square) and mud rip-up clasts in the contact between fine-grained sandstone and mudrock (arrows). The circles indicate disseminated pyrites in sandy interval. (f) Thin section photomicrograph (plane parallel light, 10×) showing a fine-grained sandstone at the base of a fining-upward cycle with a mud-rich matrix (arrow).

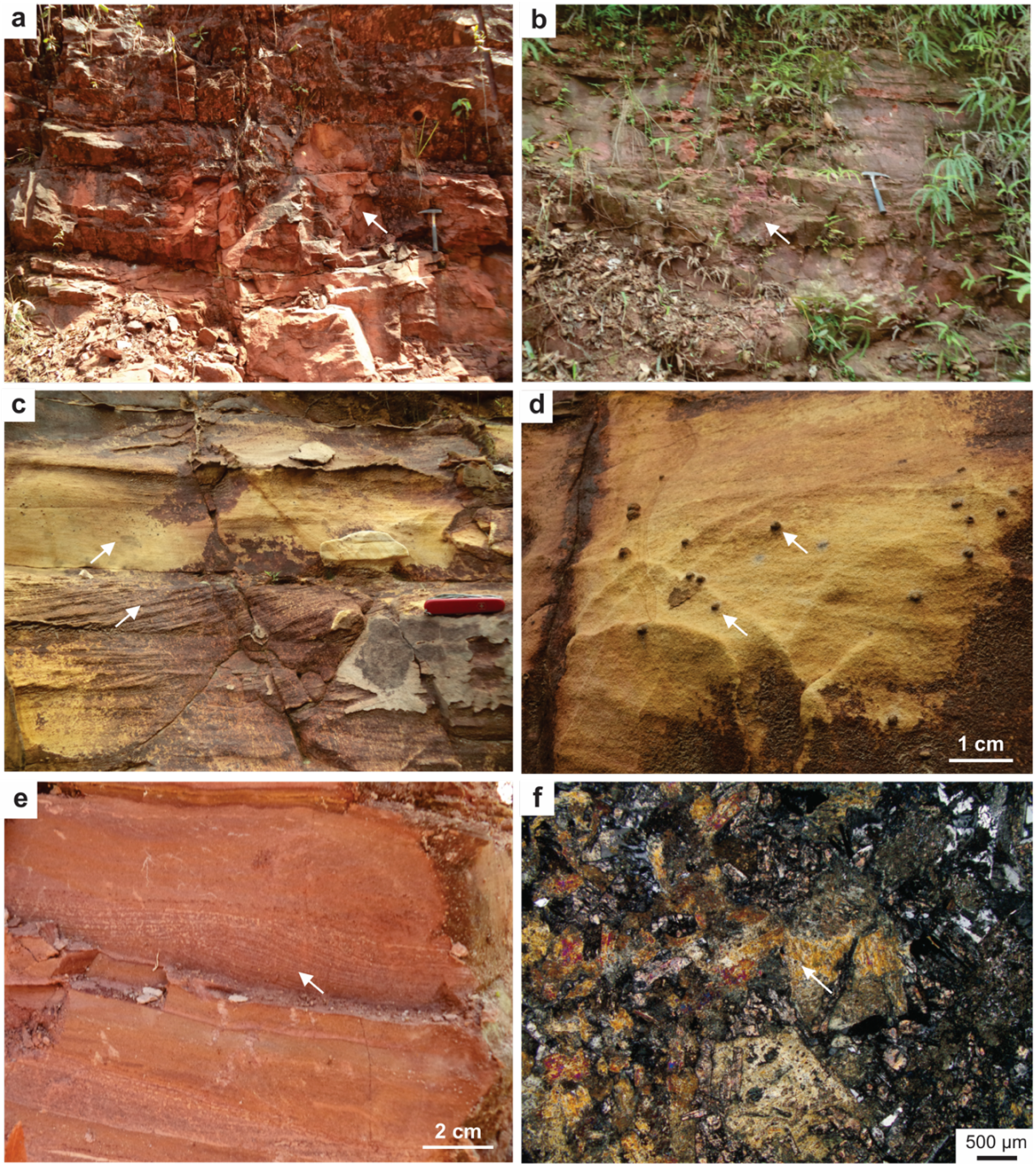

Figure 7.6: Sedimentological features of the Rhythmite-Sandstone Facies Association (RSFA) of the Azul Formation. (a) Outcrop on the Bahia road showing amalgamated bedset of meter-scale hummocky cross-stratified sandstone (arrow). (b) Hummocky cross-stratified sandstone (arrow) sandwiched by rhythmite strata. (c) Climbing ripple cross-laminated (arrow) and plane-parallel laminated sandstone (arrow) bedset repeatedly stacked. (d) Pyrite crystals (arrow) disseminated in sandstone. (e) Rhythmite facies showing mudrock interbedded with fine-grained sandstone with intricately interwoven cross-lamination (arrow). (f) Thin section photomicrograph (plane polarized light, 10×) of gabbro from a dike swarm, intrusive in this facies association, showing a highly altered primary mineralogy by chloritization (arrow).

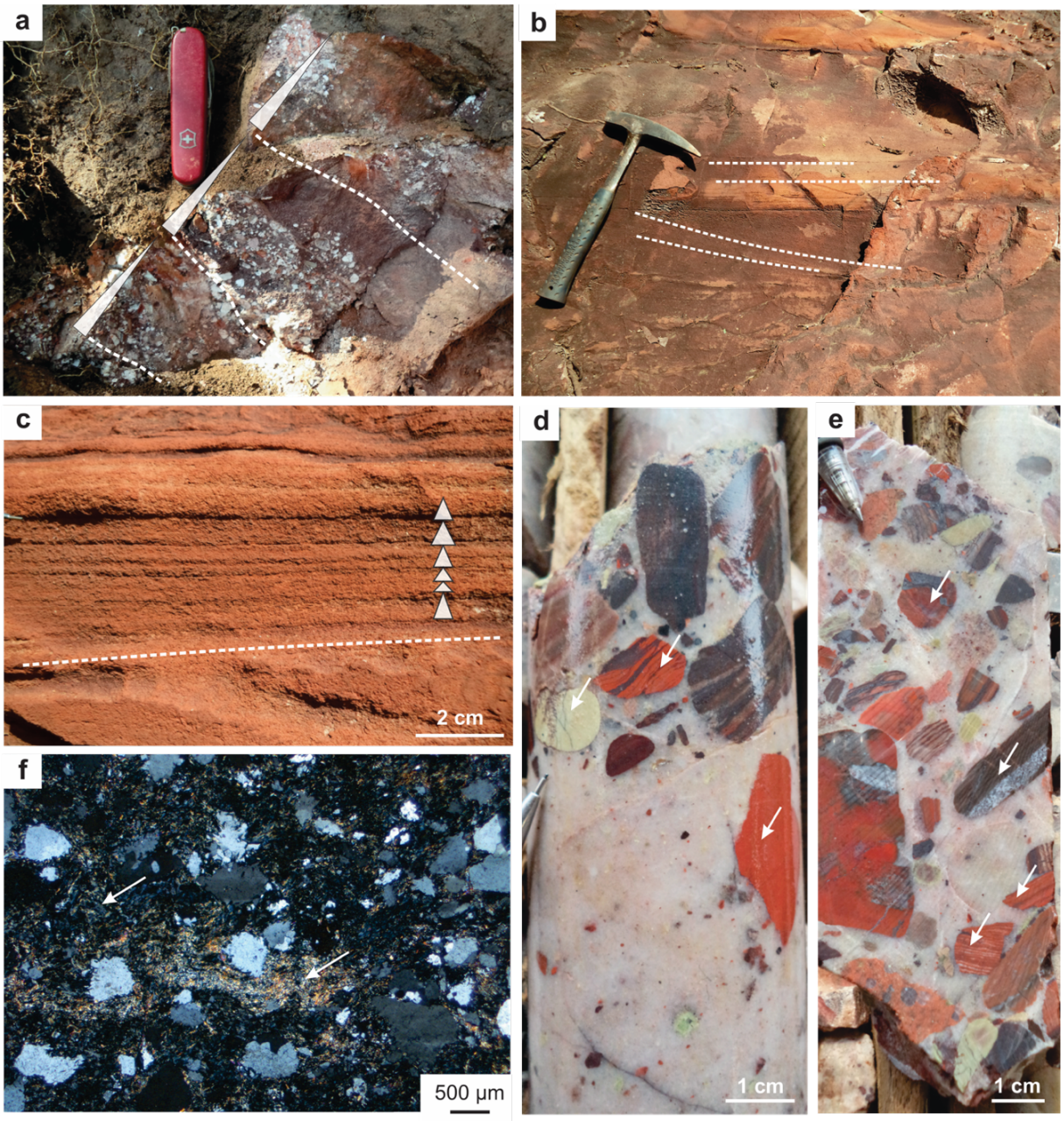

Figure 7.7: Sedimentological features of the Sandstone-Conglomerate Facies Association (SCFA) of the Águas Claras Formation. (a) Centimeter intercalation between the massive conglomerate and the weakly stratified sandstone, constituting fining-upward cycles. (b) A bedset of trough cross-bedded and plane-parallel laminated sandstone. (c) Detail of the coarse-grained sandstone with plane-parallel lamination above a trough cross-bedded sandstone stratum. (d, e) Cut rock surface of the drill core showing jasper conglomerate with several jaspilite, banded iron formation, chert, and mafic to felsic volcanic pebbles (arrows) embedded in a granular-sandy matrix. (f) Thin section photomicrograph (cross-polarized light, 10×) of tuffaceous sandstone showing its fluidal texture, in which altered plagioclase and quartz occur embedded in a chlorite-rich matrix (arrows).

7.5 U-Pb ZIRCON GEOCHRONOLOGY

7.5.1 General detrital zircon morphological features

The handpicked zircon grains from the Azul and Águas Claras formations present a typical oscillatory magmatic zoning varying from low–high brightness in the cathodoluminescence (CL) images (Fig. 7.8). In some grains, a high CL-brightness core is surrounded by a CL-dark rim, and vice versa. Inclusions are commonly observed, although they have not been characterized. In all the analyzed zircon grains, the morphology is heterogeneous and the size varies depending on the rock they were derived from. The zircon grains separated from the rhythmite not exceed 100 µm in size, whereas those extracted from conglomerate reaches up to *ca.* 400 µm in size. Those derived from sandstone and conglomerate are markedly more rounded than those derived from tuffaceous sandstone and rhythmite. In general, the grains show a typical red color, while rare grains range from translucent to light brown. They vary from rounded to subhedral, and few grains show a euhedral prismatic shape or are elongated in the growth direction. Some grains are cracked or constitute pieces of broken zircon grains. No relationship between the morphology and age could be established in any of the samples.

7.5.2 Dating results

7.5.2.1 Azul Formation sample

A total of 132 zircon grains separated from one sample of the Azul Formation were dated using the LA-ICP-MS method. Among this, 76 (*ca*. 57%) yielded $^{207}Pb/^{206}Pb$ dates suitable for age calculations (Fig. 7.9a). The results are highlighted as follows:

- DEQ-387 sample (rhythmite): A total of 132 zircon grains were dated using LA-ICP-MS, of which 76 (*ca*. 57%) those proved to be analytically robust. The dating yielded $^{207}Pb/^{206}Pb$ weighted average ages of 2273 ± 25 Ma (2σ, MSWD=0.097, n=3), 2344 ± 34 Ma (2σ, MSWD=0.98, n=3), 2478 ± 40 Ma (2σ, MSWD=0.14, n=3), 2546 ± 32 Ma (2σ, MSWD=0.77, n=3), 2653 ± 26 Ma (2σ, MSWD=0.30, n=8), 2741 ± 15 Ma (2σ, MSWD=0.69, n=20), 2841 ± 12 Ma (2σ, MSWD=0.71, n=29), and 2995 ± 59 MA (2σ, MSWD=0.43, n=6). The youngest and the oldest $^{207}Pb/^{206}Pb$ date obtained corresponds to 2259 ± 35 Ma and 3387 ± 69 Ma, respectively (Fig. 7.9a; Tab. 7.4; Table S-2);

In the probability histogram (Fig. 7.10a), the main peaks of the ages obtained from the U-Pb zircon dating of the Azul Formation are positioned at 2.83 Ga, and 2.71 Ga, and subordinately at 2.27 Ga, 2.34 Ga, and 3.39 Ga, respectively.

Figure 7.8: Cathodoluminescence (CL) images of some zircon grains dated (U-Pb) with their respective values of $^{207}Pb/^{206}Pb$ dates. (a) Zircon grains dated from the Azul Formation. (b–f) Zircon grains dated from the Águas Claras Formation. The yellow and red circles indicate the site of the laser spots positioned for dating using LA-ICPMS and SHRIMP, respectively.

7.5.2.2 Águas Claras Formation samples

A total of 230 zircon grains separated from five samples of the Águas Claras Formation were dated using LA-ICP-MS and SHRIMP methods. Among this, 170 (*ca*. 73%) yielded

$^{207}Pb/^{206}Pb$ dates suitable for age calculations (Figs. 7.9b–f). For each sample, the main results are highlighted as follows:

- DEQ-388 sample (sandstone): A total of 117 zircon grains were dated using LA-ICP-MS, of which 78 (*ca*. 66%) proved to be analytically robust. The dating yielded $^{207}Pb/^{206}Pb$ weighted average ages of 2668 ± 33 Ma (2σ, MSWD=1.01, n=3), 2752 ± 17 Ma (2σ, MSWD=2.0, n=16), 2878 ± 15 Ma (2σ, MSWD=2.8, n=28), 3002 ± 18 Ma (2σ, MSWD=3.0, n=23), and 3148 ± 20 Ma (2σ, MSWD=1.2, n=6). The youngest and the oldest $^{207}Pb/^{206}Pb$ dates obtained correspond to 2617 ± 59 Ma and 3505 ± 27 Ma, respectively (Fig. 7.9b; Tab. 7.4; Table S-2);
- DEO-066 sample (jasper conglomerate): A total of 58 zircon grains were dated using LA-ICP-MS, of which 51 (*ca*. 87%) proved to be analytically robust. The dating yielded $^{207}Pb/^{206}Pb$ weighted average ages of 3107 ± 6 Ma (2σ, MSWD=1.3, n=4), 3121 ± 3 Ma (2σ, MSWD=0.16, n=4), 3133 ± 3 Ma (2σ, MSWD=1.9, n=11), 3153 ± 5 Ma (2σ, MSWD=2.4, n=8), 3171 ± 4 Ma (2σ, MSWD=2.3, n=8). Additionally, the intervals of $^{207}Pb/^{206}Pb$ dates of 2.95–3.04 Ga, 3.07–3.09 Ga, and 3.19–3.33 Ga were calculated. The youngest and the oldest $^{207}Pb/^{206}Pb$ date obtained correspond to 2607 ± 7 Ma and 3414 ± 7 Ma, respectively (Fig. 7.9c; Tab. 7.4; Table S-2);
- DEQ-581 sample (tuffaceous sandstone): A total of 16 zircon grains were dated using SHRIMP, of which 13 (*ca*. 81%) proved to be analytically robust. The dating yielded $^{207}Pb/^{206}Pb$ weighted average ages of 2881 ± 14 Ma (2σ, MSWD=1.9, n=4), 2945 ± 10 Ma (2σ, MSWD=0.25, n=2) and 2979 ± 7 Ma (2σ, MSWD=0.57, n=4). The youngest and the oldest $^{207}Pb/^{206}Pb$ dates obtained correspond to 2831 ± 10 Ma and 3045 ± 5 Ma, respectively (Fig. 7.9d; Tab. 7.4; Table S-3);
- DEQ-582 (tuffaceous sandstone): A total of 16 zircon grains were dated using SHRIMP, of which 14 (*ca*. 87%) proved to be analytically robust. The dating yielded $^{207}Pb/^{206}Pb$ weighted average ages of 2840 ± 20 Ma (2σ, MSWD=3.9, n=3), 2928 ± 8 Ma (2σ, MSWD=0.004, n=2), 2948 ± 11 Ma (2σ, MSWD=1.3, n=4), and 2973 ± 20 Ma (2σ, MSWD=2.2, n=3). The youngest and the oldest $^{207}Pb/^{206}Pb$ dates obtained correspond to 2813 ± 5 Ma and 2981 ± 9 Ma, respectively (Fig. 7.4e; Tab. 7.4; Table S-3);
- DEQ-583 sample (tuffaceous sandstone): A total of 23 zircon grains were dated using SHRIMP, of which 14 (ca. 60%) proved to be analytically robust. The dating yielded $^{207}Pb/^{206}Pb$ weighted average ages of 2876 ± 7 Ma (2σ, MSWD=1.2, n=5), 2912 ± 25 Ma (2σ, MSWD=2.1, n=3), and 2949 ± 8 Ma (2σ, MSWD=0.035, n=3). The youngest and the

oldest $^{207}Pb/^{206}Pb$ dates obtained correspond to 2716 ± 7 Ma and 3058 ± 6 Ma, respectively (Fig. 7.4f; Tab. 7.4; Table S-3).

In the probability histogram (Fig. 7.10b), the main peaks of the ages obtained from the U-Pb zircon dating of the Águas Claras Formation are positioned at 2.94 Ga, and 2.87 Ga, and subordinately at 2.71 Ga, 3.27 Ga, and 2.66 Ga, respectively.

Table 7.4: Summary of U-Pb (LA-ICP-MS and SHRIMP) zircon dating results.

Sample name	**Formation (lithofacies)**	**Number of analyzed zircon grains**		**$^{207}Pb/^{206}Pb$ weighted average ages (Ma)**	**Youngest and oldest $^{207}Pb/^{206}Pb$ zircon (Ma)**
		Total	**≤ ±10% discordant**		
DEQ-387	Azul Fm. (rhythmite)	132	76	2273 ± 25 (n=3), 2344 ± 34 (n=3), 2478 ± 40 (n=3), 2546 ± 32 (n=3), 2653 ± 26 (n=8), 2741 ± 15 (n=20), 2841 ± 12 (n=29), 2995 ± 59 (n=6)	2259 ± 35, 3387 ± 69
DEQ-388	Águas Claras Fm. (sandstone)	117	78	2668 ± 33 (n=3), 2752 ± 17 (n=16), 2878 ± 15 (n=28), 3002 ± 18 (n=23), 3148 ± 20 (n=6)	2617 ± 59, 3505 ± 27
DEO-066	Águas Claras Fm. (Jasper conglomerate)	58	51	3107 ± 6 (n=4), 3121 ± 3 (n=4), 3133 ± 3 (n=11), 3153 ± 5 (n=8), 3171 ± 4 (n=8)	2609 ± 7, 3414 ± 7
DEQ-581	Águas Claras Fm. (tuffaceous sandstone)	16	13	2881 ± 14 (n=4), 2945 ± 10 (n=2), 2979 ± 7 (n=4)	2831 ± 10, 3045 ± 5
DEQ-582		16	14	2840 ± 20 (n=3), 2928 ± 8 (n=2), 2948 ± 11 (n=4), 2973 ± 20 (n=3)	2813 ± 5, 2981 ± 9
DEQ-583		23	14	2876 ± 7 (n=5), 2912 ± 25 (n=3), 2949 ± 8 (n=3),	2716 ± 7, 3058 ± 6

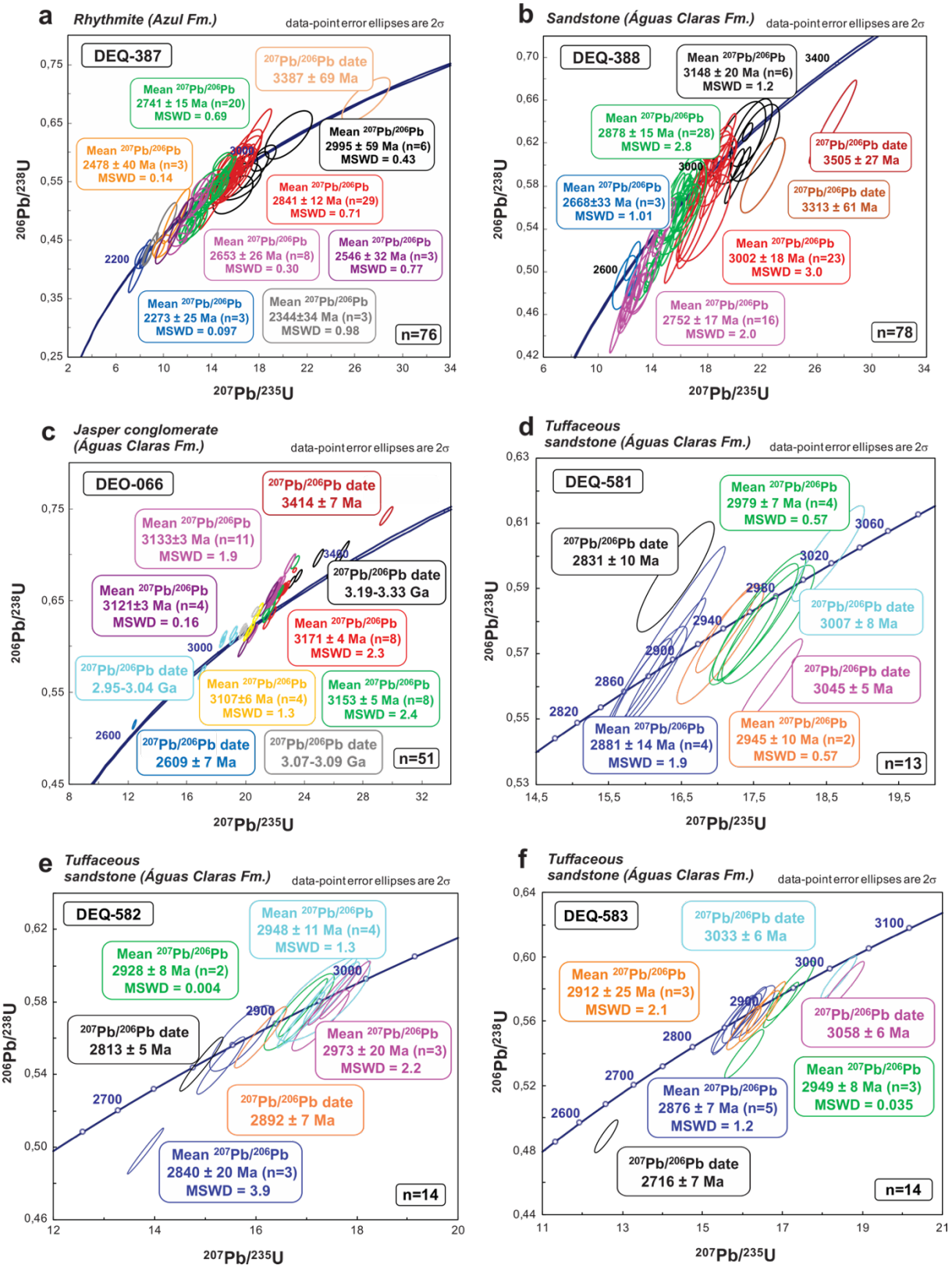

Figure 7.9: U-Pb Concordia plots obtained from the dating of samples of the (a) Azul Formation and (b–f) the Águas Claras Formation (only analysis with <±10% of discordance).

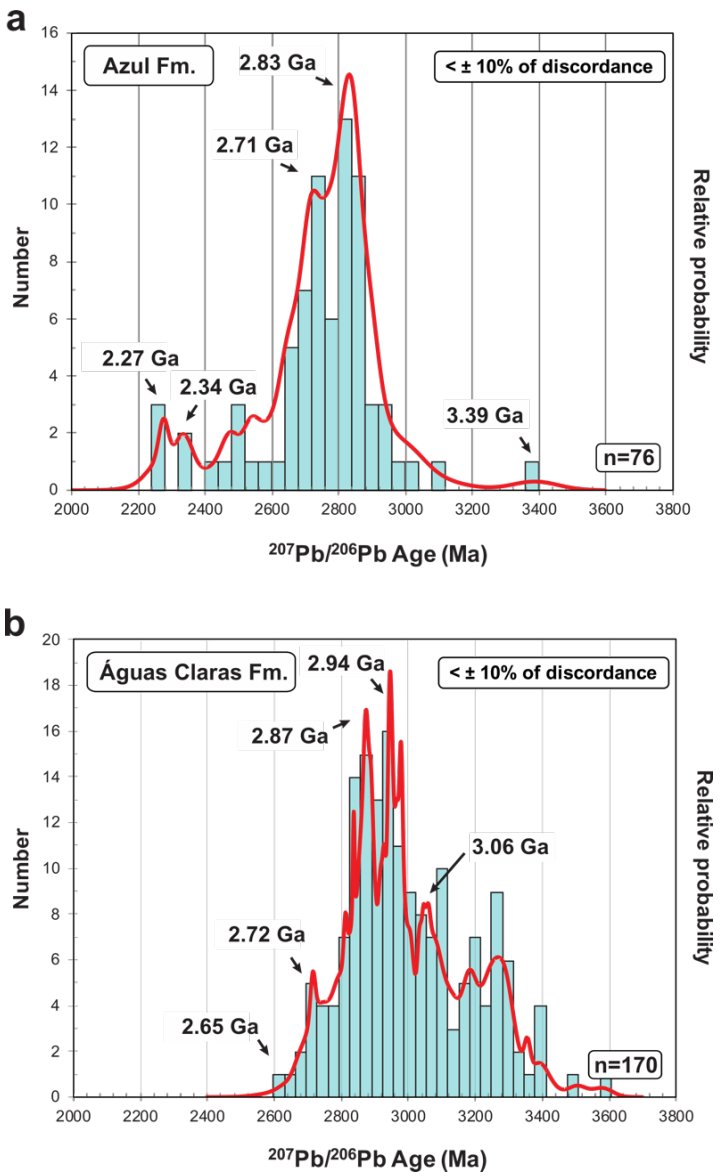

Figure 7.10: Probability histograms showing the $^{207}Pb/^{206}Pb$ Age distribution of (a) the 76 concordant analyses of the Azul Formation, and (b) the 170 concordant analyses of the Águas Claras Formation.

7.6 DISCUSSION

7.6.1 Reconstructing the sedimentary environment

In the RFA deposits of the Azul Formation, the observation that normally graded sandstone occurs repeatedly interbedded with structureless to even-laminated mudrock, compounding millimeter- to centimeter scale fining-upward cycles, suggests that it constitutes low density turbidity strata deposited in subaqueous conditions within the basin (e.g., Bouma 1962, Amy *et al.* 2005). Moreover, the observation that these deposits constitute a monotonous thick and laterally extensive succession of the order of kilometers suggests a deposition in a marine environment. These interpretations are similar to those presented in previous works (e.g., Nogueira *et al.* 1995, Araújo Filho *et al.* 2020).

The occurrence of red beds (Fig. 7.5b) and black shale (Fig. 7.5d) deposits side-by-side in the Azul deposits strongly suggests a stratified basin, in which the oxygenated and shallow waters were a sinks for red bed deposition, and the deep zones remained unoxygenated and filled by black shale deposits (e.g., Force & Cannon 1988, Roy 1997, 2006). Manganese oxides were possibly reduced in the shallow waters and subsequently transported to deep parts of the basin through downwelling currents, where it was deposited with black shale strata (e.g., Dasgupta *et al.* 1992, Roy 1997, 2006).

The occurrence of several intervals with wave-generated structures, including hummocky cross-stratification in rhythmite deposits of the RSFA, indicate that the Azul marine platform had repeatedly been affected by storm episodes (Cheel & Leckie 1993, Dumas & Arnott 2006). Although not necessarily, the absence of dropstone features and ice-rafted debris intervals in the Azul rhythmite deposits, as well as, the wide occurrence of wave-generated structures within these deposits, it is suggestive of an ice-free condition in effect during the deposition of the Azul Formation (e.g., Le Heron *et al.* 2011, Le Heron 2015). Based on the stratigraphic record of the Serra Sul Formation (see Araújo & Nogueira 2019), it is plausible to suppose that the during final deposition of this formation, the Serra Sul glaciation was already in its last stages of glacial expansion. Subsequently, the rise of the sea level caused the transgression of the Azul Sea towards the hinterland of the Carajás protocontinent and deposition of the Azul Formation in a marine environment.

The wide occurrence of wave-generated structures in the RSFA deposits, as well as, the near absence of these structures in the RFA indicate that these facies associations are representatives of the offshore zone and offshore transition/shoreface zone deposits, respectively. Moreover, the absence of high-density turbiditic facies (e.g., submarine fan deposits) in these deposits suggest that the marine environment was relatively shallow, in comparison to the marine environment associated with the underlying Serra Sul Formation, in which the glacially-derived conglomerate deposits is widely observed (Araújo & Nogueira 2019). Therefore, although the sea level rose after the Serra Sul glaciation, the sedimentation occurred in a shallow and wide marine basin, in which strata enriched in manganese were deposited along with black shale in the deepest parts of the marine basin.

In the Águas Claras Formation, the occurrence of cross-stratified to massive sandstone strata interbedded with massive to weakly stratified conglomerate—constituting a succession of hundreds of meters in thickness—suggest that this formation was deposited in a well-developed braided fluvial system (Miall 1977, Hjellbakk 1997). This interpretation is quite similar to that presented in several previous studies (e.g., Nogueira *et al.* 1995, Araújo & Sousa 2018, Araújo

& Nogueira 2019, Araújo Filho *et al.* 2020). Tidal influenced structures were reported to the Águas Claras Formation in the Bahia road area by Nogueira *et al.* (1995). However, in this study we not observe these structures in the Águas Claras Formation, although we not dispute its occurrences.

Moreover, as Nogueira *et al.* (1995) interpreted, the occurrence of tidal-influenced intervals at the lowermost part of the Águas Claras Formation is indicative of a progradational stacking from the coastal to fluvial deposits within this formation. The subordinate occurrence of the jasper conglomerate lithofacies in the Águas Claras Formation was interpreted just as results of the lateral variation of facies, whereas the occurrence of lapilli in tuffaceous sandstone lithofacies suggest subaerial volcanic activities nearby to the Águas Claras fluvial braided plain (e.g., MacPhie *et al.* 1993, Orton 1996). This interpretation is similar to that presented by Araújo Filho *et al.* (2020) for the same deposits.

7.6.2 New insights on the sequence stratigraphy of the Carajás Basin

Araújo & Nogueira (2019) proposed that the Serra Sul Formation unconformably overlie the Grão Pará Group, suggesting that this surface may represents a sequence boundary within the Carajás Basin succession. Additionally, Araújo Filho *et al.* (2020), based on the concepts brought forth by Embry (2002), proposed that the Azul and Águas Claras formations are the stratigraphic records associated with a transgressive-regressive (T-R) sequence. In this study, our new insights on the sequence stratigraphy of this basin, supported by the stratigraphic framework envisaged (Fig. 7.4), indicate that the upper part of the Serra Sul Formation constitutes the lowermost portion of the transgressive systems tract (TST) of the T-R sequence. In addition, we suggest that the basal part of the Serra Sul Formation is the stratigraphic record associated with a regressive systems tract (RST). The contact between the basal part and the upper part of the Serra Sul Formation most likely represents a maximum regressive surface (MRS), below which submarine fan deposits occur stacked, and above which shallow marine deposits lie (Fig. 7.11).

During the final deposition of the Serra Sul Formation, it is plausible to assume that the sea level raised as result of deglaciation. The observation that several ice-rafted debris-bearing intervals occur in the upper part of the Serra Sul Formation strengthened this interpretation. Consequently, it strongly suggests that the Azul Formation possibly was possibly deposited as a result of the rise of the sea level and probably marks the maximum stage of marine transgression of the marine basin, as previously suggested by Araújo Filho *et al.* (2020). As interpreted by these authors, as well, the Azul Formation is limited from the overlying Águas

Claras Formation by a maximum flooding zone (MFZ), which represents the point of maximum transgression, and from which the base level upward started to fall.

Although studies in the past have pointed out that the Gorotire Formation is part of the Paleoproterozoic succession of the Carajás Basin (e.g., Araújo & Nogueira 2019, Araújo Filho *et al.* 2020), an interpretation that we are supportive of as well, little is known about the role of this formation in the evolutionary context of the Carajás Basin. In our view, the coarse-grained strata encompassed by this formation (i.e., an alluvial to fluvial braided deposits; Nascimento & Oliveira 2015) constitutes the uppermost part of the T-R sequence. The Gorotire Formation was likely deposited soon after the deposition of the Águas Claras Formation and represents the end member of the coarsening-upward succession that fill the Carajás Basin. It is possible that the Gorotire alluvial to fluvial system was at least in part connected to the Águas Claras fluvial system.

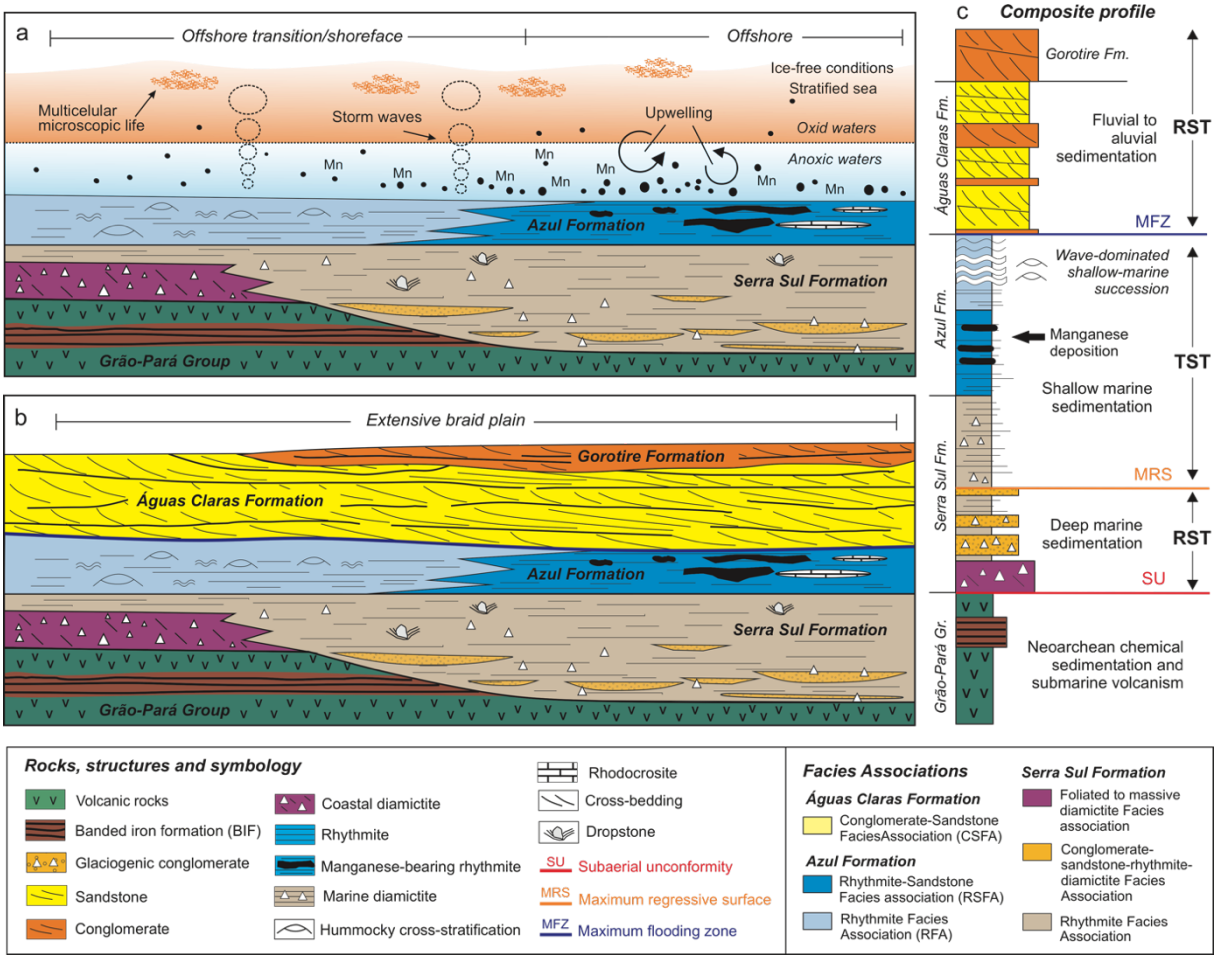

Figure 7.11: Simple models showing the paleoenvironmental reconstruction of two distinct steps of the sedimentary evolution of the Paleoproterozoic succession of the Carajás Basin (Amazonian Craton, Brazil). (a) A shallow marine platform in which the Azul Formation was deposited immediately above

the Serra Sul Formation. (b) A fluvial braided system in which the Águas Claras Formation was deposited after the deposition of the Azul Formation. It is possible that the Gorotire Formation was deposited soon after or coevally with the Águas Claras Formation. (c) Composite profile of the Paleoproterozoic succession of Carajás Basin, showing new insights on the sequence stratigraphy of this basin.

7.6.3. Provenance of studied succession: A proof of a connection between the Carajás and Bacajá domains during the Paleoproterozoic?

The geochronological results obtained in this study strongly suggests that the Azul and Águas Claras formations were supplied mainly by Mesoarchean and Neoarchean rocks, whereas Siderian to Rhyacian and Paleoarchean rocks were subordinate sources. Bizarrely, no Paleoarchean rocks have been reported in the Carajás region and it is likely that the zircon grains of that age were sourced from a Paleoarchean proto-crust reworked by crustal recycling in this area during the Mesoarchean and the Neoarchean, as previously admitted for some authors (e.g., Feio *et al.* 2013, Teixeira *et al.* 2019b). On the other hand, Meso to Neoarchean rocks are widely distributed in the Carajás and Rio Maria domains (Vasquez *et al.* 2008a, and references therein), and Siderian to Rhyacian rocks occur largely distributed in the Bacajá Domain (Macambira *et al.* 2009).

In that context, we suggest that the Rio Maria and Carajás country rocks were potentially the main sources of sediments to the Azul and Águas Claras formations, while the Bacajá domain possibly remained a subordinate source-area (Fig. 7.12). It is also plausible to assume that the Carajás protocontinent and Bacajá Domain were, at least partially, connected during the Siderian to Rhyacian periods. This may explain the occurrence of zircon grains of those ages in the Azul Formation (Fig. 7.10). Another possible explanation for the occurrence of Paleoproterozoic zircon grains in the Azul Formation (that does not involve a connection between the Carajás and Bacajá domains) is the existence of small-scale igneous bodies of that age within the Carajás Domain that were not yet mapped in the region or that were simply eroded over time.

Although this last hypothesis may not be mistaken or mutually exclusive from the former, we suggest that the Carajás and Bacajá domains were partially connected during the Rhyacian period. This interpretation is strongly strengthened by the observation that the paleocurrents obtained from fluvial cross-bedded strata of the Águas Claras Formation, which indicate a main paleoflow toward the SW–SE (Nogueira 1995). This data suggests relative highlands and source-areas of sediments towards the N–NE, with regards to the present-day

configuration. This interpretation is compatible with a scenario in which the Bacajá Domain was nearby and somehow connected to the Carajás Domain during the Rhyacian period, and was possibly a subordinate source-area of sediments.

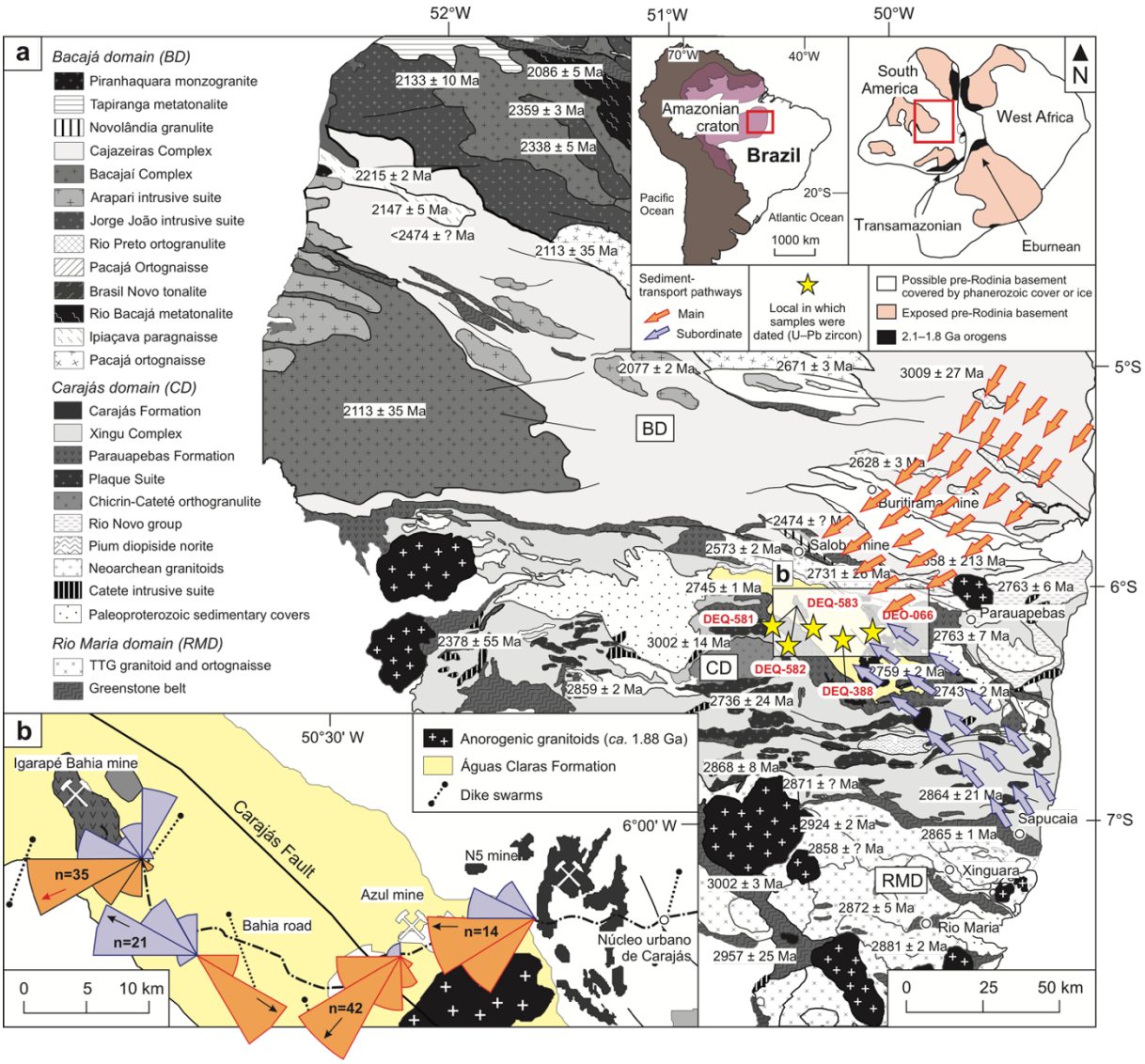

Figure 7.12: (a) Simplified geological map of the Carajás region (modified from Vasquez *et al.* 2008a) showing potential source-rocks of the Águas Claras Formation and the inferred sediment transport pathways. The paleogeographic map shows the southern portion of the Columbia supercontinent with approximate location of the Carajás region (Modified from Zhao *et al.* 2004). (b) Simplified map of the Bahia road area showing the location of points where paleocurrent data were obtained by Nogueira (1995) from the fluvial strata of the Águas Claras Formation.

Strangely, Paleoproterozoic zircon grains occur strictly in the Azul Formation, while in the Águas Claras Formation they are not founded. It is not expected since, based on the

provenance analysis of these units, the Águas Claras Formation should contain many more Paleoproterozoic zircon grains than the Azul Formation. On the other hand, abundant Rhyacian zircon grains are reported from the Gorotire Formation (e.g., Pereira *et al.* 2009, Justo *et al.* 2018). Many hypotheses may explain the absence of Paleoproterozoic zircon grains in the Águas Claras Formation as paleogeographic controls, changes in the source of sediments or even the sedimentary dynamic related to the Águas Claras fluvial system. Moreover, the sources of sediment could be located far from the basin. The difficulty to reconstruct the paleogeography of this area prevents to accurately indicate the sources of sediments outside the Carajás area.

7.6.4 Unraveling the Carajás foreland basin

Plate tectonics, a process which intrinsically involves subduction and crustal reworking, seems to have taken place in the Carajás region from the Mesoarchean to the Neoarchean (e.g., Feio *et al.* 2013, Martins *et al.* 2017, Marangoanha *et al.* 2019). A collisional event between the Carajás and Rio Maria domains at *ca*. 2.85 Ga is said to have produced a collisional orogen and triggered a continental rifting, in which the Carajás Basin was installed (Martins *et al.* 2017). Initially, the Carajás rift basin was filled by a *ca*. 2-3 km thick pile of mafic to felsic volcanics and banded iron formation strata during the Neoarchean (e.g., Olszewski *et al.* 1989, Trendall *et al.* 1998). However, as previously mentioned, the evolution of this basin along the Paleoproterozoic still remains unknown.

Based on the stratigraphic framework constructed for the Paleoproterozoic succession of the Carajás Basin, the geochronological results achieved in this study, and regional data on the Carajás area (e.g., Cordani *et al.* 1984, Macambira *et al.* 2009, Tavares *et al.* 2018), we envisage that the Carajás Basin evolved during the greater part of the Paleoproterozoic in a foreland style (Fig. 7.13). The evolution of this basin with this setting is directly related to the collision between the Bacajá Domain and the Carajás protocontinent that took place during the *ca*. 2.0 Ga Transamazonian orogenetic cycle, which is generally considered the last major tectonic event that affected the Carajás region and structured the basin in its current configuration (e.g., Machado *et al.* 1991).

Regarding the tectono-sedimentary evolution of the Carajás foreland basin, it may be divided into three distinct stages of evolution, as is generally observed in basins that evolved in a foreland style (e.g., Catuneanu *et al.* 2004). In the underfilled stage, deep marine deposits (i.e., conglomerate and sandstone strata deposited in a submarine fan system) of the Serra Sul Formation were deposited. Subsequently, in the filled and overfilled stages, the shallow marine

deposits of the Azul Formation and fluvial to alluvial deposits of the Águas Claras and Gorotire formations were deposited, respectively. The collision between the Bacajá and Carajás landmasses resulted not only in the shutdown of the sedimentation, but also the deformation and erosion of the basin-fill succession.

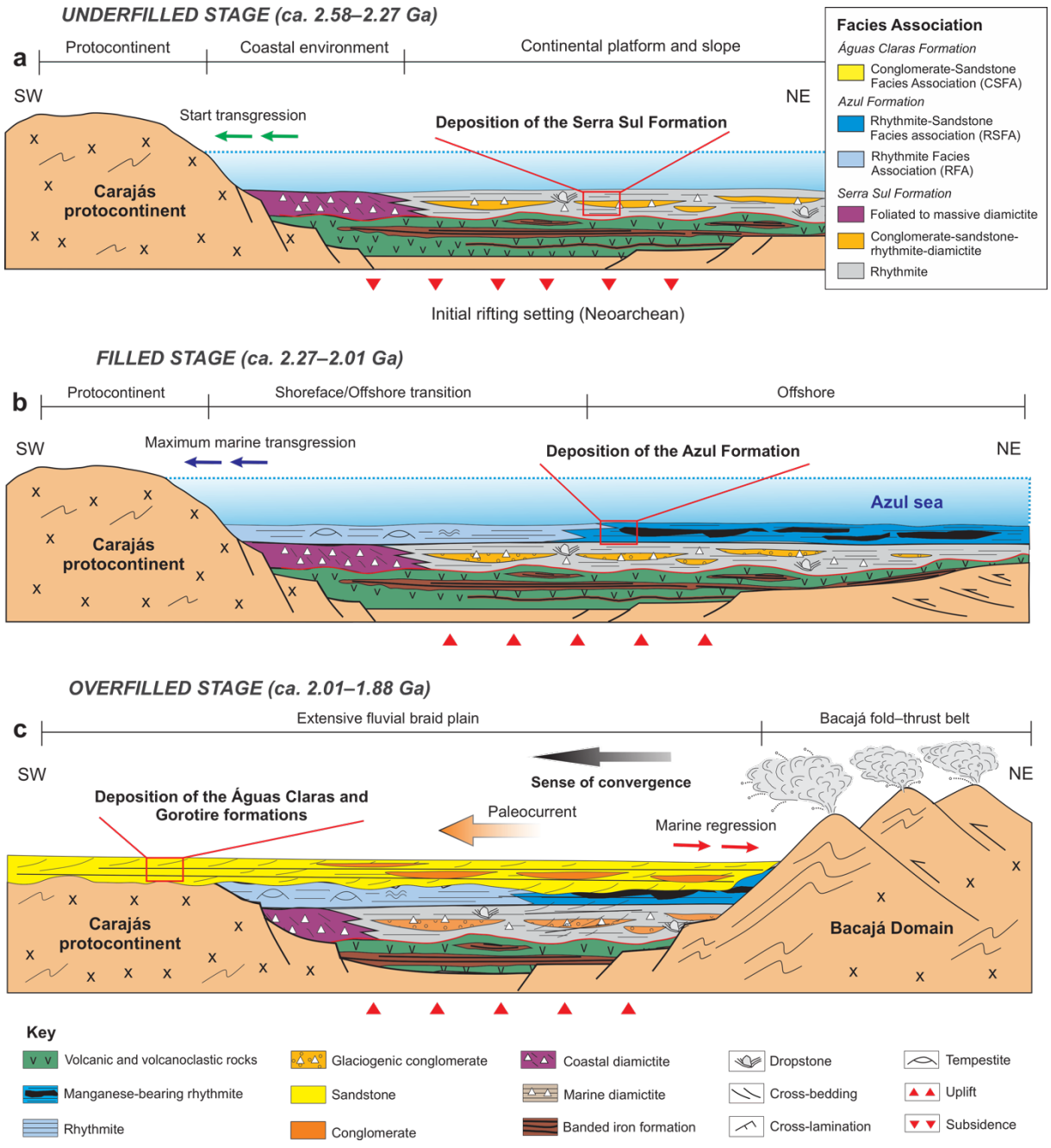

Figure 7.13: Evolutive stages envisaged for the Carajás foreland Basin during the Paleoproterozoic. (a) Underfilled stage (*ca.* 2.58–2.27 Ga): deposition of coarse-grained deposits (i.e., submarine fan conglomerate and sandstone) of the Serra Sul Formation. These deposits represent the basal deep marine sedimentation of the basin. (b) Filled stage (*ca.* 2.27–2.06 Ga): deposition of fine-grained deposits (i.e.,

rhythmite and sandstone) of the Azul Formation. These deposits represent the middle shallow marine sedimentation of the Carajás foreland basin. (c) Overfilled stage (*ca.* 2.06–1.88 Ga): deposition of coarse-grained deposits (i.e., sandstone and conglomerate) of the Águas Claras and Gorotire formations. These deposits represent the upper fluvial to alluvial sedimentation of the Carajás foreland basin.

Finally, we estimate the intervals of the ages that the underfilled, filled, and overfilled stages may have occurred in: 2.58–2.27 Ga, 2.27–2.01 Ga, and 2.01–1.88 Ga, respectively. Theses intervals were relatively constrained to the maximum depositional age (MDA) of the Serra Sul Formation at *ca.* 2.58 Ga (Araújo & Nogueira 2019), the MDA of the Azul Formation at *ca.* 2.27 Ga obtained from this study (Fig. 7.10), the MDA of the Gorotire Formation at *ca.* 2.01 Ga (Pereira *et al.* 2009, Justo *et al.* 2018), and the crystallization age of the Carajás Granite and dike swarms at *ca.* 1.88 Ga (e.g., Machado *et al.* 1991, Teixeira *et al.* 2019b), that cross-cut the Carajás Basin and post-date its succession.

7.6.5 Implications on the Columbia supercontinent configuration and glimpses on the Paleogeographic scenario

As previously mentioned, the collision between the Bacajá Domain and the Carajás protocontinent has been argued to be directly related to the Transamazonian orogenetic cycle (Macambira *et al.* 2009). In turn, this cycle is considered to be related to the Columbia supercontinent assembly, which took place on a global scale at *ca.* 2.1–1.8 (Zhao *et al.* 2004). Based on this, we interpret that the origin of the Carajás foreland Basin is directly related to the configuration of the Columbia supercontinent. Moreover, the convergent movements of the Bacajá Domain against to the Carajás protocontinent increased the continentalization of the Carajás foreland basin toward the end of Paleoproterozoic (Fig. 7.14).

With regard to paleogeography, the collision between these landmasses promoted the closure of the Azul Sea and the installation of a wide fluvial braided system, in which the Águas Claras Formation was deposited. This interpretation is supported by the observation that the Paleoproterozoic succession of the Carajás Basin is coarsening-upward and by the fact that the fluvial deposits of the Águas Claras Formation is thick and laterally extensive (Fig. 7.4). As previously suggested by Araújo Filho *et al.* (2020), these paleogeographic changes were a direct result of the tectonic changes at the end of the Paleoproterozoic, that promoted the uplifting of the Carajás protocontinent.

It is possible that the Carajás Basin was wider than its current limits (Nogueira *et al.* 1995). This assumption suggests that several others basins in the Carajás region (e.g.,

Buritirama basin, Andorinhas Basin, Serra Pelada syncline, etc.) are also segmented parts of the ancient and wider Carajás Basin. With regard to the magmatism that took place soon after to this putative collisional episode, some authors have suggested that the *ca*. 1.88 Ga A-type granitoids like the Carajás Granite are related to a post-collisional scenario (e.g., Machado *et al.* 1991). Additionally, others authors have suggested that the *ca*. 1.88 Ga mafic dike swarms are related to a supra-subduction or a post-collisional setting and were formed coevally with the Uatumã Silicic Large Igneous Province (SLIP) (Giovanardi *et al.* 2019). This magmatism could be derived from significant perturbations of the upper mantle during the partial assembly of Columbia supercontinent (Teixeira *et al.* 2019a).

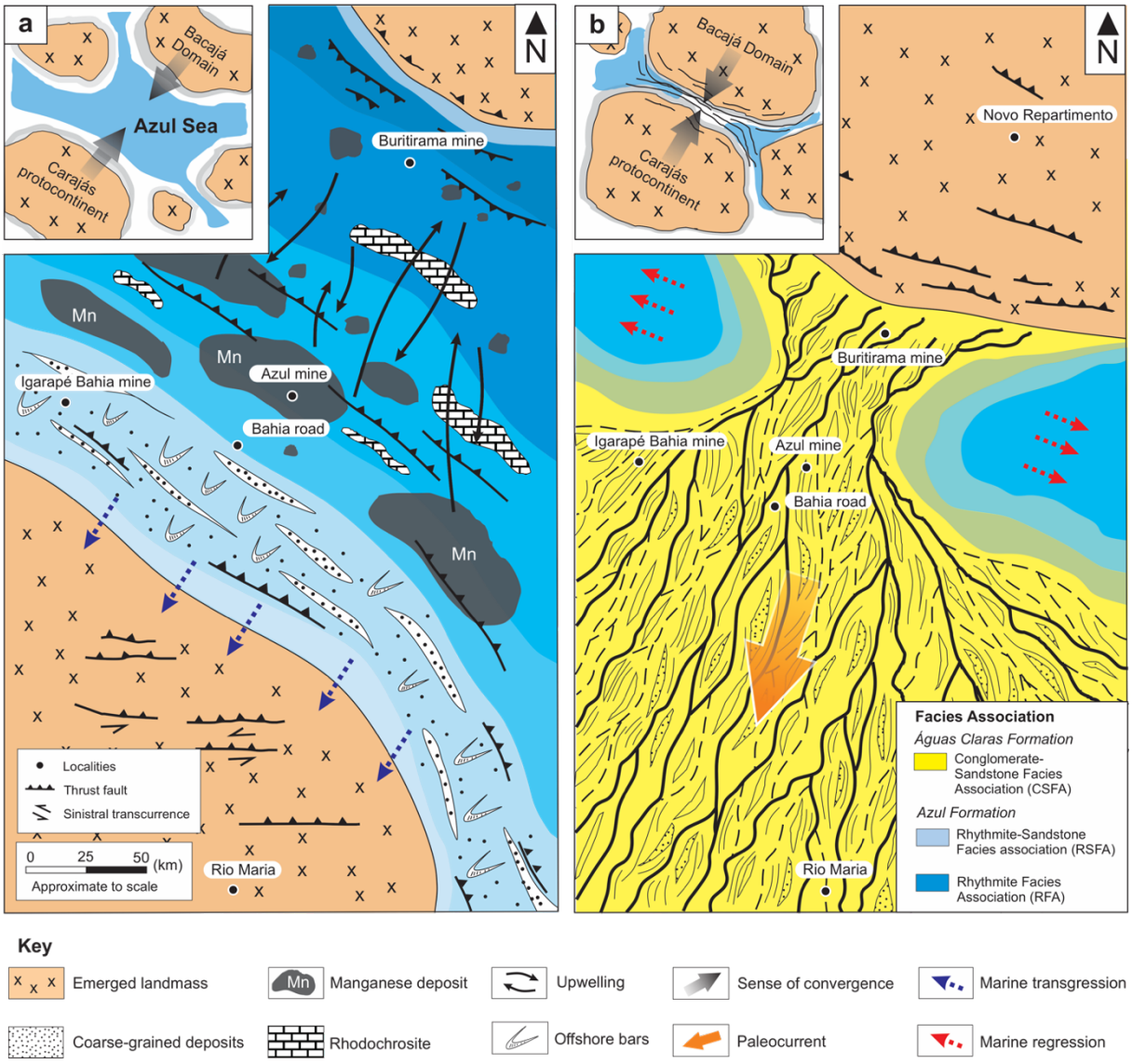

Figure 7.14: Paleogeographic reconstruction of the Carajás region (southeastern Amazonian Craton, Brazil) in two different evolutionary steps of the Carajás foreland basin evolution. (a) Paleogeographic scenario envisaged during the deposition of the Azul Formation, in which the Azul Sea bordered the

Carajás protocontinent during its the maximum transgression. (b) Paleogeographic scenario envisaged during the deposition of the Águas Claras Formation, in which the Águas Claras fluvial system covered a large area of the Carajás protocontinent and nearby areas.

7.7 CONCLUSIONS

- A large part (*ca.* 1500-m-thick) of the stratigraphic framework of the Paleoproterozoic succession of the Carajás Basin (southeastern Amazonian Craton, Brazil) is presented for the first time. The stratigraphy envisaged supports the previous suggestion that the Azul Formation was deposited in a shallow-marine setting after the Siderian–Rhyacian (2.58–2.06 Ga) Serra Sul glaciation and the Águas Claras formation was strictly deposited in fluvial braided system as a result of the uplift of the Carajás protocontinent;
- The geochronological results indicate that the Azul and Águas Claras formations were deposited after *ca*. 2.27 Ga, and were mainly supplied mainly by Meso- to Neoarchean source-rocks of the Rio Maria and the Carajás domains. The occurrence of Rhyacian to Siderian zircon grains in the Azul Formation was interpreted as the result of a partial connection between the Bacajá domain and the Carajás protocontinent during the Paleoproterozoic;
- Integrating the previous data on the regional geology and the results achieved herein, it is suggested that the Carajás Basin evolved as a foreland basin during the Paleoproterozoic. The Carajás foreland basin originated in a scenario of collision between the Bacajá Domain and the Carajás protocontinent during the *ca*. 2.2–2.0 Ga Transamazonian cycle. We suggest that these dramatic paleoenvironmental, paleogeographic, and tectonic changes are directly related to the emergence of the Columbia supercontinent during that period.

ACKNOWLEDGMENTS

The authors are very grateful to the Vale S.A. for making the drill cores available to study; the Geological Survey of Brazil for providing support through the Área de Relevante Interesse mineral de Carajás (ARIM-Carajás) project; the PROPESP/UFPA for providing financial support for the language proofreading service (Edital 01/2020–PAPQ); and the Conselho Nacional de Desenvolvimento Científico e Tecnológico (CNPq; grant 428287/2016-6) for laboratorial support. We would like to thank L.C. Costa, R.C Araújo Filho and A. Ribeiro for their support during fieldwork. We also extend our gratitude to M.L. Vasquez and M.R.C. Coelho for their support in preparing samples for the geochronological analysis and during the acquisition of cathodoluminescence images of zircon grains. This paper is a part of the PhD

thesis of the first author, who is grateful to the Post-graduate Program in Geology and Geochemistry (PPGG/UFPA).

APPENDIX A. Methodology applied in the sedimentological and stratigraphic investigation of drill cores

The drill cores investigated in this study are owned by mining company Vale S.A. and were available at their core sheds at Parauapebas (State of Pará, Brazil) during the four fieldwork stages at November 2015, April 2016, November 2017, and May 2018. In all these field stages, a thorough selection of the best cores for description was made within a set of cores available prior to the detailed analysis of each drill core. Priority was given to studying cores with greater depth, lithological diversity, and greater amount of lithological contacts, which could be used as stratigraphic surfaces. This methodology is the same as that used by Araújo & Nogueira (2019) and Araújo Filho *et al.* (2020).

The stratigraphic surfaces were interpreted based on either the abrupt and consistent changes of the stacking patterns or through the gradual change of lithofacies along the core. The surfaces were correlated by observing the repetition of the stacking patterns in a set of cores laterally spaced from each other. The cores were cleaned before each description with water, not with any cleaning chemicals. Although all cores were not cut in half, the description of those cut were prioritized in order to ensure the accurate visualization of the sedimentary structures and allow inferences on the geometry of the beds.

The description of the boxes with the cores followed the descriptions of the last (deeper) for the first box (shallower), in order to carry out the stratigraphic stacking and description more accurately as possible. Subsequently, each stratigraphic profile was individually digitized using CorelDRAW® Graphics Suite 2019. The logs were then correlated with each other to create a stratigraphic framework for the studied succession.

The cores located near the tectonic deformation and hydrothermal alteration zones, as well as those extensively cross-cut by dike swarms and veins, were avoided. In general, the tectonic overprint observed in the drill cores only included the tilting of beds, folding, and faulting. No evidence of metamorphism on a sample scale or in a thin section was seen. Closer to the surface, the holes had a mantle of weathering that reached up to 10 m in thickness. The samples collected for petrography was free from weathering or metamorphic/hydrothermal alterations.

APPENDIX B. Methodology applied in sample preparation for geochronology analysis

From the drill cores (n=5) and outcrops (n=1), approximately 5–10 Kg of rocks were sampled for the U-Pb zircon geochronological investigation. With the drill cores, priority was given to sampling 1/4 of the cores, so an interval of *ca*. 4–8 m thickness was required for adequate sampling. The samples were packed in resistant and hermetically sealed bags to avoid contamination. Individual zircon grains were separated at the Laboratório de Análises Minerais (Lamin-BE) at the Geological Survey of Brazil (Belém, Brazil), following the classical procedures for zircon mineral separation as described by Fedo *et al.* (2003).

Before the mineral separation began, the samples were washed with running water and were weighed to control material loss. Initially, the samples were crushed in a clean jaw crusher. Afterwards, the samples were grounded in a disk mill and sieved in fractions of 0.250–0.125 µm and <0.125 µm. The magnetic minerals were removed firstly by using a hand magnet, followed by the Frantz magnetic separator at different currents (0.5A, 1.0A and 1.5A). The heavy minerals were separated from the light ones using bromoform, an organic heavy liquid (d=2.89 g/cm³).

From the fraction of heavy minerals, zircon grains were handpicked regardless of size, color, or morphology under a binocular microscope. A total of 80–100 representative zircon grains were mounted in an epoxy resin and polished to approximately half their thickness using a 0.25 µm diamond paste. The mounts were coated in high vacuum with a 20-µm-thick gold coating. The cathodoluminescence images were obtained from individual zircon grains through the scanning electron microscope (SEM)–model LS15 of Zeiss at the LAMIN-BE (Belém, Brazil)–equipped with a detector operating at 15 kv, 20 µA, and 11 mm working distance. The preparation of the mounts to be analyzed using SHRIMP at the GeoLab-IGc-USP followed the procedures described by Sato *et al.* (2014).

APPENDIX C. Methodology applied in the LA-ICP-MS zircon U-Pb geochronology

The isotopic determinations at the Pará-Iso/UFPA were performed using a high resolution multi-collector Neptune Thermo Finnigan mass spectrometer coupled with a Nd:YAG LSX-213 G2 CETAC laser microprobe. The spots were positioned in such a way that metamitic areas, inclusions, fractures, and the borders of zircon grains were avoided. The ablation occurred at 10 µm, 20 µm, and 25 µm, according to the size of the zircon grain analyzed. The He (450–500 ml/min) and Ar (10 Hz) carrier gases delivered the sample aerosol to the plasma. The data were acquired in 50 cycles of 1.049 s with ablation time of 52 s. A standard-sample bracketing method was employed, following the acquisition sequence of 1 blank, 1 primary

reference zircon (GJ-1), 9 samples, and 1 secondary reference zircon (e.g., 91500, BB and Plešovice).

The laser-induced elemental fractionation and instrumental mass discrimination were corrected using the isotopic ratios of the homogeneous GJ-1 reference zircon (608.5 ± 1.5 Ma; Jackson *et al.* 2004). The 91500 (1065 ± 0.3 Ma; Wiedenbeck *et al.* 1995) and BB (562 ± 9 Ma; Santos *et al.* 2017) zircon crystals were used as secondary reference materials to test the method's reliability and reproducibility. The weighted mean $^{206}Pb/^{238}U$ ages obtained were 1069 ± 5 Ma (2σ, MSWD = 0.27, n=24) and 561 ± 13 Ma (2σ, MSWD = 0.006, n=3), respectively (see results in Table S-2). The values considered for the calculations of the isotopic ratios ($^{206}Pb/^{238}U$, $^{207}Pb/^{235}U$, and $^{207}Pb/^{206}Pb$) and consequently the ages, were those properly corrected from the backgrounds and the ^{204}Hg interference on the ^{204}Pb.

For the correction of the common lead, we used the terrestrial Pb evolution model over time proposed by Stacey & Kramers (1975). All the corrections and raw data reductions were done using an in-house Excel spreadsheet in order to calculate the corrected values of the isotopic ratios ($^{206}Pb/^{238}U$, $^{232}Th/^{238}U$, and $^{207}Pb/^{206}Pb$) and the uncertainties (1σ level in %). All the reported uncertainties (1σ) were calculated in the same way as described by Gerdes & Zeh (2006). The degree of concordance was calculated using the equation: ($^{206}Pb/^{238}U$ age * 100) / ($^{207}Pb/^{206}Pb$ age); according to Horstwood *et al.* (2016). The analytical method for isotope dating with LA-ICP-MS at the Pará-Iso/UFPA laboratory is similar to that reported by Milhomem Neto & Lafon (2019).

The isotopic determinations at the Laboratório de Geoquímica Isotópica of the DEGEO/UFOP (Ouro Preto, Brazil) were performed on the LA-MC-ICP-MS Neptune (Thermo-Finnigan) coupled with the ArF Excimer Laser (λ=193 nm) (Photon Machines). The ablation occurred at 20 μm spots, with a frequency of 6 Hz and fluency of 10%. The pulverized material was carried by a flow of He (0.1 L/min), Ar (0.5 L/ min), and N (0.09 L/min). The GJ-1 reference zircon was used for the correction of the bias of the equipment, as well as the fractionation between the U and Pb isotopes. To check the accuracy, analyses were performed using the Plešovice zircon (337 ± 0.4 Ma; Sláma *et al.* 2008) as a secondary reference material.

The data were acquired in 460 cycles of 0.1 second each, following the acquisition sequence of 3 analyses of GJ-1, 2 analyses of Plešovice and 15 analyses of samples. In each reading, the intensities of the masses were ^{202}Hg, $^{204}(Pb + Hg)$, ^{206}Pb, ^{207}Pb, ^{208}Pb, and ^{238}U, respectively. The uncertainties were given at the 2σ level. The spot was preferentially positioned at preserved areas of the zircon grains, away from the cracked zones and dark and metamitic areas. The reduction of the raw data included corrections for the background, derived

from both the equipment and common lead using the Excel spreadsheet created by Gerdes & Zeh (2006). The analytical method for isotope dating with LA-ICP-MS at the UFOP laboratory is similar to that reported by Farina et al. (2015) & Moreira et al. (2016).

APPENDIX D. Methodology applied in the SHRIMP zircon U-Pb geochronology

The dating of three samples by U-Pb zircon using a SHRIMP IIe system installed at the Laboratory of High Resolution Geochronology, University of São Paulo, Brazil (GeoLab-IGc-USP), followed the instrumental performance and the analytical procedures documented by Sato *et al.* (2014). The standards used were SL 13 (238 ppm) for the U composition reference (Sato *et al.* 2014) and for the isotope ratios standard. The concentrations in the U-Th-Pb were calibrated relative to the certified contents of the material of reference TEMORA 2 zircon (416.78 ± 0.33 Ma; Black *et al.* 2003), where the laser's spot was fixed at 30 µm. The data were reduced with SQUID 1.6 software (Ludwig 2009). The Concordia plots were constructed and the $^{207}Pb/^{206}Pb$ ages were calculated using Isoplot/Ex v. 4.15 software package by Ludwig (2003). According to Stacey & Kramer (1975), common lead corrections usually use ^{204}Pb, but the SQUID software only had options to use ^{207}Pb and ^{208}Pb corrections. Analytical uncertainties were shown in 1σ error for each analysis.

REFERENCES

Amy, L.A., Peakall, J., Talling, P.J., 2005. Density-and viscosity-stratified gravity currents: Insight from laboratory experiments and implications for submarine flow deposits. Sedimentary Geology, (179), pp. 5-29.

Araújo Filho, R.C., Nogueira, A.C., Araújo, R N., 2020. New stratigraphic proposal of a Paleoproterozoic siliciclastic succession: Implications for the evolution of the Carajás Basin, Amazonian craton, Brazil. J. S. Am. Earth Sci., (102), 102665.

Araújo, O.J.B, Maia, R.G.N, João, X.S.J., Costa, J.B.S., 1988. A megaestruturação arqueana da Folha da Serra dos Carajás. In: Congresso Latino Americano de Geologia, vol. 7. Anais do 35° Simpósio Brasileiro de Geologia. SBG, Belém, pp. 324–338 (in Portuguese).

Araújo, O.J.B, Maia, R.G.N., 1991. Projeto especial mapas de recursos minerais, de solos e de vegetação para a área do Programa Grande Carajás; Subprojeto Recursos Minerais; Folha SB. 22-Z-A: Serra dos Carajás – Estado do Pará, 164, p. 164 (in Portuguese).

Araújo, R.N, Nogueira, A.C.R, 2019. Serra Sul diamictite of the Carajás Basin (Brazil): A Paleoproterozoic glaciation on the Amazonian craton. Geology 12 (47), pp. 1166–1170.

Bekker, A., Holland, H.D., Wang, P.L., Rumble, III D., Stein, H.J., Hannah, J.L., Coetzee, L.L., Beukes, N.J., 2004. Dating the rise of atmospheric oxygen. Nature (427), pp. 117–120.

Black, L.P., Kamo, S.L., Williams, I.S., Mundil, R., Davis, D.W., Korsch, R.J., Foudoulis, C., 2003. The application of SHRIMP to Phanerozoic geochronology: a critical application of four zircon standards. Chem. Geol., 200, pp. 171-188.

Bouma, A.H., 1962. Sedimentology of some flysch deposits: a graphic approach to facies interpretation. Amsterdam, Elsevier, 168 p.

Cabral, A.R., Creaser, R. A., Nägler, T., Lehmann, B., Voegelin, A. R., Belyatsky, Belyatsky, B., Pašava, J., Seabra Gomes Jr, A.A., Galbiatti, H., Böttcher, M.E., Escher, P., 2013. Trace-element and multi-isotope geochemistry of Late-Archean black shales in the Carajás iron-ore district, Brazil. Chemical Geology 362, pp. 91–104.

Catuneanu, O. Retroarc foreland systems—evolution through time, 2004. Journal of African Earth Sciences (38), pp. 225–242.

Cheel, R.J., Leckie, D.A., 1993. Hummocky Cross-Stratification: Sedimentology Review. Oxford, U.K., Blackwell Scientific Publications, pp. 103–122.

Cohen, K.M., Finney, S.C., Gibbard, P.L., Fan, J.-X., 2013 (updated). The ICS International Chronostratigraphic Chart. Episodes (36), pp. 199–204.

Cordani, U.G., Tassinari, C.C.G., Kawashita, K.A., 1984. A Serra dos Carajás como região limítrofe entre províncias tectônicas. Ciências da Terra (9), pp. 6–11 (in Portuguese).

Coutts, D.S., Matthews, W.A., Hubbard, S.M. 2019. Assessment of widely used methods to derive depositional ages from detrital zircon populations. Geoscience Frontiers (10), pp. 1421-1435.

Dardenne, M.A., Ferreira Filho, C.F., Meirelles, M.R., 1988. The role of shoshonitic and calc-alkaline suites in the tectonic evolution of the Carajás District, Brazil. J. S. Am. Earth Sci. (1), pp. 363–372.

Dasgupta, S., Roy, S., Fukuoka, M., 1992. Depositional Models for manganese oxide and carbonate deposits of the Precambrian Sausar Group, India. Economic Geology (87), pp. 1412–1418.

Docegeo, 1988. Revisão litoestratigráfica da Província Mineral de Carajás. In: Congresso Brasileiro de Geologia, 35, Belém, SBG. Província Mineral de Carajás - Litoestratigrafia e principais depósitos minerais, Belém. Anexo aos Anais. 165 pp (in Portuguese).

Dumas, S., Arnott, R.W.C., 2006. Origin of hummocky and swaley cross-stratification—The controlling influence of unidirectional current strength and aggradation rate. Geology (34), pp. 1073–1076.

Embry, A. F. 2002. Transgressive-regressive (TR) Sequence Stratigraphy. In: Armentrout, J.M., Rosen, N.C (Eds.). Sequence Stratigraphic Models for Exploration and Production: Evolving Methodology, Emerging Models and Application Histories (52), pp. 151–172.

Farina, F., Albert, C., Lana, C., 2015. The Neoarchean transition between medium-and high-K granitoids: clues from the Southern São Francisco Craton (Brazil). Precambrian Res., (266), pp. 375-394.

Fedo C.M., Sircombe K., Rainbird R., 2003. Detrital zircon analysis of the sedimentary record. In: Hanchar, J.M., Hoskin, P.W.O. (Eds.). Zircon: Reviews in Mineralogy and geochemistry (53), pp. 277-303.

Feio, G.R.L., Dall'Agnol, R., Dantas, E.L., Macambira, M.J.B., Santos, J.O.S., Althoff, F.J., Soares, J.E.B., 2013. Archean granitoid magmatism in the Canaã dos Carajás area: implications for crustal evolution of the Carajás province, Amazonian craton, Brazil. Precambrian Res. (227), pp. 157–185.

Force, E.R., Cannon, W.F. 1988. Depositional Model for Shallow-Marine Manganese Deposits around Black Shale Basins. Economic Geology (83), pp. 93–117.

Galarza, M.A., Macambira, M.J.B., Villas, R.N.N., 2008. Dating and isotopic characteristics (Pb and S) of the Fe oxide-Cu-Au-U-REE Igarapé Bahia ore deposit, Carajás mineral province, Pará state, Brazil. Journal of South American Earth Sciences (25), pp. 377–397.

Gerdes, A., Zeh, A., 2006. Combined U–Pb and Hf isotope LA-(MC-) ICP-MS analyses of detrital zircons: comparison with SHRIMP and new constraints for the provenance and age of an Armorican metasediment in Central Germany. Earth and Planetary Science Letters (249), pp. 47-61.

Giovanardi, T., Girardi, V.A., Teixeira, W., Mazzucchelli, M., 2019. Mafic dyke swarms at 1882, 535 and 200 Ma in the Carajás region, Amazonian Craton: Sr-Nd isotopy, trace

element geochemistry and inferences on their origin and geological settings. Journal of South American Earth Sciences (92), pp. 197–208.

Gumsley, A. P., Chamberlain, K. R., Bleeker, W., Söderlund, U., de Kock, M. O., Larsson, E. R., Bekker, A., 2017. Timing and tempo of the Great Oxidation Event. Proc. Natl. Acad. Sci. USA (114), pp. 1811–1816.

Hjellbakk, A., 1997. Facies and fluvial architecture of a high-energy braided river: the upper Proterozoic Seglodden Member, Varanger peninsula, Northern Norway. Sedimentary Geology (114), pp. 131–161.

Holdsworth, R.E., Pinheiro, R.V.L., 2000. The anatomy of shallow-crustal transpressional structures: insights from the Archaean Carajás fault zone, Amazon, Brazil. Journal of Structural Geology 22, pp. 1105–1023.

Holland, H.D., 2002. Volcanic gases, black smokers, and the Great Oxidation Event. Geochimica et Cosmochimica Acta, 66 (21), pp. 3811–3826.

Horstwood, M.S.A., Košler, J., Gehrels, G., Jackson, S.E., McLean, N.M., Paton, C., Pearson, N.J., Sircombe, K., Sylvester, P., Vermeesch, P., Bowring, J.F., Condon, D.J., Schoene, B., 2016. Community-derived standards for LA-ICP-MS U-Th-Pb geochronology – uncertainty propagation, age interpretation and data reporting. Geostandards and Geoanalytical Research, 40 (3), pp. 311-332.

Jackson, S.E., Pearson, N.J., Griffin, W.L., Belousova, E.A., 2004. The application of laser ablation-inductively coupled plasma-mass spectrometry to in situ U–Pb zircon geochronology. Chemical geology (211), pp. 47-69.

Justo, A.P., Dantas, E.L., Freitas-Silva, F.H., Rodrigues, J.B., 2018. Detrital zircon populations in the Neoarchean to Paleoproterozoic sedimentary coverage of Carajás, Amazon Cráton, Brazil. Congresso Brasileiro de Geologia, 49, Rio de Janeiro, SBG (in Portuguese).

Le Heron, D. P., Cox, G., Trundley, A., Collins, A., 2011. Sea ice−free conditions during the Sturtian glaciation (early Cryogenian), South Australia. Geology (39), pp. 31-34.

Le Heron, D.P., 2015. The significance of ice-rafted debris in Sturtian glacial successions,

Sedimentary Geology, (322), pp. 19-33.

Ludwig, K., 2009. SQUID 2: A user's manual: Berkeley Geochronology Center Special Publication 5, 110 pp.

Ludwig, K.R., 2003. Isoplot 3.00: A geochronological toolkit for Microsoft Excel. Berkeley Geochronology Center Special Publication 4, 70 pp.

Ludwig, K.R., 2008. User's Manual for Isoplot 3.6: a Geochronological Toolkit for Microsoft Excel. Berkeley Geochronology Center Special Publication, Berkeley.

Macambira, M.J.B, Vasquez, M.L., Silva, D.C.C., Galarza, M.A., Barros, C.E.M., Camelo, J.F., 2009. Crustal growth of the central-eastern Paleoproterozoic domain, SE Amazonian craton: Juvenile accretion vs. reworking. Journal of South American Earth Sciences (27), pp. 235–246.

Machado, N., Lindenmayer, Z., Krogh, T. E., Lindenmayer, D., 1991. U-Pb geochronology of Archaean magmatism and basement reactivation in the Carajás area, Amazon shield, Brazil. Precambrian Research (49), pp. 329–354.

Marangoanha, B., Oliveira, D.C., Dall'Agnol, R., 2019. The Archean granulite-enderbite complex of the northern Carajás province, Amazonian craton (Brazil): Origin and implications for crustal growth and cratonization. Lithos (350-351), 105275.

Martins, P.L.G., Toledo, C.L.B., Silva, A.M., Chemale Jr, F., Santos, J.O.S., Assis, L.M., 2017. Neoarchean magmatism in the southeastern Amazonian Craton, Brazil: Petrography, geochemistry and tectonic significance of basalts from the Carajás Basin. Precambrian Research (302), pp. 340–357.

McPhie, J., Doyle, M., Allen, R., 1993. Volcanic Textures: a guide to the interpretation of textures in volcanic rocks. Tasmania, University of Tasmania, 197 p.

Meirelles, M.R., Dardenne, M.A., 1991. Vulcanismo basáltico de afinidade shoshonítica e ambiente de arco arqueano, Grupo Grão-Pará, Serra dos Carajás, Pará. Revista Brasileira de Geociências (21), pp. 41–50 (in Portuguese).

Miall, A.D., 1977. A review of the braided-river depositional environment. Earth Science Reviews (13), pp. 1–62.

Milhomem Neto, J.M., Lafon, J.M., 2019. Zircon U-Pb and Lu-Hf isotope constraints on Archean crustal evolution in Southeastern Guyana Shield. Geoscience Frontiers (10), pp. 1477–1506.

Moreira, H., Lana, C., Nalini, H.A., 2016. The detrital zircon record of an Archaean convergent basin in the Southern São Francisco Craton, Brazil. Precambrian Res. (275), pp. 84-99.

Mougeot, R., Respaut, J.P., Briqueu, L., Ledru, P., Milesi, J.P., Lerouge, C., Marcoux, E., Huhn, S.B., Macambira, M.J.B., 1996a. Isotope geochemistry constraints for Cu, Au mineralization and evolution of the Carajás 763 province (Pará, Brazil). In: Congresso Brasileiro de Geologia, 39, Salvador, SBG. 7:321–324.

Mougeot, R., Respaut, J.P., Briqueu, L., Ledru, P., Milesi, J.P., Macambira, M.J., Huhn, S.B., 1996b. Geochronological constraints for the age of the Águas Claras Formation (Carajás Province, Pará, Brazil). In: Congresso Brasileiro de Geologia, 39, Salvador, SBG. 6:579–581.

Nascimento, M.S., Oliveira, D.A., 2015. Ambiente deposicional e proveniência da Formação Gorotire, Província Carajás, sudeste do Cráton Amazônico. In: Gorayeb P., Meiguins A. (Eds.). Contribuições à Geologia da Amazônia, 9, Belém, SBG-Norte (in Portuguese).

Nogueira, A.C.R., 1995. Análise faciológica e aspectos estruturais da Formação Águas Claras, Região Central da Serra dos Carajás-Pará. MS Dissertation, Instituto de Geociências, Universidade Federal do Pará, Belém, 168 p.

Nogueira, A.C.R., Truckenbrodt, W., Pinheiro, R.V.L., 1995. Formação Águas Claras, Pré-Cambriano da Serra dos Carajás, redescrição e redefinição litoestratigráfica. Boletim do Museu Paraense Emílio Goeldi, Série Ciências da Terra 7, pp. 177–197 (in Portuguese).

Olszewski, W.J., Wirth, K.R., Gibbs, A.K., Gaudette, H.E., 1989. The age, origin, and tectonics of the Grão Pará Group and associated rocks, Serra dos Carajás, Brazil: Archean continental volcanism and rifting. Precambrian Res. (42), pp. 229–254.

Orton, G.J., 1996. Volcanic environments. In: Reading, H.G. (Ed.). Sedimentary Environments: Processes, Facies and Stratigraphy. Third ed. Blackwell, Oxford, pp. 485–567.

Pereira, R.M.P., Rosiere, C.A., Santos, J.O.S., Lobato, L.M., Silva, R.C.F., McNaughton, N.J., 2009. Unidade Caninana: sequência clástica Paleoproterozoica revelada por datação U-Pb em zircões detríticos da Província Mineral Carajás. Simpósio de Geologia da Amazônia, 11, SBG (in Portuguese).

Pinheiro, R.V.L., Holdsworth, R.E., 1997. The structure of the Carajás N-4 ironstone deposit and associated rocks: relationship to Archaean strike-slip tectonics and basement reactivation in the Amazon region, Brazil. Journal of South American Earth Sciences (10), pp. 305–319.

Rasmussen, B., Bekker, A., Fletcher, I.R., 2013. Correlation of Paleoproterozoic glaciations based on U-Pb zircon ages for tuff beds in the Transvaal and Huronian Supergroups. Earth Planet. Sci. Lett. (382), pp. 173–180.

Rogers, J.W., Santosh, M., 2002. Configuration of Columbia, a Mesoproterozoic Supercontinent. Gondwana Research (5), pp. 5-22.

Roy, S., 1997. Genetic diversity of manganese deposition in the terrestrial geological record. In: Nicholson, K., Hein, J.R., Buhn, B., Dasgupta, S. (Eds). Manganese Mineralization: Geochemistry and Mineralogy of Terrestrial and Marine Deposits, Geological Society Special Publication (199), pp. 5–27.

Roy, S., 2006. Sedimentary manganese metallogenesis in response to the Evolution of the Earth system. Earth-Science Reviews (77), pp. 273-305.

Santos, M.M., Lana, C., Scholz, R., Buick, I., Schmitz, M.D., Kamo, S.L., Gerdes, A., Corfu, F., Tapster, S., Lancaster, P., Storey, C.D., Basei, M.A.S., Tohver, E., Alkmim, A., Nalini, H., Krambrock, K., Fantini, C., Wiedenbeck, M., 2017. A new appraisal of Sri Lankan BB zircon as a reference material for LA-ICP-MS U-Pb geochronology and Lu-Hf isotope tracing. Geostand. Geoanal. Res. 41(3), pp. 335-358.

Sato, K., Tassinari, C.C.G., Basei, M.A.S., Siga Júnior, O., Onoe, A.T., Souza, M.D., 2014. Sensitive High Resolution Ion Microprobe (SHRIMP IIe/MC) of the Institute of Geosciences of the University of São Paulo, Brazil: analytical method and first results. Geologia USP, Série Científica, 14 (3), pp. 3-18.

Sláma, J., Košler, J., Condon, D.J., Crowley, J.L., Gerdes, A., Hanchar, J.M., Horstwood, M.S.A., Morris, G.A., Nasdala, L., Norberg, N., Schaltegger, U., Schoene, B., Tubrett, M.N., Whitehouse, M.J., 2008. Plešovice zircon – a new natural reference material for U-Pb and Hf isotopic microanalysis. Chem. Geol. (249), pp. 1-35.

Spencer, C.J., Kirkland, C.L., Taylor, R.J.M., 2016. Strategies towards statistically robust interpretations of in situ U-Pb zircon geochronology. Geoscience Frontiers 7 (37), pp. 581–589.

Stacey, J.S., Kramers, J.D., 1975. Approximation of terrestrial lead isotope evolution by a two-stage model. Earth and Planetary Science Letters, (26), pp. 207-221.

Tallarico, F.H.B., Figueiredo, B.R., Groves, D.I., Kositcin, N., McNaughton, N.J., Fletcher, I.R., Rego, J.L., 2005. Geology and SHRIMP U-Pb geochronology of the Igarapé Bahia

deposit, Carajás copper-gold belt, Brazil: an Archean (2.57 Ga) example of iron-oxide Cu-Au-(U-REE) mineralization. Economic Geology (100), pp. 7–28.

Tang, H., Chen, Y., 2013. Global glaciations and atmospheric change at ca. 2.3 Ga. Geoscience Frontiers (4), pp. 583–596.

Tavares, F.M., Trouw, R.A.J., da Silva, C.M.G., Justo, A.P., Oliveira, J.K.M., 2018. The multistage tectonic evolution of the northeastern Carajás Province, Amazonian Craton, Brazil: Revealing complex structural patterns. Journal of South American Earth Sciences (88), pp. 238–252.

Teixeira, W., Hamilton, M.A., Girardi, V.A.V., Faleiros, F.M., Ernst, R.E., 2019a. U-Pb baddeleyite ages of key dyke swarms in the Amazonian Craton (Carajás/Rio Maria and Rio Apa areas): Tectonic implications for events at 1880, 1110 Ma, 535 Ma and 200 Ma. Precambrian Research (329), pp. 138–155.

Teixeira, M.F.B, Dall'Agnol, R., Santos, J.O.S, Kemp, A., Noreen Evans, N., 2019b. Petrogenesis of the Paleoproterozoic (Orosirian) A-type granites of Carajás Province, Amazon Craton, Brazil: Combined in situ Hf—O isotopes of zircon. Lithos (332–333), pp. 1–22.

Trendall, A.F., Basei, M.A.S., De Laeter, J.R., Nelson, D.R., 1998. SHRIMP U-Pb constraints on the age of the Carajás Formation, Grão Pará Group, Amazon Craton. Journal of South American Earth Sciences (11), pp. 265–277.

Vasquez, M.L., Rosa-Costa, L.T., Silva, C.G., Ricci, P.F., Barbosa, J.O., Klein, E.L., Lopes, E.S., Macambira, E.B., Chaves, C.L., Carvalho, J.M., Oliveira, J.G., Anjos, G.C., Silva, H.R., 2008a. Geologia e Recursos Minerais do Estado do Pará: Sistema de Informações Geográficas-SIG: Texto Explicativo dos Mapas Geológico e Tectônico e de Recursos Minerais do Estado do Pará. Escala 1:1.000.000. In: Vasquez M.L., Rosa-Costa L.T. (Eds.). Belém, Geological Survey of Brazil - CPRM, 329 pp (in Portuguese).

Vasquez, M.L., Sousa, C.S., Carvalho, J.M.A., 2008b. Mapa Geológico e de Recursos Minerais do Estado do Pará. Escala 1:1.000.000. Geological Survey of Brazil – CPRM (in Portuguese).

Wendt, L., Carl, 1991. The statistical distribution of the mean square weighted deviation. Chemical Geology Isotope Geoscience Section (86), pp. 275–285.

Wiedenbeck, M., Allé, P., Corfu F., Griffin, W.L., Meier, M., Oberli, F., Von Quadt, A., Roddick, J.C., Spiegel, W., 1995. Three natural zircon standards for U–Th–Pb, Lu–Hf, trace element and REE analyses. Geostandards Newsletter (19), pp. 1-23.

Young, G.M., 2014. Contradictory correlations of Paleoproterozoic glacial deposits: Local, regional or global controls? Precambrian Research (247), pp. 33–44.

Zhao, G., Sun, M., Wilde, S.A., Li, S., 2004. A Paleo-Mesoproterozoic supercontinent: assembly, growth and breakup. Earth-Science Reviews (67), pp. 91–123.

8 CONSIDERAÇÕES FINAIS

Com base nos resultados obtidos é possível elaborar um sumário estratigráfico e de eventos reconhecidos para a Bacia de Carajás na transição Neoarqueano-Paleoproterozoico (Figura 8.1). É provável que a Bacia de Carajás tenha sua origem ligada a um sistema rifte em cerca de 2,75 Ga, instalado durante um estágio pós-colisional relacionado a colisão entre os domínios Rio Maria e Carajás ocorrido na passagem entre o Mesoarqueano e o Neoarqueano (Trendall *et al*. 1998, Martins *et al.* 2017). A bacia foi preenchida inicialmente por uma espessa sucessão de rochas vulcânicas, associado ao vulcanismo Parauapebas, seguido de ampla deposição de formação ferrífera bandada atribuídos à Formação Carajás ainda no Neoarqueano. Esses depósitos da base da Bacia de Carajás devem ser necessariamente desassociados daqueles depósitos associados aos *greenstone belt* e TGG (tonalito-trondhjemito-granodiorito) que caracterizam as unidades do Mesoarqueano, e são melhor representados na região de Rio Maria. Essa sedimentação vulcânica e química que caracteriza o Neoarqueano da Bacia de Carajás foi substituída por uma sedimentação predominantemente siliciclástica durante o Paleoproterozoico, no qual uma sucessão com mais de 1500 m de espessura foi depositada. O reconhecimento de estratos de diamictito de origem glacial, imediatamente acima dos depósitos de rochas vulcânicas e de formação ferrífera bandada do Neoarqueano por Araújo & Nogueira (2019) levou a descoberta de um evento glacial importante no início do Paleoproterozoico, reconhecido pela primeira vez no Cráton Amazônico, denominado de glaciação Serra Sul.

O diamictito Serra Sul representa o primeiro registro de depósitos glaciais do Paleoproterozoico na América do Sul e podem ser correlatos ou não aos eventos glaciais de mesma idade amplamente reconhecidos ao redor do mundo associados ao HGE. A Formação Serra Sul foi depositada em um sistema subglacial costeiro a um sistema de leque submarino nos quais é possível o amplo reconhecimento de evidências de glaciotectônica, como foliação glacial, e *ice-rafting*, como estruturas do tipo *dropstone* e *dumpstone*. O empilhamento estratigráfico sugere fortemente que os depósitos Serra Sul são recobertos em conformidade por uma sucessão dominantemente pelítica depositada em um sistema marinho raso (*offshore* e *offshore transition/shoreface*) no qual depósitos enriquecidos com manganês foram amplamente depositados em uma bacia marinha estratificada. Esses depósitos marinhos haviam sido atribuídos ao membro basal da Formação Águas Claras por Nogueira *et al*. (1995). Araújo Filho *et al.* (2020) em uma revisão litoestratigráfica denominou esses depósitos marinhos basais de Formação Azul, e redefiniu a Formação Águas Claras para designar somente os estratos de arenito e conglomerado de origem fluvial que ocorrem em discordância sobre os depósitos

pelíticos da Formação Azul. De acordo com Araújo *et al*. (em preparação), os depósitos de manganês ocorrem hospedados em depósitos de *red bed* dessa unidade. Os estratos enriquecidos primariamente compreendem dominantemente estratos de *black shale*, nos quais rodocrosita foi originada durante diagênese.

Durante a deformação tectônica desses depósitos, os intervalos enriquecidos com rodocrosita funcionaram como fontes para a geração de óxidos de manganês em condições hidrotermais. Esses óxidos foram remobilizados através de falhas, como os sistema da Falha Carajás, para zonas de baixa tensão dentro da rocha encaixante (camadas de *red bed* da Formação Azul), em um processo análogo a migração de hidrocarbonetos. Por sua vez, a Formação Gorotire provavelmente representa os últimos estágios de sedimentação da Bacia de Carajás. Essa formação foi depositada logo após, ou sincronicamente a deposição da Formação Águas Claras em torno de 2,01 Ga. A sucessão siliciclástica que preenche a Bacia de Carajás apresenta um padrão granocrescente ascendente. O empilhamento estratigráfico desses depósitos sugere continentalização dessa bacia em topo da sua sucessão. Nesse contexto, a Formação Azul representa o último evento transgressivo da bacia, como resultado do aumento do nível do mar durante a fase de deglaciação ocorrida logo após a glaciação Serra Sul. A transgressão do mar Azul para dentro do protocontinente Carajás foi seguida de uma regressão abrupta e consequente instalação de um amplo e bem desenvolvido sistema fluvial/aluvial, no qual foram depositadas as formações Águas Claras e Gorotire. Araújo Filho *et al.* (2020) interpretaram as formações Azul e Águas Claras como os representantes estratigráficos de uma sequencia transgressiva-regressiva (T-R), limitados por uma zona de inundação máxima. Adicionalmente, Araújo *et al.* (submetido), interpretou que parte do topo da Formação Serra Sul integra o trato de sistemas transgressivo (TST) juntamente com a Formação Azul e é separado na base por outro trato de sistemas regressivo (TSR) representado pelos depósitos basais (conglomerados glaciogênicos e arenitos) de leque submarino da Formação Serra Sul.

Os resultados da datação U-Pb em zircão detrítico (LA-ICP-MS e SHRIMP) revelaram que as formações Azul e Águas Claras foram supridas majoritariamente por rochas do Neo e Mesoarqueano, enquanto que rochas do Paleoarqueano e Paleoproterozoico funcionaram como fontes subordinadas de sedimentos. Nenhuma rocha do Paleoarqueano foi mapeada na região de Carajás, o que corrobora a hipótese de que fragmentos crustais dessa idade foram retrabalhados durante os ciclos orogenéticos do Meso e Paleoproterozoico. A ocorrência de grãos de zircão do Sideriano e Riaciano em amostra de ritmito da Formação Azul é sugestiva (embora não necessariamente) de uma conexão, pelo menos parcial, entre os domínios Carajás e Bacajá durante o Paleoproterozoico. Essa interpretação é corroborada pela observação de que

rochas do Sideriano e Riaciano até o momento não foram mapeadas ou ocorrem subordinadamente na região dos domínios Carajás e Rio Maria, ao passo que rochas desses períodos ocorrem amplamente distribuídas no Domínio Bacajá. Crucialmente, essa provável conexão entre esses domínios fortalece a hipótese de que a Bacia de Carajás evoluiu em grande parte do Paleoproterozoico como uma bacia do tipo *foreland*. É provável que a Bacia *foreland* de Carajás tenha se formado como resultado da colisão entre os domínios Carajás e Bacajá durante o ciclo orogenético Transamazônico (2,2–2,0 Ga).

Em um primeiro estágio, a colisão entre esses dois blocos promoveu o soerguimento do protocontinente Carajás; fechamento do mar Azul e instalação do sistema fluvial Águas Claras. A continuidade na evolução do cenário colisional ocasionou a inversão, deformação e segmentação da Bacia de Carajás muito mais ampla do que seus atuais limites geográficos. Em termos paleogeográficos, a colisão entre esses dois domínios levou a uma mudança abrupta na paisagem, anteriormente dominada por um mar raso (epírico?) que deu lugar a um cenário dominado por uma planície fluvial *braided* que cobria grande parte do protocontinente. Com base no arcabouço estratigráfico construído foi proposto que a bacia foreland de Carajás evoluiu em três estágios distintos, nos quais diferentes depósitos preencheram essa bacia: i) *Underfilled stage*: deposição dos estratos de origem glacial e de leque submarino (sistema marinho profundo) da Formação Serra Sul; ii) *Filled stage*: deposição de estratos de ritmito, localmente enriquecidos em manganês da Formação Azul (sistema marinho raso); iii) *Overfilled stage*: deposição dos estratos fluviais a aluviais da Formação Águas Claras e Formação Gorotire (sistema fluvial bem desenvolvido). Importantemente, estes estágios evolutivos são comumente observados em bacias do tipo *foreland* (Catuneanu 2004).

Finalmente, é sugerido que essas mudanças paleoambientais, paleoclimáticas, tectônicas e paleogeográficas precederam e estiveram diretamente relacionadas a formação do supercontinente Columbia no final do Paleoproterozoico. A colisão dos blocos Carajás e Bacajá durante o ciclo orogenético Transamazônico é interpretada como parte dos ciclos orogenéticos ligados a configuração do supercontinente Columbia. Inequivocamente, a caracterização desses importantes eventos na Bacia de Carajás insere o Cráton Amazônico dentro de um contexto global de modificações paleoambientais e paleoclimáticas ocorridos na transição Neoarqueano-Paleoproterozoico. Esses eventos ocorrem excelentemente preservados nas rochas dessa bacia e são registros importantíssimos das modificações dramáticas ocorridas nesse período. Trabalhos futuros devem melhorar o grau de conhecimento a respeito desses depósitos, e estabelecer correlações precisas entre os eventos registrados na Bacia de Carajás com aqueles bem reconhecidos e estudados em outros crátons ao redor do mundo.

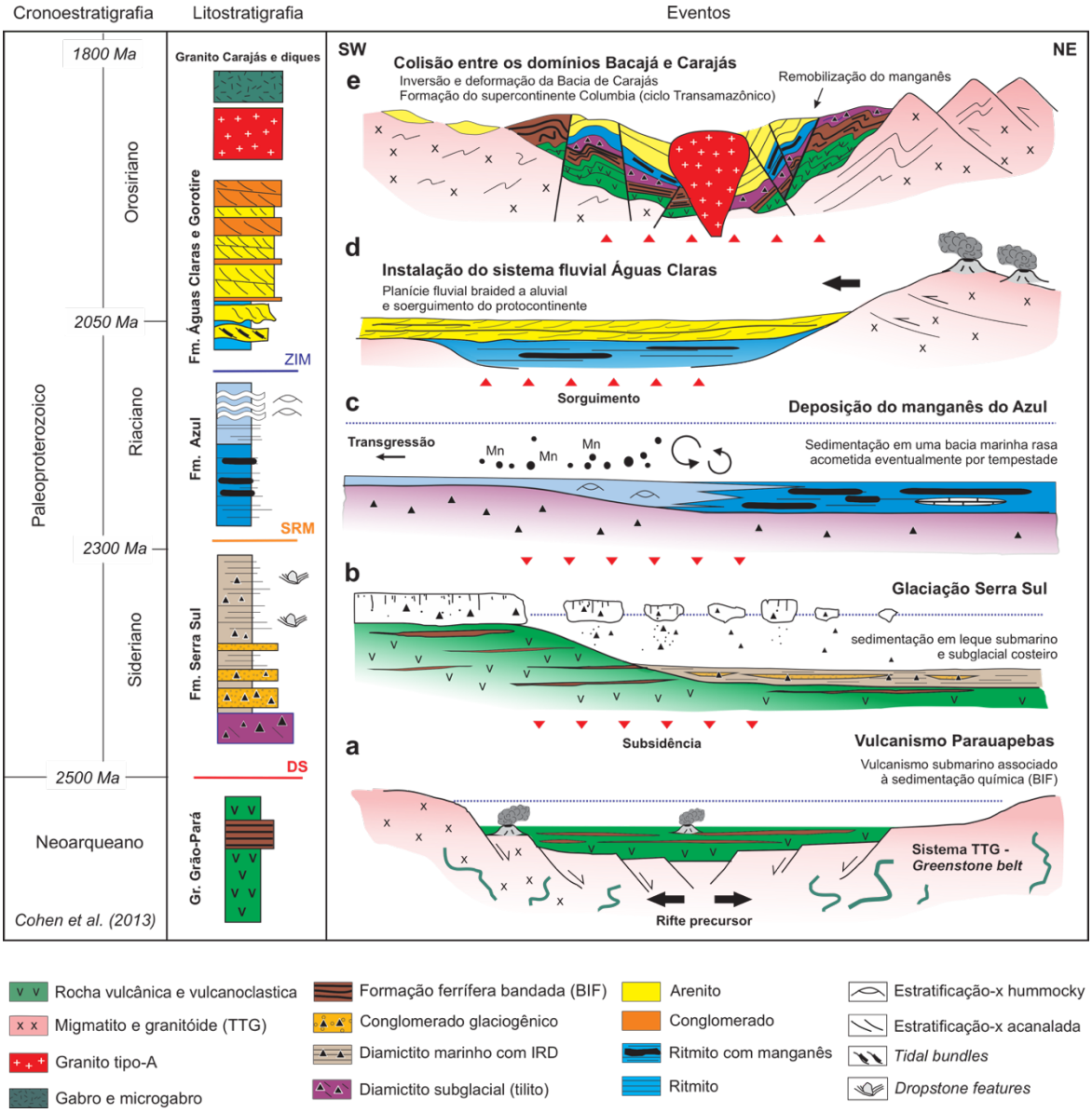

Figura 8.1: Sumário estratigráfico e de eventos reconhecidos na Bacia de Carajás a partir dos resultados obtidos nesta tese, ocorridos na transição Neoarqueano-Paleoproterozoico. (a) Neoarqueano: deposição das dos espessas derrames de rochas vulcânicas associados ao vulcanismo Parauapebas em *ca.* 2,75 Ga. Camadas de BIF foram depositadas imediatamente acima dos estratos vulcânicos. (b) Sideriano–Riaciano: deposição de diamictito glacial, e depósitos de leque submarino associados a glaciação Serra Sul. (c) Riaciano: deposição da Formação Azul durante a fase transgressiva do mar Azul em direção ao protocontinente Carajás após *ca.* 2,27 Ga. Camadas enriquecidas com manganês foram depositadas nas partes distais marinhas em associação com depósitos de *black shale*. (d) Riaciano–Orosiriano: Deposição das formações Águas Claras e Gorotire em um sistema fluvial aluvial, como resultado de soerguimento tectônico causado pela movimentação convergente entre os domínios Carajás e Bacajá. (e) Orosiriano: colisão entre os domínios Carajás e Bacajá, inversão da Bacia de Carajás e colocação do Granito Carajás e enxames de diques em *ca.* 1,88 Ga (DS: discordância subaérea; SRM: superfície de regressão máxima; ZIM: zona de inundação máxima).

REFERÊNCIAS

Adams A.E., Mackenzie W.S., Guilford C. 1984. Atlas of sedimentary rocks under the microscope. Longman, Harlow, 140 p.

Amy L.A., Peakall J., Talling P.J. 2005. Density-and viscosity-stratified gravity currents: Insight from laboratory experiments and implications for submarine flow deposits. *Sedimentary Geology*, **179**:5-29.

Anbar A.D., Duan Y., Lyons T.W., Arnold G.L., Kendall B., Creaser R.A., Kaufman A.J., Gordon G.W., Scott C., Garvin J., Buick R. 2007. A whiff of oxygen before the great oxidation event. *Science,* **317**:1903-1906.

Araújo Filho R.C., Nogueira A.C., Araújo R.N. 2020. New stratigraphic proposal of a Paleoproterozoic siliciclastic succession: Implications for the evolution of the Carajás Basin, Amazonian craton, Brazil. *Journal of South American Earth Sciences*, **102**:102665.

Araújo R.N., Milhomem Neto J.M., Macambira M.J.B., Nogueira A.C.R. (submetido). Tectono-sedimentary evolution of a Paleoproterozoic succession of the Carajás Basin, southeastern Amazonian Craton, Brazil: Insights from stratigraphy, sedimentology, and U-Pb detrital zircon geochronology.

Araújo O.J.B & Maia R.G.N. 1991. *Serra dos Carajás, Folha SB.22-Z-A: Estado do Pará.* Projeto especial mapas de recursos minerais, de solos e de vegetação para a área do Programa Grande Carajás; Subprojeto Recursos Minerais. Brasília, Companhia de Pesquisa de recursos Minerais – CPRM (Relatório, 136 p).

Araújo O.J.B., Maia R.G.N., Jorge João X.S., Costa J.B.S. 1988. A megaestruturação arqueana da Folha de Serra dos Carajás. *In*: VII Congresso latino-americano de Geologia, Belém. *Anais*, v. 1, p. 324-338.

Araújo R.N. & Nogueira A.C.R. 2019. Serra Sul diamictite of the Carajás Basin (Brazil): a paleoproterozoic glaciation on the amazonian craton. *Geology*, **47**:1166-1170.

Araújo R.N. & Sousa M.J. 2018. Geologia, Estratigrafia e análise do minério dos depósitos de manganês de Carajás: regiões do Azul, Sereno Buritirama e Antônio Vicente. *In*: Belém, CPRM- Companhia de Pesquisa de Recursos Minerais. Relatório técnico, 198 p.

Aspler L.B. & Chiarenzelli J.R. 1998. Two Neoarchean supercontinents? Evidence from the Paleoproterozoic. *Sedimentary Geology*, **120**:75-104.

Barbosa O., Ramos J.R.A., Gomes F.A., Hembold R. 1966. Geologia estratigráfica, estrutural e econômica da área do "Projeto Araguaia". DNPM, Rio de Janeiro (Monografia DGM 18/19), v. 19, 94 p.

Barros C. E. M., Dall'agnol R., Lafon J. M., Teixeira N. P., Ribeiro J. W. 1992. Geologia e Geocronologia Rb-Sr do Gnaisse Estrela, Curionópolis, Pa. *Boletim do Museu paraense Emilio Goeldi*, **4**:85-104.

Beauvais A., Melfi A., Nahon D., Trescases J. J. 1987. Pétrologie du gisement latérique manganésifêre d'Azu1 (Brésil). *Mineral Deposita*, **22**:124-134.

Beisiegel V.R., Bernardelli A.L., Drummond N.F., Ruff A.W., Tremaine J.W. 1973. Geologia e recursos minerais da Serra dos Carajás. *Revista Brasileira de Geociências*, **3**:215-242.

Bekker A. & Holland H.D. 2012. Oxygen overshoot and recovery during the early Paleoproterozoic. *Earth and Planetary Science Letters*, **317-318**:295-304.

Bekker A., Holland H.D., Wang P.L., Rumble D., Stein H.J., Hannah J.L., Coetzee L.L., Beukes N.J. 2004. Dating the rise of atmospheric oxygen. *Nature*, **427**:117-120.

Bekker A. & Kaufman A.J. 2007. Oxidative forcing of global climate change: a biogeochemical record across the oldest Paleoproterozoic ice age in North America. *Earth and Planetary Science Letters*, **258**:486-499.

Bekker A., Sial A.N., Karhu J.A, Ferreira V.P., Noce C.M., Kaufman A.J., Romano A.W., Pimentel M.M. 2003. Chemostratigraphy of carbonates from the Minas Supergroup, Quadrilátero Ferrífero (Iron Quadrangle), Brazil: a stratigraphic record of Early Proterozoic atmospheric, biogeochemical and climatic change. *American Journal of Science*, **303**:865-904.

Bekker A., Slack J.F., Planavsky N., Krapez B., Hofmann A., Konhauser K.O., Rouxel O.J. 2010. Iron formation: the sedimentary product of a complex interplay among mantle, tectonic, oceanic, and biospheric processes. *Economic Geology*, **105**:467-508.

Bellefroid E.J., Hooda Ashleigh v. S., Hoffman P.F., Thomasa M.D., Reinhard C.T., Planavsky N.J. 2018. Constraints on Paleoproterozoic atmospheric oxygen levels. *Proceedings of the National Academy of Sciences of the United States of America*, **115**(32):8104-8109.

Bernardelli A.L. & Beisiegel V.R. 1978. Geologia econômica da jazida de manganês do Azul. *In*: 30º Congresso Brasileiro de Geologia. *Anais*, v. 4, p. 1431-1444.

Black L.P., Kamo S.L., Williams I.S., Mundil R., Davis D.W., Korsch R.J., Foudoulis C. 2003. The application of SHRIMP to Phanerozoic geochronology: a critical application of four zircon standards. *Chemical Geology*, **200**:171-188.

Bleeker W. 2003. The late Archean record: A puzzle in ca. 35 pieces. *Lithos*, **71**:99-134.

Bouma A.H. (ed.). 1962. *Sedimentology of Some Flysch Deposits: a Graphic Approach to Facies Interpretation.* Elsevier, Amsterdam, 168 p.

Brocks J.J., Logan G.A, Buick R., Summons R. 1999. Archaean molecular fossils and the early rise of eukaryotes. *Science*, **285**:1033-1036.

Brocks J.J., Buick R., Summons R.E, Logan G.A. 2003. A reconstruction of Archean biological diversity based on molecular fossils from the 2.78 to 2.45 billion-year-old Mount Bruce Supergroup, Hamersley Basin, Western Australia. *Geochimica et Cosmochimica Acta*, 67(22):4321-4335.

Busfield M.E. & Le Heron D.P. 2013. Glacitectonic deformation in the Chuos Formation of northern Namibia: Implications for Neoproterozoic ice dynamics. *Proceedings of the Geologists' Association*, **124**:778-789.

Busfield M.E. & Le Heron D.P. 2018. Snowball Earth under the microscope. *Journal of Sedimentary Research*, **88**:659-677.

Cabral A.R., Creaser R.A., Nägler T., Lehmann B., Voegelin A.R., Belyatsky B., Pašava J., Seabra Gomes Jr. A.A., Galbiatti H., Böttcher M.E., Escher P. 2013. Trace-element and multi-isotope geochemistry of Late-Archean black shales in the Carajás iron-ore district, Brazil. *Chemical Geology*, **362**:91-104.

Cabral A.R., Bühn B., Gomes Jr. A.A.S., Galbiatti H.F., Lehmann B., Halder S. 2017. Multiple sulfur isotopes from the Neoarchaean Serra Sul black shale, Carajás mineral province, northern Brazil. *Journal of South American Earth Sciences*, **79**:377-383.

Canfield D.E. 2005. The early history of atmospheric oxygen. *Annual Review of Earth Planetary Sciences*, **33**:1-36.

Canfield D.E., Habicht K.S., Thamdrup B. 2000. The Archean sulfur cycle and the early history of atmospheric oxygen. *Science*, **288**:658-661.

Canfield D.E., Pembab L.N., Hammarlunda E.U., Bengtsonc S., Chaussidond M., Lafayee F.G., Meunierb A., Riboulleauf A., Bardd C.R., Rouxelg O., Asaelg D., Pierson-Wickmannh A.C.P., Albanib A.E. 2013. Oxygen dynamics in the aftermath of the Great Oxidation of Earth's atmosphere. *Proceedings of the National Academy of Sciences of the United States of America*, **110**(42):16736-16741

Caquineau T., Paquette J.L., Philippot P. 2018. U-Pb detrital zircon geochronology of the turee creek group, Hamersley Basin, western Australia: timing and correlation of the paleoproterozoic glaciations. *Precambrian Research*, **307**:34-50.

Catuneanu O. 2004. Retroarc foreland systems—evolution through time. *Journal of African Earth Sciences*, **38**:225-242.

Catuneanu O., Martins-Neto M. A., Eriksson P. G. 2005. Precambrian sequence stratigraphy. *Sedimentary Geology*, **176**:67-95.

Cheel R.J. & Leckie D.A. 1993. Hummocky Cross-Stratification. *In*: Wright, V.P. (ed.). Sedimentology Review. Oxford, U.K., *Blackwell Scientific Publications*, p. 103-122.

Chen Y., Chen W., Li Q., Santosh M., Li J. 2019. Discovery of the Huronian Glaciation Event in China: Evidence from glacigenic diamictites in the Hutuo Group in Wutai Shan. *Precambrian Research*, **320**:1-12.

Ciborowski T.J.R. & Kerr A.C. 2016. Did mantle plume magmatism help trigger the Great Oxidation Event? *Lithos*, **246-247**:128-133.

Coe A.L., Bosence D., Church K.D., Flint S.S., Howell J.A., Wilson R.C.L. 2003. (ed.). The Sedimentary Record of Sea-Level Change. Cambridge University Press and The Open University, 288 p.

Cohen K.M., Finney S.C., Gibbard P.L., Fan J.-X. 2013. The ICS international chronostratigraphic chart (updated). *Episodes*, **36**:199-204.

Cordani U.G., Tassinari C.C.G., Kawashita K.A. 1984. A Serra dos Carajás como região limítrofe entre províncias tectônicas. *Ciências da Terra*, **9**:6-11.

Costa F.F.O. 2017. *A Sucessão Siliciclástica paleoproterozoica associada ao depósito de manganês do Azul da Serra dos Carajás*. MS Dissertation. Instituto de Geociências, Universidade Federal do Pará, Belém, 62 p.

Costa M.L., Fernandez O.J.C., Requelme M.E.R. 2005. Depósito de manganês do Azul, Carajás: estratigrafia, mineralogia, geoquímica e evolução geológica. *In*: Marini O.J., Queiroz E.T., Ramos B.W. (ed.). Caracterização de depósitos minerais em distritos mineiros da Amazônia. Brasília, DNPM, FINEP. ADIMB, p. 231-333.

Coutts D.S., Matthews W.A., Hubbard S.M. 2019. Assessment of widely used methods to derive depositional ages from detrital zircon populations. *Geoscience Frontiers*, **10**:1421-1435.

D'Agrella-Filho M.S., Bispo-Santos F., Trindade R.I.F, Antonio P.Y.J. 2016. Paleomagnetism of the Amazonian Craton and its role in paleocontinents. *Brazilian Journal of Geology*, **46**(2):275-299.

Dall'Agnol R., Oliveira D.C., Lamarão C.N. 2013. Magmatismo granitoide arqueano e evolução geológica do Subdomínio de Transição da Província Carajás, sudeste do Cráton Amazônico, Brasil. *Boletim Museu Paraense Emílio Goeldi Ciências Naturais*, **8**(3):251-256.

Dall'Agnol R., Souza Z.S., Althoff F.J., Barros C.E.M., Leite A.A.S., Jorge João X.S. 1997. General aspects of the granitogenesis of the Carajás metallogenic province. *Extended Abstracts of the International Symposium on Granites and Associated Mineralizations*, **1**:135-161.

Dall'Agnol R., Oliveira M.A., Almeida J.A.C., Althoff F.J., Leite A.A.S., Oliveira D.C., Barros C.E.M. 2006. Archean and Paleoproterozoic granitoids of the Carajás Metallogenetic Province, eastern Amazonian craton. *Abstracts of Symposium on magmatism, crustal evolution, and metallogenesis of the Amazonian craton*, **1**:99-150.

Dardenne M.A., Brod T.C.J., Guimarães E.M., Santos R.V. 2009. Modelo metalogenético da mineralização primária do depósito de manganês do Azul (Carajás). *In*: XI Simpósio de Geologia da Amazônia, Manaus. Resumo expandido.

Dardenne M.A., Ferreira Filho C.F., Meirelles M.R. 1988. The role of shoshonitic and calc-alkaline suites in the tectonic evolution of the Carajás District, Brazil. *Journal of South American Earth Sciences*, **1**:363-372.

Dasgupta S., Roy S., Fukuoka M. 1992. Depositional Models for Manganese Oxide and Carbonate Deposits of the Precambrian Sausar Group, India. *Economic Geology*, **87**:1412-1418.

De Raaf J.F.M., Boersma J.R., Van Gelder A. 1977. Wave generated structures and sequences from a shallow marine succession, Lower Carboniferous, County Cork, Ireland. *Sedimentology*, **24**:451-483.

Dias G.S., Macambira M.J.B., Dall'agnol R., Soares A.D.V., Barros C.E. 1996. Datação de zircões de sill de metagabro: comprovação da idade Arqueana da Formação Águas Claras, Carajás - Pará. *In*: V Simpósio de Geologia Da Amazônia, Belém. *Resumos expandidos*. p. 376-379.

Docegeo. 1988. Revisão litoestratigráfica da Província Mineral de Carajás – Litoestratigrafia e principais depósitos minerais. *In*: 35º Congresso Brasileiro de Geologia, Belém. Anexo aos Anais, p. 11-54.

Dreher A.M. 2004. *O depósito primário de Cu-Au de Igarapé Bahia, Carajás*: rochas fragmentarias, fluidos mineralizantes e modelo metalogenético. PhD Thesis, Universidade Estadual de Campinas, São Paulo, 221 p.

Dreher A.M., Xavier R.P., Martini S.L. 2005. Fragmental rocks of the Igarapé Bahia Cu-Au deposit, Carajás mineral province, Brazil. *Revista Brasileira de Geociências*, **35**:359-368.

Dreher A.M., Xavier R.P., Taylor B.E., Martini S.L. 2008. New geologic, fluid inclusion and stable isotope studies on the controversial Igarapé Bahia Cu-Au deposit, Carajás Province, Brazil. *Mineral Deposita*, **43**:161-184.

Dumas S. & Arnott R.W.C. 2006. Origin of hummocky and swaley cross-stratification—the controlling influence of unidirectional current strength and aggradation rate. *Geology*, **34**:1073-1076.

Eguchi J., Seales J. Dasgupta R. 2020. Great Oxidation and Lomagundi events linked by deep cycling and enhanced degassing of carbon. *Nature Geoscience*, **13:**71-76.

Embry A.F. & Johannessen E. 1992. T–R sequence stratigraphy, facies analysis and reservoir distribution in the uppermost Triassic–Lower Jurassic succession, Western Sverdrup Basin, Arctic Canada. *In*: Vorren T. et al. (ed.). Arctic Geology and Petroleum Potential: Norwegian Petroleum Society, v. 2, p. 121-146. (Special Publication).

Embry A.F. 2002. Transgressive-regressive (TR) sequence stratigraphy. *In*: Armentrout J.M., Rosen N.C. (ed.). Sequence Stratigraphic Models for Exploration and Production: Evolving Methodology, Emerging Models and Application Histories, **22**:151-172.

Embry A.F. 2009. (ed.). Practical Sequence Stratigraphy. Canadian Society of Petroleum Geologists, 79 p.

Evans D.A., Beukes N.J., Kirschvink J.L. 1997. Low-latitude glaciation in the Paleoproterozoic era. *Nature*, **386**:262-266.

Fabre S., Nédélec A., Poitrasson F., Strauss H., Thomazo C., Nogueira A. 2011. Iron and sulphur isotopes from the Carajás mining province (Pará, Brazil): Implications for the oxidation of the ocean and the atmosphere across the Archaean-Proterozoic transition. *Chemical Geology*, **289**:124-139.

Farina F., Albert C., Lana C. 2015. The Neoarchean transition between medium-and high-K granitoids: clues from the Southern São Francisco Craton (Brazil). *Precambrian Research*, **266**:375-394.

Farquhar J. & Wing B.A. 2003. Multiple sulfur isotopes and the evolution of the atmosphere. *Earth Planetary Science Letters*, **213**:1-13.

Farquhar J., Namping W., Canfield D.E., Oduro H. 2010. Connections between sulfur cycle evolution, sulfur isotopes, sediments, and base metal sulfide deposits. *Economic Geology*, **105**:509-533.

Fedo C.M., Sircombe K., Rainbird R. 2003. Detrital zircon analysis of the sedimentary record. *In*: Hanchar, J.M., Hoskin, P.W.O. (ed.). Zircon. *Reviews in Mineralogy and geochemistry*, **53**:277-303.

Feio G.R.L., Dall'Agnol R., Dantas E.L., Macambira M.J.B., Santos J.O.S., Althoff F.J., Soares J.E.B. 2013. Archean granitoid magmatism in the Canaã dos Carajás area: implications for crustal evolution of the Carajás province, Amazonian craton, Brazil. *Precambrian Research*, **227**:157-185.

Force E.R. & Cannon W.F. 1988. Depositional Model for Shallow-Marine Manganese Deposits around Black Shale Basins. *Economic Geology*, **83**(1):93-117.

Frei R., Gaucher C., Poulton S.W., Canfield D.E. 2009. Fluctuations in Precambrian atmospheric oxygenation recorded by chromium isotopes. *Nature*, **461**:250-253.

Galarza M.A., Macambira M.J.B., Moura C.A.V. 2003. Geocronologia Pb-Pb e Sm-Nd das rochas máficas do depósito Igarapé Bahia, província mineral de carajás (PA). *In*: VIII Simpósio de Geologia da Amazônia, Manaus. CD-ROM.

Galarza M.A., Macambira M.J.B., Villas R.N. 2008. Dating and isotopic characteristics (Pb and S) of the Fe oxide–Cu–Au–U–REE Igarapé Bahia ore deposit, Carajás mineral province, Pará state, Brazil. *Journal of South American Earth Sciences*, **25**:377-397.

Galarza M.A.T., Macambira M.J.B., Moura C.A.V. 2002. Geocronologia e evolucão crustal das sequências vulcanossedimentares hospedeiras dos depósitos de Cu-Au Igarapé Bahia e Gameleira. *In*: 41º Congresso Brasileiro de Geologia, João Pessoa. *Anais*, 519 p.

Gauthier-Lafaye F., Nogueira A.C.R., Pinheiro R.V.L., Albani A.E. 2010. The Paleoproterozoic Francevilian Series: witness of a geochemical and biological upheaval. *In*: 45º Congresso Brasileiro de Geologia, Belém. *Anais*.

Gerdes A. & Zeh A. 2006. Combined U–Pb and Hf isotope LA-(MC-) ICP-MS analyses of detrital zircons: comparison with SHRIMP and new constraints for the provenance and age of an Armorican metasediment in Central Germany. *Earth and Planetary Science Letters*, **249**:47-61.

Ghosh R., Chakraborty D., Halder M., Baidya T.K. 2015. Manganese mineralization in Archean greenstone belt, Joda-Noamundi sector, Noamundi basin, East Indian Shield. *Ore Geology Reviews*, **70**:96-109.

Gibbs A.K., Wirth K.R., Hirata W.K., Olszewski W.J. 1986. Age and composition of the Grão Pará group volcanics, Serra dos Carajás. *Revista Brasileira de Geociências*, **16**:201-211.

Giovanardi T., Girardi V.A., Teixeira W., Mazzucchelli M. 2019. Mafic dyke swarms at 1882, 535 and 200 Ma in the Carajás region, Amazonian Craton: Sr-Nd isotopy, trace element geochemistry and inferences on their origin and geological settings. *Journal of South American Earth Sciences*, **92**:197-208.

Glasby G.P. 1997. Fractionation of manganese from iron in Archaean and Proterozoic sedimentary ores. *In*: Nicholson K., Hein J.R., Buhn B. & Dasgupta S. (ed.). Manganese Mineralization: Geochemistry and Mineralogy of Terrestrial and Marine Deposits. *Geological Society Special Publication*, **199**:29-42.

Gumsley A. P., Chamberlain K. R., Bleeker W., Söderlund U., de Kock M. O., Larsson E. R., Bekker A. 2017. Timing and tempo of the Great Oxidation Event. *Proceedings of the National Academy of Sciences of the United States of America,* **114**:1811-1816.

Guo Q., Strauss H., Kaufman A.J., Schroder S., Gutzmer J., Wing B., Baker M.A., Bekker A., Qusheng J., Sang-Tae K., Farquahar J. 2009. Reconstructing Earth's surface oxidation across the Archean-Proterozoic transition. *Geology*, **37**:399-402.

Hedges S.B. & Kumar S. 2009. (ed.). The timetree of life. United Kingdom, Oxford, 551 p.

Hjellbakk A. 1997. Facies and fluvial architecture of a high-energy braided river: the upper Proterozoic Seglodden Member, Varanger peninsula, Northern Norway. *Sedimentary Geology*, **114**:131-161.

Hoffman P.F. 1997. Tectonic genealogy of North America. *In*: van der Pluijm B.A. & Marshak S. (ed.). An introduction to structural geology and tectonics. McGraw Hill, New York, p. 459-464.

Hoffman P.F. 2013. The Great Oxidation and a Siderian snowball Earth: MIF-S based correlation of Paleoproterozoic glacial epochs. *Chemical Geology*, **362**:143-156.

Holdsworth R.E. & Pinheiro R.V.L. 2000. The anatomy of shallow-crustal transpressional structures: insights from the Archaean Carajás fault zone, Amazon, Brazil. *Journal of Structural Geology*, **22**:1105-1023.

Holland H.D. 2002. Volcanic gases, black smokers, and the Great Oxidation Event. *Geochimica et Cosmochimica Acta*, **66**(21):3811-3826.

Holland H.D. 2006. The oxygenation of the atmosphere and oceans. *Philosophical Transactions of the Royal Society*, **361**:903-915.

Holland H.D. 2009. Why the atmosphere became oxygenated: a proposal. *Geochimica et Cosmochimica Acta*, **73**:5241-5255.

Horstwood M.S.A., Košler J., Gehrels G., Jackson S.E., McLean N.M., Paton C., Pearson N.J., Sircombe K., Sylvester P., Vermeesch P., Bowring J.F., Condon D.J., Schoene B. 2016.

Community-derived standards for LA-ICP-MS U-Th-Pb geochronology – uncertainty propagation, age interpretation and data reporting. *Geostandards and Geoanalytical Research*, **40**(3):311-332.

Immonen N. 2013. Surface microtextures of icerafted quartz grains revealing glacial ice in the Cenozoic Arctic. *Palaeogeography, Palaeoclimatology, Palaeoecology*, **374**:293-302.

Jackson S.E., Pearson N.J., Griffin W.L., Belousova E.A. 2004. The application of laser ablation-inductively coupled plasma-mass spectrometry to in situ U–Pb zircon geochronology. *Chemical Geology*, **211**:47-69.

Johansson A. 2009. Baltica, Amazonia and the SAMBA connection—1000 million years of neighbourhood during the Proterozoic? *Precambrian Research,* **175**:221-234

Johnson J.E., Webb S.M., Chi Ma, Fischer W.W. 2016. Manganese mineralogy and diagenesis in the sedimentary rock record. *Geochimica et Cosmochimica Acta*, **173**:210-231.

Johnson J.E., Webb S.M., Thomas K., Ono S., Kirschvink J.L., Fischer W.W. 2013. Manganese-oxidizing photosynthesis before the rise of cyanobacteria. *Proceedings of the National Academy of Sciences of the United States of America,* **110**(28):11238-11243.

Jones S. 2011. Proterozoic deformation in the East Pilbara and tectonic setting of fault-hosted manganese at Woodie Woodie mine. *Australian Journal of Earth Sciences*, **58**:639-673.

Jones S., McNaughton N. J., Grguric B. 2013. Structural controls and timing of fault-hosted manganese at Woodie Woodie, East Pilbara, Western Australia. *Ore Geology Reviews*, **50**:52-82.

Justo A.P., Dantas E.L., Freitas-Silva F.H., Rodrigues J.B. 2018. Detrital Zircon Populations in the Neoarchean to Paleoproterozoic Sedimentary Coverage of Carajás, Amazon Cráton, Brazil. *In*: 49º Congresso Brasileiro de Geologia, Rio de Janeiro. *Anais*.

Karhu J.A. & Holland H.D. 1996. Carbon isotopes and the rise of atmospheric oxygen. *Geology*, **24**:867-870.

Kasting J.F., Eggler D.H., Raeburn S.P. 1993. Mantle redox evolution and the oxidation state of the Archean atmosphere. *The Journal of Geology*, **101**:245-257.

Kasting J.F. 2001. The rise of atmospheric oxygen. *Science*, **293**:819-820.

Kasting J.F. & Siefert J.L. 2002. Life and the evolution of Earth's atmosphere. *Science*, **296**:1066-1068.

Kirschvink J.L., Gaidos E.J., Bertani L.E., Beukes N.J., Gutzmer J., Maepa L.N., Steinberger R.E. 2000. Paleoproterozoic snowball Earth: extreme climatic and geochemical global change and its biological consequences. *Proceedings of the National Academy of Sciences of the United States of America,* **97**(4):1400-1405.

Konhauser K.O., Lalonde S.V., Planavsky N.J., Pecoits E., Lyons T.W., Mojzsis S.J., Rouxel O.J., Barley M.E., Rosìere C., Fralick P.W., Kump L.R., Bekker A. 2011. Aerobic bacterial pyrite oxidation and acid rock drainage during the Great Oxidation Event. *Nature*, **478**:369-373.

Konhauser K.O., Pecoits E., Lalonde S.V., Papineau D., Nisbet E.G., Barley M.E., Arndt N.T., Zahnle K., Kamber B.S. 2009. Oceanic nickel depletion and a methanogen famine before the Great Oxidation Event. *Nature*, **458**:750-753.

Kopp R.E, Kirschvink J.L., Hilburn I.A., Nash C.Z. 2005. The Paleoproterozoic snowball Earth: a climatic disaster triggered by the evolution of oxygenic photosynthesis. *Proceedings of the National Academy of Sciences of the United States of America*, **102**:11131-11136.

Kump L.R. 2008. The rise of atmospheric oxygen. *Nature*, **451**:277-278.

Kump L.R. & Barley M.E. 2007. Increased subaerial volcanism and the rise of atmospheric oxygen 2.5 billion years ago. *Nature*, **448**:1033-1036.

Kump L.R., Fallick A.E., Melezhik V.A., Strauss H., Lepland A. 2013. The Great Oxidation Event. *In*: V.A. Melezhik et al. (ed.). *Reading the Archive of Earth's Oxygenation*, Global Events and the Fennoscandian Arctic Russia – Drilling Early Project, Springer-Verlag Berlin Heidelberg, **3**:1517-1533.

Lacasse C.M., Ganade C.E, Mathieu L., Teixeira N.A., Lopes L.B.L., Monteiro C.F. 2020. Restoring original composition of hydrothermally altered Archean metavolcanic rocks of the Carajás Mineral Province (Brazil): Geodynamic implications for the transition from lid to mobile tectonics. *Lithos*, **372-373**:105647.

Laznicka P. 1992. Manganese deposits in the global lithogenic system: quantitative approach. *Ore Geology Reviews*, **7**:279-356.

Lechte M. & Wallace M. 2016. Sub–ice shelf ironstone deposition during the Neoproterozoic Sturtian glaciation. *Geology*, **44**:891-894.

Le Heron D. P., Cox G., Trundley A., Collins A. 2011. Sea ice−free conditions during the Sturtian glaciation (early Cryogenian), South Australia. *Geology*, **39**:31-34.

Le Heron D.P. 2015. The significance of ice-rafted debris in Sturtian glacial successions. *Sedimentary Geology*, **322**:19-33.

Le Heron D.P., Tofaif S., Vandyk T., Ali D.O. 2017. A diamictite dichotomy: Glacial conveyor belts and olistostromes in the Neoproterozoic of Death Valley, California, USA. *Geology*, **45**:31-34.

Lima F.D. & Pinheiro R.V.L. 2001. Formação Gorotire: Consideração sobre uma unidade siliciclástica particular da Serra dos Carajás-PA. *In*: Reis N.J & Monteiro M.A.S. Contribuição à Geologia da Amazônia, Manaus. v.2, p. 205-229.

Lindenmayer Z.G, Laux J.H., Teixeira J.B.G. 2001. Considerações sobre a origem das formações ferríferas da Formação Carajás, Serra dos Carajás. *Revista Brasileira de Geociências,* 31(1):21-28.

Ludwig K.R. 2003. (ed.). Isoplot 3.00: A geochronological toolkit for Microsoft Excel. Berkeley Geochronology Center, 70 p. (Special Publication, 4).

Ludwig K.R. 2008. (ed.). User's Manual for Isoplot 3.6 - A Geochronological Toolkit for Microsoft Excel. Berkeley Geochronology Center Special Publication, Berkeley.

Ludwig K. 2009. (ed.). SQUID 2: A user's manual. Berkeley Geochronology Center, 110 p. (Special Publication, 5).

Luo G., Ono S., Beukes N.J., Wang D.T., Xie S., Summons R.E. 2016. Rapid oxygenation of Earth's atmosphere 2.33 billion years ago. *Science Advances*, **2**(5):e1600134.

Luz B.R. & Crowley J.K. 2012. Morphological and chemical evidence of stromatolitic deposits in the 2.75 Ga Carajás banded iron formation, Brazil. *Earth and Planetary Science Letters*, **355**:60-72.

Lyons T.W. & Reinhard C.T. 2009. Early Earth: oxygen for heavy-metal fans. *Nature*, **461**:179-181.

Lyons T.W., Reinhard C.T., Planavsky N.J. 2014. The rise of oxygen in Earth's early ocean and atmosphere. *Nature*, **506**:307-315.

Macambira J.B., Macambira M.J.B., Scheller T., Gomes A.C.B. 1996. Geocronologia Pb/Pb e tipologia de zircões de rochas vulcânicas da Formação Carajás - Pará: Indicador da idade dos BIFs. *In*: 39º Congresso Brasileiro de Geologia, Salvador. *Anais*, **6**:516-518.

Macambira J.B. 2003. *O ambiente deposicional da Formação Carajás e uma proposta de modelo evolutivo para a Bacia Grão Pará*. Ph.D Thesis, Universidade Estadual de Campinas, São Paulo, 217 p.

Macambira J.B. & Schrank A. 2002. Quimio-estratigrafia e evolução dos jaspilitos da Formação Carajás (PA). *Revista Brasileira de Geociências,* **32**(4):567-578.

Macambira J.B., Ramos J.F.F., Assis J. F. P., Figueiras A. J. M. 1990. Projeto Serra Norte. Conv. Seplan/DOCEGEO/UFPa. Projeto Pojuca. Convênio DNPM/DOCEGEO/UFPa. Relatório final. 150 p.

Macambira M.J.B, Vasquez M.L., Silva D.C.C., Galarza M.A., Barros C.E.M., Camelo J.F. 2009. Crustal growth of the central-eastern Paleoproterozoic domain, SW Amazonian craton: Juvenile accretion vs. reworking. *Journal of South American Earth Sciences*, **27**:235-246.

Macambira, J.B. 2010. Método estratigráfico de exploração de depósitos de Cu-Au do tipo Igarapé Bahia - Carajás, Pará. *In*: 45° Congresso Brasileiro de Geologia, Belém. CD-ROM.

Machado N., Lindenmayer Z., Krogh T.E., Lindenmayer D. 1991. U-Pb geochronology of Archean magmatism and basement reactivation in the Carajás area, Amazon shield, Brazil. *Precambrian Research*, **49**:329-354.

Mahaney W.C., Claridge G., Campbell I. 1996. Microtextures on quartz grains in tills from Antarctica. *Palaeogeography, Palaeoclimatology, Palaeoecology*, **121**:89-103.

Marangoanha B., Oliveira D.C., Dall'Agnol R. 2019. The Archean granulite-enderbite complex of the northern Carajás province, Amazonian craton (Brazil): Origin and implications for crustal growth and cratonization. *Lithos*, **350-351**:105275.

Martin A.P., Condon D.J., Prave A.R., Lepland A. 2013. A review of temporal constraints for the Palaeoproterozoic large, positive carbonate carbon isotope excursion (the Lomagundi–Jatuli Event). *Earth-Science Reviews*, **127**:242-261.

Martins P.L.G., Toledo C.L.B., Silva A.M., Chemale F.Jr., Santos J.O.S., Assis L.M. 2017. Neoarchean magmatism in the southeastern Amazonian Craton, Brazil: Petrography, geochemistry and tectonic significance of basalts from the Carajás Basin. *Precambrian Research*, **302**:340-357.

Maynard J.B. 2010. The chemistry of manganese ores through time: A signal of increasing diversity of earth-surface environments. *Economic Geology*, **105**(3):535-552.

Maynard J.B. 2003. Manganiferous sediments, rocks, and ores. *In*: Mackenzie F.T., Holland H.D., Turekion K.K. (ed.). Treatise on Geochemistry, Sediments, Diagenesis, and Sedimentary Rocks, v. 7, p. 289-308.

Melo G.H.C, Monteiro L.V.S, Xavier R.P, Moreto C.P.N, Arquaz R.M., Silva M.A.D. 2019. Evolution of the Igarapé Bahia Cu-Au deposit, Carajás Province (Brazil): Early syngenetic chalcopyrite overprinted by IOCG mineralization. *Ore Geology Reviews*, **111**:102993.

Meirelles M.R. 1986. *Geoquímica e Petrologia dos jaspilitos e rochas vulcânicas associadas, Grupo Grão Pará, Serra dos Carajás-PA*. MS Dissertation, Instituto de Geociências, Universidade de Brasília, Brasília, 150 p.

Meirelles M.R. & Dardenne M.A. 1991. Vulcanismo basáltico de afinidade shoshonítica em ambiente de arco arqueano, Grupo Grão Pará, Serra dos Carajás, PA. *Revista Brasileira de Geociências*, **21**:41-50.

Menzies J. 2012. Strain pathways, till internal architecture and microstructures - Perspectives on a general kinematic model - A 'blueprint' for till development. *Quaternary Science Reviews*, **50**:105-124.

Menzies J., Van der Meer J.J.M., Rose J. 2006. Till—As a glacial "tectomict", its internal architecture, and the development of a "typing" method for till differentiation. *Geomorphology*, **75**:172-200.

McPhie J., Doyle M., Allen R. 1993. Volcanic Textures: a Guide to the Interpretation of Textures in Volcanic Rocks. University of Tasmania, Tasmania, 197 p.

Miall A.D. 1977. A review of the braided-river depositional environment. *Earth-Science Reviews*, **13**(1):1-62.

Miall A.D. 1983. Glaciomarine sedimentation sedimentation in the Gowganda Formation (Huronian), northern Ontario. *Journal of Sedimentary Research*, **53**:477-491.

Miall A.D. 1985. Sedimentation on an early Proterozoic continental margin under glacial influence: The Gowganda Formation (Huronian), Elliot Lake area, Ontario, Canada. *Sedimentology*, **32**:763-788.

Milhomem Neto, J.M. & Lafon J.M. 2019. Zircon U-Pb and Lu-Hf isotope constraints on Archean crustal evolution in Southeastern Guyana Shield. *Geoscience Frontiers*, **10**:1477-1506.

Moreira H., Lana C., Nalini H.A. 2016. The detrital zircon record of an Archaean convergent basin in the Southern São Francisco Craton, Brazil. *Precambrian Research*, **275:**84-99.

Mougeot R., Respaut J.P., Briqueu L., Ledru P., Milesi J.P., Lerouge C., Marcoux E., Huhn S.B., Macambira M.J.B. 1996a. Isotope geochemistry constraints for Cu, Au mineralization and evolution of the Carajás 763 province (Pará, Brazil). *In*: 39º Congresso Brasileiro de Geologia, Salvador. *Anais*, v. 7, p. 321-324.

Mougeot R., Respaut J.P., Briqueu L., Ledru P., Milesi J. P., Macambira M. J. B., Huhn S.B. 1996b. Geochronological constrains for the age of the Águas Claras Formation (Carajás Province, Pará, Brazil). *In*: 39º Congresso Brasileiro de Geologia, Salvador. *Anais*. v. 6, p. 579-581.

Mutti E. 1992. (ed.). Turbidite Sandstone. Agip Intituto di Geologia Università di Parma, Milano, 277 p.

Mutti E. & Ricci Lucchi F. 1975. Turbidite facies and facies associations. *In*: E. Mutti et al. (ed.). Examples of Turbidite facies and Facies Associations from Selected Formations of the Northern Apennines. Field Trip Guidebook A-11. IX International Sedimentological Congress, Nice, p. 21-36.

Nascimento M.S. & Oliveira D.A. 2015. Ambiente deposicional e proveniência da Formação Gorotire, Província Carajás, sudeste do Cráton Amazônico. *In*: Gorayeb P., Meiguins A. (ed.). Contribuições à Geologia da Amazônia, v. 9.

Nichols G. 2009. (ed.). Sedimentology and Stratigraphy. Blackwell, Oxford, 355 p.

Nogueira A.C.R. 1995. *Análise faciológica e aspectos estruturais da Formação Águas Claras, Região Central da Serra dos Carajás-Pará*. MS Dissertation, Universidade Federal do Pará, Belém, 167 p.

Nogueira A.C.R., Truckenbrodt W., Pinheiro R.V.L. 1995. Formação Águas Claras, Pré-Cambriano da Serra dos Carajás, redescrição e redefinição litoestratigráfica. *Boletim do Museu Paraense Emílio Goeldi*, Série Ciências da Terra, **7**:177-197.

Och L.M. & Shields-Zhou G.A. 2012. The Neoproterozoic oxygenation event: Environmental perturbations and biogeochemical cycling. *Earth Science Reviews*, **110**:26-57.

Olszewski W.J., Wirth K.R., Gibbs A.K., Gaudette H.E. 1989. The age, origin, and tectonics of the Grão Pará Group and associated rocks, Serra dos Carajás, Brazil: Archean continental volcanism and rifting. *Precambrian Research*, **42**:229-254.

Orton G.J. 1996. Volcanic environments. *In*: Reading H.G. (ed.). *Sedimentary Environments: Processes, Facies and Stratigraphy*. Blackwell, Oxford, p. 485-567.

Ossa Ossa F., Hofmann A., Vidal O., Kramers J.D., Belyanin G., Cavalazzi B. 2016. Unusual manganese enrichment in the Mesoarchean Mozaan Group, Pongola Supergroup, South Africa. *Precambrian Research*, **281**:414-433.

Papineau D, Mojzsis S.J, Schmitt A.K. 2007. Multiple sulfurisotopes from Paleoproterozoic Huronian interglacial sedimentsand the rise of atmospheric oxygen. *Earth Planetary Science Letters*, **255**:188-212.

Pavlov A.A., Kasting J.F., Brown L.L. 2000. Greenhouse warming by CH_4 in the atmosphere of early Earth. *Journal of Geophysical Research,* **105**:11981e11990.

Pavlov A.A. & Kasting J.F. 2002. Mass-independent fractionation of sulfur isotopes in Archean sediments: strong evidence for an anoxic Archean atmosphere. *Astrobiology,* **2**(1):27-41.

Pettijohn F.J., Potter P.E., Seiver R. (ed.). 1987. Sand and sandstones. Berlin, Springer-Verlag, 553 p.

Pereira R.M.P., Rosiere C.A., Santos J.O.S., Lobato L.M., Silva R.C.F., McNaughton N.J. 2009. Unidade Caninana: Sequência clástica Paleoproterozóica revelada por datação U-Pb em zircões detríticos da Província Mineral Carajás. *In*: XI Simpósio de Geologia da Amazônia, Manaus. CD-ROM.

Pickering K.T., Corregidor J., Clark J.D. 2015. Architecture and stacking patterns of lower-slope and proximal basin-floor channelized submarine fans, Middle Eocene Ainsa System, Spanish Pyrenees: An integrated outcrop–subsurface study. *Earth-Science Reviews*, **144**:47-81.

Philippot P., Ávila J.N, Killingsworth B.A., Tessalina S., Baton F., Caquineau T., Muller E., Pecoits E., Cartigny P., Lalonde S.V., Ireland T.R., Thomazo C., Van Kranendonk M.J., Busigny V. 2018. Globally asynchronous sulphur isotope signals require re-definition of the Great Oxidation Event. *Nature Communications*, **9:**2245.

Pinheiro R.V.L. 1997. *Reactivation history of the Carajás and Cizento strike-slip systems, Amazon, Brazil.* PhD Thesis, Departament of Geological Sciences, University of Durham, England, 408 p.

Pinheiro R.V.L. & Holdsworth R.E. 1997a. Reactivation of Archaean strike-slip fault systems, Amazon region, Brazil. *Journal of the Geological Society*, **154:**99-103.

Pinheiro R.V.L. & Holdsworth R.E. 1997b. The structure of the Carajás N-4 ironstone deposit and associated rocks: relationship to Archaean strike-slip tectonics and basement reactivation in the Amazon region, Brazil. *Journal of South American Earth Sciences*, **10**:305-319.

Pufahl P.K. & Hiatt E.E. 2012. Oxygenation of the Earth's atmosphere–ocean system: a review of physical and chemical sedimentologic responses. *Journal of Marine and Petroleum Geology*, **32**:1-20.

Rasmussen B., Bekker A., Fletcher I.R. 2013. Correlation of Paleoproterozoic glaciations based on U–Pb zircon ages for tuff beds in the Transvaal and Huronian Supergroups. *Earth and Planetary Science Letters*, **382**:173-180.

Reinhard C.T., Planavsky N.J., Lyons T.W. 2013. Long-term sedimentary recycling of rare sulphur isotope anomalies. *Nature,* **497**:100-103.

Rogers J.J.W. & Santosh M. 2002. Configuration of Columbia, a Mesoproterozoic Supercontinent. *Gondwana Research*, **5**:5-22.

Rogers J.J.W. 1996. A history of continents in the past three billion years. *The Journal of Geology*, **104**:91-107.

Roy S. 1997. Genetic diversity of manganese deposition in the terrestrial geological record. *In*: Nicholson K., Hein J.R., Buhn B., Dasgupta S. (ed.). *Manganese Mineralization: Geochemistry and Mineralogy of Terrestrial and Marine Deposits*. Geological Society, p. 5-27. (Special Publication, 199).

Roy S. 2006. Sedimentary manganese metallogenesis in response to the Evolution of the Earth system. *Earth-Science Reviews*, **77**:273-305.

Ruffet G., Innocent C., Michard A., Féraud G., Beauvais A., Nahon D., Hamelin B. 1996. A geochronological $^{40}Ar/^{39}Ar$ and $^{87}Rb/^{87}Sr$ study of K-Mn oxides from the weathering sequence of Azul, Brazil. *Geochimica Cosmochimica Acta*, **60**(12):2219-2232.

Rye R. & Holland H.D. 1998. Paleosols and the evolution of atmospheric oxygen: a critical review. *American Journal of Science*, **298**:621-672.

Santos M.G.S. 2002. *Estudo dos isótopos de Pb e Nd do depósito de Cu-Au (U-ETR) Alemão, Província Mineral de Carajás (PA)*. MS Dissertation, Centro de Geociências, Universidade Federal do Pará, Belém, 121 p.

Santos M.M., Lana C., Scholz R., Buick I., Schmitz M.D., Kamo S.L., Gerdes A., Corfu F., Tapster S., Lancaster P., Storey C.D., Basei M.A.S., Tohver E., Alkmim A., Nalini H., Krambrock K., Fantini C., Wiedenbeck M. 2017. A new appraisal of Sri Lankan BB zircon as a reference material for LA-ICP-MS U-Pb geochronology and Lu-Hf isotope tracing. *Geostandards and Geoanalytical Research*, **41**(3):335-358.

Sato K., Tassinari C.C.G., Basei M.A.S., Siga Júnior O., Onoe A.T., Souza M.D. 2014. Sensitive High Resolution Ion Microprobe (SHRIMP IIe/MC) of the Institute of Geosciences of the University of São Paulo, Brazil: analytical method and first results. *Geologia USP, Série Científica*, **14**(3):3-18.

Sekine Y., Tajika E., Tada R., Hirai T., Goto K.T., Kuwatani T., Goto K., Yamamoto S., Tachibana S., Isozaki Y., Kirschvink J.L. 2011a. Manganese enrichment in the Gowganda Formation of the Huronian Supergroup: A highly oxidizing shallow-marine environment after the last Huronian glaciation. *Earth and Planetary Science Letters*, **307**:201-210.

Sekine Y., Suzuki K., Senda R., Goto K. T., Tajika E., Tada R., Goto K., Yamamoto S., Ohkouchi N., Ogawa N. O., Maruoka T. 2011b. Osmium evidence for synchronicity between a rise in atmospheric oxygen and Palaeoproterozoic deglaciation. *Nature communications*, **2**(1):502.

Silva D.C.C. 2006. *Estudo da geometria e cinemática das rochas sedimentares arqueanas da Mina do Igarapé Azul – Carajás-PA*. MS Dissertation, Instituto de Geociências, Universidade Federal do Pará, Belém, 124 p.

Sláma J., Košler J., Condon D.J., Crowley J.L., Gerdes A., Hanchar J.M., Horstwood M.S.A., Morris G.A., Nasdala L., Norberg N., Schaltegger U., Schoene B., Tubrett M.N., Whitehouse M.J. 2008. Plešovice zircon – a new natural reference material for U-Pb and Hf isotopic microanalysis. *Chemical Geology*, **249**:1-35.

Somelar P., Soomer S., Driese S.G., Lepland A., Stinchcomb G.E., Kirsimäe K. 2020. CO_2 drawdown and cooling at the onset of the Great Oxidation Event recorded in 2.45 Ga paleoweathering crust. *Chemical Geology*, **548**:119678.

Song H., Jiang G., Poulton S.W., Wignall P.B., Tong J., Song H., An Z., Chu D., Tian L., She Z. & Wang C. 2017. The onset of widespread marine red beds and the evolution of ferruginous oceans. *Nature Communications*, **8**:399.

Souza S. Z., Dall'Agnol R., Althoff F.J., Leite A.A.S., Barros C.E.M. 1996. Carajás Mineral Province: geological, geochronological and tectonic constrasts on the Archean evolution of the Rio Maria Granite-Greenstone Terrain and the Carajás block. Extended Abstracts, Symposium on Archean Terranes of South America Platform, v. 1, p. 31-32.

Spencer C.J., Kirkland C.L., Taylor R.J.M. 2016. Strategies towards statistically robust interpretations of in situ U-Pb zircon geochronology. *Geoscience Frontiers*, **7**(37):581-589.

Stacey J.S. & Kramers J.D. 1975. Approximation of terrestrial lead isotope evolution by a two-stage model. *Earth and Planetary Science Letters*, **26**:207-221.

Stow D.A., Reading H.G., Collinson J.D. 1996. Deep seas. *In*: Reading, H.G. (ed.). *Sedimentary Environments: Process, Facies and Stratigraphy*. Blachwell, Oxford, p. 395-483.

Stow D.A.V. & Piper D.W. (ed.). 1984. Fine-grained Sediments: Deep-water Processes and Facies. Geot. Soc. Lond., Bristol, 659 p. (Special Publication, 15).

Strand K. 2012. Global and continental-scale glaciations on the Precambrian Earth. *Marine and Petroleum Geology*, **33**:69-79.

Tallarico F.H.B., Oliveira C.G., Figueiredo B.R. 2000. The Igarape Bahia Cu-Au mineralization, Carajás Province. *Revista Brasileira de Geociências*, **30**(2):230-233.

Tallarico F.H.B., Figueiredo B.R., Groves D.I., Kositcin N., McNaughton N.J., Fletcher I.R., Rego J.L. 2005. Geology and SHRIMP U-Pb geochronology of the Igarapé Bahia deposit, Carajás copper-gold belt, Brazil: an Archean (2.57 Ga) example of iron-oxide Cu-Au-(U-REE) mineralization. *Economic Geology*, **100**:7-28.

Tang H. & Chen Y. 2013. Global glaciations and atmospheric change at ca. 2.3 Ga. *Geoscience Frontiers*, **4**:583-596.

Tang H.S., Chen Y.J., Santosh M., Yang T. 2012. REE geochemistry of carbonates from the Guanmenshan Formation, Liaohe Group, NE Sino-Korean Craton: implications for seawater compositional change during the Great Oxidation Event. *Precambrian Research*, **227**:316-336.

Tang H.S., Chen Y.J., Wu G., Lai Y. 2011. Paleoproterozoic positive $\delta^{13}C_{carb}$ excursion in northeastern Sino-Korean craton: evidence of the Lomagundi Event. *Gondwana Research*, **19:**471-481.

Tassinari C.C.G. & Macambira M.J.B. 2004. A evolução tectônica do Cráton Amazônico. *In*: Mantesso-Neto V., Bartorelli A., Carneiro C.D.R., Brito Neves B.B. (ed.). *Geologia do Continente Sul-Americano: Evolução da Obra de Fernando Flávio Marques de Almeida*, p. 471-485.

Tavares F.M. 2015. *Evolução Geotectônica do nordeste da Província Carajás*. PhD Thesis, Instituto de Geociências, Universidade Federal do Rio de Janeiro, 143 f.

Tavares F.M., Trouw R.A.J., Silva C.M.G., Justo A.P., Oliveira J.K.M. 2018. The multistage tectonic evolution of the northeastern Carajás Province, Amazonian Craton, Brazil: Revealing complex structural patterns. *Journal of South American Earth Sciences*, **88**:238-252.

Teixeira J.B.G. 1994. *Geochemistry, petrology, and tectonic setting of Archean basaltic and dioritic rocks from the N4 Iron deposit, Serra dos Carajás, Pará, Brazil*. PhD Thesis, Department of Geosciences, Penn State University, Pennsylvania, 161 p.

Teixeira M.F.B., Dall'Agnol R., Santos J.O.S., Oliveira D.C., Lamarão C.N., McNaughton N.J. 2018. Crystallization ages of Paleoproterozoic A-type granites of Carajás Province, Amazon Craton: Constraints from U-Pb geochronology of zircon and titanite. *Journal of South American Earth Sciences*, **88**:312-331.

Teixeira M.F.B, Dall'Agnol R., Santos J.O.S, Kemp A., Noreen Evans N. 2019. Petrogenesis of the Paleoproterozoic (Orosirian) A-type granites of Carajás Province, Amazon Craton, Brazil: Combined in situ Hf–O isotopes of zircon. *Lithos*, **332-333**:1-22.

Teixeira W., Hamilton M.A., Girardi V.A.V., Faleiros F.M., Ernst R.E. 2019. U-Pb baddeleyite ages of key dyke swarms in the Amazonian Craton (Carajás/Rio Maria and Rio Apa areas): Tectonic implications for events at 1880, 1110 Ma, 535 Ma and 200 Ma. *Precambrian Research*, **329**:138-155.

Thomas G.S.P. & Connell R.J. 1985. Iceberg drop, dump, and grounding structures from Pleistocene glacio-lacustrine sediments, Scotland. *Journal of Sedimentary Petrology*, **55**:243-249.

Trendall A.F., Basei M.A.S., De Laeter J.R., Nelson D.R. 1998. SHRIMP U-Pb constraints on the age of the Carajás Formation, Grão Pará Group, Amazon Craton. *Journal of South American Earth Sciences*, **11**:265-277.

Tsikos H., Beukes N.J., Moore J.M., Harris C. 2003. Deposition, diagenesis, and secondary enrichment of metals in the Paleoproterozoic Hotazel iron formation, Kalahari manganese field, South Africa. *Economic Geology*, **98**:1449-1462.

Valarelli J.V., Bernardelli A.L., Beisiegel V.R. 1978. Aspectos geneticos do minerio de manganês do Azul. *In*: 30º Congresso Brasileiro de Geologia. v. 4, p. 1670-1679.

Vasconcelos P. M., Renne P. R., Brimhall G. H., Becker T. A., 1994. Direct dating of weathering phenomena by $^{40}Ar/^{39}Ar$ and K-Ar analysis of supergene K-Mn oxides. *Geochimica Cosmochimica Acta*, **58:**1635-1665.

Vasquez M.L., Sousa C.S., Carvalho J.M.A. 2008a. *Mapa Geológico e de Recursos Minerais do Estado do Pará*. Companhia de Pesquisa de Recursos Minerais – CPRM. 1 mapa. Escala 1:1.000.000.

Vasquez M.L., Rosa-Costa L.T., Silva C.G., Ricci P.F., Barbosa J.O., Klein E.L., Lopes E.S., Macambira E.B., Chaves C.L., Carvalho J.M., Oliveira J.G., Anjos G.C., Silva H.R. 2008b. Geologia e Recursos Minerais do Estado do Pará: sistema de Informações Geográficas-SIG: Texto Explicativo dos Mapas Geológico, Tectônico e de Recursos Minerais do Estado do Pará. Escala 1:1.000.000. *In*: Vasquez M.L. & Rosa-Costa L.T. (ed.). Belém, Companhia de Pesquisa de Recursos Minerais – CPRM, p. 1-329.

Walker R.G. 1990. Facies Modelling and Sequence Stratigraphy. *Journal of Sedimentary Petrology*, **60**:777-786.

Walker R.G. 1992. Facies, facies models and modern stratigraphic concepts. *In*: Walker R.G. & James N.P. (ed.). *Facies Models - Response to Sea Level Change*. Geological Association of Canada, Ontario, Canada, p. 1-14.

Wentworth C.K. 1922. A scale of grade and class terms for clastic sediments. *The Journal of Geology,* **30**:377-392.

Wendt L. & Carl C. 1991. The statistical distribution of the mean square weighted deviation. *Chemical Geology Isotope Geoscience Section*, **86**:275-285.

Whalley W.B. & Krinsley D.H. 1974. A scanning electron microscope study of surface textures of quartz grains from glacial environments. *Sedimentology*, **21**:87-105.

Wiedenbeck M., Allé P., Corfu F., Griffin W.L., Meier M., Oberli F., Von Quadt A., Roddick J.C., Spiegel W. 1995. Three natural zircon standards for U–Th–Pb, Lu–Hf, trace element and REE analyses. *Geostandards Newsletter*, **19**:1-23.

Wirth K.R., Gibbs A.K., Olszewski Jr. 1986. U-Pb ages of zircons from the Grão-Pará Group and Serra dos Carajás Granite, Pará, Brazil. *Revista Brasileira de Geociências*, **16**:195-200.

Young G.M. 1970. An extensive early Proterozoic glaciation in North America? *Palaeogeography, Palaeoclimatology, Palaeoecology*, **7**:85-101.

Young G.M. 1991. The geologic record of glaciations: relevance to the climatic history of the Earth. *Geoscience Canada*, **18**(3):100-8.

Young G.M. 2012. Secular changes at the Earth's surface: evidence from palaeosols, some sedimentary rocks, and palaeoclimatic perturbations of the Proterozoic Eon. *Gondwana Research*, **24**(2):453-467.

Young G.M. 2013a. Secular changes at the Earth's surface: evidence from palaeosols, some sedimentary rocks, and palaeoclimatic perturbations of the Proterozoic Eon. *Gondwana Research*, **24**(2):453-467.

Young G.M. 2013b. Precambrian supercontinents, glaciations, atmospheric oxygenation, metazoan evolution and an impact that may have changed the second half of Earth history. *Geoscience Frontiers*, **4**:247-261.

Young G.M. 2014. Contradictory correlations of Paleoproterozoic glacial deposits: Local, regional or global controls? *Precambrian Research*, **247**:33-44.

Young G.M. 2019. Aspects of the Archean-Proterozoic transition: How the great Huronian Glacial Event was initiated by rift-related uplift and terminated at the rift-drift transition during break-up of Lauroscandia. *Earth-Science Reviews,* **190**:171-189.

Young G.M., Long D.G.F., Fedo C.M., Nesbitt H.W. 2001. Paleoproterozoic Huronian basin: product of a Wilson cycle punctuated by glaciations and a meteorite impact. *Sedimentary Geology*, **141-142**:233-254.

Zhao G.C., Cawood P.A., Wilde S.A., Sun M. 2002. Review of global 2.1–1.8 orogens: implications for a pre-Rodinia supercontinent. *Earth-Science Reviews*, **59**:125-162.

Zhao G., Sun M., Wilde S.A., Li S. 2004. A Paleo-Mesoproterozoic supercontinent: assembly, growth and breakup. *Earth-Science Reviews*, **67**:91-123.

Zuffa G.G. 1985. Optical analysis of arenites: influence of methodology on compositional results. *In:* Zuffa G.G, (ed.). Provenance of Arenites, NATO-ASI Series C:165-189.

ANEXO A – ARTIGO: NEW STRATIGRAPHIC PROPOSAL OF A PALEOPROTEROZOIC SILICICLASTIC SUCCESSION: IMPLICATIONS FOR THE EVOLUTION OF THE CARAJÁS BASIN, AMAZONIAN CRATON, BRAZIL

Journal of South American Earth Sciences 102 (2020) 102665

Contents lists available at ScienceDirect

Journal of South American Earth Sciences

journal homepage: www.elsevier.com/locate/jsames

New stratigraphic proposal of a Paleoproterozoic siliciclastic succession: Implications for the evolution of the Carajás Basin, Amazonian craton, Brazil

Roberto Costa Araújo Filho[a,*], Afonso C.R. Nogueira[a], Raphael Neto Araújo[a,b]

[a] Postgraduate Program in Geology and Geochemistry, Federal University of Pará, 66075-110, Belém, Brazil
[b] Management of Geology and Mineral Resources, Geological Survey of Brazil, 66095-904, Belém, Brazil

ARTICLE INFO

Keywords:
Paleoproterozoic
Stratigraphic framework
Azul Formation
Amazonian craton
Columbia supercontinent

ABSTRACT

In this study, we propose a new stratigraphic framework for a well-preserved Paleoproterozoic succession of the Carajás Basin (Amazonian craton) in northern Brazil. A core-based facies analysis is coupled with a critical review of previous data on this succession. We are proposing that the studied succession, which was previously considered as a single lithostratigraphic unit called the Águas Claras Formation, consists of two different formations of Paleoproterozoic age (~2.37–2.06 Ga). The lower formation, which is composed of ~250-m-thick mudstone strata locally enriched with manganese, is formally proposed here and is designated as the Azul Formation, referring to the Azul mine, in which the type-section is described. The overlying Águas Claras Formation is redefined as a stratigraphic unit composed exclusively of an ~800-m-thick succession of sandstone and conglomerate strata. The contact between these two formations is an easily recognizable surface; thus, these formations can be accurately mapped and distinguished within the basin. We suggest that the Azul and Águas Claras formations are the stratigraphic record associated with a transgressive–regressive sequence, in which these formations are limited one from the other by a maximum flooding zone. The Azul Formation was deposited during a marine transgression related to the latest incursion of the Azul sea towards the Carajás protocontinent. On the other hand, the overlying Águas Claras Formation was deposited in a fluvial system that developed during a period of marine regression. Whereas the marine transgression may have been influenced by the deglaciation occurred aftermath the Siderian–Rhyacian Serra Sul glaciation, the subsequent marine regression was triggered, at least in part, by uplifting related to the Transamazonian cycle (~2.0 Ga). In addition to our results shed new light on the Carajás Basin evolution, they support the hypothesis that the Azul and Águas Claras formations can be correlated with other Paleoproterozoic successions worldwide, mainly those registered in ancient landmasses that amalgamated and later formed the Columbia supercontinent during the Paleo-to Mesoproterozoic.

1. Introduction

The accurate reconstruction of the stratigraphic architecture of Paleoproterozoic successions and their paleoenvironmental interpretation are key in investigating the important geological events that occurred during that time interval. Among them, what stands out is the emergence of an oxygenated atmosphere at ~2.45 Ga (Bekker et al., 2004), the onset of the Great Oxidation Event (GOE; Holland, 2002), which was accompanied by paleoclimatic changes that culminated in a protracted cooling episode, generally named the Huronian Glacial Event at ~2.45–2.2 Ga (Tang and Chen, 2013; Young, 2014). Deposits resulting from these events are recorded in sedimentary basins that are scatteredly exposed in cratonic areas around the Earth. In the cratons, most basins are located in preserved segments from the global-scale tectonic deformation that occurred between ~2.1 and 1.8 Ga linked to the Columbia supercontinent assembly (Zhao et al., 2004).

In the Carajás Basin of the eastern Amazonian craton (Brazil), siliciclastic deposits attributed to the Águas Claras Formation are exposed immediately above the glaciogenic diamictite strata of Paleoproterozoic age (~2.58–2.06 Ga) that are grouped into the Serra Sul Formation (Araújo and Nogueira, 2019). Although the Águas Claras Formation has already been the object of stratigraphic and sedimentological studies (Docegeo, 1988; Nogueira, 1995; Nogueira et al., 1995; Costa, 2017; Araújo and Sousa, 2018), its stratigraphy remains controversial. According to previous work (e.g., Nogueira et al., 1995; Costa et al., 2005; Costa, 2017; Araújo and Sousa, 2018; Araújo and Nogueira, 2019), the Águas Claras Formation consists of various lithologies, some containing manganese deposits. Nogueira et al. (1995) proposed that the Águas

* Corresponding author.
E-mail addresses: rcaraujo@ufpa.br, costa.araujjo@gmail.com (R.C. Araújo Filho).

https://doi.org/10.1016/j.jsames.2020.102665
Received 7 January 2020; Received in revised form 22 May 2020; Accepted 24 May 2020
Available online 28 May 2020
0895-9811/

Claras Formation was deposited in various sedimentary environments, ranging from continental and coastal to marine.

The concentration of several mineral deposits in the Carajás Basin has motivated intense exploratory drilling, which has resulted in the large-scale sampling of the volcano-sedimentary succession that infills the basin. Although this basin was deformed during the ~2.0 Ga Transamazonian tectonic cycle (Cordani et al., 1984; Machado et al., 1991; Tavares et al., 2018), the most important recent tectonic event that the basin experienced, its stratigraphy is extensively preserved. Furthermore, delicate primary features are well preserved (Araújo and Nogueira, 2019). In that context, an investigation of the Águas Claras Formation from drill cores is crucial for the reconstruction of the internal architecture and facies distribution of this unit within the Carajás Basin.

In this study, we carried out a core-based facies analysis of the Águas Claras Formation in order to define in a more detailed fashion its stratigraphy and understand the variations in the depositional environment with time. Our new data provide new insights into the sedimentary evolution of the Carajás Basin, allowing us to correlate some of them with global-scale events that occurred during the Paleoproterozoic. Our results suggest that the studied succession consists of two formations: an older unit named the Azul Formation and defined for the first time in this study, and the overlying Águas Claras Formation that we redefine according to our new observations. Such lithostratigraphic units were deposited during distinct times of evolution of the Carajás Basin and record important paleoenvironmental changes that occurred in this part of the Amazonian craton.

2. Geological setting

The Carajás Basin, also known as the central sigmoid of Carajás (Araújo et al., 1988; Araújo and Maia, 1991; Pinheiro, 1997; Pinheiro and Holdsworth, 1997; Holdsworth and Pinheiro, 2000), is situated in the eastern portion of the Amazonian craton in northern Brazil (Fig. 1). This basin is located in the Carajás block, which along with the Transition subdomain and Rio Maria block constitutes the Carajás province (Dall'Agnol et al., 1997, 2006; Althoff et al., 2000). The basement of the Carajás Basin comprises ~2.85 Ga Mesoarchean igneous and metamorphic rocks, which include granite and gneiss of tonalite–trondhjemite–granodiorite (TTG) type, belonging to the Xingu Complex (Machado et al., 1991). Besides that, the Pium Diopside-Norite Complex which comprises norite, gabbro and diorite of ~3.0 Ga (Pidgeon et al., 2000) and the Chicrim-Cateté orthogranulite unit are considered by many authors (Araújo and Maia, 1991; Vasquez et al., 2008b) to be part of the basement assembly of this basin as well.

The limits of the Carajás Basin are difficult to establish. During the Transamazonian cycle that took place at ~2.0 Ga (Cordani et al., 1984; Machado et al., 1991; Macambira et al., 2009; Tavares et al., 2018), a large part of the Carajás Basin was segmented into different compartments that present a complex history of deformation and metamorphism. Currently, the Carajás Basin is limited by the Bacajá block to the north and by the Transition subdomain to the south (Dall'Agnol et al., 2006; Feio et al., 2013). The ~1.88 Ga Carajás granite and dike swarms (Machado et al., 1991; Teixeira et al., 2018a, 2018b; Giovanardi et al., 2019) cross-cut the Carajás Basin, post-dating the deposition within the basin.

One of the crucial problems regarding the stratigraphy of this basin is related to the diversity of stratigraphic proposals, some of which designate the same set of rocks using different names (e.g., Docegeo, 1988; Araújo et al., 1988; Araújo and Maia, 1991; Pinheiro, 1997; Tavares et al., 2018). Araújo and Nogueira (2019) proposed that the volcano-sedimentary succession of the Carajás Basin is composed from the base to the top of the following: the Grão-Pará Group (Parauapebas, Carajás, and Igarapé Bahia formations), Serra Sul Formation, Águas Claras Formation and Gorotire Formation (Fig. 2). The oldest unit of the basin, according to these authors, is represented by the Parauapebas Formation, which encompasses a pile ~2–3-km-thick of felsic to mafic volcanic rocks dated at ~2.75 Ga (Gibbs et al., 1986; Wirth et al., 1986; Olszewski et al., 1989; Gibbs and Wirth, 1990; Trendall et al., 1998a; Macambira, 2003; Zucchetti, 2007; Cabral et al., 2013; Martins et al., 2017).

The overlying Carajás Formation contains banded iron formation (BIF) strata with a thickness of ~250–300 m (Cabral et al., 2013), which an origin linked to biomats was attributed to its deposition during the Neoarchean (Luz and Crowley, 2012). The BIF deposits are overlain by a set of volcanic and volcaniclastic rocks, as well as subordinate deep-water marine turbidite strata belonging to the Igarapé Bahia Formation (Dreher, 2004; Dreher et al. 2005, 2008; Tallarico et al., 2005; Galarza et al., 2008). Although this unit has been considered as a group by some authors (e.g., Docegeo, 1988; Machado et al., 1991; Dreher et al., 2005), we follow in this work the stratigraphic framework proposed by Araújo and Nogueira (2019), who defined this unit as a formation. The mafic volcanic rocks of the Igarapé Bahia Formation have an age of ~2.74 Ga (Tallarico et al., 2005) and Cu–Au mineralization age of ~2.74 Ga (Galarza et al., 2008) as well, indicating that these events were coeval. This Cu–Au mineralization was remobilized at ~2.57 Ga, suggesting that a tectonic and/or a hydrothermal event may have occurred at this age (Tallarico et al., 2005).

The Grão-Pará Group is overlain in unconformity by siliciclastic rocks ~600 m in thickness, of the Serra Sul Formation. This formation is composed of subglacial and marine diamictite interbedded with mudstone and black shale strata of Siderian–Rhyacian age (~2.58–2.06 Ga; Araújo and Nogueira, 2019). Above these glaciogenic deposits, siliciclastic deposits of the Águas Claras and Gorotire formations occur. The Gorotire Formation, which comprises a set of conglomerate and sandstone strata deposited in an alluvial to the fluvial system (Beisiegel et al., 1973; Araújo et al., 1988; Pinheiro and Holdsworth, 1997; Pinheiro, 1997; Nascimento and Oliveira, 2015), presents a maximum depositional age of ~2.0 Ga (Pereira et al., 2009; Justo et al., 2018).

The Águas Claras Formation consists of a set of mudstone, siltstone, sandstone, and conglomerate that crops out in the central part of the Carajás Basin and is commonly folded and faulted as a result of deformation and very low-grade metamorphism (Araújo et al., 1988; Pinheiro, 1997). These rocks are known for hosting the Azul manganese deposits, which include claystone, siltstone, and fine-grained sandstone with shale partings rich in organic matter, oxides, and hydroxides of manganese, marl and manganesiferous carbonate (Costa et al., 2005; Costa, 2017). Due to the Águas Claras Formation being so heterogeneous, a wide range of depositional environments was interpreted, such as marine to coastal, braided fluvial, meandering fluvial, fluvial/aeolian and lagoonal to deltaic (Barbosa et al., 1966; Beisiegel et al., 1973; Hirata et al., 1982; Figueiras and Villas, 1984; Ramos et al., 1984; Gibbs et al., 1986; Docegeo, 1988; Macambira et al., 1990; Araújo and Maia, 1991).

Nogueira et al. (1995), studying outcrops of the Águas Claras Formation along the Bahia road, redefined the Águas Claras Formation and divided it into two members. The Lower Member comprises marine platform deposits, which transitionally grade stratigraphically upward into the Upper Member that consists dominantly of sandstone and conglomerate deposited in a coastal to fluvial system. Additionally, Nogueira et al. (1995) interpreted this succession as the result of upward shallowing, which caused the progradation of the fluvial system on the coastal and platformal deposits.

3. Materials and methods

A core-based stratigraphic and facies analysis was undertaken in this study. The drill cores were made available by Vale S.A., a mining company situated in Parauapebas county in northern Brazil. This company has a vast collection of cores drilled during the last several decades of mineral exploration of the region. The studied drill cores

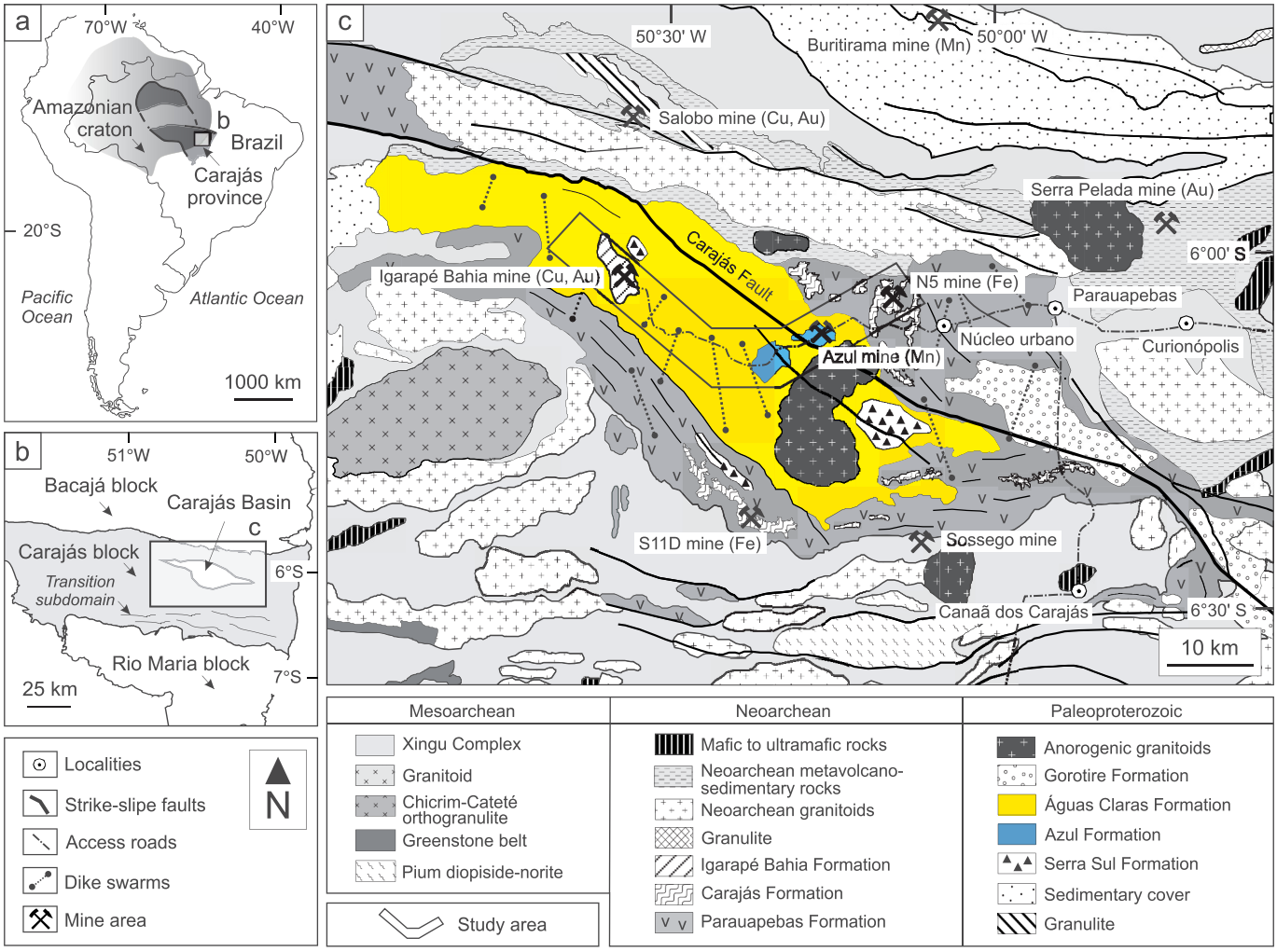

Fig. 1. Map of study area. (a) South America map showing the location of the Amazonian craton and the Carajás province in northern Brazil. (b) Carajás province map showing the location of the Carajás Basin in the Carajás block. (c) Geological map of the Carajás Basin showing the location of study area. Modified from Vasquez et al. (2008a). The areas in which the Azul and Serra Sul formations occur were based on data presented in Nogueira et al. (1995) and Araújo and Nogueira (2019), respectively. The lithostratigraphic units investigated in this study are highlighted.

varied in depth from ~150 m to ~1009 m. They were selected in order to encompass as great a lateral variation as possible. In general, we selected those cores which were as lithologically heterogeneous as possible and in which lithological contacts may be recognized. Additionally, we correlated the core-based logs obtained from this study with previously studied outcrops within the Carajás Basin (Table 1; Supplementary Table A1).

The selection of these outcrops was strategic as well, as they help to improve the stratigraphic resolution of the succession. They include the outcrops in the Igarapé Bahia mine described in Docegeo (1988), those along the Bahia road described in Nogueira et al. (1995), those in the Azul mine described in Araújo and Sousa (2018), and the ones observed in the drill core FD-706 described in Costa (2017). Whereas no samples were collected from the previously studied outcrops, small pieces of rock were sampled from the drill cores investigated in this study, and petrographic analysis was performed to improve the field description. The thin sections were prepared and analyzed in the Laboratory of Petrography of the Federal University of Pará (Institute of Geoscience), Belém, Brazil.

The facies analysis followed the methodology proposed by Walker (1992, 2006), which requires that the paleoenvironmental reconstruction of a sedimentary unit should be carried out from the detailed study of the sedimentary facies, a full understanding of the depositional processes, and the identification of genetically related sets of facies, which must be subsequently organized in facies associations that reflect different depositional systems. Accordingly, the facies were interpreted mainly based on the lithology that constitutes them and the sedimentary processes were interpreted through the structures and textures observed in the different lithofacies. The key surface was identified and interpreted with respect to their depositional significance from the stratigraphic definitions based on the Sequence Stratigraphy concepts presented in Embry (2002).

4. Results

4.1. The newly defined Azul Formation

In this study, we are proposing that the two members of the Águas Claras Formation may both be elevated to the category of formation, thereby constituting two different formations, which are limited one from the other by a stratigraphic surface that may be mapped throughout this basin. The lower formation is being formally proposed in this study, and was designated as the Azul Formation. This formation encompasses rhythmite deposit ~250–300-m-thick, in which manganese-bearing mudstone occurs subordinately interlayered. Similarly, the Águas Claras Formation is being redefined herein as well. We propose that this formation encompasses only sandstone and conglomerate deposits ~800–850-m-thick stacked in meter-scale fining-upward

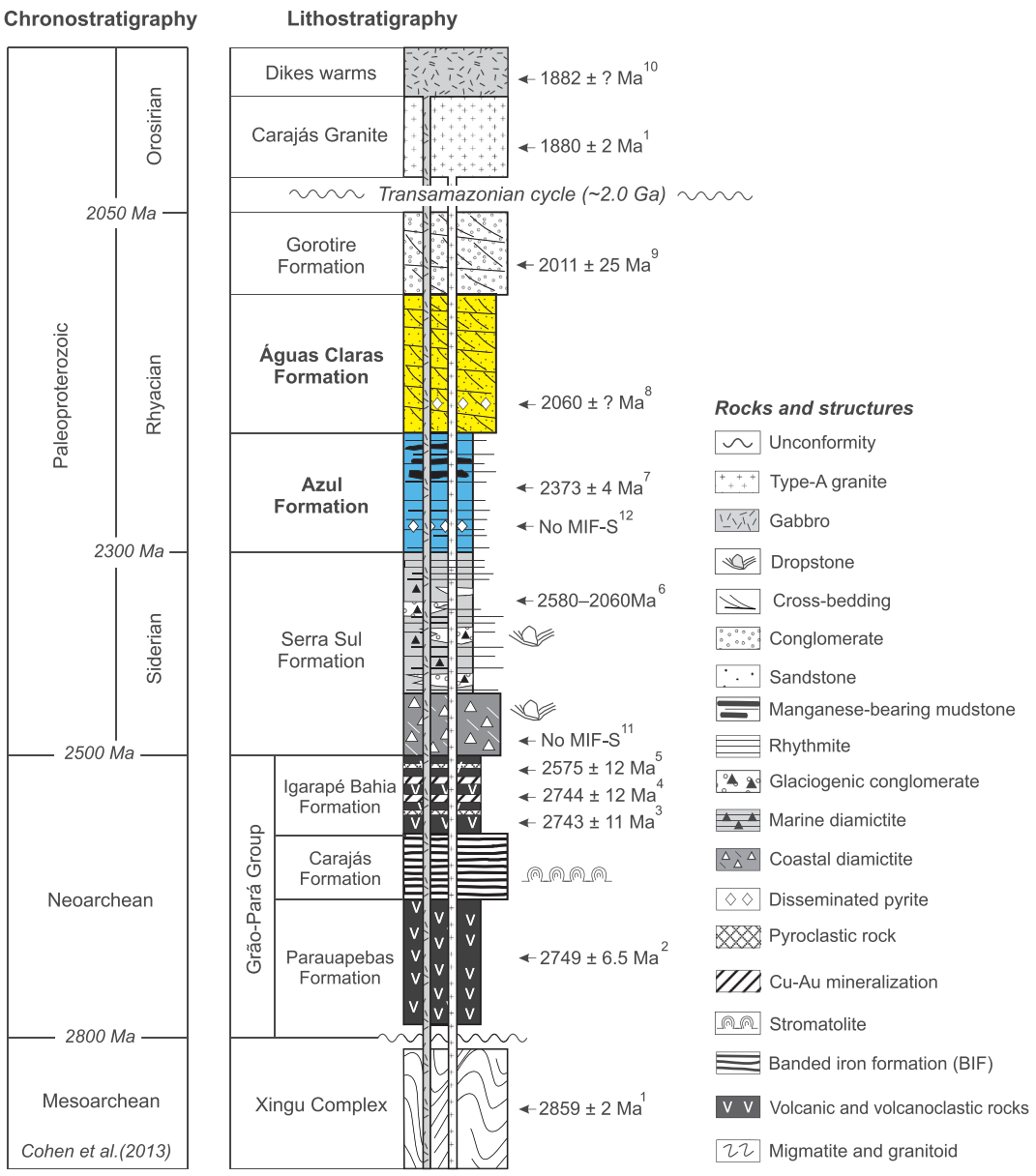

Fig. 2. Stratigraphy of the Carajás Basin, Amazonian craton, Brazil (modified from Araújo and Nogueira, 2019). Geochronological data compiled from: 1—Machado et al. (1991); 2—Martins et al. (2017); 3—Trendall et al. (1998a); 4—Galarza et al. (2008); 5—Tallarico et al. (2005); 6—Araújo and Nogueira (2019); 7—Justo et al. (2018); 8—Mougeot et al. (1996b); 9—Pereira et al. (2009); 10—Giovanardi et al. (2019). The data of mass-independent sulfur isotope fractionation (MIF-S) was compiled from: 11—Cabral et al. (2013); 12—Fabre et al. (2011). The age of Transamazonian cycle was based on data presented in Cordani et al. (1984) and Macambira et al. (2009). The chronostratigraphic column was adapted from Cohen et al. (2013). The significance of geochronological and geochemical data is discussed in the text.

Table 1
Summary of drill cores and outcrops investigated in this study.

Type of occurrence	Name	Thickness	Location	Lithostratigraphic units	Reference
Drill core	ALV8-FD06	~1009 m	Igarapé Bahia mine area	Igarapé Bahia and Águas Claras formations	This study
Drill core	AN10-DH0001	~201 m	Bahia road area	Azul Formation	
Drill core	AN10-DH0002	~204 m	Bahia road area	Azul and Águas Claras formations	
Drill core	MNA-FD-1096	~208 m	Azul mine area	Azul Formation	
Drill core	MNA–FH–0933	~150 m	Azul mine area	Azul Formation	
Drill core	ITA-GT-58-FD0002	~316 m	Bahia road area	Azul and Águas Claras formations	
Outcrop	Bahia mine	~30 m	Igarapé Bahia mine area	Igarapé Bahia and Águas Claras formations	Docegeo (1988)
Outcrop	Bahia road	~300 m	Bahia road area	Azul and Águas Claras formations	Nogueira et al. (1995)
Drill core	FD-706	~100 m	Azul mine area	Azul Formation	Costa (2017)
Outcrop	Azul mine	~60 m	Azul mine area	Azul and Águas Claras formations	Araújo and Sousa (2018)

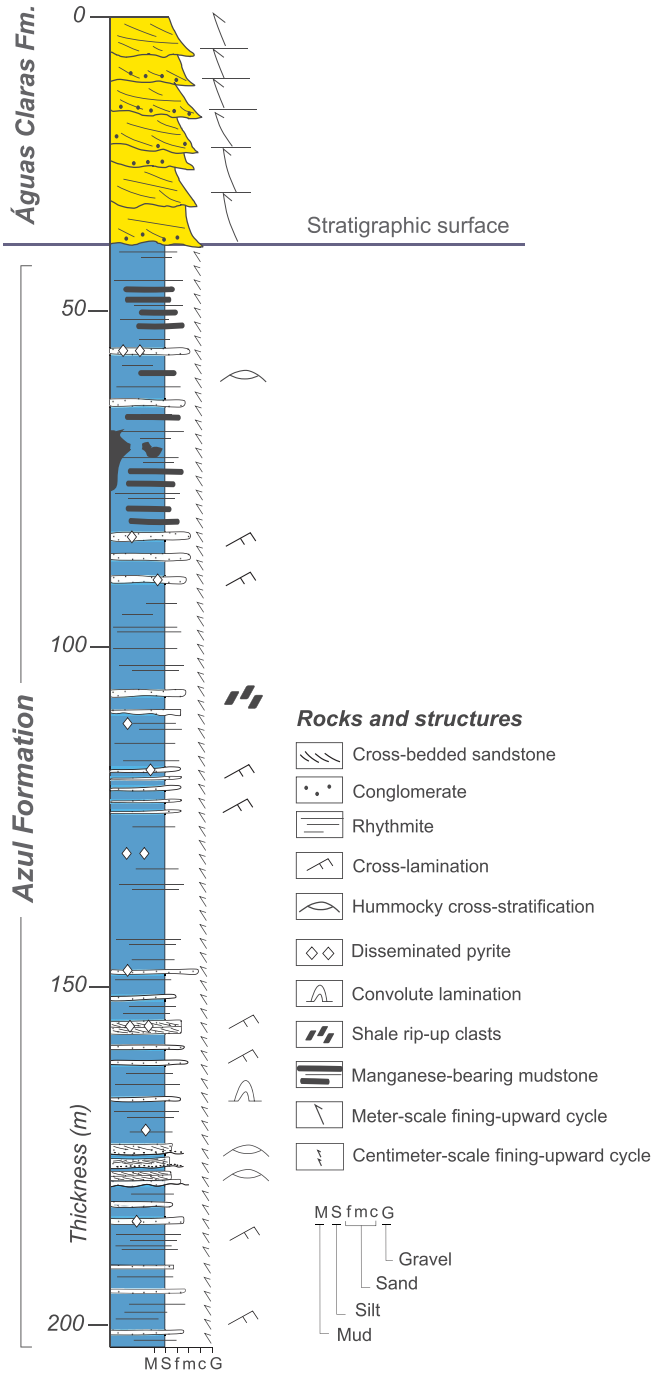

Fig. 3. Type section of Azul Formation, which may be described in the Azul mine, showing its sedimentological and stratigraphic stacking pattern.

cycles, which occur above the Azul Formation.

The type section of the Azul Formation was defined within the homonymous mine, in which these deposits occur well exposed both in outcrops along the mine pit and in drill cores from the base of this mine (Fig. 3). Thus, the type section of this formation corresponds to the composite profile of the Azul mine. Although we choose this name to designate the Azul Formation, obviously this lithostratigraphic unit is not restricted to the limits of this mine. On the other hand, the type section of the Águas Claras Formation is maintained along the Bahia road, as previously defined by Nogueira et al. (1995).

The proposition of the Azul Formation as a formal lithostratigraphic unit of the Carajás Basin is appropriate for several reasons and can be justified as follows: 1) The Azul Formation encompasses a set of rocks (rhythmite and mudstone) starkly contrasting with the Águas Claras Formation rocks (sandstone and conglomerate); 2) The Azul Formation constitutes a thick deposit that may be mapped separately from the Águas Claras Formation throughout the Carajás Basin, both surface and subsurface; 3) The manganese deposits that are strictly hosted in the Azul Formation are a distinctive feature of this unit, which makes this formation unmistakable vis-à-vis the adjacent units, and; 4) This new stratigraphic framework simplifies the stratigraphy of the Carajás Basin, allowing these formations to be widely correlated with other units within and outside the basin.

4.2. Stratigraphy and sedimentology of studied succession

4.2.1. General aspects

The siliciclastic succession investigated in this study is approximately 1100-m-thick (Fig. 4). This succession encompasses mudstone, sandstone, tuffaceous sandstone, and conglomerate strata belonging to the Azul and Águas Claras formations. The succession is intruded by gabbroic dikes up to ~30-m-thick, which cross-cut the succession indistinctly. We defined five lithofacies to these formations, which were subsequently arranged into two distinct facies associations. The lower facies association belongs to the Azul Formation, while the upper belongs to the Águas Claras Formation (Table 2). These facies associations are limited by a stratigraphic surface that may be observed in almost all cores studied and in the reevaluated outcrops of the Azul and Águas Claras formations. This stratigraphic surface may be mapped in several parts of the basin, and represents the contact between these formations, presenting in some sections an abrupt feature and in others a transitional one.

On the other hand, neither the basal contact of the Azul Formation nor the top contact of the Águas Claras Formation was observed. In some places (e.g., drill core ALV8-FD06 and Igarapé Bahia mine outcrop), the Águas Claras Formation deposits occur above the volcanic rock of the Igarapé Bahia Formation, which shows its typical features such as amygdaloidal and aphanitic textures and greenish colors.

In general, the succession is greyish to black colored. The black to grey colors result from the occurrence of organic matter and oxides/hydroxides of manganese, while the green color is mainly due to chloritization. This last mineral alteration is possibly related to the percolation of fluids associated with hydrothermal events. The hydrothermalism partially altered the primary mineralogy of the rocks, causing the less resistant minerals to be replaced by hydrothermal mineral phases, mainly chlorite and silica. Importantly, although the succession is tilted and faulted, these aspects did not hinder the facies analysis, and the primary textures and structures are well preserved.

4.2.2. Facies associations

4.2.2.1. Facies association 1 (FA1): offshore deposits

4.2.2.1.1. Description. The first facies association described in this study belongs to the Azul Formation, occurring at the base of the studied succession, and was designed as Facies Association 1 (FA1). In the stratigraphic succession, this facies association comprises a monotonous interval ~200-m-thick (Fig. 4). In the study area, it extends laterally in the order of kilometers and comprises rhythmite, mudstone, and sandstone lithofacies (Fig. 5; Table 2). Rhythmite is the dominant lithofacies of this facies association and is constituted by intercalation between normally graded sandstone and mudstone, stacked in millimeter-to centimeter-scale fining-upward cycles. Soft-sediment deformation structures, such as convolute laminations, load clasts, ball-and-pillow, and flame structures are widespread, being in contact between sandy and muddy laminations.

Mudstone and sandstone beds occur subordinately. Mudstone beds are up to ~10-m-thick and display even-parallel lamination and massive bedding. Manganese-enriched intervals occur locally in rhythmite lithofacies. Fine-to medium-grained sandstone generally shows a mud-rich matrix, and the quartz grains are rounded-to well-rounded and

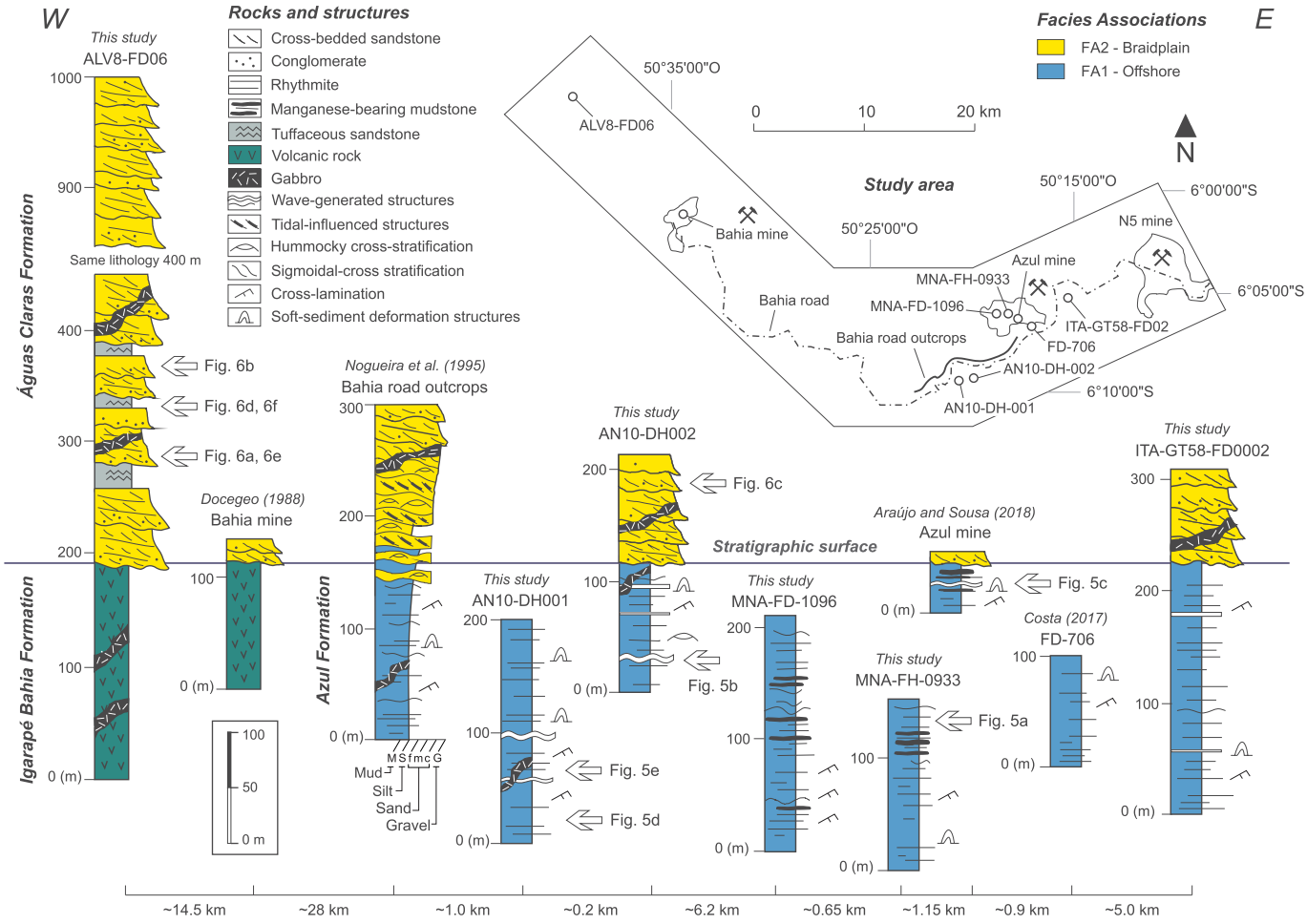

Fig. 4. Stratigraphic correlation between studied drill cores and outcrops in Azul and Águas Claras formations. Numbers and letters to right of the columns correspond to photos in Figs. 5 and 6.

well-to moderately sorted. Sandstone beds are up to ~6-m-thick, in which even-parallel lamination, climbing ripple cross-lamination, intrinsically interwoven cross-lamination, pinch-and-swell structure, and hummocky cross-stratification are recurrent. In these beds euhedral pyrite occurs finely disseminated, varying from ~0.5 to ~2.5 mm in size.

4.2.2.1.2. Interpretation. The lateral distribution of rhythmite and mudstone facies in order of kilometers, as well as the great thickness of these deposits indicate that these were sedimented in a well-developed, extensive, mud-dominated, and low energy environment. These sedimentological features strongly suggest that the Azul sediments were deposited in the offshore zone of a marine setting, which was partially connected with a coastal environment influenced by tidal and wave processes. This interpretation is strongly supported by the data presented in several previous studies (e.g., Nogueira et al., 1995; Pinheiro, 1997; Araújo and Sousa, 2018; Costa, 2017). Moreover, the interpretation of these sediments having been deposited in a marine environment is strengthened by the fact that primary manganese deposits are widespread in ancient marine deposits, mainly those Paleoproterozoic in age (e.g., Sekine et al., 2011; Dasgupta et al., 1992; Roy, 1997, 2006).

The rhythmite facies was interpreted as turbiditic deposits. This facies is generally pointed out as the diagnosis of an offshore zone in marine deposits (Stow et al., 1996). They originated from the passage of low-density turbidity currents, with the predominance of suspension and subordinate traction at the bottom of the marine basin (Lowe, 1982). The alternation between normally graded sandstone and mudstone stacked in millimeter-to centimeter-scale fining-upward cycles strongly suggests that these deposits correspond to the T_d and T_e divisions of Bouma (1962), respectively. These deposits may be correlated to the fine-grained turbidite deposits of Stow et al. (1996), which correspond to T_0–T_8 intervals of Stow (1979) and to E_1–E_3 intervals of Piper (1978). In this sense, the sandstone beds could match the T_b and T_c divisions of Bouma (1962). It is hypothesized that these turbidity deposits were deposited below the storm wave base as well. During periods of expansion of the marine basin, thick deposits of turbidity were deposited on the seafloor. Similarly, manganese precipitated as oxides during marine transgression, when upwelling currents promoted the maximum circulation of oxygenated waters into the basin (Roy, 1997, 2006).

The synsedimentary deformation structures were interpreted as possibly having originated from hydroplastic adjustments of water-saturated horizons (Lowe, 1975, 1976). The sandstone beds, which occur intercalated with rhythmite and mudstone beds, originated possibly during the passage of predominantly unidirectional currents at the bottom of the basin, associated with rapid sedimentation and upward fall in flow energy. Besides, the poorly observed internal lamination in such sandstone facies is possibly related to the low granulometric contrast of the sediments (De Raaf et al., 1977). The occurrence of wave-generated structures at some intervals indicates that eventually oscillatory flows reworked sediments, linked possibly to recurrent fluctuations at the base level. Similarly, the occurrence of hummocky cross-stratification in these strata strongly suggests the action of storm waves on the marine platform (Cheel and Leckie, 1993; Dumas and Arnott, 2006).

Table 2
Summary of facies, sedimentary processes and facies associations interpreted to the Azul and Águas Claras formations.

Formation	Facies association	Facies	Description	Interpreted processes
Azul Formation	(FA1) Offshore	Rhythmite	Normally graded sandstone and laminated mudstone repeatedly stacked in millimeter to centimeter-scale fining-upward cycles. Disseminated pyrite in sandstone beds. Soft-sediment deformation structures.	Alternation of sedimentation by traction and suspension in low-density turbidity currents. High rates of suspended load fallout.
		Mudstone	Laminated and massive bedding, with high organic matter content. Tabular geometry (inferred).	Deposition by suspension. Low-energy environment, associated with preservation of organic matter.
		Sandstone	Fine- to medium-grained. Parallel lamination. Disseminated pyrite. Wave-generated cross-lamination. Hummocky cross-stratification. Climbing ripple-cross lamination.	Deposition by predominant unidirectional flow (currents) and oscillatory flow (wave). Combined flow, predominantly oscillatory (storm wave).
Águas Claras Formation	(FA2) Braidplain	Sandstone	Medium- to coarse-grained. Massive bedding, plane-parallel lamination, planar cross-bedding and trough cross-bedding. Predominantly quartz and chert grains.	Rapid deposition, unidirectional flow and migration of 2D and 3D bedforms. Lower flow-regime conditions.
		Conglomerate	Massive to incipient cross-bedding. Normal grading. Quartz, BIF, iron formation and chert clasts. Stacked with sandstone in meter-scale fining-upward cycles.	Rapid deposition by high-energy traction currents. Migration of longitudinal bedforms and sediments reworking. Lower flow-regime conditions.
		Tuffaceous sandstone	Layers with sand grains, crystals, rock fragments and fine matrix. Poorly sorted. Preserved eutaxitic texture.	Subaerial pyroclastic flow with deposition of sand-sized grains and ash-fall.
		Mudstone	Laminated to massive. Subordinately interbedded with sandstone. Top of fining-upward cycles.	Deposition in low-energy environment, possibly in standing water.

4.2.2.2. Facies association 2 (FA2): braidplain deposits

4.2.2.2.1. Description. The second facies association described in this study, belonging to the Águas Claras Formation, occurs at the top of the succession and was designated as Facies Association 2 (FA2). In the stratigraphic succession, this facies association occurs overlying the FA1 deposits and comprises a thick interval of ~800-m-thick (Fig. 4). In the study area, this facies association extends laterally in the order of dozens of kilometers and encompasses sandstone, conglomerate, and tuffaceous sandstone lithofacies (Fig. 6; Table 2). Sandstone and conglomerate are the dominant lithofacies, which occur stacked in centimeter-to meter-scale (~0.3–3-m-thick) fining-upward cycles. The sandstone facies are fine-to coarse-grained, showing massive bedding, even-parallel stratification, planar cross-bedding, and trough cross-bedding. The grains are sub-to well-rounded and well-to poorly sorted, and composed mainly by quartz and chert.

The conglomerate facies is massively to incipiently cross-bedded, occurring at the base of fining-upward cycles. This lithofacies show an erosive base as an intrinsic feature and graded toward the top to sandstone lithofacies. The clasts are predominantly composed of chert, jaspilite, and BIF fragments. They vary from ortho-to para-conglomerate, and the matrix is granular to sandy, in which well-rounded pebbles occur embedded. Tuffaceous sandstone and mudstone lithofacies occur subordinately in this facies association. The former comprise beds up to ~8-m-thick, in which altered feldspar grains (chloritized) and fine tuff laminations occur repeatedly interbedded with sandy laminations. Mudstone facies on the other hand comprise beds up to ~20-cm-thick, which occur interbedded with sandstone strata close to the top of fining-upward cycles. Pyrite, finely disseminated, occurs in these strata as well.

4.2.2.2.2. Interpretation. The occurrence of conglomerate beds with erosive base, repeatedly interbedded with sandstone facies, stacked in meter-scale fining-upward cycles, strongly suggests that these deposits occurred in a braidplain environment. The occurrence of sandstone with planar cross-bedding and trough cross-bedding indicates a predominance of migration of sinuous-crested bars (3D) and straight-crested bars (2D) under unidirectional flow in lower flow regime (Lindholm, 1987; Collinson, 1996; Tucker, 2003; Miall, 2006). The massive texture of this facies probably originated through rapid deposition, or alternatively due to the destruction of primary structures by soft-sediment deformation process (Lowe, 1975; Hjellbakk, 1997; Tucker, 2003; Miall, 2006). In turn, the occurrence of conglomeratic facies showing incipient cross-bedding and normal grading suggests rapid deposition from high-energy traction currents in lower flow regime, associated with high rates of water discharge and sediment concentration under unidirectional flow.

The migration of longitudinal bars is suggested by the occurrence of incipient cross-bedding, associated with sediments having a granulometric contrast and/or as a result of variations in the flow energy in the fluvial channels (Steel and Thompson, 1983; Collinson, 1996; Miall, 2006). These facies suggest that sandy to conglomeratic bars deposited in the fluvial channels were constantly reworked by variations in flow energy on the braidplains. The recurrent fining-upward cycles consisting of sandy and conglomeratic beds, combined with the absence of floodplain muddy facies, indicate the predominance of bedload and the high rate of sediment influx in the filling of channels in the fluvial plain. Such characteristics are consistent with the fluvial system of the braided type, which had been the predominant fluvial system in Precambrian times.

These systems comprise a network of shallow, broad, interconnected and unconfined channels, with high rates of fluvial erosion and migration favored by the existence of easily erodible margins due to the absence of vegetation and because of poorly developed soil (Miall, 1977, 1981; Long, 1978, 2004; Bhattacharyya and Morad, 1993; Hjellbakk, 1997; Eriksson et al., 1998, 2004; Bose et al., 2012). The occurrence of tuffaceous sandstone facies in this facies association is interpreted as events of subaerial pyroclastic flow that occurred

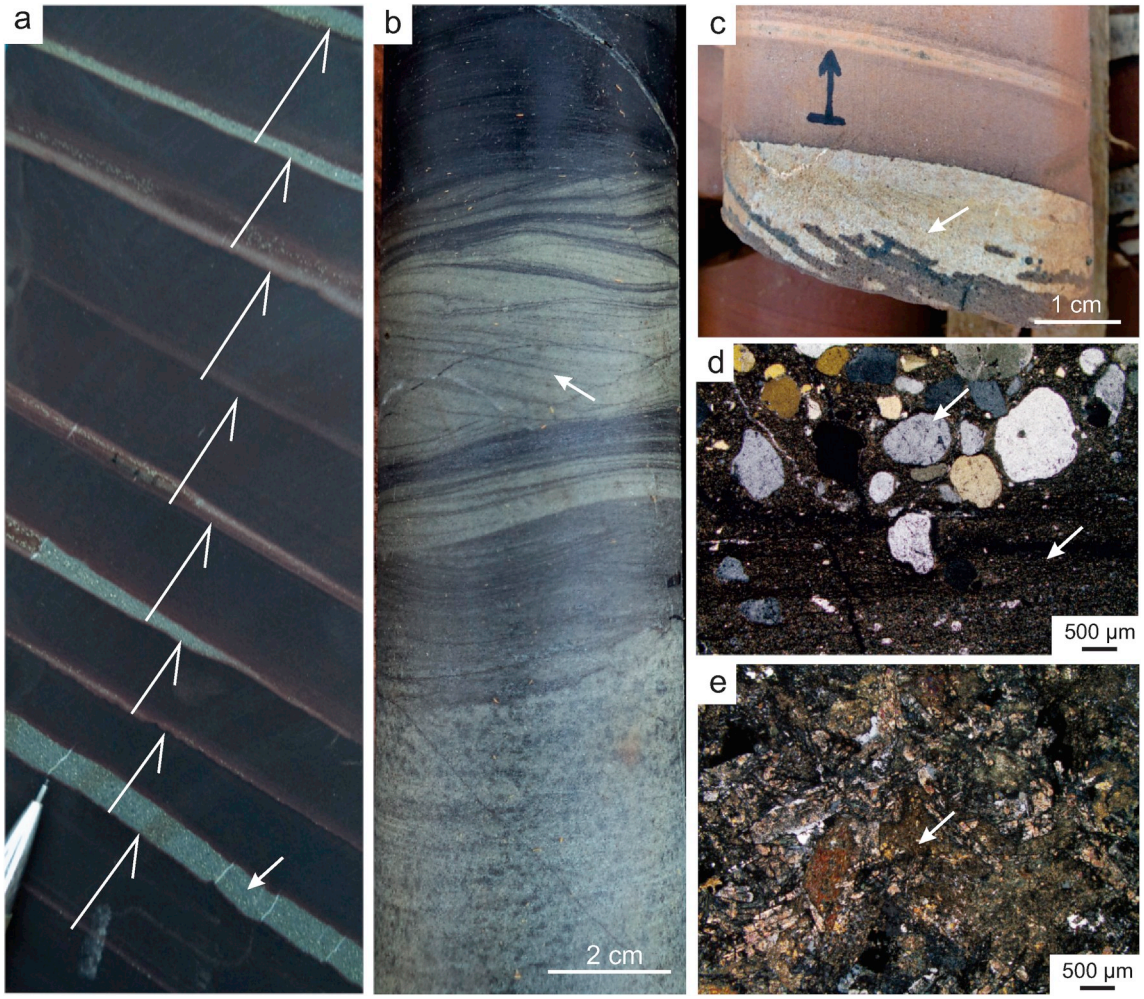

Fig. 5. Sedimentological features of the Facies Association 1 (FA1) representative of offshore deposits belonging to the Azul Formation of the Carajás Basin (Amazonian craton, Brazil). (a) Rhythmite facies showing intercalation between normally graded sandstone and mudstone stacked in centimeter-scale fining-upward cycles. Disseminated pyrite (arrow) occurs in sandy laminations. (b) Rhythmite facies showing a complete fining-upward cycle, in which a bed of wave-generated cross-laminated sandstone (arrow) is sandwiched by mudstone intervals. (c) Rhythmite facies showing a centimeter-scale sandy interval in which current-generated cross-lamination enriched with manganese may be observed (arrow). (d) Thin section photomicrograph (cross-polarized light, 10 ×) of rhythmite showing a contact observed at the base of millimeter-scale fining-upward cycle between plane-parallel laminated mudstone (arrow) and normally graded to matrix-supported sandstone (arrow). (e) Thin section photomicrograph (cross-polarized light, 10 ×) of gabbro from a dike, intrusive in the Azul and Águas Claras formations, showing an intensely altered (arrow) primary mineralogy (chloritization).

relatively close to the fluvial system. On the other hand, the lack of fragments of lapilli, blocks, or bombs suggests distal sedimentation (Fisher, 1961; McPhie et al., 1993; Orton, 1996), which was dominated by the deposition of sand-sized grains and ash-fall.

5. Discussions

5.1. Re-evaluating outcrops and units of the Carajás Basin

Historically, the correlation between outcrops and drill cores that extend through the Azul and Águas Claras formations has always been hindered by the failure to recognize and correlate key surfaces and stratigraphic horizons in these lithostratigraphic units. In this study, based on the stratigraphic proposal presented, it was possible to undertake a re-evaluation of outcrops and units of the Carajás Basin. The reinterpretation of these units and outcrops provides important information on the lateral variation of facies and facies associations and allows the establishment of a more exhaustive stratigraphic framework for the studied succession. The stratigraphic framework observed in these outcrops is quite similar to that observed in drill cores investigated in this study.

In the Igarapé Bahia mine, Docegeo (1988) described a thick package >1 km (in thickness) of volcano-sedimentary and pyroclastic rocks interbedded with subordinate amounts of rhythmite and BIF strata, which was named as the Grota do Vizinho Formation. According to this author also, the Grota do Vizinho Formation is overlain by ~100-m-thick sandstone deposits, which was named as the Sumidouro Formation. These two formations would belong to a single unit, called the Igarapé Bahia Group. In our reevaluation of this outcrop in the Igarapé Bahia mine, the Grota do Vizinho Formation is correlative to the Igarapé Bahia Formation (sensu Araújo and Nogueira, 2019), whereas the Sumidouro Formation is correlative to the newly redefined Águas Claras Formation. The stratigraphic framework observed in the Igarapé Bahia mine is similar to that observed in the drill core ALV8-FD-06 described in this study (Fig. 4).

As mentioned previously, at the outcrops along the Bahia road, Nogueira et al. (1995) described the Águas Claras Formation as being constituted of two members, in which the mud-dominated Lower Member grades up into the sand-dominated Upper Member. In this study, we are elevating these members to the formation category, in which the Lower Member is correlative to the Azul Formation, and the Upper Member is correlative to the Águas Claras Formation. Therefore,

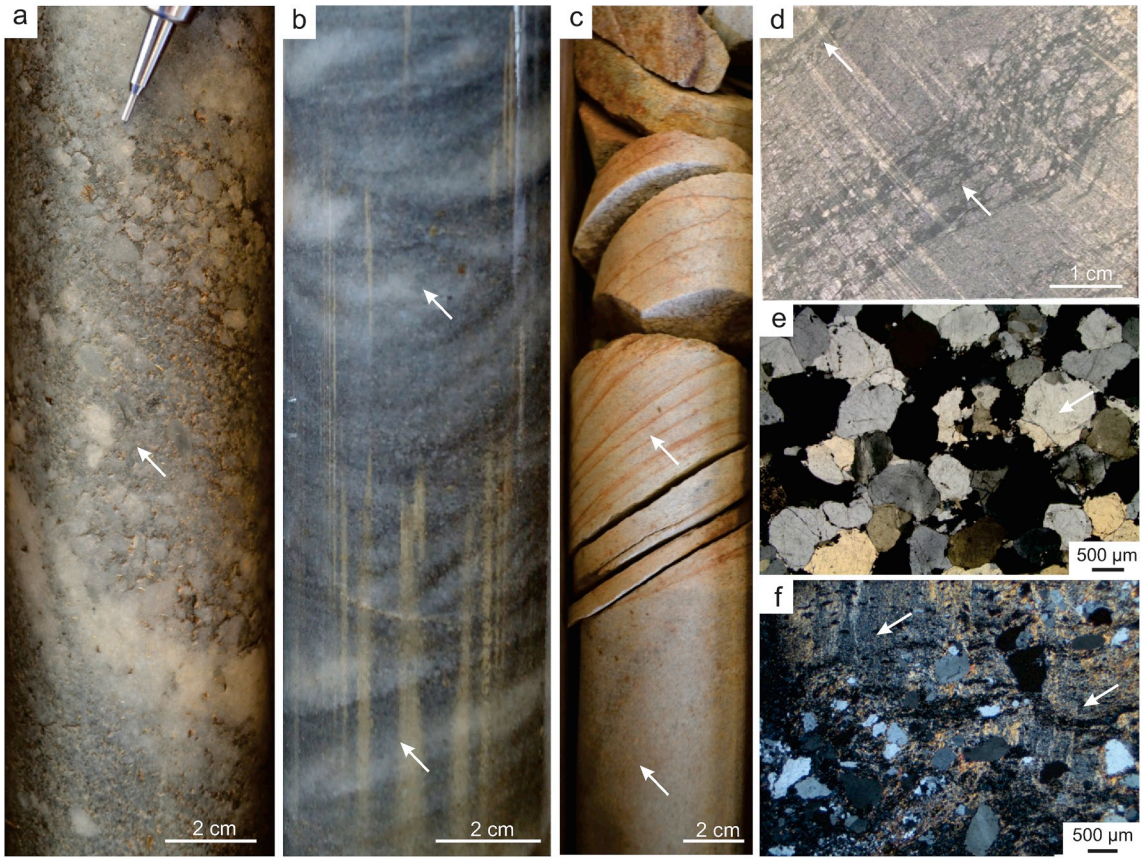

Fig. 6. Sedimentological features of the Facies Association 2 (FA2) representative of braidplain deposits belonging to the Águas Claras Formation of the Carajás Basin (Amazonian craton, Brazil). (a) Trough cross-bedding conglomerate (arrow) observed at base of meter-scale fining-upward cycles, tending to sandstone facies toward the top. (b) A coset of cross-stratified sandstone showing trough cross-bedding from two perspectives, oblique and perpendicular from bottom to top (arrows). (c) Massive and planar cross-bedded sandstone upward stacked (arrows). (d) Intervals of tuffaceous sandstone (arrows) repeatedly interbedded with medium-to coarse-grained sandstone. (e) Thin section photomicrograph (cross-polarized light, 10 ×) of sandstone showing quartz grains (arrow) varying from medium-to coarse-sand in size. (f) Thin section photomicrograph (cross-polarized light, 10 ×) of tuffaceous sandstone showing an intensely altered (arrow) primary mineralogy (chloritization).

along the Bahia road, both the Azul and Águas Claras formations are exposed, and may be mapped on the surface and subsurface. The stratigraphy observed at these outcrops correlates to the stratigraphy observed in drill cores AN10-DH001 and AN10-DH002 described in this study (Fig. 4).

Macambira et al. (1990) and Macambira (2003) proposed the names Igarapé Cigarra and Igarapé Boa Sorte formations respectively to refer to the units that occur immediately above the BIF strata of the Carajás Formation. In this study, we correlate the Igarapé Cigarra Formation to the Igarapé Bahia Formation and the Igarapé Boa Sorte Formation with the Azul Formation. We opted to use the latter designations instead of others, considering that the Igarapé Cigarra and Igarapé Boa Sorte formations are not formally proposed units and that these designations are rarely used in the literature. Importantly, in this study we did not observe the contact between the Igarapé Bahia and Azul formations.

Araújo and Sousa (2018) presented the measured stratigraphic profile of the Azul mine. They attributed the entire profile to the Águas Claras Formation. In this study, we correlate the lower unit, which hosts manganese-enriched mudrock strata, with the Azul Formation, whereas the upper unit, which comprises a set of sandstone and conglomerate strata, is correlated with the Águas Claras Formation. The stratigraphy observed in the Azul mine is similar to that observed in the drill cores MNA-FD-1096, MNA–FH–0933 and ITA-GT58-FD0002 described in this study. Furthermore, the stratigraphy observed in the core FD-706 (Costa, 2017) is similar to that observed in the Azul mine (Fig. 4).

5.2. Reassessing the depositional age of the Azul and Águas Claras formations

One of the main challenges in the study of Precambrian terranes, especially those Archean-Paleoproterozoic in age, is determining the depositional age of sedimentary rocks. This problem persists in the Carajás Basin, too. The most reliable method for dating Precambrian sedimentary rocks is the U–Pb geochronology of zircon in intercalated volcanic rocks (Rasmussen and Fletcher, 2010). Although the Águas Claras and Azul formations have been the subject of several geochronological studies using this methodology (U–Pb zircon dating), most of these studies dated detrital zircon grains, which yielded only provenance ages (e.g., Dias et al., 1996; Araújo and Sousa, 2018; Justo et al., 2018). The absence of synsedimentary volcanic rocks has been hindering the accurate dating of these formations, causing the depositional age of these formations to remain controversial. Whereas some previous authors argued that these units were deposited during the Neoarchean (e.g., Docegeo, 1988; Araújo et al., 1988; Dias et al., 1996; Nogueira et al., 1995; Pinheiro, 1997), some others have suggested that they were deposited during the Paleoproterozoic (e.g., Fabre et al., 2011; Tavares et al., 2018; Araújo and Sousa, 2018; Araújo Filho, 2018; Araújo and Nogueira, 2019). A Neoarchean age was proposed mainly based on the results obtained from the dating of ~2.6 Ga dike swarms that cross-cut these formations (Dias et al., 1996; Mougeot et al., 1996a). In this study, we support a Paleoproterozoic age for the Azul and Águas Claras formations (Table 3). This interpretation is strengthened by considerable geological evidence, as well as by several

Table 3
Summary of main geochronological data used to constrain the depositional age of Azul and Águas Claras formations.

Formation	Lithology	Age (Ma)	Method	Mineral	Significance	Constraints	Reference
Carajás granite	A-type granite	1880 ± 2	U–Pb	Zircon	Crystallization age	Minimum depositional age	Machado et al. (1991)
Dike swarms	Gabbro	1882 ± ?	U–Pb	Baddeleyite	Crystallization age	Minimum depositional age	Giovanardi et al. (2019)
	Gabbro	2645 ± 12	Pb–Pb	Zircon	Crystallization age	No constraint	Dias et al. (1996)
	Gabbro	2708 ± 37	U–Pb	Zircon	Crystallization age	No constraint	Mougeot et al. (1996a)
Águas Claras Formation	Sandstone	2778 ± ?	U–Pb	Zircon	Detrital zircon age	Maximum depositional age	Mougeot et al. (1996a)
	Sandstone	2681 ± 5	U–Pb	Zircon	Detrital zircon age	Maximum depositional age	Trendall et al. (1998a)
	Conglomerate	2609 ± 7	U–Pb	Zircon	Detrital zircon age	Maximum depositional age	Araújo and Sousa (2018)
	Sandstone	2060 ± ?	Pb–Pb	Pyrite	Hydrothermalism or diagenesis age	Minimum depositional age	Mougeot et al. (1996b)
	Sandstone	2796 ± 36	U–Pb	Zircon	Detrital zircon age	Maximum depositional age	Justo et al. (2018)
Azul Formation	Mudstone	2373 ± 4	U–Pb	Zircon	Detrital zircon age	Maximum depositional age	Justo et al. (2018)

counter-arguments which militate against an Archean age for these formations, as we discuss below.

Firstly, some recent studies based on U–Pb dating of monazite grains from the dike swarm cutting the Azul and Águas Claras formations yielded different ages for these dikes at ~1882, ~535 and ~200 Ma (Giovanardi et al., 2019). These results show that some dikes may be younger than previously supposed. Besides that, the zircon grains dated from these dikes may be inherited from the country rock. This hypothesis is strongly supported by the observation that some studies documented a younger zircon population age for these country rocks of ~2.6 Ga (Trendall et al., 1998a; Araújo and Sousa, 2018). In other words, if we admit that these ~2.6 Ga intrusive gabbroic rocks do not present any evidence of having been emplaced simultaneously with sedimentation (i.e., produced by a magmatic activity coeval with deposition)—for instance the occurrence of peperites which form typically when magma is emplaced in a water-saturated recently deposited sediment (Skilling et al., 2002)—it is unlikely that they would cross-cut country rocks that present a maximum depositional age coincident at ~2.6 Ga.

Secondly, although the age of ~2.68 Ga obtained by Trendall et al. (1998a) from dating sandstone of the Águas Claras Formation has been interpreted as corresponding to the age of an event of syndepositional volcanism associated with these sedimentary rocks, due to the nearly unweathered zircon appearance, this aspect does not sustain this interpretation. Alternatively, the occurrence of these unweathered zircon grains may be justified by the fact that they may be sourced from a rock close to the depositional site. Furthermore, the lack of any evidence of weathering in detrital zircons (e.g., edge pits and leached margins) may have resulted from the short time lag between source rocks' exposure and subsequent sediment deposition, as noted by Fabre et al. (2011). Therefore, the occurrence of unweathered zircon grains of ~2.68 Ga in age in these rocks does not necessarily indicate a sedimentation age at that time period but must only be interpreted as being the maximum depositional age.

Thirdly, some recent studies based on detrital zircon dating from the Azul and Águas Claras formations have pointed, even in small amounts, to concordant Paleoproterozoic ages for some zircon grains. Justo et al. (2018), for example, dated detrital zircon grains from mudstone of the Azul Formation and sandstone of the Águas Claras Formation and the analyzed grains return ages of ~2.37 and ~2.79 Ga respectively for the youngest detrital zircon population of these formations. This age of ~2.37 Ga may be used to indicate the maximum depositional age of the Azul and Águas Claras formations.

Fourthly, disseminated euhedral pyrite in sandstone beds from the Águas Claras Formation yielded a Pb-model age of ~2.06 Ga (Mougeot, 1996; Mougeot et al., 1996b). Although some authors interpreted these pyrites as epigenetic, and suggest that this age is related to hydrothermalism, possibly by emplacing of intrusive gabbroic dikes (e.g., Mougeot et al., 1996b; Dias et al., 1996), other authors have interpreted these pyrites as being diagenetic (e.g., Fabre et al., 2011). Anyway, whether these pyrite grains were formed by hydrothermalism or diagenesis, the pyrite age post-dates the deposition of the country rock. Therefore, the age of ~2.06 Ga may be interpreted as a minimum depositional age for the Azul and Águas Claras formations.

Fifthly, the data of mass-independent sulfur isotope fractionation (MIF-S) from pyrite embedded in black shale and sandstone strata of the Serra Sul and Azul formations show $\Delta^{33}S$ values near zero, suggesting an oxygenated atmosphere at the time of deposition (Fabre et al., 2011). Although Cabral et al. (2017) interpreted this same result as being caused by endogenic effects and used this explanation to counter-argue the interpretations discussed in Fabre et al. (2011), the black shale intervals analyzed by Cabral et al. (2017) are positioned at the base of the Serra Sul Formation (Fig. 2). Therefore, the occurrence of minimal MIF-S in both deposits strongly suggests an oxygenated atmosphere-hydrosphere system at the time of deposition, and an age younger than ~2.45 Ga for these deposits, or post-GOE (Bekker et al., 2004; Kump, 2008). Furthermore, these results are compatible with a syn-to post-glacial scenario in the aftermath of the Paleoproterozoic Serra Sul glaciation.

Sixthly, the expressive manganese deposits of the Azul Formation have been correlated to other similar deposits worldwide (e.g., Fabre et al., 2011; Gauthier-Lafaye et al., 2010), such as the Franceville Group (Congo Craton), the Transvaal Supergroup (Kaapvaal Craton) and the Magondi Supergroup (Zimbabwe Craton), which are typically of Paleoproterozoic age (Bonhomme et al., 1982; Gauthier-Lafaye and Weber, 2003; Tsikos et al., 2003; Gauthier-Lafaye et al., 2010; Master et al., 2010; Maynard, 2010; Fabre et al., 2011; Dubois et al., 2017). Furthermore, manganese oxides and hydroxides require a high redox potential to precipitate, and the presence of a highly oxidizing environment, conditions that occurred only after the GOE (Kopp et al., 2005; Sekine et al., 2011).

5.3. Similarities between the Azul and Águas Claras formations and other Paleoproterozoic successions worldwide

The stratigraphic architecture observed in the Carajás Basin is very similar to other Archean-Paleoproterozoic volcano-sedimentary basins which occur in the interior of some ancient landmasses, such as the São Francisco, Congo, Pilbara and Kaapvaal cratons (Fig. 7; Bonhomme et al., 1982; Cheney and Winter 1995; Alkmim and Marshak, 1998; Catuneanu and Eriksson, 1999; Martin, 1999; Coetzee, 2001; Ossa et al., 2013; Rasmussen et al., 2013; Van Kranendonk et al., 2015; Farina et al., 2016; Dopico et al., 2017; Caquineau et al., 2018). Although an accurate correlation between the succession of the Carajás Basin and the successions that occur in these basins is difficult to assess, stratigraphic and sedimentological similarities between these successions strongly suggest that they are at least partly correlated.

These similarities may be explained to an extent by these basins being located within ancient landmasses which were close to each other at the time of deposition. It is suggested that these masses were assembled to construct the Columbia supercontinent in the Paleo-to Mesoproterozoic at ~2.1–1.8 Ga (Zhao et al., 2004; Teixeira et al.,

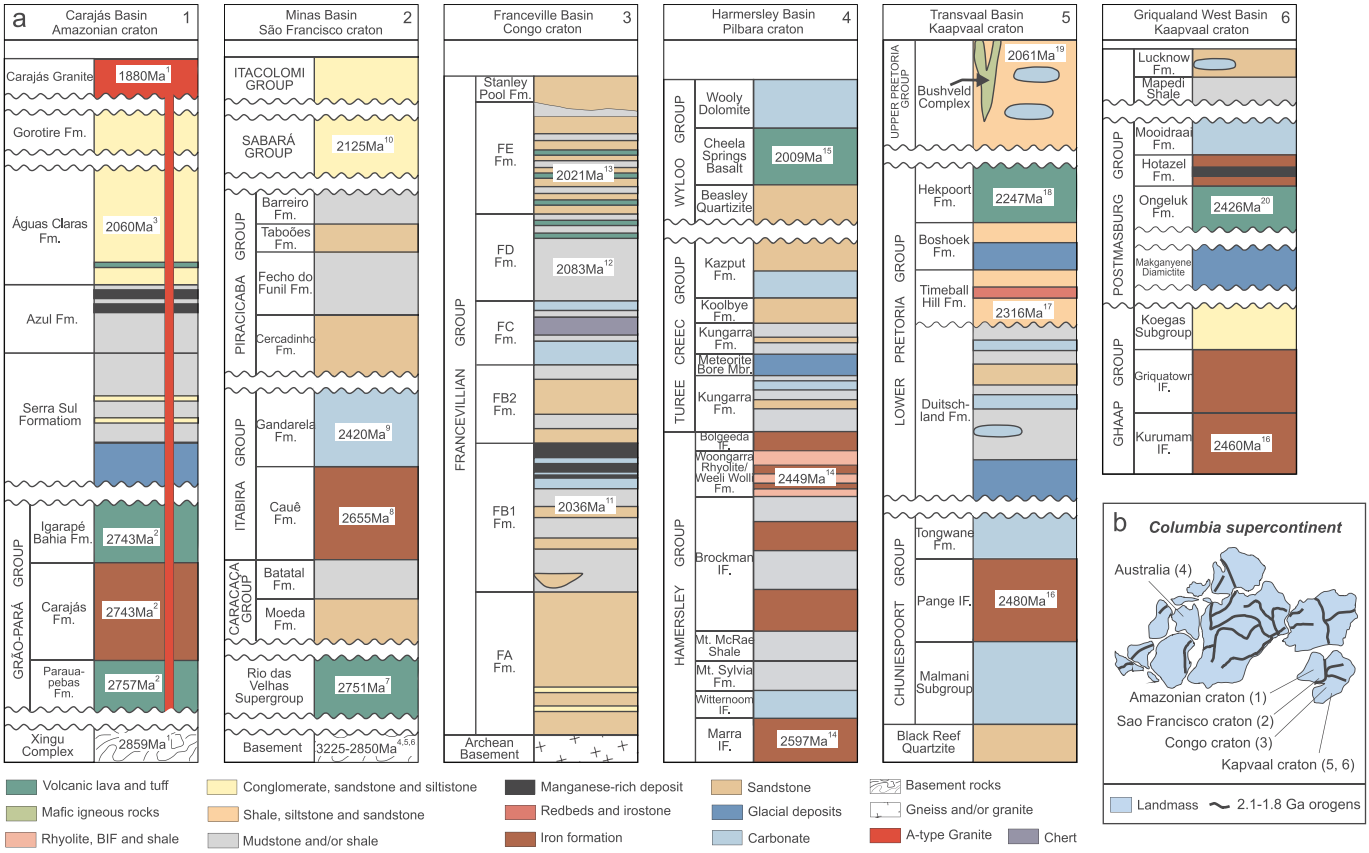

Fig. 7. Stratigraphic comparison between the Carajás Basin (Amazonian craton, Brazil) and some basins located in other cratons worldwide. (a) Stratigraphic columns of basins. Data compiled from: Carajás Basin (Araújo and Nogueira, 2019); Minas Basin (Dopico et al., 2017); Franceville Basin (Gauthier-Lafaye and Weber, 2003); Hamersley Basin (Tang and Chen, 2013; Caquineau et al., 2018); Transvaal and Griqualand West basins (Bekker et al., 2004; Rasmussen et al., 2013). Geochronological data compiled from: 1—Machado et al. (1991); 2—Trendall et al. (1998a); 3—Mougeot (1996b); 4—Machado and Carneiro (1992); 5—Lana et al. (2013); 6—Romano et al. (2013); 7—Noce et al. (2005); 8—Cabral et al. (2012); 9—Babinski et al. (1995); 10—Machado et al. (1996); 11—Bros et al. (1992); 12—Horie et al. (2005); 13—Thiéblemont et al. (2009); 14—Trendall et al. (1998b); 15—Muller et al. (2005); 16—Pickard (2003); 17—Hannah et al. (2004); 18—Schroder et al. (2016); 19—Walraven (1997); 20—Gumsley et al. (2017). (b) Paleogeographic reconstruction of Columbia supercontinent (modified from Zhao et al., 2004) showing the different cratons in which the basins are located.

2007). Therefore, it is plausible that they share similar stratigraphic and sedimentological features, as they have evolved somewhat simultaneously, despite having been influenced by regional and/or local events. The main similarities that we find between the succession of the Carajás Basin and these other successions that occur in these basins are:

1) In the Carajás Basin, the Serra Sul, Azul, Águas Claras, and Gorotire formations constitute a thick siliciclastic succession, which occurs above the Neoarchean BIF strata and volcanic rocks (Fig. 2). In these other cratons as well, the BIF units appear to be restricted to the base of the successions, although thin layers are observed to be interbedded with siliciclastic beds. Besides, in some of these cratons, glacial diamictite strata linked to the Paleoproterozoic Huronian Glaciation Event have already been documented. In the Carajás Basin, these strata were recently noticed and attributed to the Siderian–Rhyacian Serra Sul Formation (Araújo and Nogueira, 2019). Although these authors interpreted that the Serra Sul glaciation may be correlated with any of the known Paleoproterozoic glaciations, or with none of them, a possible correlation between the Serra Sul glaciation and the Huronian Glaciation Event should not be disregarded;
2) The manganese deposits observed in the Azul Formation show similarities to other occurrences of this metal, especially in the occurrences described in the Franceville Basin of the Congo Craton (Gauthier-Lafaye et al., 2010; Fabre et al., 2011; Araújo and Sousa, 2018). These manganese-enriched strata are generally positioned above the glaciogenic horizons, similar to what is observed in the Carajás Basin. This stratigraphic pattern resulted from the dramatic emergence of oxygen at ~2.45 Ga, which was followed by the paleoclimatic recovery aftermath of these protracted refrigeration episodes, causing the acceleration of GOE (Sekine at al., 2011). These paleoenvironmental and paleoclimatic changes allowed the large-scale precipitation of manganese in the stratified marine basin during Paleoproterozoic (Roy, 2006). A similar scenario is envisaged for the deposition of manganese in the Carajás Basin, as previously admitted (e.g., Gauthier-Lafaye et al., 2010; Fabre et al., 2011; Costa, 2017; Araújo and Sousa, 2018);
3) The thick package of sandstone and conglomerate observed at the top of these successions, which in the Carajás Basin is represented by the Águas Claras and Gorotire formations, strongly suggests a tending to continentalization of these deposits, related to the uplift of the landmasses as a result of Columbia amalgamation (c.f. Rogers, 1996; Rogers and Santosh, 2002). The Gorotire Formation, which was described as a set of sandstone and conglomerate strata containing lithic fragments that include sandstone, gneiss, BIF, plutonic and volcanic rocks and hydrothermalite (Nascimento and Oliveira, 2015), was possibly deposited during the last stages of sedimentation of the Carajás Basin. The coarse-grained nature of these deposits and the low textural and compositional maturity of rocks, besides the fact that these sediments were deposited in an alluvial fan to fluvial setting at ~2.0 Ga (Pereira et al., 2009; Justo et al., 2018), strongly support this interpretation.

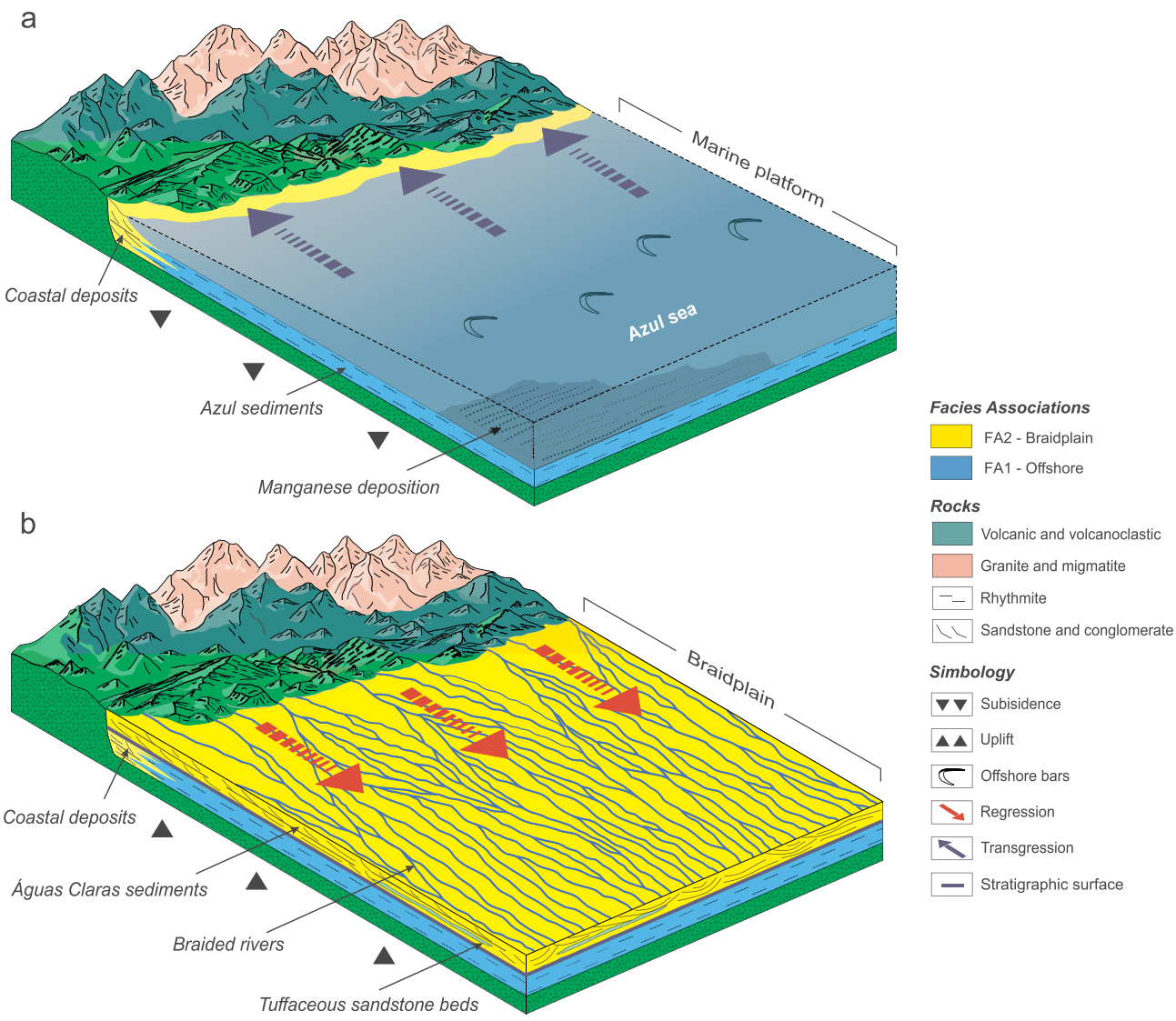

Fig. 8. Simple models showing the envisaged paleoenvironmental reconstruction of the Paleoproterozoic Azul and Águas Claras formations of the Carajás Basin (Amazonian craton, Brazil), respectively. (a) Deposition of fine-grained sediments belonging to the Azul Formation in a marine basin during the last incursion of the Azul sea onto the Carajás protocontinent. Manganese-enriched sediments were widely deposited in deep waters. (b) Deposition of coarse-grained sediments belonging to the Águas Claras Formation in an extensive fluvial braidplain. Tuffaceous sandstone strata were sparsely deposited within this formation.

Critically, although we establish stratigraphic and sedimentological comparisons between these successions, a precise correlation between them will only be possible with an accurate dating of these successions. The dating of synsedimentary volcanic strata interbedded with siliciclastic strata, similar to what has been described here, is crucial to allow these precise correlations, as performed by Rasmussen et al. (2013), who dated millimetric tuff layers interbedded with mudstone to establish an intercontinental correlation between Paleoproterozoic glaciogenic strata in the Transvaal and Pilbara cratons.

5.4. Sedimentary evolution and sequence stratigraphy

Based on the results achieved herein, we envisaged that the sedimentary environments interpreted to the Azul and Águas Claras formations are connected in an uninterrupted evolutive history, in which they were deposited during distinct scenarios (Fig. 8). Initially, the Azul sediments were deposited in an extensive marine platform, in which manganese-enriched strata were coevally sedimented (FA1 deposits). The occurrence of thick deposits of turbidite, interbedded subordinately by sandstone with wave-generated cross-lamination, including hummocky cross-stratification, strongly suggests that these sediments were deposited in the offshore marine zone, eventually affected by storm episodes.

Afterward, the marine environment was suddenly followed by the installation of a fluvial braided system that accommodated the Águas Claras sediments (FA2 deposits). The observation of these fluvial strata shows that they constitute a thick deposit, extending laterally for dozens of kilometers, strongly suggesting that the Águas Claras braidplain was extensive, well-developed, and possibly long-lived. Besides, the occurrence of tuffaceous sandstone beds in these deposits (Fig. 6) suggests small-scale volcanic episodes close to the fluvial system, during which the pyroclastic material was reworked into the fluvial channels.

It is probable that the Azul and Águas Claras formations were supplied mainly by Meso-to Neoarchean granitic and volcanic rocks, which include the Xingu and Grão-Pará lithostratigraphic units. This interpretation is supported by petrographic results obtained in this study, and by previously published data presented in several studies (e.g., Mougeot et al., 1996a; Anaisse Junior, 1997; Araújo and Sousa, 2018).

Regarding the sequence stratigraphy, the stratigraphic architecture

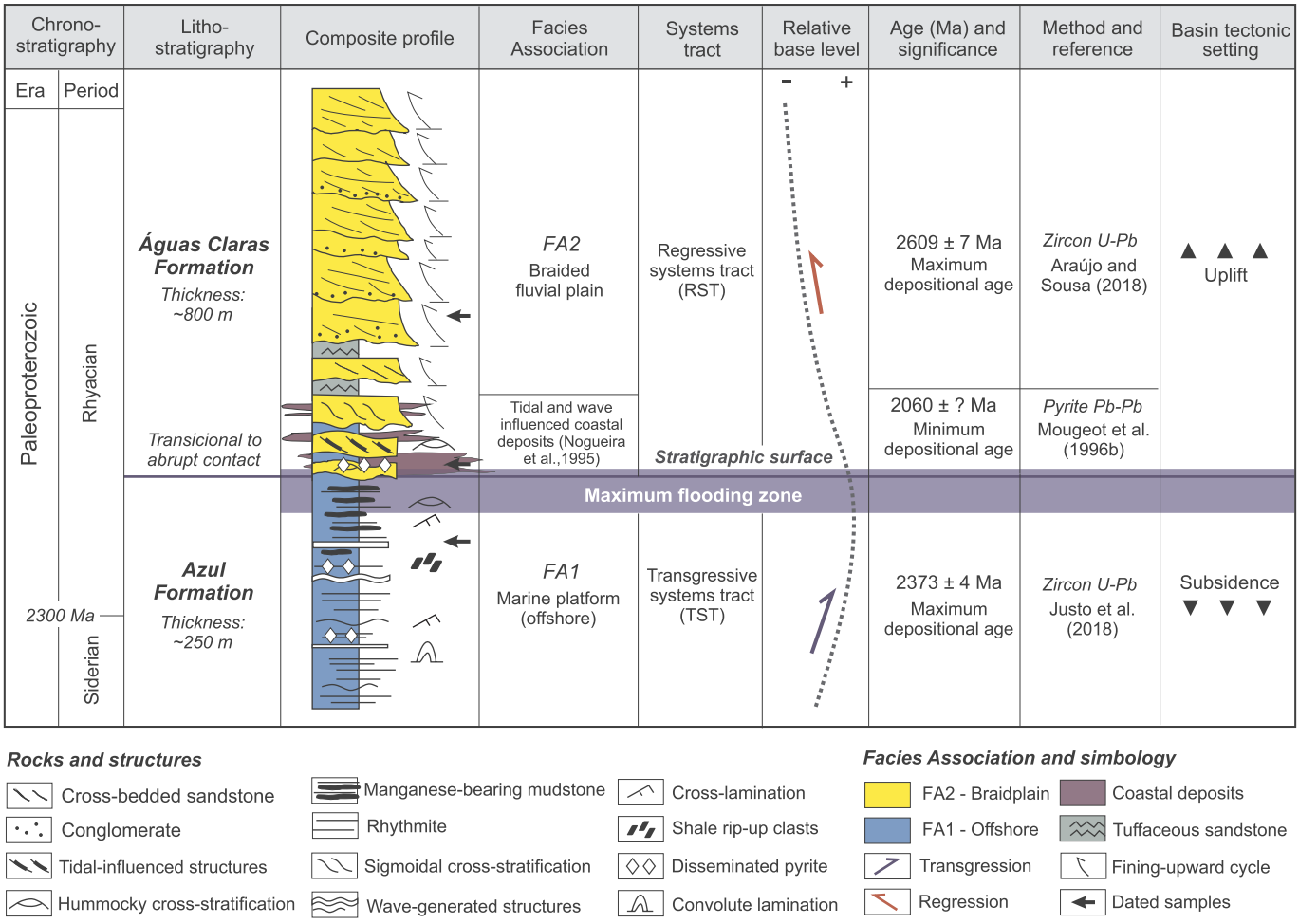

Fig. 9. Summary of stratigraphic and paleoenvironmental interpretations obtained from this study for the Azul and Águas Claras formations of the Carajás Basin (Amazonian craton, Brazil). The previously published geochronological data available are being re-positioned in the composite profile, according to the new stratigraphy proposed herein.

of the studied succession strongly suggests that the Azul and Águas Claras formations are the stratigraphic record associated with a transgressive–regressive sequence (Fig. 9). These formations are limited each other by a maximum flooding zone, which in the field corresponds to the stratigraphic surface. This surface marks a change in shoreline trajectory, when transgression ends and regression begins, and takes place in the waning phases of base-level rise, when the rate of sediment supply begins to exceed the rate of base-level rise (Embry, 2002). On the other hand, the abrupt contact between the Águas Claras and the Igarapé Bahia formations observed in some cores (Fig. 4) resulted from an extensive erosion promoted by the fluvial dynamic on the pre-fluvial strata or simply as result of paleogeographic controls.

Accordingly, the Azul sediments were deposited during a transgressive systems tract (TST), related to transgression of the Azul sea into the Carajás protocontinent. We suggest that this marine incursion was possibly triggered by the deglaciation occurred aftermath the Serra Sul glaciation. The subsequent marine regression was accompanied by installation of the Águas Claras fluvial system during a regressive systems tract (RST). This marine regression is interpreted as result of uplift of the Carajás protocontinent during the Transamazonian cycle at ~2.0 Ga (Cordani et al., 1984; Macambira et al., 2009; Tavares et al., 2018). This orogenetic cycle is intrinsically linked to the Columbia supercontinent assembly at ~2.1–1.8 Ga (Zhao et al., 2004). The inversion and deformation of the Carajás Basin was completed during the collision of protocontinents, and finally by the emplacement of the Carajás A-type granitoid at ~1.88 Ga (Machado et al., 1991).

6. Conclusions

A new stratigraphic framework for a siliciclastic succession of the Carajás Basin (Amazonian craton, Brazil) is being proposed. This succession, which so far has been considered a single formation, the called Águas Claras Formation, was subdivided here into two different units. The lower unit which encompasses a set of rhythmite and mudstone strata deposited in an offshore marine setting, in which manganese occurs enriched, is being formally proposed in this study, and was named as the Azul Formation. On the other hand, the upper unit correspond to the redefined Águas Claras Formation, which occurs immediately above the Azul Formation, encompassing a set of sandstone and conglomerate strata deposited in a coastal to fluvial braided system. The results achieved herein strongly suggest that these formations were deposited during the Rhyacian-Orosirian, more precisely between ~2.37 and 2.06 Ga, in an oxygenated atmosphere, post-GOE.

In evolutive terms, the Azul and Águas Claras formations were interpreted as a transgressive–regressive sequence. In this sense, the Azul sediments were deposited during the latest marine transgression of the Azul sea towards the hinterland of the Carajás protocontinent. In stark contrast, the Águas Claras sediments were deposited during the marine regression, triggered by the uplift of the protocontinent caused by the Transamazonian orogenetic cycle occurring at ~2.0 Ga. This continentalization tendency observed in this studied succession of the Carajás Basin is observed in other Paleoproterozoic successions worldwide as well, especially those that are recorded in ancient

landmasses which were amalgamated and later formed the Columbia supercontinent during the Paleo-to Mesoproterozoic.

Author statement

Roberto Costa Araújo Filho: Writing- Original draft; Conceptualization; Methodology; Writing - review & editing; Investigation; Afonso César Rodrigues Nogueira: Writing - review & editing; Methodology; Supervision; Raphael Neto Araújo: Writing - review & editing; Validation; Methodology.

Acknowledgments

We are very grateful to Vale S.A. (Parauapebas, Brazil) for making the drill cores available for the research; the Geological Survey of Brazil (Belém, Brazil) for support during fieldwork; Luiz Cláudio Costa and Alexandre Ribeiro for help during fieldwork; and the PROPESP/UFPA (Belém, Brazil) for supporting this work. This paper is part of the dissertation thesis of the first author, who gratefully acknowledges the grant from the Conselho Nacional de Desenvolvimento Científico e Tecnológico (CNPq), process number 133399/2016-8. We are also very grateful to the anonymous peer-reviewers for reviewing our manuscript and to Michelangelo Martini for his editorial work.

Appendix A. Supplementary data

Supplementary data to this article can be found online at https://doi.org/10.1016/j.jsames.2020.102665.

References

Alkmim, F.F., Marshak, S., 1998. Transamazonian orogeny in the southern sao Francisco craton region, Minas gerais, Brazil: evidence for paleoproterozoic collision and collapse in the quadrilátero ferrífero. Precambrian Res. 90, 29–58.
Althoff, F., Barbey, P., Boullier, A.M., 2000. 2.8–3.0 Ga plutonism and deformation in the SE amazonian craton: the archaean granitoids of marajoara (Carajás mineral province, Brazil). Precambrian Res. 104, 187–206.
Anaisse Junior, J., 1997. Petrografia dos arenitos da Formação Águas Claras, Arqueano, Serra dos Carajás. Trabalho de Conclusão de Curso (graduação em geologia). Instituto de Geociências, Universidade Federal do Pará, Belém, pp. 36.
Araújo Filho, R.C., 2018. O Grupo Águas Claras da Serra dos Carajás, Paleoproterozoico do Cráton Amazônico: fácies, litoestratigrafia e sequências deposicionais. MS Dissertation. Instituto de Geociências, Universidade Federal do Pará, Belém, pp. 67.
Araújo, R.N., Nogueira, A.C.R., 2019. Serra Sul diamictite of the Carajás Basin (Brazil): a paleoproterozoic glaciation on the amazonian craton. Geology 47, 1166–1170.
Araújo, R.N., Sousa, M.J., 2018. Geologia, Estratigrafia e análise do minério dos depósitos de manganês de Carajás: regiões do Azul, Sereno Buritirama e Antônio Vicente. In: Belém, CPRM- Companhia de Pesquisa de Recursos Minerais. Relatório técnico, pp. 198.
Araújo, O.J.B., Maia, R.G.N., Jorge João, X.S., Costa, J.B.S., 1988. A megaestruturação arqueana da Folha Serra dos Carajás. In: Congresso Latino-americano de Geologia, vol. 7. SBG, Belém, pp. 324–333 1.
Araújo, O.J.B., Maia, R.G.N., 1991. Serra dos Carajás, folha SB.22-ZA, estado do Pará In: Programa de Levantamentos geológicos Básicos do Brasil. Brasília. CPRM-Companhia de Pesquisa de Recursos Minerais, pp. 136.
Babinski, M., Chemale Jr., F., Van Schmus, W.R., 1995. The Pb/Pb age of the Minas Supergroup carbonate rocks, quadrilátero ferrífero, Brazil. Precambrian Res. 72, 235–245.
Barbosa, O., Ramos, J.R.A., Gomes, F.A., Hembold, R., 1966. Geologia estratigráfica, estrutural e econômica da área do "Projeto Araguaia". Monografia, vol. 19. DNPM, Rio de Janeiro, pp. 94.
Beisiegel, V.R., Bernardelli, A.L., Drummond, N.F., Ruff, A.W., Tremaine, J.W., 1973. Geologia e recursos minerais da Serra dos Carajás. Rev. Bras. Geociencias 3, 215–242.
Bekker, A., Holland, H.D., Wang, P.L., Rumble III, D., Stein, H.J., Hannah, J.L., Coetzee, L.L., Beukes, N.J., 2004. Dating the rise of atmospheric oxygen. Nature 427, 117–120.
Bhattacharyya, A., Morad, S., 1993. Proterozoic braided ephemeral fluvial deposits: an example from the dhandraul sandstone formation of the kaimur group, son valley, central India. Sediment. Geol. 84, 101–114.
Bonhomme, M.G., Gauthier-Lafaye, F., Weber, F., 1982. An example of lower Proterozoic sediments: the Francevillian in Gabon. Precambrian Res. 18, 87–102.
Bose, P.K., Eriksson, P.G., Sarkar, S., Wright, D.T., Samanta, P., Mukhopadhyay, S., Mandal, S., Banerjee, S., Altermann, W., 2012. Sedimentation patterns during the Precambrian: a unique record? Mar. Petrol. Geol. 33, 34–68.
Bouma, A.H., 1962. Sedimentology of Some Flysch Deposits: a Graphic Approach to Facies Interpretation. Elsevier, Amsterdam, pp. 168.
Bros, R., Stille, P., Gauthier-Lafaye, F., Weber, F., Clauer, N., 1992. Sm-Nd isotopic dating of Proterozoic clay material: an example from the Francevillian sedimentary series Gabon. Earth Planet Sci. Lett. 113, 207–218.
Cabral, A.R., Zeh, A., Koglin, N., Seabra Gomes Jr., A.A., Viana, D.J., Lehmann, B., 2012. Dating the Itabira iron formation, Quadrilátero Ferrífero of Minas Gerais, Brazil, at 2.65 Ga: depositional U-Pb age of zircon from a metavolcanic layer. Precambrian Res. 204, 40–45.
Cabral, A.R., Creaser, R.A., Nägler, T., Lehmann, B., Voegelin, A.R., Belyatsky, Belyatsky, B., Pašava, J., Seabra Gomes Jr., A.A., Galbiatti, H., Böttcher, M.E., Escher, P., 2013. Trace-element and multi-isotope geochemistry of Late-Archean black shales in the Carajás iron-ore district, Brazil. Chem. Geol. 362, 91–104.
Cabral, A.R., Bühn, B., Gomes Jr., A.A.S., Galbiatti, H.F., Lehmann, B., Halder, S., 2017. Multiple sulfur isotopes from the Neoarchaean Serra Sul black shale, Carajás mineral province, northern Brazil. J. S. Am. Earth Sci. 79, 377–383.
Caquineau, T., Paquette, J.L., Philippot, P., 2018. U-Pb detrital zircon geochronology of the turee creek group, Hamersley Basin, western Australia: timing and correlation of the paleoproterozoic glaciations. Precambrian Res. 307, 34–50.
Catuneanu, O., Eriksson, P.G., 1999. The sequence stratigraphic concept and the Precambrian rock record: an example from the 2.7–2.1 Ga Transvaal Supergroup, Kaapvaal craton. Precambrian Res. 97, 215–251.
Cheel, R.J., Leckie, D.A., 1993. Hummocky Cross-Stratification: Sedimentology Review Blackwell Scientific Publications, Oxford, U.K., pp. 103–122.
Cheney, E.S., Winter, H.D.L.R., 1995. The late archean to mesoproterozoic major unconformity-bounded units of the kaapvaal province of southern africa. Precambrian Res. 74, 203–223.
Coetzee, L.L., 2001. Genetic Stratigraphy of the Paleoproterozoic Pretoria Group in the Western Transvaal. MS dissertation. Rand Afrikaans University, Johannesburg, pp. 220.
Cohen, K.M., Finney, S.C., Gibbard, P.L., Fan, J.-X., 2013. The ICS international chronostratigraphic chart (updated). Episodes 36, 199–204.
Collinson, J.D., 1996. Alluvial sediments. In: In: Reading, H.G. (Ed.), Sedimentary Environments: Processes, Facies and Stratigraphy, vol. 3. Blackwell Science, Oxford, pp. 37–82.
Cordani, U.G., Tassinari, C.C.G., Kawashita, K.A., 1984. A Serra dos Carajás como região limítrofe entre províncias tectônicas. Cien. Terra 9, 6–11.
Costa, F.F.O., 2017. A Sucessão Siliciclástica paleoproterozoica associada ao depósito de manganês do Azul da Serra dos Carajás. MS Dissertation. Instituto de Geociências, Universidade Federal do Pará, Programa de Pós-graduação em Geologia e Geoquímica, Belém, pp. 62.
Costa, M.L., Fernandez, O.J.C., Requelme, M.E.R., 2005. Depósito de manganês do Azul, Carajás: estratigrafia, mineralogia, geoquímica e evolução geológica. In: Marini, O.J., Queiroz, E.T., Ramos, B.W. (Eds.), Caracterização de depósitos minerais em distritos mineiros da Amazônia. Brasília, DNPM, FINEP. ADIMB, pp. 231–333.
Dall'Agnol, R., Souza, Z.S., Althoff, F.J., Barros, C.E.M., Leite, A.A.S., Jorge João, X.S., 1997. General aspects of the granitogenesis of the Carajás metallogenic province. Excursions guide, salvador, companhia baiana de Pesquisa mineral. Superintendência de Geologia e Recursos Minerais 135–161.
Dall'Agnol, R., Oliveira, M.A., Almeida, J.A.C., Althoff, F.J., Leite, A.A.S., Oliveira, D.C., Barros, C.E.M., 2006. Archean and paleoproterozoic granitoids of the Carajás metallogenic province, eastern amazonian craton. In: Dall'Agnol, R., Rosa-Costa, L.T., Klein, E.L. (Eds.), Symposium on Magmatism, Crustal Evolution, and Metallogenesis of the Amazonian Craton. Volume and Field Trip Guide. Belém, PRONEX-UFPA-SBGNO, pp. 99–150.
De Raaf, J.F.M., Boersma, J.R., Van Gelder, A., 1977. Wave generated structures and sequences from a shallow marine succession, Lower Carboniferous, County Cork, Ireland. Sedimentology 24, 451–483.
Dasgupta, S., Roy, S., Fukuoka, M., 1992. Depositional models for manganese oxide and carbonate deposits of the precambrian sausar group, India. Econ. Geol. 87, 1412–1418.
Dias, G.S., Macambira, M.B., Dall'Agnol, R., Soares, A.D.V., Barros, C.E.M., 1996. Datações de zircões de sill de metagabro: comprovação de idade arqueana da Formação Águas Claras, Carajás, Pará In: Simpósio de Geologia da Amazônia, vol. 5. Belém, SBG, pp. 376–378 5.
Docegeo, 1988. Revisão litoestratigráfica da Província Mineral de Carajás. In: Congresso Brasileiro de Geologia, 35, Belém, SBG. Província Mineral de Carajás - Litoestratigrafia e principais depósitos minerais, Belém. Anexo aos Anais, pp. 165.
Dopico, C.I.M., Lana, C., Moreira, H.S., Cassino, L.F., Alkmim, F.F., 2017. U-Pb ages and Hf-isotope data of detrital zircons from the late Neoarchean-Paleoproterozoic Minas Basin, SE Brazil. Precambrian Res. 291, 143–161.
Dreher, A.M., 2004. O depósito primário de Cu-Au de Igarapé Bahia, Carajás: rochas fragmentárias, fluidos mineralizantes e modelo metalogenético. Ph.D. Thesis. Instituto de Geociências, Universidade Estadual de Campinas, Campinas, pp. 221.
Dreher, A.M., Xavier, R.P., Martini, S.L., 2005. Fragmental rocks of the Igarapé Bahia Cu-Au deposit, Carajás mineral province, Brazil. Rev. Bras. Geociencias 35, 359–368.
Dreher, A.M., Xavier, R.P., Taylor, B.E., Martini, S.L., 2008. New geologic, fluid inclusion and stable isotope studies on the controversial Igarapé Bahia Cu-Au deposit, Carajás Province, Brazil. Miner. Deposita 43, 161–184.
Dubois, M., Lopez, M., Orberger, B., Gay, A., Moussavou, M., Pambo, F., Rodrigues, S., 2017. The 2.1 Ga-old injectite network of the Franceville Basin, Gabon: architecture, origin and implications on manganese mineralization. Precambrian Res. 302, 255–278.
Dumas, S., Arnott, R.W.C., 2006. Origin of hummocky and swaley cross-stratification—the controlling influence of unidirectional current strength and aggradation rate. Geology 34, 1073–1076.
Embry, A.F., 2002. Transgressive-regressive (TR) sequence stratigraphy. In: In: Armentrout, J.M., Rosen, N.C.((Eds.), Sequence Stratigraphic Models for Exploration and Production: Evolving Methodology, Emerging Models and Application Histories,

vol. 52. pp. 151–172.
Eriksson, P.G., Condie, K.C., Tirsgaard, H., Mueller, W.U., Altermann, W., Miall, A.D., Aspler, L.B., Catuneanu, O., Chiarenzelli, J.R., 1998. Precambrian clastic sedimentation systems. Sediment. Geol. 120, 5–53.
Eriksson, P.G., Bumby, A.J., Popa, M., 2004. Sedimentation through time. In: Eriksson, P.G., Altermann, W., Nelson, D.R., Mueller, W.U., Catuneanu, O. (Eds.), The Precambrian Earth: Tempos and Events. Elsevier, Amsterdam, pp. 593–680.
Fabre, S., Nédélec, A., Poitrasson, F., Strauss, H., Thomazo, C., Nogueira, A., 2011. Iron and sulphur isotopes from the Carajás mining province (Pará, Brazil): implications for the oxidation of the ocean and the atmosphere across the Archaean-Proterozoic transition. Chem. Geol. 289, 124–139.
Farina, F., Albert, C., Dopico, C.M., Gil, C.A., Moreira, H., Hippertt, J., Cutts, K., Alkmim, F., Lana, C., 2016. The Archean-Paleoproterozoic evolution of the Quadrilátero Ferrífero (Brazil): current models and open questions. J. S. Am. Earth Sci. 68, 4–21.
Feio, G.R.L., Dall'Agnol, R., Dantas, E.L., Macambira, M.J.B., Santos, J.O.S., Althoff, F.J., Soares, J.E.B., 2013. Archean granitoid magmatism in the Canaã dos Carajás area: implications for crustal evolution of the Carajás province, Amazonian craton, Brazil. Precambrian Res. 227, 157–185.
Figueiras, A.J.M., Villas, R.N.N., 1984. Estudo petrológico e sedimentológico da sequência clástica (pós-Grupo Grão-Pará) da Serra dos Carajás, estado do Pará In: Congresso Brasileiro de Geologia, vol. 33. Rio de Janeiro, SBG, pp. 823–846 2.
Fisher, R.V., 1961. Proposed classification of volcaniclastic sediments and rocks. Geol. Soc. Am. Bull. 72, 1409–1414.
Galarza, M.A., Macambira, M.J.B., Villas, R.N.N., 2008. Dating and isotopic characteristics (Pb and S) of the Fe oxide-Cu-Au-U-REE Igarapé Bahia ore deposit, Carajás mineral province, Pará state, Brazil. J. S. Am. Earth Sci. 25, 377–397.
Gauthier-Lafaye, F., Nogueira, A.C.R., Pinheiro, R.V.L., Albani, A.E., 2010. The Paleoproterozoic Francevilian Series: witness of a geochemical and biological upheaval. In: Congresso Brasileiro de Geologia, vol. 45 SBG, Belém.
Gauthier-Lafaye, F., Weber, F., 2003. Natural nuclear fission reactors; time constraints for occurrence, and their relation to uranium and manganese deposits and to the evolution of the atmosphere. Precambrian Res. 120, 81–100.
Gibbs, A.K., Wirth, K.R., 1990. Geologic setting of the Serra dos Carajás iron deposits, Brazil. In: Chauve, J.-J., Yuqi, C.A., El Shazly, E.M., Gross, G.A., Laajoki, K., Markov, M.S., Rai, K.L., Stulchikov, V.A., Augustithis, S.S. (Eds.), Ancient Banded Iron Formations. Theophrastus Publications, Athens, pp. 83–102.
Gibbs, A.K., Wirth, K.R., Hirata, W.K., Olszewski, W.J., 1986. Age and composition of the Grão Pará group volcanics, Serra dos Carajás. Rev. Bras. Geociencias 16, 201–211.
Giovanardi, T., Girardi, V.A., Teixeira, W., Mazzucchelli, M., 2019. Mafic dyke swarms at 1882, 535 and 200 Ma in the Carajás region, Amazonian Craton: Sr-Nd isotopy, trace element geochemistry and inferences on their origin and geological settings. J. S. Am. Earth Sci. 92, 197–208.
Gumsley, A.P., Chamberlain, K.R., Bleeker, W., Söderlund, U., de Kock, M.O., Larsson, E.R., Bekker, A., 2017. Timing and tempo of the great oxidation event. Proc. Natl. Acad. Sci. Unit. States Am. 114, 1811–1816.
Hannah, J.L., Bekker, A., Stein, H.J., Markey, R.J., Holland, H.D., 2004. Primitive Os and 2316 Ma age for marine shale: implications for Paleoproterozoic glacial events and the rise of atmospheric oxygen. Earth Planet Sci. Lett. 225, 43–52.
Hirata, W.K., Rigon, J.C., Kadekaru, K., Cordeiro, A.A.C., Meireles, E.M., 1982. Geologia da Província Mineral de Carajás. In: Simpósio de Geologia da Amazônia, 1, Belém, SBG, vol. 1. pp. 100–110.
Hjellbakk, A., 1997. Facies and fluvial architecture of a high-energy braided river: the upper proterozoic Seglodden Member, Varanger peninsula, Northern Norway. Sediment. Geol. 114, 131–161.
Holdsworth, R.E., Pinheiro, R.V.L., 2000. The anatomy of shallow-crustal transpressional structures: insights from the Archaean Carajás fault zone, Amazon, Brazil. J. Struct. Geol. 22 1105–1023.
Holland, H.D., 2002. Volcanic gases, black smokers, and the great oxidation event. Geochem. Cosmochim. Acta 66, 3811–3826.
Horie, K., Hidaka, H., Gauthier-Lafaye, F., 2005. U-Pb geochronology and geochemistry of zircon from the Franceville series at Bidoudouma, Gabon. In: The 15th Annual Goldschmidt Conference Abstracts, Accessory Mineral Geochemistry.
Justo, A.P., Dantas, E.L., Freitas-Silva, F.H., Rodrigues, J.B., 2018. Detrital Zircon Populations in the Neoarchean to Paleoproterozoic Sedimentary Coverage of Carajás, Amazon Cráton, Brazil, vol. 49 Congresso Brasileiro de Geologia, Rio de Janeiro, SBG.
Kopp, R.E., Kirschvink, J.L., Hilburn, I.A., Nash, C.Z., 2005. The Paleoproterozoic snowball Earth: a climate disaster triggered by the evolution of oxygenic photosynthesis. Proc. Natl. Acad. Sci. Unit. States Am. 32, 11131–11136.
Kump, L.R., 2008. The rise of atmospheric oxygen. Nature 451, 277–278.
Lana, C., Alkmim, F.F., Armstrong, R., Scholz, R., Romano, R., Nalini, H.A., 2013. The ancestry and magmatic evolution of Archaean TTG rocks of the Quadrilátero Ferrífero province, southeast Brazil. Precambrian Res. 231, 157–173.
Lindholm, R.C., 1987. A Practical Approach to Sedimentology. Allen & Unwin, London, pp. 276.
Long, D.G.F., 1978. Proterozoic stream deposits: some problems of recognition and interpretation of ancient sand fluvial systems. In: Miall, A.D. (Ed.), Fluvial Sedimentology. Calgary. vol. 5. Canadian Society of Petroleum Geologists, Memoir, pp. 313–341.
Long, D.G.F., 2004. Precambrian rivers. In: Eriksson, P.G., Altermann, W., Nelson, D.R., Mueller, W.U., Catuneanu, O. (Eds.), The Precambrian Earth: Tempos and Events. Elsevier, Amsterdam, pp. 660–663.
Lowe, D.R., 1975. Water scape structures in coarser-grained sediments. Sedimentology 22, 157–204.
Lowe, D.R., 1976. Subaqueous liquefied and fluidized sediment flows and their deposits. Sedimentology 23, 285–308.
Lowe, D.R., 1982. Sediment gravity flows; II, Depositional models with special reference to the deposits of high-density turbidity currents. J. Sediment. Res. 52, 279–297.
Luz, B.R., Crowley, J.K., 2012. Morphological and chemical evidence of stromatolitic deposits in the 2.75 Ga Carajás banded iron formation, Brazil. Earth Planet Sci. Lett. 355, 60–72.
Macambira, J.B., 2003. O ambiente deposicional da Formação Carajás e uma proposta de modelo evolutivo para a Bacia Grão Pará Ph.D. Thesis. Instituto de Geociências, Universidade Estadual de Campinas, Unpublished, pp. 217.
Macambira, J.B., Ramos, J.F.F., Assis, J.F.P., Figueiras, A.J.M., 1990. Projetos Serra Norte e Pojuca. Belém, convênio DNPM/Docegeo/UFPA (Relatório final), pp. 150.
Macambira, M.J.B., Vasquez, M.L., Silva, D.C.C., Galarza, M.A., Barros, C.E.M., Camelo, J.F., 2009. Crustal growth of the central-eastern Paleoproterozoic domain, SW Amazonian craton: juvenile accretion vs. reworking. J. S. Am. Earth Sci. 27, 235–246.
Machado, N., Carneiro, M., 1992. U-Pb evidence of Late Archean tectonothermal activity in southern São Francisco shield Brazil. Can. J. Earth Sci. 29, 2341–2346.
Machado, N., Lindenmayer, Z., Krogh, T.E., Lindenmayer, D., 1991. U-Pb geochronology of Archaean magmatism and basement reactivation in the Carajás area, Amazon shield, Brazil. Precambrian Res. 49, 329–354.
Machado, N., Schrank, A., Noce, C.M., Gauthier, G., 1996. Ages of detrital zircon from Archean-Paleoproterozoic sequences: implications for Greenstone Belt setting and evolution of a Transamazonian foreland basin in Quadrilátero Ferrífero, southeast Brazil. Earth Planet Sci. Lett. 141, 259–276.
Martin, D.M., 1999. Depositional setting and implications of paleoproterozoic glaciomarine sedimentation in the Hamersley province, western Australia. Geol. Soc. Am. Bull. 111, 189–203.
Martins, P.L.G., Toledo, C.L.B., Silva, A.M., Chemale Jr., F., Santos, J.O.S., Assis, L.M., 2017. Neoarchean magmatism in the southeastern Amazonian Craton, Brazil: Petrography, geochemistry and tectonic significance of basalts from the Carajás Basin. Precambrian Res. 302, 340–357.
Master, S., Bekker, A., Hofmann, A., 2010. A review of the stratigraphy and geological setting of the Palaeoproterozoic Magondi Supergroup, Zimbabwe-Type locality for the Lomagundi carbon isotope excursion. Precambrian Res. 182, 254–273.
Maynard, J.B., 2010. The chemistry of manganese ores through time: a signal of increasing diversity of earth-surface environments. Econ. Geol. 105, 535–552.
McPhie, J., Doyle, M., Allen, R., 1993. Volcanic Textures: a Guide to the Interpretation of Textures in Volcanic Rocks. University of Tasmania, Tasmania, pp. 197.
Miall, A.D., 1977. A review of the braided-river depositional environment. Earth Sci. Rev. 13, 1–62.
Miall, A.D., 1981. Analysis of fluvial depositional systems. American Association of Petroleum Geologists, Education Course, Note Series 20, 75.
Miall, A.D., 2006. In: The Geology of Fluvial Deposits: Sedimentary Facies, Basin Analysis, and Petroleum Geology, vol. 4. Springer, Berlin, pp. 582.
Mougeot, R., 1996. Etude de la limite Archéen - Proterozoique et des mineralizations Au, ±U associées. Exemples des régions de Jacobina (Etat de Bahia, Brésil) et de Carajás (Etat de Pará, Brésil). Ph.D. Thesis. Université Montpellier II, pp. 249.
Mougeot, R., Respaut, J.P., Briqueu, L., Ledru, P., Milesi, J.P., Macambira, M.J., Huhn, S.B., 1996a. Geochronological constraints for the age of the Águas Claras formation (Carajás province, Pará, Brazil). In: Congresso Brasileiro de Geologia, 39, Salvador, SBG, vol. 6. pp. 579–581.
Mougeot, R., Respaut, J.P., Briqueu, L., Ledru, P., Milesi, J.P., Lerouge, C., Marcoux, E., Huhn, S.B., Macambira, M.J.B., 1996b. Isotope geochemistry constraints for Cu, Au mineralizations and evolution of the Carajás 763 province (Pará, Brazil). In: Congresso Brasileiro de Geologia, 39, Salvador, SBG, vol. 7. pp. 321–324.
Müller, S.G., Krapez, B., Barley, M.E., Fletcher, I.R., 2005. Giant iron-ore deposits of the Hamersley province related to the breakup of Paleoproterozoic Australia: new insights from in situ SHRIMP dating of baddeleyite from mafic intrusions. Geology 33, 577–580.
Nascimento, M.S., Oliveira, D.A., 2015. Ambiente deposicional e proveniência da Formação Gorotire, Província Carajás, sudeste do Cráton Amazônico. In: Gorayeb, P., Meiguins, A. (Eds.), Contribuições à Geologia da Amazônia, 9. Belém, SBG-Norte.
Noce, C., Zuccheti, M., Baltazar, O., Armstrong, R., Dantas, E., Renger, F., Lobato, L., 2005. Age of felsic volcanism and the role of ancient continental crust in the evolution of the Neoarchean Rio das Velhas Greenstone belt (Quadrilátero Ferrífero, Brazil): U-Pb zircon dating of volcaniclastic graywackes. Precambrian Res. 141, 67–82.
Nogueira, A.C.R., 1995. Análise faciológica e aspectos estruturais da Formação Águas Claras, Região Central da Serra dos Carajás-Pará MS Dissertation. Instituto de Geociências, Universidade Federal do Pará, Belém, pp. 168.
Nogueira, A.C.R., Truckenbrodt, W., Pinheiro, R.V.L., 1995. Formação Águas Claras, Pré-Cambriano da Serra dos Carajás, redescrição e redefinição litoestratigráfica. Boletim do Museu Paraense Emílio Goeldi. Série Ciências da Terra 7, 177–197.
Olszewski, W.J., Wirth, K.R., Gibbs, A.K., Gaudette, H.E., 1989. The age, origin, and tectonics of the Grão Pará Group and associated rocks, Serra dos Carajás, Brazil: Archean continental volcanism and rifting. Precambrian Res. 42, 229–254.
Orton, G.J., 1996. Volcanic environments. In: Reading, H.G. (Ed.), Sedimentary Environments: Processes, Facies and Stratigraphy, third ed. Blackwell, Oxford, pp. 485–567.
Ossa Ossa, F., El Albani, A., Hofmann, A., Bekker, A., Gauthier-Lafaye, F., Pambo, F., Meunier, A., Fontaine, C., Boulvais, F., Pierson-Wickmann, A., Cavalazzi, B., Macchiarelli, R., 2013. Exceptional preservation of expandable clay minerals in the ca. 2.1 Ga black shales of the Francevillian basin, Gabon and its implication for atmospheric oxygen accumulation. Chem. Geol. 362, 181–192.
Pereira, R.M.P., Rosiere, C.A., Santos, J.O.S., Lobato, L.M., Silva, R.C.F., McNaughton, N.J., 2009. Unidade Caninana: sequência clástica Paleoproterozóica revelada por datação U-Pb em zircões detríticos da Província Mineral Carajás. In: Simpósio de Geologia da Amazônia, vol. 11 SBG.
Pickard, A.L., 2003. SHRIMP U-Pb zircon ages for the paleoproterozoic kuruman iron

formation, northern cape province, South Africa: evidence for simultaneous BIF deposition on kaapvaal and Pilbara cratons. Precambrian Res. 125 (3/4), 275–315.
Pidgeon, R.T., Macambira, M.J.B., Lafon, J.M., 2000. Th-U-Pb isotopic systems and internal structures of complex zircons from the Pium Complex, Carajás Province, Brazil: evidence for the ages of the granulite facies metamorphism and the protolith of the enderbite. Chem. Geol. 166, 159–171.
Pinheiro, R.V.L., 1997. Reactivation History of the Carajás and Cinzento Strike Slip Systems, Amazon, Brazil. Ph.D. Thesis. University of Durham, England, pp. 408.
Pinheiro, R.V.L., Holdsworth, R.E., 1997. The structure of the Carajás N-4 ironstone deposit and associated rocks: relationship to Archaean strike-slip tectonics and basement reactivation in the Amazon region, Brazil. J. S. Am. Earth Sci. 10, 305–319.
Piper, J.D.A., 1978. Geological and geophysical evidence relating to continental growth and dynamics and the hydrosphere in Precambrian times: a review and analysis. In: Tidal Friction and the Earth's Rotation. Springer, Berlin, Heidelberg, pp. 197–241.
Ramos, J.F.F., Moura, C.A.V., Melo, C.F., Pereira, J.L., Serique, J.S.B., Rodrigues, R.M., 1984. Uma discussão sobre sequências sedimentares tidas como Formação Rio Fresco, sudeste do Pará In: Congresso Brasileiro de Geologia, 33, vol. 2. Rio de Janeiro, SBG, pp. 862–872.
Rasmussen, B., Fletcher, I.R., 2010. Dating sedimentary rocks using in situ U-Pb geochronology of syneruptive zircon in ash-fall tuffs< 1 mm thick. Geology 38, 299–302.
Rasmussen, B., Bekker, A., Fletcher, I.R., 2013. Correlation of Paleoproterozoic glaciations based on U–Pb zircon ages for tuff beds in the Transvaal and Huronian Supergroups. Earth Planet Sci. Lett. 382, 173–180.
Rogers, J.J.W., 1996. A history of continents in the past three billion years. J. Geol. 104, 91–107.
Rogers, J.J.W., Santosh, M., 2002. Configuration of Columbia, a mesoproterozoic supercontinent. Gondwana Res. 5, 5–22.
Romano, R., Lana, C., Alkmim, F.F., Stevens, G., Armstrong, R., 2013. Stabilization of the southern portion of the São Francisco Craton, SE Brazil, through a long-lived period of potassic magmatism. Precambrian Res. 224, 143–159.
Roy, S., 1997. Genetic diversity of manganese deposition in the terrestrial geological record. In: In: Nicholson, K., Hein, J.R., Buhn, B., Dasgupta, S. (Eds.), Manganese Mineralization: Geochemistry and Mineralogy of Terrestrial and Marine Deposits, vol. 199. Geological Society Special Publication, pp. 5–27.
Roy, S., 2006. Sedimentary manganese metallogenesis in response to the evolution of the Earth system. Earth-Sci. Rev. 77, 273–305.
Schröder, S., Beukes, N.J., Armstrong, R.A., 2016. Detrital zircon constraints on the tectonostratigraphy of the paleoproterozoic pretoria group, South Africa. Precambrian Res. 278, 362–393.
Skilling, I.P., White, J.D., McPhie, J., 2002. Peperite: a review of magma–sediment mingling. J. Volcanol. Geoth. Res. 114, 1–17.
Sekine, Y., Tajika, E., Tada, R., Hirai, T., Goto, K.T., Kuwatani, T., Goto, K., Yamamoto, S., Tachibana, S., Isozaki, Y.m Kirschvink J.L., 2011. Manganese enrichment in the Gowganda Formation of the Huronian Supergroup: a highly oxidizing shallow-marine environment after the last Huronian glaciation. Earth Planet Sci. Lett. 307, 201–210.
Steel, R.J., Thompson, D.B., 1983. Structures and textures in triassic braided stream conglomerates ('Bunter' pebble beds) in the sherwood sandstone group, north staffordshire, england. Sedimentology 30, 341–367.
Stow, D.A., 1979. Distinguishing between fine-grained turbidites and contourites on the Nova Scotian deep water margin. Sedimentology 26, 371–387.
Stow, D.A., Reading, H.G., Collinson, J.D., 1996. Deep seas. In: Reading, H.G. (Ed.), Sedimentary Environments: Process, Facies and Stratigraphy, third ed. Blachwell, Oxford, pp. 395–483.
Tallarico, F.H.B., Figueiredo, B.R., Groves, D.I., Kositcin, N., McNaughton, N.J., Fletcher, I.R., Rego, J.L., 2005. Geology and SHRIMP U-Pb geochronology of the Igarapé Bahia deposit, Carajás copper-gold belt, Brazil: an Archean (2.57 Ga) example of iron-oxide Cu-Au-(U-REE) mineralization. Econ. Geol. 100, 7–28.
Tang, H., Chen, Y., 2013. Global glaciations and atmospheric change at ca. 2.3 Ga. Geoscience Frontiers 4, 583–596.
Tavares, F.M., Trouw, R.A.J., da Silva, C.M.G., Justo, A.P., Oliveira, J.K.M., 2018. The multistage tectonic evolution of the northeastern Carajás Province, Amazonian Craton, Brazil: revealing complex structural patterns. J. S. Am. Earth Sci. 88, 238–252.
Teixeira, J.B.G., Misi, A., Silva, M.G., 2007. Supercontinent evolution and the proterozoic metallogeny of south America. Gondwana Res. 11, 346–361.
Teixeira, M.F.B., Dall'Agnol, R., Santos, J.O.S., Oliveira, D.C., Lamarão, C.N., McNaughton, N.J., 2018a. Crystallization ages of paleoproterozoic A-type granites of Carajás province, amazon craton: constraints from U-Pb geochronology of zircon and titanite. J. S. Am. Earth Sci. 88, 312–331.
Teixeira, W., Hamilton, M.A., Girardi, V.A.V., Faleiros, F.M., Ernst, R.E., 2018b. U-Pb baddeleyite ages of key dyke swarms in the amazonian craton (Carajás/Rio Maria and Rio apa areas): tectonic implications for events at 1880, 1110 Ma, 535 Ma and 200 Ma. Precambrian Res. 329, 138–155.
Thiéblemont, P., Castaing, C., Billa, M., Bouton, P., Préat, A., 2009. Notice explicative de la carte géologique et des Ressources minérales de la République gabonaise à 1/1000 000. Libreville, Gabon. Editions DGMG – Ministère des Mines, du Pétrole, des Hydrocarbures, Libreville, pp. 381.
Trendall, A.F., Basei, M.A.S., De Laeter, J.R., Nelson, D.R., 1998a. SHRIMP U-Pb constraints on the age of the Carajás Formation, Grão Pará group, amazon craton. J. S. Am. Earth Sci. 11, 265–277.
Trendall, A.F., Nelson, D.R., de Laeter, J.R., Hassler, S.W., 1998b. Precise zircon U-Pb ages from the marra mamba iron formation and the wittenoom formation, Hamersley group, western Australia. Aust. J. Earth Sci. 45, 137–142.
Tsikos, H., Beukes, N.J., Moore, J.M., Harris, C., 2003. Deposition, diagenesis, and secondary enrichment of metals in the Paleoproterozoic Hotazel iron formation, Kalahari manganese field, South Africa. Econ. Geol. 98, 1449–1462.
Tucker, M.E., 2003. In: Sedimentary Rocks in the Field: the Geological Field Guide Series, 3ª ed. John Wiley & Sons, pp. 234.
Van Kranendonk, M.J., Mazumder, R., Yamaguchi, K.E., Yamada, K., Ikehara, M., 2015. Sedimentology of the paleoproterozoic kungarra formation, turee creek group, western Australia: a conformable record of the transition from early to modern earth. Precambrian Res. 256, 314–343.
Vasquez, M.L., Sousa, C.S., Carvalho, J.M.A., 2008a. Mapa Geológico e de Recursos Minerais do Estado do Pará. Escala 1:1.000.000. Brazilian Geological Survey – CPRM.
Vasquez, M.L., Rosa-Costa, L.T., Silva, C.G., Ricci, P.F., Barbosa, J.O., Klein, E.L., Lopes, E.S., Macambira, E.B., Chaves, C.L., Carvalho, J.M., Oliveira, J.G., Anjos, G.C., Silva, H.R., 2008b. Geologia e Recursos Minerais do Estado do Pará: sistema de Informações Geográficas-SIG: texto Explicativo dos Mapas Geológico e Tectônico e de Recursos Minerais do Estado do Pará. Escala 1:1.000.000. In: Vasquez, M.L., Rosa-Costa, L.T. (Eds.), Belém, Brazilian Geological Survey - CPRM, pp. 1–329.
Walker, R.G., 1992. Facies, facies models and modern stratigraphic concepts. In: Walker, R.G., James, N.P. (Eds.), Facies Models: Response to Sea Level Change. Ontario. Geological Association of Canada, pp. 1–14.
Walker, R.G., 2006. Facies models revisited: an introduction. In: In: Posamentier, H.W., Walker, R.G. (Eds.), Facies Models Revisited, vol. 84. SEPM, Society for Sedimentary Geology -SEPM, Special Publications, Tulsa, Oklahoma, pp. 1–18.
Walraven, F., 1997. Geochronology of the Rooiberg Group, Transvaal Supergroup, South Africa. Economic Geology Research Unit, University of the Witwatersrand, Johannesburg, South Africa. Information Circular 316. Economic Geology Research Unit, University of the Witwatersrand, Johannesburg, South Africa 21.
Wirth, K.R., Gibbs, A.K., Olszewski, W., 1986. U-Pb zircon ages of the grão-pará group and Serra dos Carajás granite. Rev. Bras. Geociencias 16, 195–200.
Young, G.M., 2014. Contradictory correlations of Paleoproterozoic glacial deposits: local, regional or global controls? Precambrian Res. 247, 33–44.
Zhao, G., Sun, M., Wilde, S.A., Li, S., 2004. A Paleo-Mesoproterozoic supercontinent: assembly, growth and breakup. Earth Sci. Rev. 67, 91–123.
Zucchetti, M., 2007. Rochas máficas do Supergrupo Grão Pará e sua relação com a mineralização de ferro dos depósitos N4 e N5, Carajás, PA. Unpublish. Ph.D. Thesis. Universidade Federal de Minas Gerais, Brazil, pp. 165 (in Portuguese).

Appendix A: Summary of drill cores and outcrops investigated in this study.

MEASURED SECTIONS	LAT	LONG
DRILL CORE ALV8-FD06	5°56'0.35"S	50°39'47.95"W
BAHIA MINE OUTCROP	6°1'43.20"S	50°34'19.23"W
BAHIA ROAD OUTCROP	6°7'38.79"S	50°29'45.18"W
DRILL CORE AN10-DH001	6°9'5.11"S	50°20'22.11"W
DRILL CORE AN10-DH002	6°8'59.50"S	50°20'17.79"W
DRILL CORE MNA-FD-1096	6°6'7.35"S	50°18'28.45"W
DRILL CORE MNA-FH-0933	6°6'13.29"S	50°18'08.00"W
AZUL MINE OUTCROP	6°6'35.22"S	50°17'33.29"W
DRILL CORE FD-706	6°6'43.56"S	50°17'33.84"W
DRILL CORE ITA-GT58-FD0002	6°5'28.80"S	50°15'5.99"W

ANEXO B – MATERIAL SUPLEMENTAR DO ARTIGO SERRA SUL DIAMICTITE OF THE CARAJÁS BASIN (BRAZIL): A PALEOPROTEROZOIC GLACIATION ON THE AMAZONIAN CRATON

Supplementary Material

Paper: Serra Sul diamictite of the Carajás Basin (Brazil): A Paleoproterozoic glaciation on the Amazonian craton

By Raphael Araújo and Afonso Nogueira, 2019

Geology

Table of contents

Figure DR1. Photographs of the drill core SSD-FD927 06

Figure DR2. Photographs of the drill core GT41-F13 07

Figure DR3. Complete set of core-based sedimentary logs 02

Table DR4. GPS coordinates of boreholes..... 03

Table DR5. Terrigenous lithofacies of the Serra Sul Formation..... 04

Figure DR6. Images of the main features observed in subglacial diamictite (foliated to massive diamictite facies association)..... 08

Figure DR7. Images of the main features observed in rhythmite (rhythmite facies association) 09

Figure DR8. Images of the main features observed in sandstones and clast-supported conglomerate (conglomerate-sandstone-rhythmite-diamictite facies association). 10

Figure DR9. Images of the main features observed in diamictite (conglomerate-sandstone-rhythmite-diamictite facies association)..... 12

Figure DR10. Scanning electron microscope (SEM) images showing microtextures observed on very angular quartz sand grain surfaces 13

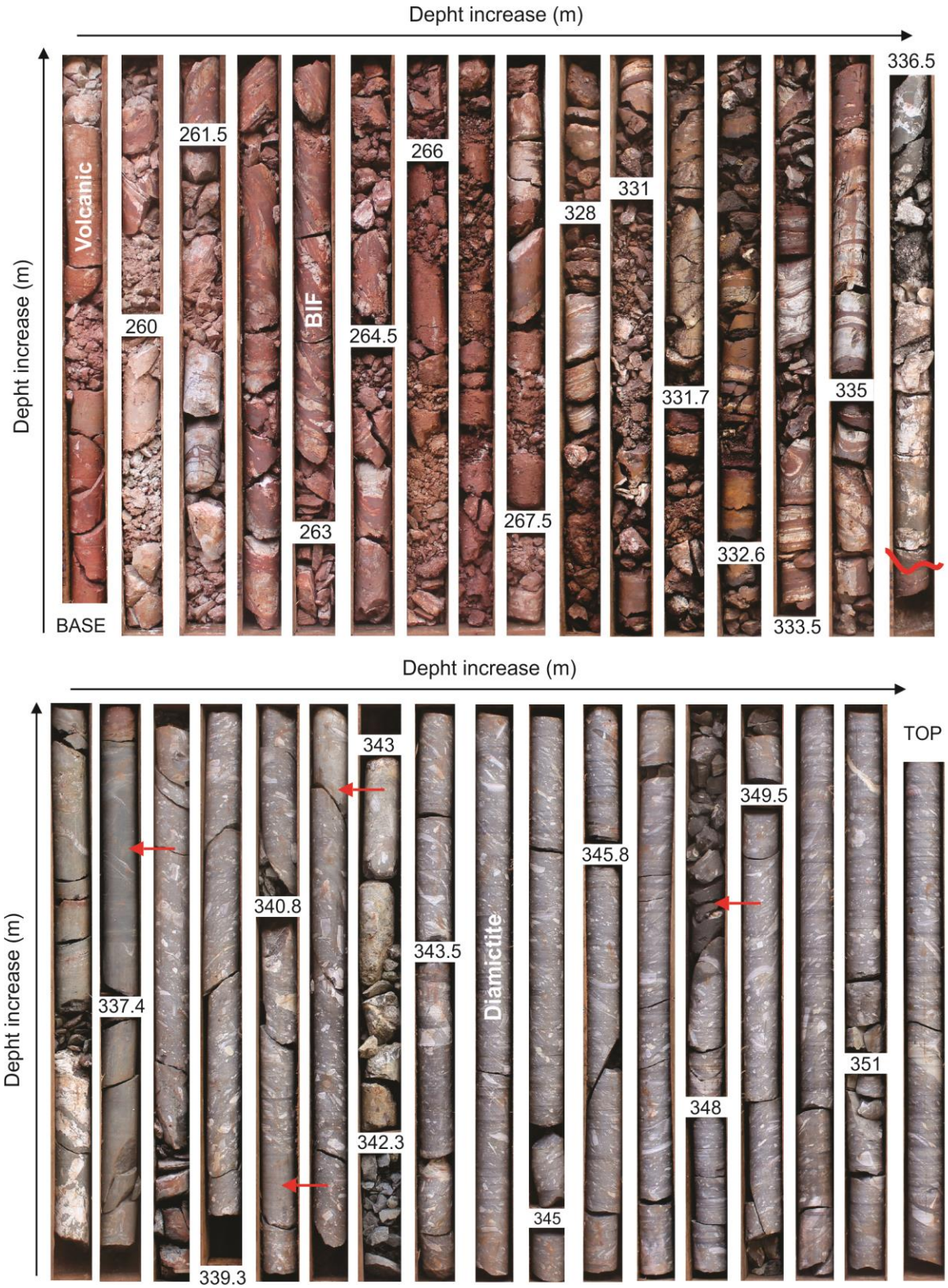

Figure DR1. Photograph of the drill core SSD-FD927 showing the contact (unconformity) between volcanic rock and BIF of the Neoarchean Grão-Pará Group and diamictite and black shale of the Serra Sul Formation (foliated to massive diamictite facies association). Arrows point to shale intervals that are interbedded with diamictite. The sedimentary structures indicate that the succession is stratigraphically inverted.

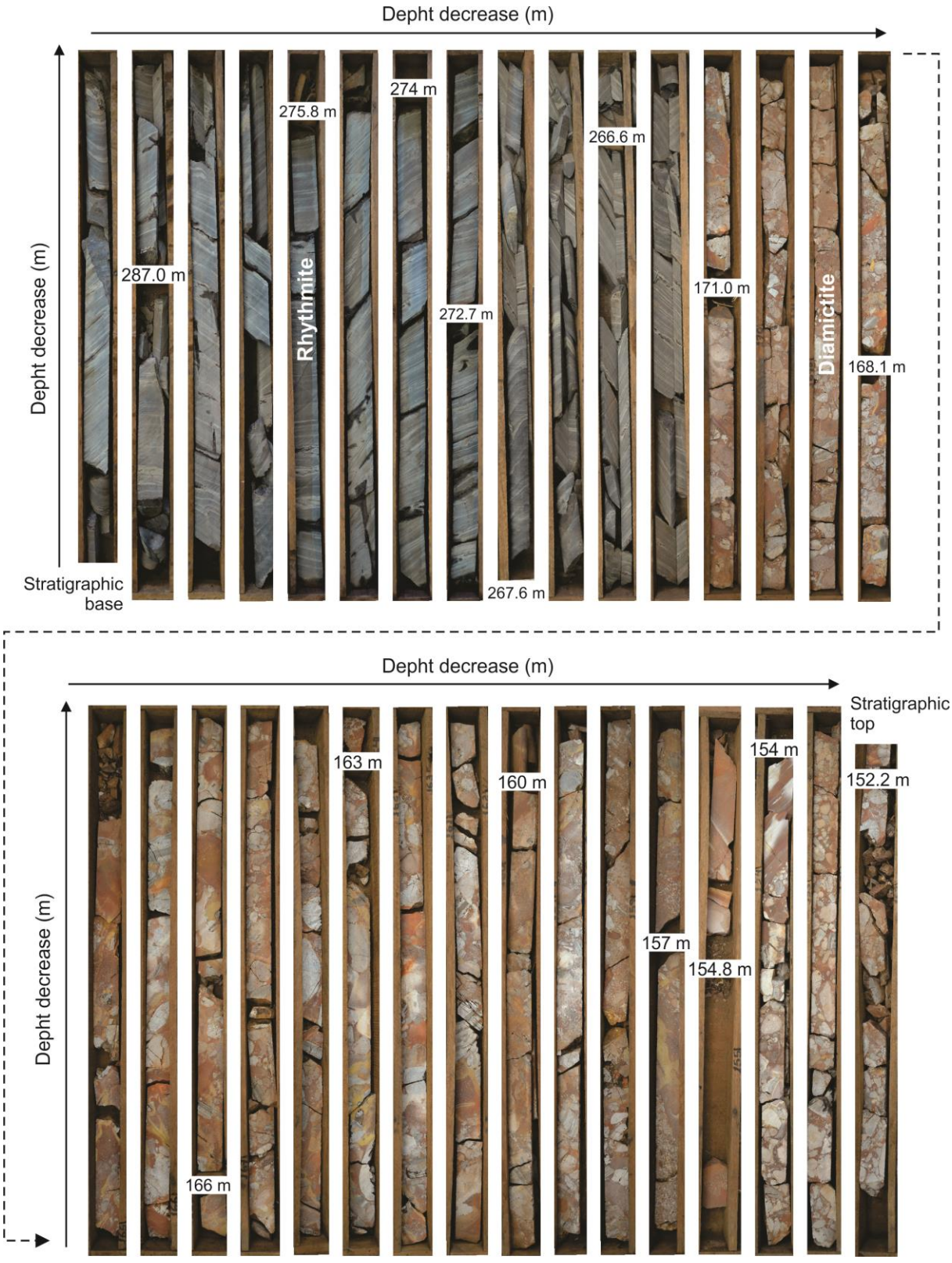

Figure DR2. Photograph of the drill core GT41-F13 showing the contact between the rhythmite facies association at the base, and conglomerate-sandstone-rhythmite-diamictite facies association at the top. Note that the stratigraphy is not inverted.

Figure DR3. Complete set of core-based sedimentary logs showing the interpreted lateral relationship and distribution of the facies associations. Positions of logged sections are shown on the map to the far right.

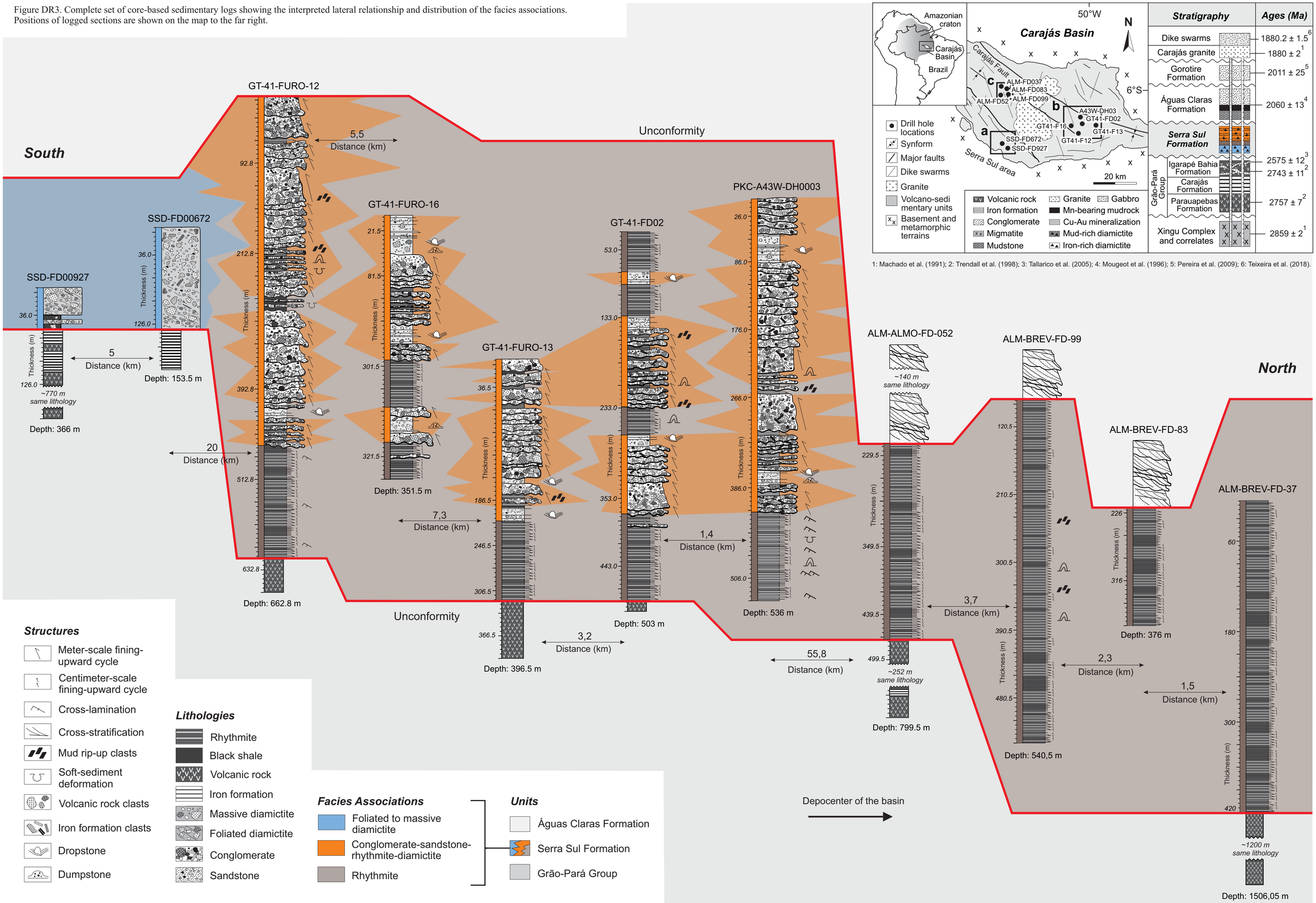

1: Machado et al. (1991); 2: Trendall et al. (1998); 3: Tallarico et al. (2005); 4: Mougeot et al. (1996); 5: Pereira et al. (2009); 6: Teixeira et al. (2018).

Table DR4. GPS coordinates of boreholes.

#Area a

Borehole	Latitude	Longitude	Date of description
SSD-FD00927	-6.38038850692	-50.3054460162	30th May 2018
SSD-FD00672	-6.35261051256	-50.3521129974	30th May 2018

#Area b

Borehole	Latitude	Longitude	Date of description
GT-41-FURO-12	-6.30288813137	-50.16877829	30th November 2017
GT-41-FURO-16	-6.2687212183	-50.2023896165	01th December 2017
GT-41-FURO-13	-6.26927683397	-50.1357224653	30th November 2017
GT-41-FD02	-6.25872118821	-50.1626670969	05th December 2017
PKC-A43W-DH0003	-6.25149891073	-50.1735005029	13th November 2015

#Area c

Borehole	Latitude	Longitude	Date of description
ALM-ALMO-FD052	-6.02955267811	-50.6240591362	06th December 2017
ALM-BREV-FD-99	-6.01816374201	-50.5935033509	21th June 2015
ALM-BREV-FD-83	-6.00038584039	-50.6068367659	18th June 2015
ALM-BREV-FD-37	-5.99871915223	-50.620170194	12th June 2015

Table DR5. Terrigenous lithofacies of the Serra Sul Formation.

Lithofacies	Description	Processes	Depositional environment
Massive diamictite	Unstratified and unsheared. The matrix is very poorly sorted and composed of micrometer-scale fragments of quartz and magnetite, and sometimes by mud. The clasts comprise chert, BIF-derived grains, and volcanic rock fragments. The clasts vary from angular to well-rounded. Faceted clasts occur widely. There are dropstones and dumpstones.	Glacial erosion of the bedrock (BIF and volcanic rock); ice-rafted debris associated with sedimentation by suspension	Subglacial coastal and marine setting
Foliated diamictite	Stratified and sheared. The matrix is very poorly sorted and composed of quartz and magnetite. Faceted, flattened, rotated, boudinaged, sheared, and lens-shaped clasts are widespread. The clasts are pebble to cobble-sized, vary in shape from very angular to rounded, and comprise chert, BIF-derived clasts, and volcanic rock fragments.	Glacial erosion (rock flour) of the bedrock (BIF and volcanic rock) associated with glaciotectonic deformation	Subglacial coastal
Black shale	Laminated and enriched in organic matter. Tabular geometry (inferred).	Sedimentation by suspension associated with the preservation of organic matter	Subglacial coastal
Rhythmite	Even parallel laminations. Composed of millimeter-scale to centimeter-scale intercalated fine-grained sandstone and argillite. Sulfides are disseminated in the sandstone layers. Ball-and-pillow, flame, and convolute laminations occur at facies contacts. Cross-laminae occur locally in the sandstone beds.	Regular alternation of sedimentation by traction and suspension; deposition by very low-density turbidite currents; plastic adjustments resulting in soft-sediment deformation; starved ripples	Basin floor (turbidite)

Conglomerate	Unstratified to weakly cross-stratified. Concave-up geometry (inferred). The clasts vary in size from pebbles to cobbles, subangular to well-rounded, and are composed of fragments of chert, BIF-derived clasts, and volcanic rock. The matrix varies from sandy to granular.	Deposition by high-density turbidity current	Glaciogenic submarine fan
Sandstone	Massive to weakly cross-stratified. Fine-grained to coarse-grained. The sand grains are composed of chert and quartz. Very well- to poorly sorted	Deposition by high-density turbidity current associated with a decline in velocity	Glaciogenic submarine fan

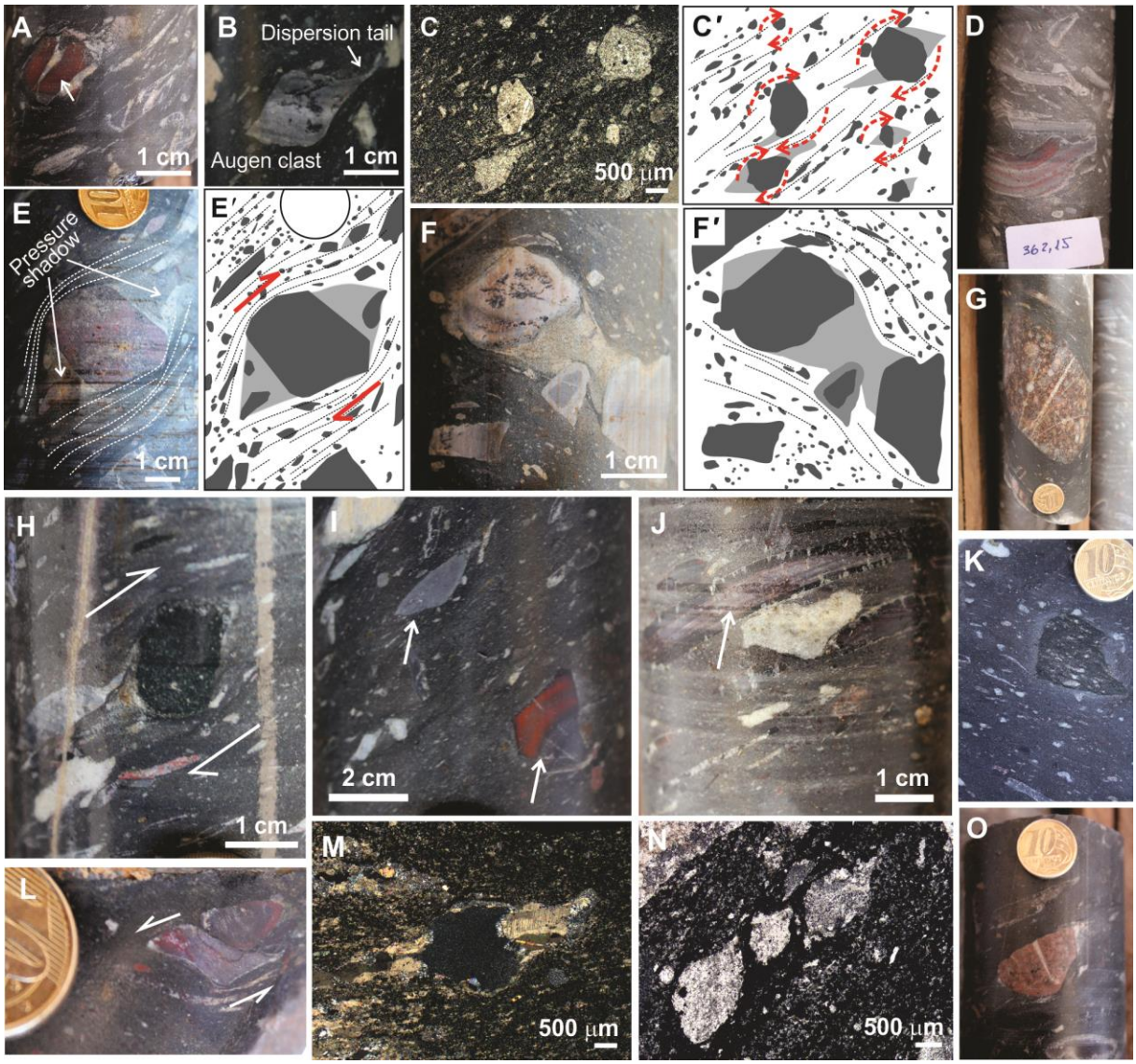

Figure DR6. Images of the main features observed in subglacial diamictite (foliated to massive diamictite facies association). A: Fractured and boudinaged clast of felsic volcanic rock (arrow). B: Augen clast of chert with a well-developed dispersion tail. C and C′: Photomicrograph (plane polarized light, 5x) and line interpretation of foliated diamictite showing faceted and rotated chert clasts with an asymmetrical pressure shadow. D: Several tabular BIF clasts scattered randomly in a fine-grained matrix. E and E′: Image and line interpretation of a faceted and rotated felsic volcanic rock (rhyolite) clast with an asymmetrical pressure shadow. F and F′: Image and line interpretation showing a classical boudinaged chert clast immersed in a poorly sorted and fine-grained matrix. G: Porphyritic volcanic rock clast suspended in a fine-grained matrix. The coin is 2 cm in diameter. H: Sheared clast of mafic volcanic rock with an asymmetrical pressure shadow. I: Flattened and faceted clasts of chert and BIF (arrows). J: Flattened clasts of BIF and chert showing fractures along the borders (arrow). K: Mafic volcanic rock clast embedded in a dark-colored and fine-grained matrix. L: Sheared clast of a BIF. M: Photomicrograph (cross-polarized light, 10x) showing a sheared chert clast with an asymmetrical pressure shadow composed of dolomite and quartz. N: Photomicrograph (plane polarized light, 10x) showing a micro-boudinaged chert clast. O: Faceted felsic volcanic rock with a pressure shadow exhibiting fractures perpendicular to foliation. The coin is 2 cm in diameter.

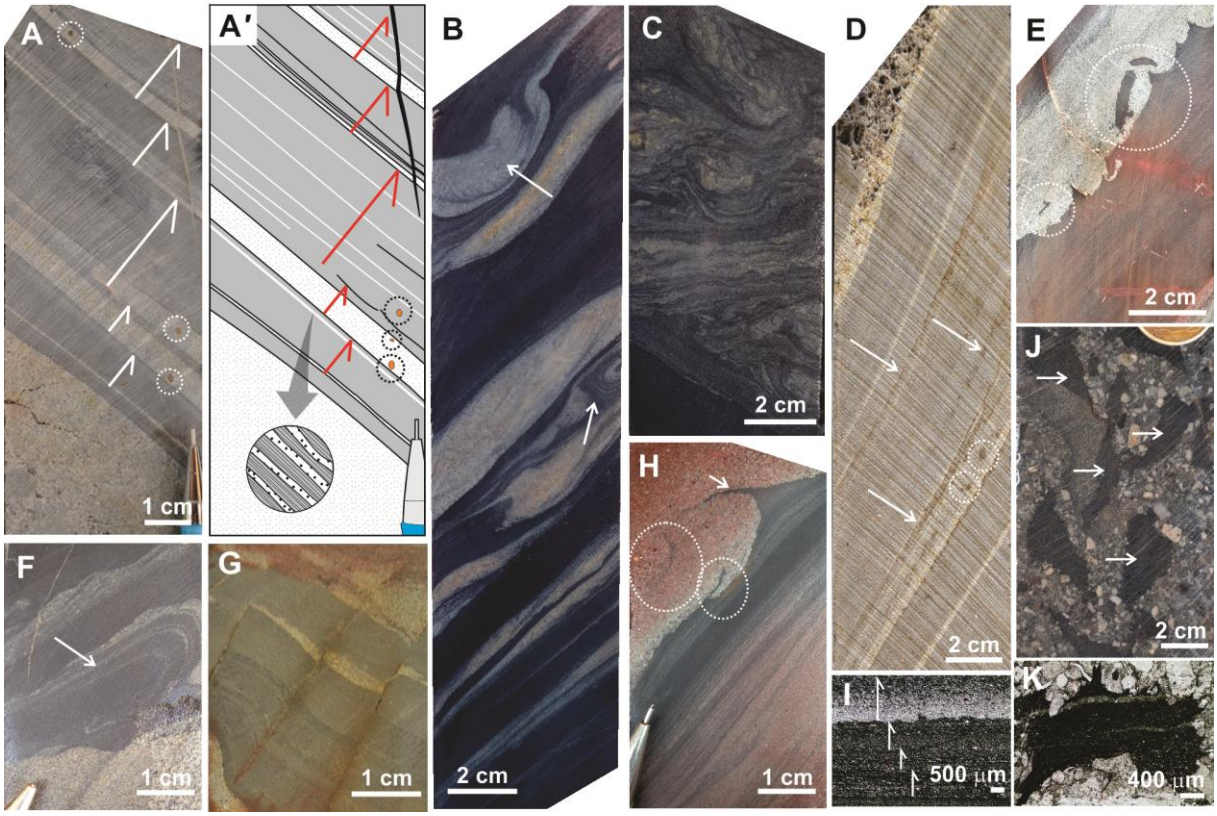

Figure DR7. Images of the main features observed in rhythmite (rhythmite facies association). A and A′: Image and line interpretation showing centimeter-scale fining-upward cycles between sandstone with normal gradations and mudstone. B: Black shale interbedded with fine-grained sandstone with normal gradation (rhythmite). Soft-sediment deformation (e.g., ball-and-pillow and convolute lamination) is widely developed contact zone between these two lithotypes. Cross-laminae sandwiched by muddy beds (starved ripples) occur locally and sulfide occurs within the sandstone layers. C: Completely convoluted sandy bed above an undeformed muddy bed. D: Rhythmite showing sulfide (arrows) disseminated in beds of fine-grained sandstone. E: Mud rip-up clasts (circles) in the base of a sandstone bed. F: Convoluted laminae. G: Syndepositional fault. H: Erosive contact between mudstone and sandstone showing flame (arrow) and curled mud flakes suspended at the base of the sandy bed (circles). I: Photomicrograph (plane polarized light, 5x) showing micrometer-scale fining-upward cycles between sandstone with normal gradation and mudstone. J: Several mud rip-up clasts (arrows) suspended in a conglomerate bed. K: Photomicrograph (plane polarized light, 5x) showing a mud clast deformed within a sandstone layer.

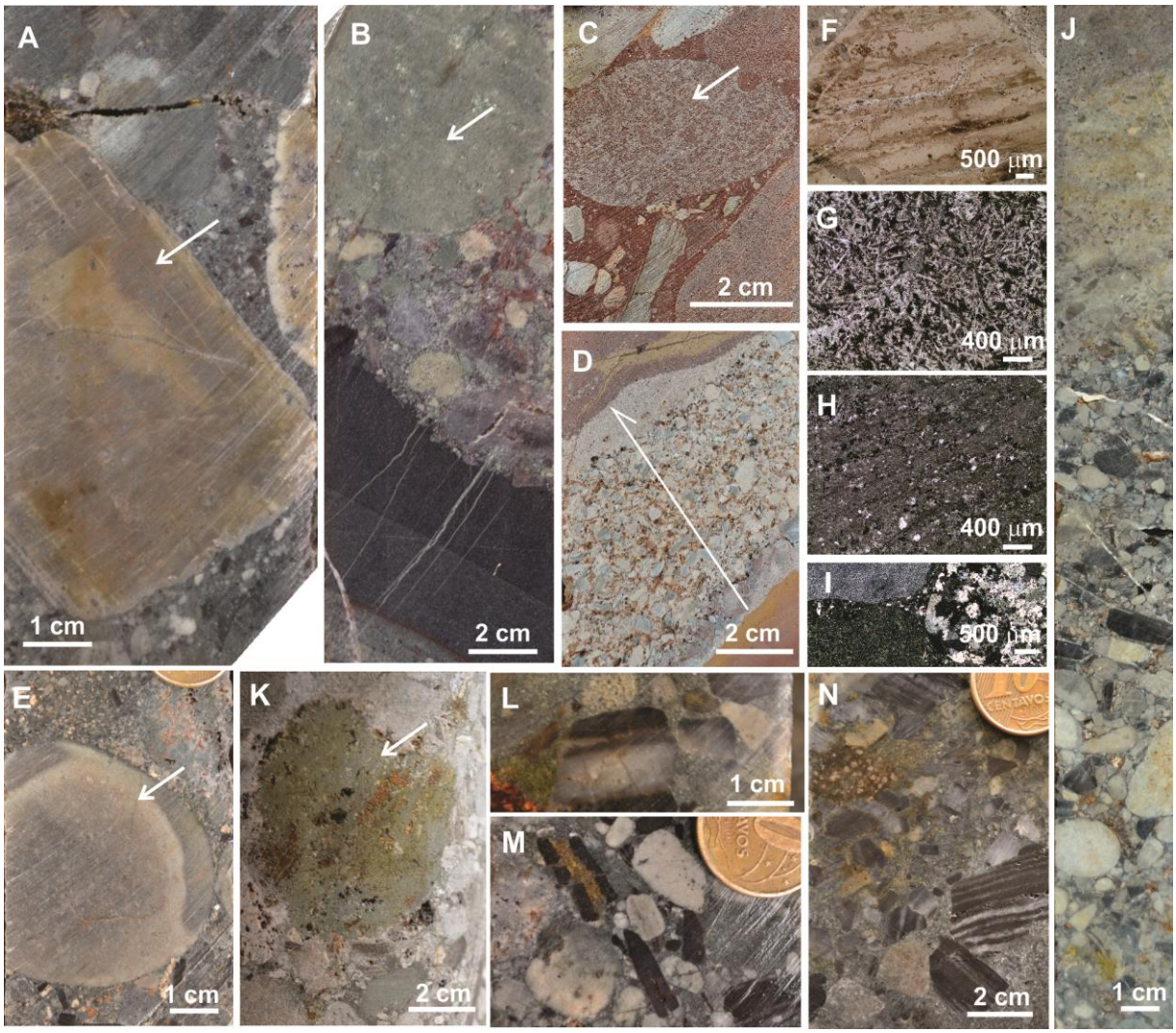

Figure DR8. Images of the main features observed in sandstone and clast-supported conglomerate (conglomerate-sandstone-rhythmite-diamictite facies association). A: Clast-supported conglomerate with faceted volcanic rock clasts (arrow). B: Clast-supported conglomerate with rounded volcanic rock clasts above a mudstone bed. C: Rounded volcanic rock clast (arrow) showing punctuated contact with other clasts in a clast-supported conglomerate. D: Conglomerate bed with normal gradation (arrow). E: Rounded volcanic rock clast (arrow) embedded in a sandy/conglomeratic matrix. F-H: Photomicrographs (plane polarized light, 5x) showing chert, volcanic rock, and volcanoclastic rock clasts, respectively. I: Photomicrograph (cross-polarized light, 5x) showing different volcanic to subvolcanic rock clasts. J: Fining-upward cycle showing a conglomerate with normal gradation trending up-section to massive sandstone. K: Mineralized mafic volcanic rock clasts (arrow) in a clast-supported conglomerate. L-N: Clast-supported conglomerate showing BIF, iron chert, mineralized volcanic rock, and mafic to felsic volcanic/subvolcanic rock clasts. The coin is 2 cm in diameter.

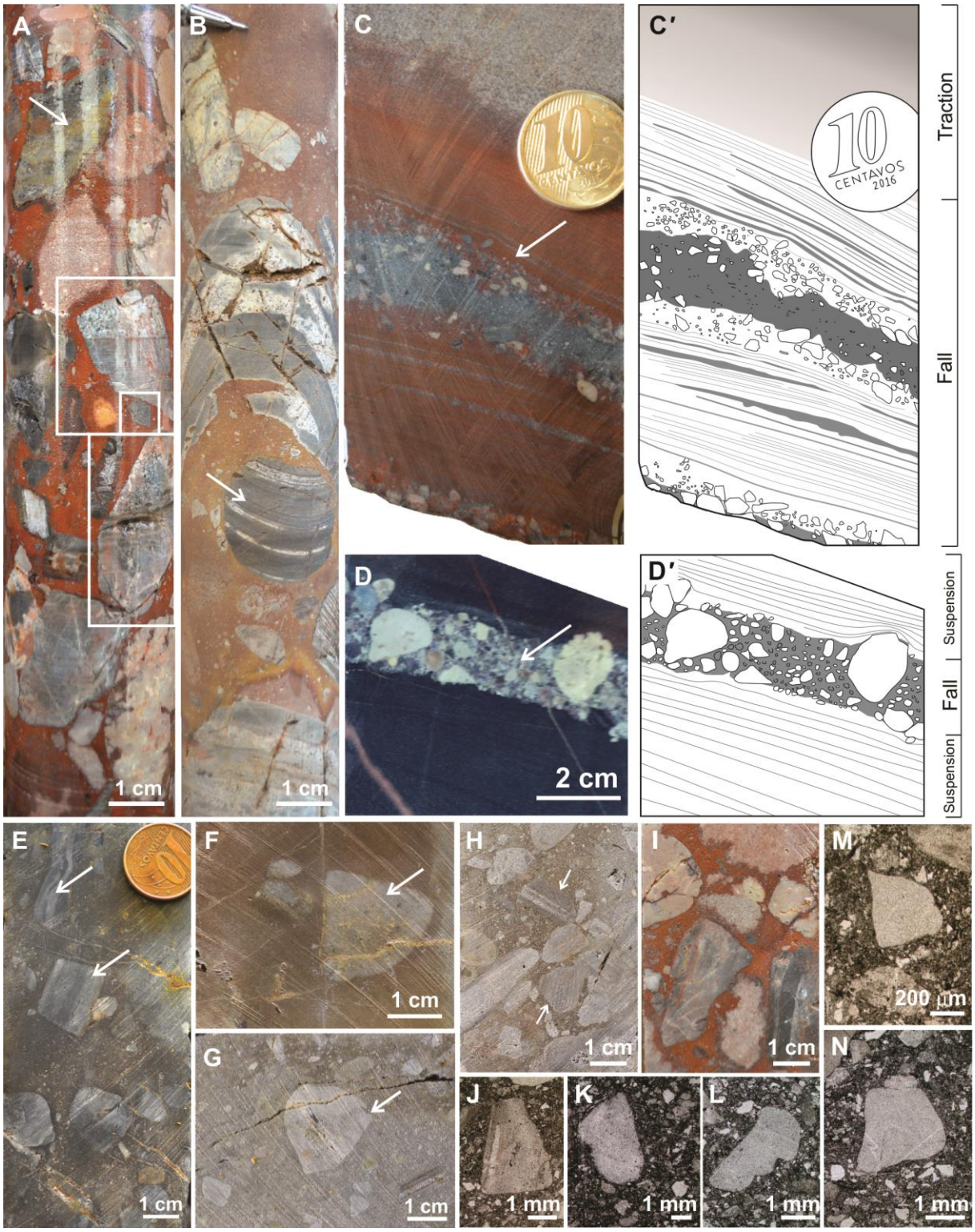

Figure DR9. Images of the main features observed in diamictite (conglomerate-sandstone-rhythmite-diamictite facies association). A: Clasts of mineralized volcanic rock (arrow), chert, and BIF suspended in a mud-rich matrix. Some faceted clasts are perfect elongated pentagons (boxes). B: BIF clasts, varying in shape from faceted to well-rounded (arrow), scattered in a mud-rich matrix. C-C′ and D-D′: Images and line interpretations showing a dumpstone structure defined by mounds of coarse-grained clasts (arrows) of volcanic rock, chert, and BIF suspended in and sandwiched by mudstone beds. E: Chert and BIF clasts with high dip angles (arrows) suspended in a mud-rich matrix. F and G: Faceted chert clast (arrows) suspended in a

poorly-sorted mud-rich matrix. H-I: Clasts of chert, BIF and volcanic rock, sometimes faceted (arrows), randomly scattered in a muddy matrix. J-N: Photomicrograph (plane polarized light, 5x) showing several faceted chert clasts in a poorly-sorted mud-rich matrix.

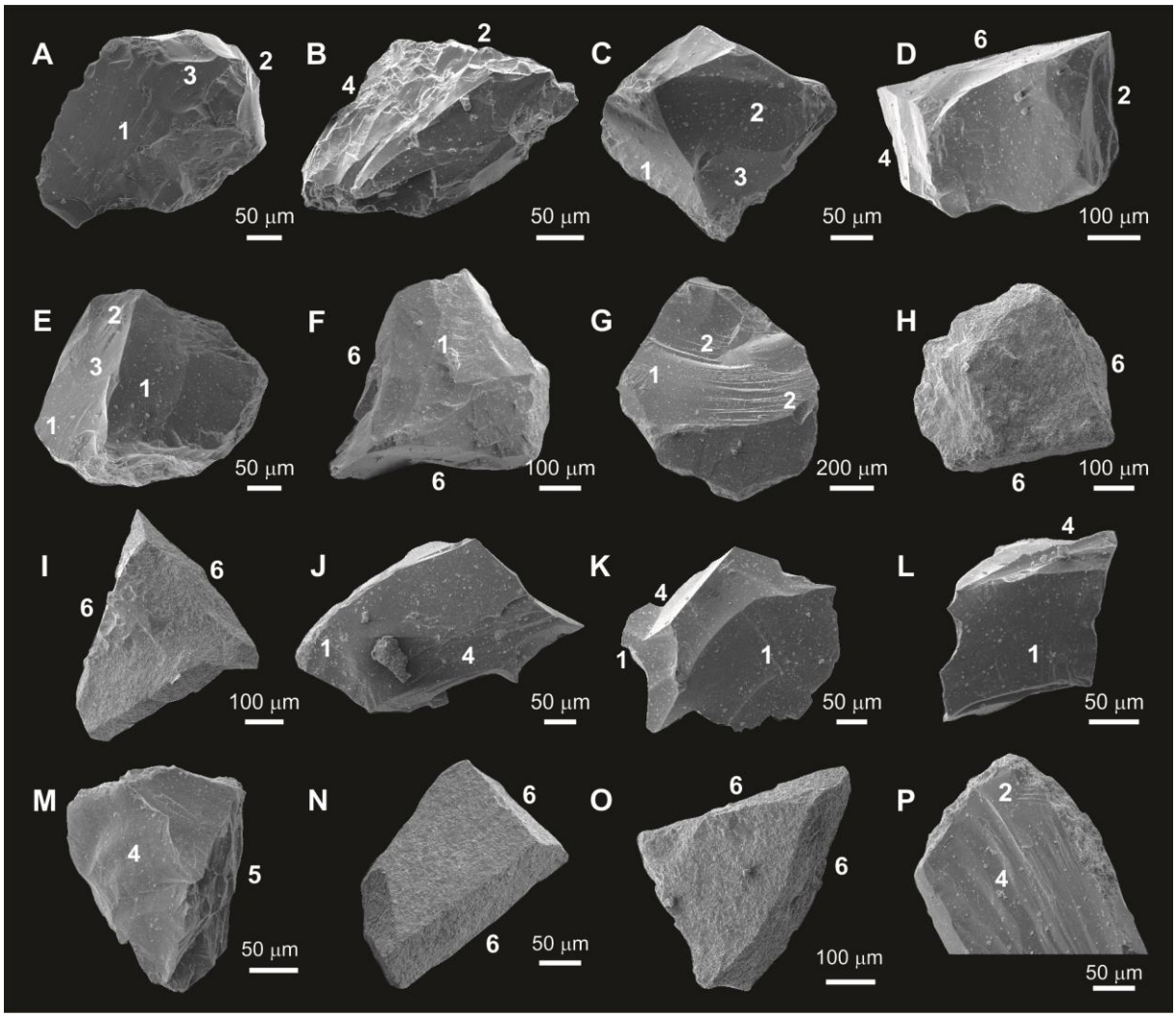

Figure DR10. Scanning electron microscope (SEM) images showing microtextures observed on very angular quartz sand grain surfaces: subparallel fractures (1), steps (2), conchoidal fractures (3), grooves (4), crushed surfaces (5), and smoothed surfaces (6).

ANEXO C - MATERIAL SUPLEMENTAR DO ARTIGO EVIDENCES OF AN 'OIL-LIKE' MANGANESE REMOBILIZATION IN THE PALEOPROTEROZOIC AZUL RED BEDS OF THE CARAJÁS BASIN (AMAZONIAN CRATON, BRAZIL): AN INTERPLAY AMONG SEDIMENTARY AND TECTONIC CONTROLS

Table S-1: Major oxides (wt %) analyzed by ICP-AES.

Perte 110	Somme	Perte 1000	SiO_2	Al_2O_3	MgO	CaO	Fe_2O_3	MnO	TiO_2	Na_2O	K_2O	P_2O_5
1,35	87,41	14,66	3,25	5,58	0,51	0,33	6,26	55,23	0,21	0,01	1,22	0,14
0,81	85,99	13,50	26,48	22,17	0,19	0,13	7,08	14,70	1,02	0,00	0,62	0,11
1,72	86,85	13,68	6,43	8,65	0,49	0,37	6,46	49,04	0,42	0,00	1,15	0,16
0,89	90,68	12,37	23,52	20,56	0,19	0,11	18,33	13,54	1,02	0,00	0,72	0,32
0,41	97,80	9,35	59,40	12,51	4,17	0,11	4,95	3,12	0,58	0,00	3,54	0,06
0,79	95,33	13,86	31,84	26,41	0,24	0,09	10,89	10,23	1,17	0,00	0,49	0,09
0,69	88,72	14,48	27,53	23,89	0,26	0,13	7,68	13,15	1,05	0,00	0,47	0,08
0,22	92,04	16,29	9,15	11,00	0,74	0,38	8,43	43,66	0,96	0,00	1,27	0,15
0,76	86,35	11,16	0,28	1,41	0,00	0,26	0,52	67,95	0,01	0,03	4,00	0,73
0,88	87,84	13,42	4,92	5,10	0,00	0,22	11,61	50,14	0,18	0,00	1,74	0,52

ANEXO D - MATERIAL SUPLEMENTAR DO ARTIGO TECTONO-SEDIMENTARY EVOLUTION OF A PALEOPROTEROZOIC SUCCESSION OF THE CARAJÁS BASIN, SOUTHEASTERN AMAZONIAN CRATON, BRAZIL: INSIGHTS FROM STRATIGRAPHY, SEDIMENTOLOGY, AND U-Pb DETRITAL ZIRCON GEOCHRONOLOGY

Table S-1: Summary of drill cores and outcrops investigated in this study.

Area	Type	Name	Lat	Long	Thickness	Reference
Serra Sul	Drill core	LOG A	6.380388° S	50.305446° W	*ca.* 210 m	Araújo and Nogueira (2019)
Tarzan	Drill core	LOG B	6.268721° S	50.202389° W	*ca.* 630 m	Araújo and Nogueira (2019)
Igarapé Bahia	Drill core	LOG C	6.029552° S	50.624059° W	*ca.* 360 m	Araújo and Nogueira (2019)
	Drill core	PKC-LILI-DH001	6.033368° S	50.644291° W	*ca.* 513 m	This study
	Drill core	PKC-SALV-DH002	6.005912° S	50.591539° W	*ca.* 407 m	This study
	Drill core	PKC-SALV-DH001	6.005785° S	50.590943° W	*ca.* 255 m	This study
	Drill core	ALV8-FD06	6.012500° S	50.544049° W	*ca.* 1009 m	Araújo Filho et al. (2020)
Bahia road	Outcrop	ROAD-1	6.167353° S	50.357424° W	*ca.* 15 m	This study
	Outcrop	ROAD-2	6.162166° S	50.354177° W	*ca.* 21 m	This study
	Outcrop	ROAD-3	6.147006° S	50.325735° W	*ca.* 45 m	This study
	Outcrop	ROAD-4	6.161490° S	50.348971° W	*ca.* 18 m	This study
	Drill core	AN10-DH0001	6.151420° S	50.339476° W	*ca.* 203 m	Araújo Filho et al. (2020)
	Drill core	AN10-DH0002	6.149862° S	50.338276° W	*ca.* 204 m	Araújo Filho et al. (2020)
	Drill core	AN10-DH0003	6.157541° S	50.330485° W	*ca.* 205 m	This study
	Outcrop	ROAD-5	6.143779° S	50.342133° W	*ca.* 40 m	This study
Azul mine	Drill core	MNA-FD-1096	6.101973° S	50.308097° W	*ca.* 208 m	Araújo Filho et al. (2020)
	Drill core	MNA-FD-1427	6.095124° S	50.336201° W	*ca.* 75 m	This study
	Drill core	MNA-FD-0913	6.112292° S	50.306556° W	*ca.* 129 m	This study
	Drill core	MNA-FD-1062	6.103254° S	50.305981° W	*ca.* 153 m	This study

Outcrop	AZUL MINE	6.111935° S	50.298835° W	*ca*. 60 m	Araujo and Sousa (2018)
Drill core	MNA-FD-1056	6.107795° S	50.305866° W	*ca*. 120 m	This study
Drill core	MNA-FD-0933	6.103693°S	50.302221° W	*ca*. 150 m	Araújo Filho et al. (2020)
Drill core	MNA-FD-1068	6.112205° S	50.295567° W	*ca*. 138 m	This study

Table S-2: Summary of results of U-Pb dating of zircon by LA-ICP-MS.

						Isotope ratios[c]							Ages (Ma)						
SAMPLE DEQ-387	f_{206}[a]	**Pb (ppm)**	**Th (ppm)**	**U (ppm)**	**Th/U[b]**	**207Pb/ 235U**	**1σ (%)**	**206Pb/ 238U**	**1σ (%)**	**Rho[d]**	**207Pb/ 206Pb[e]**	**1σ (%)**	**206Pb/ 238U**	**1σ (abs)**	**207Pb/ 235U**	**1σ (abs)**	**207Pb/ 206Pb**	**1σ (abs)**	**Conc.[f] (%) 6/8-7/6**
Zircon DEQ387A D5	0,0046	72	67	120	0,56	13,17	0,88	0,48	0,60	0,68	0,2	0,64	2535	15	2692	24	2812	18	90
Zircon DEQ387A D6	0,0068	130	210	266	0,8	12,28	1,48	0,47	0,84	0,57	0,19	1,22	2486	21	2626	39	2736	33	91
Zircon DEQ387A D7	0,0192	184	89	174	0,51	12,71	4,25	0,5	4,12	0,97	0,19	1,02	2598	107	2659	113	2705	28	96
Zircon DEQ387A D10	0,0025	4	5	7	0,72	12,25	2,97	0,47	2,42	0,82	0,19	1,72	2470	60	2624	78	2745	47	90
Zircon DEQ387A E2	0,0101	76	62	121	0,52	12,19	1,34	0,47	1,06	0,79	0,19	0,82	2487	26	2619	35	2723	22	91
Zircon DEQ387A E5	0,0062	4	5	6	0,79	12,53	3,79	0,48	2,54	0,67	0,19	2,81	2512	64	2645	100	2748	77	91
Zircon DEQ387A F6	0,0163	261	3720	1279	2,93	9,67	1,72	0,43	1,41	0,82	0,16	0,98	2324	33	2404	41	2472	24	94
Zircon DEQ387A F8	0,0193	226	226	376	0,61	8,95	2,84	0,43	2,63	0,93	0,15	1,06	2324	61	2333	66	2340	25	99
Zircon DEQ387A G4	0,0026	189	355	203	1,76	15,61	1,06	0,57	0,70	0,66	0,2	0,8	2897	20	2853	30	2822	23	103
Zircon DEQ387A G8	0,0119	187	315	245	1,29	11,28	2,48	0,45	0,99	0,4	0,18	2,28	2407	24	2547	63	2660	61	91
Zircon DEQ387A G10	0,0093	125	153	228	0,67	11,87	2,03	0,5	1,72	0,85	0,17	1,07	2623	45	2595	53	2573	28	102
Zircon DEQ387A H2	0,0005	95	73	131	0,56	16,18	1,21	0,58	0,88	0,72	0,2	0,83	2969	26	2888	35	2832	24	105
Zircon DEQ387A H4	0,0044	115	128	173	0,75	12,72	1,55	0,49	1,34	0,86	0,19	0,79	2587	35	2659	41	2714	22	95
Zircon DEQ387A H6	0,0028	75	88	78	1,15	14,86	1,20	0,54	0,98	0,82	0,20	0,69	2764	27	2807	34	2837	20	97
Zircon DEQ387A H7	0,0008	78	65	112	0,59	15,52	0,95	0,56	0,67	0,70	0,2	0,67	2846	19	2848	27	2849	19	100
Zircon DEQ387A H8	0,0009	77	68	103	0,66	16,00	1,17	0,57	0,90	0,77	0,2	0,75	2913	26	2877	34	2851	21	102
Zircon DEQ387A H10	0,0082	75	82	78	1,06	15,11	2,57	0,56	2,46	0,96	0,2	0,74	2873	71	2823	73	2787	21	103
Zircon DEQ387A H11	0,0041	78	65	129	0,51	12,58	1,9	0,51	1,67	0,88	0,18	0,91	2655	44	2649	50	2644	24	100
Zircon DEQ387A I8	0,0075	31	31	36	0,88	15,36	2,43	0,56	2,22	0,91	0,20	1,01	2854	63	2838	69	2826	28	101
Zircon DEQ387A I9	0,0205	18	31	29	1,08	8,76	2,38	0,43	2,05	0,86	0,15	1,22	2298	47	2313	55	2327	28	99

Zircon DEQ387A J5	0,0079	9	15	15	1	11,16	3,13	0,45	2,34	0,75	0,18	2,09	2406	56	2537	80	2643	55	91
Zircon DEQ387A K5	0,0020	19	16	30	0,53	16,7	1,18	0,58	0,88	0,75	0,21	0,79	2952	26	2918	35	2895	23	102
Zircon DEQ387A L7	0,0017	87	118	112	1,06	14,35	2,93	0,54	2,84	0,97	0,19	0,72	2788	79	2773	81	2762	20	101
Zircon DEQ387A 1B	0,0277	37	38	54	0,71	15,29	1,72	0,55	1,15	0,67	0,20	1,28	2809	32	2833	49	2851	37	99
Zircon DEQ387A 6B	0,0137	82	275	146	1,9	11,21	3,08	0,48	2,96	0,96	0,17	0,85	2548	76	2541	78	2536	22	101
Zircon DEQ387A 9B	0,0235	7	9	18	0,50	9,88	3,22	0,44	1,76	0,55	0,16	2,70	2344	41	2423	78	2491	67	94
Zircon DEQ387A 2C	0,0095	12	3	22	0,15	12,63	1,75	0,51	1,35	0,77	0,18	1,13	2658	36	2652	47	2648	30	100
Zircon DEQ387A 4C	0,0021	0,5	1,1	1,1	0,98	15,78	4,38	0,53	2,55	0,58	0,22	3,57	2729	70	2864	126	2960	106	92
Zircon DEQ387A 6C	0,0343	19	13	34	0,37	11,04	4,33	0,49	3,89	0,9	0,16	1,89	2562	100	2527	109	2498	47	103
Zircon DEQ387A 7C	0,0105	19	19	36	0,52	14,56	2,46	0,54	2,13	0,87	0,19	1,23	2800	60	2787	69	2778	34	101
Zircon DEQ387A 8C	0,0201	11	8	15	0,53	13,06	2,23	0,54	1,45	0,65	0,18	1,70	2768	40	2684	60	2621	45	106
Zircon DEQ387A 9C	0,0162	14	13	29	0,45	8,31	3,50	0,42	1,95	0,56	0,14	2,91	2263	44	2266	79	2268	66	100
Zircon DEQ387A 2D	0,0427	56	447	187	2,41	8,37	1,97	0,42	1,87	0,95	0,14	0,62	2268	42	2272	45	2275	14	100
Zircon DEQ387B A6	0,0082	8	9	14	0,68	13,9	2,58	0,53	1,2	0,46	0,19	2,28	2750	33	2743	71	2737	63	101
Zircon DEQ387B A7	0,0056	5	6	5	1,13	15,52	3,85	0,57	3,21	0,83	0,2	2,12	2910	94	2848	110	2804	59	104
Zircon DEQ387B A8	0,0019	8	8	13	0,63	14,35	3,21	0,53	2,1	0,66	0,2	2,42	2743	58	2773	89	2796	68	98
Zircon DEQ387B A9	0,0029	7	8	9	0,96	15,01	2,73	0,55	1,79	0,66	0,2	2,06	2807	50	2816	77	2823	58	99
Zircon DEQ387B A10	0,0047	6	3	9	0,37	14,48	2,54	0,54	1,51	0,59	0,2	2,04	2765	42	2782	71	2794	57	99
Zircon DEQ387B A11	0,0073	55	64	62	1,04	14,71	4,84	0,53	4,75	0,98	0,2	0,94	2745	130	2797	136	2835	27	97
Zircon DEQ387B A13	0,0060	7	5	11	0,48	17,58	2,88	0,57	2,22	0,77	0,22	1,83	2924	65	2967	85	2996	55	98
Zircon DEQ387B A14	0,0137	47	34	60	0,58	12,28	3,12	0,48	2,91	0,93	0,19	1,12	2514	73	2626	82	2713	30	93
Zircon DEQ387B B4	0,0083	87	39	138	0,28	13,26	2,99	0,53	2,69	0,9	0,18	1,31	2723	73	2699	81	2680	35	102
Zircon DEQ387B B7	0,0146	8	4	8	0,48	16,84	3,36	0,6	2,63	0,78	0,2	2,1	3045	80	2926	98	2845	60	107
Zircon DEQ387B B10	0,0043	11	15	21	0,71	13,19	2,58	0,51	1,78	0,69	0,19	1,87	2676	48	2693	70	2706	51	99
Zircon DEQ387B B11	0,0047	11	11	21	0,52	14,00	2,54	0,53	1,82	0,72	0,19	1,77	2750	50	2750	70	2750	49	100
Zircon DEQ387B B12	0,0287	20	4	27	0,15	7,97	4,79	0,41	4,53	0,95	0,14	1,56	2194	99	2228	107	2259	35	97
Zircon DEQ387B B14	0,0319	16	6	36	0,18	10,22	3,44	0,48	2,84	0,83	0,16	1,94	2519	72	2455	85	2402	47	105
Zircon DEQ387B C4	0,0031	8	5	13	0,4	15,9	2,91	0,56	1,81	0,62	0,2	2,28	2880	52	2871	84	2865	65	101
Zircon DEQ387B C6	0,0064	7	5	10	0,55	16,31	4,67	0,55	2,33	0,5	0,22	4,05	2819	66	2895	135	2948	120	96
Zircon DEQ387B C7	0,0090	17	11	21	0,5	12,96	2,39	0,52	1,56	0,65	0,18	1,81	2718	43	2677	64	2647	48	103
Zircon DEQ387B C8	0,0034	8	7	11	0,69	14,68	2,88	0,54	2,18	0,76	0,2	1,89	2787	61	2794	81	2800	53	100
Zircon DEQ387B C10	0,0089	12	10	17	0,62	13,8	3,19	0,53	2,51	0,79	0,19	1,97	2743	69	2736	87	2731	54	100

Zircon DEQ387B C13	0,0020	16	13	31	0,41	12,63	2,06	0,48	1,38	0,67	0,19	1,53	2511	35	2653	55	2763	42	91
Zircon DEQ387B C15	0,0047	9	4	12	0,3	16,76	2,43	0,59	1,28	0,53	0,21	2,06	2986	38	2921	71	2877	59	104
Zircon DEQ387B D3	0,0061	9	14	14	1,03	15,23	2,72	0,54	1,98	0,73	0,2	1,87	2781	55	2830	77	2865	54	97
Zircon DEQ387B D4	0,0041	9	1	7	0,17	26,92	3,05	0,69	2,27	0,74	0,28	2,05	3371	76	3381	103	3387	69	100
Zircon DEQ387B D6	0,0036	9	3	16	0,17	15,52	3,02	0,55	2,29	0,76	0,2	1,98	2838	65	2848	86	2855	56	99
Zircon DEQ387B D7	0,0089	9	10	14	0,71	15,29	2,79	0,55	1,91	0,69	0,2	2,03	2828	54	2833	79	2837	58	100
Zircon DEQ387B D11	0,0117	16	12	15	0,8	14,97	2,2	0,58	1,33	0,6	0,19	1,75	2941	39	2813	62	2723	48	108
Zircon DEQ387B D12	0,0037	6	6	7	0,92	16,32	3,83	0,56	2,65	0,69	0,21	2,77	2851	76	2896	111	2927	81	97
Zircon DEQ387B D12B	0,0063	11	12	17	0,69	16,2	3,08	0,58	2,4	0,78	0,2	1,92	2967	71	2889	89	2834	54	105
Zircon DEQ387B D13	0,0057	10	9	14	0,67	17,06	2,68	0,6	1,92	0,72	0,21	1,88	3022	58	2938	79	2881	54	105
Zircon DEQ387B E1	0,0082	68	48	76	0,64	16,6	2,52	0,58	2,33	0,92	0,21	0,96	2935	68	2912	73	2896	28	101
Zircon DEQ387B E2	0,0169	16	22	28	0,78	11,89	2,68	0,47	1,87	0,7	0,18	1,92	2468	46	2596	70	2698	52	92
Zircon DEQ387B E3	0,0021	3	2	4	0,35	15,75	4,82	0,56	3,54	0,73	0,20	3,27	2872	102	2862	138	2855	93	101
Zircon DEQ387B E4	0,0057	5	9	10	0,89	12,49	3,93	0,48	2,56	0,65	0,19	2,98	2515	65	2642	104	2741	82	92
Zircon DEQ387B E5	0,0091	17	26	22	1,15	10,37	4,21	0,45	3,68	0,88	0,17	2,03	2414	89	2469	104	2514	51	96
Zircon DEQ387B E6	0,0048	5	7	7	0,96	16,03	3,83	0,58	2,01	0,52	0,2	3,26	2958	59	2879	110	2824	92	105
Zircon DEQ387B E8	0,0083	5	12	5	2,21	13,95	4,33	0,54	2,36	0,55	0,19	3,63	2773	66	2747	119	2727	99	102
Zircon DEQ387B E9	0,0073	8	6	12	0,52	13,03	3,23	0,51	2,07	0,64	0,19	2,48	2642	55	2682	87	2713	67	97
Zircon DEQ387B E10	0,0119	9	7	11	0,71	14,87	2,5	0,57	1,74	0,7	0,19	1,79	2913	51	2807	70	2731	49	107
Zircon DEQ387B G3	0,0064	10	3	7	0,41	20,45	3,99	0,63	2,65	0,66	0,24	2,98	3147	83	3113	124	3091	92	102
Zircon DEQ387B J2	0,0017	13	13	19	0,69	15,58	2,38	0,55	2,03	0,85	0,2	1,25	2844	58	2851	68	2856	36	100
Zircon DEQ387B K2	0,0029	7	5	9	0,57	18,34	2,37	0,59	1,51	0,64	0,22	1,83	3003	45	3008	71	3011	55	100
Zircon DEQ387B K3	0,0117	31	32	46	0,69	17,7	3,04	0,63	2,81	0,92	0,2	1,17	3145	88	2974	91	2860	34	110
Zircon DEQ387B L3	0,0054	34	44	38	1,17	14,85	2,54	0,55	2,37	0,93	0,2	0,91	2808	67	2806	71	2804	26	100
Zircon DEQ387A D5	0,0046	72	67	120	0,56	13,17	0,88	0,48	0,60	0,68	0,2	0,64	2535	15	2692	24	2812	18	90
Zircon DEQ387A D6	0,0068	130	210	266	0,8	12,28	1,48	0,47	0,84	0,57	0,19	1,22	2486	21	2626	39	2736	33	91

[a] Fraction of the non-radiogenic ^{206}Pb in the analyzed zircon spot, where $f_{206}=[^{206}Pb/^{204}Pb]c/[^{206}Pb/^{204}Pb]s$ (c=common; s=sample)

[b] Th/U ratios and amount of Pb, Th and U (in ppm) are calculated relative to GJ-1 reference zircon

[c] Corrected for background and within-run Pb/U fractionation and normalized to reference zircon GJ-1 (ID-TIMS values/measured value); $^{207}Pb/^{235}U$ calculated using $(^{207}Pb/^{206}Pb)*(^{206}Pb/^{238}U)*(137.88)$

[d] Rho is the error correlation defined as the quotient of the propagated errors of the $^{206}Pb/^{238}U$ and the $^{207}/^{235}U$ ratio

[e] Corrected for mass-bias by normalizing to GJ-1 reference zircon and common Pb using the model Pb composition of Stacey and Kramers (1975)

[f] Degree of concordance, 6/8-7/6= ($^{206}Pb/^{238}U$ age * 100) / ($^{207}Pb/^{206}Pb$ age), according to Horstwood et al., 2016.

* Analysis with high common Pb or with >10% of discordance.

						Isotope ratios[c]							Ages (Ma)						
Sample DEQ-388	f_{206}[a]	**Pb (ppm)**	**Th (ppm)**	**U (ppm)**	**Th/U[b]**	**207Pb/ 235U**	**1σ (%)**	**206Pb/ 238U**	**1σ (%)**	**Rho[d]**	**207Pb/ 206Pb[e]**	**1σ (%)**	**206Pb/ 238U**	**1σ (abs)**	**207Pb/ 235U**	**1σ (abs)**	**207Pb/ 206Pb**	**1σ (abs)**	**Conc.[f](%) 6/8-7/6**
Zircon DEQ388A A1	0,0036	193	962	432	2,24	12,00	1,35	0,46	1,17	0,87	0,19	0,67	2457	29	2605	35	2722	18	90
Zircon DEQ388A A2	0,0024	11	5	27	0,17	14,09	2,69	0,52	2,38	0,89	0,20	1,25	2702	64	2756	74	2796	35	97
Zircon DEQ388A A3	0,0044	6	4	8	0,43	16,14	2,51	0,56	1,60	0,64	0,21	1,94	2878	46	2885	73	2890	56	100
Zircon DEQ388A A5	0,0028	9	7	17	0,42	16,77	2,63	0,54	2,31	0,88	0,22	1,25	2795	65	2922	77	3011	38	93
Zircon DEQ388A A7	0,0094	3	2	4	0,45	18,56	3,08	0,59	1,99	0,65	0,23	2,35	2991	60	3019	93	3038	71	99
Zircon DEQ388A A11	0,0025	11	12	20	0,62	13,27	2,09	0,49	1,48	0,71	0,20	1,48	2566	38	2699	57	2800	41	92
Zircon DEQ388A A13	0,0026	5	2	8	0,27	18,71	2,37	0,61	1,79	0,75	0,22	1,56	3067	55	3027	72	3001	47	102
Zircon DEQ388A B2	0,0046	3	1	4	0,26	20,31	3,95	0,62	2,54	0,64	0,24	3,02	3099	79	3106	123	3111	94	100
Zircon DEQ388A B4	0,0037	6	4	9	0,42	21,20	2,93	0,63	2,06	0,70	0,25	2,09	3134	65	3148	92	3157	66	99
Zircon DEQ388A B6	0,0093	3	2	4	0,43	16,04	4,72	0,56	3,21	0,68	0,21	3,46	2846	92	2879	136	2902	100	98
Zircon DEQ388A B8	0,0035	7	5	11	0,46	15,33	2,41	0,55	1,53	0,63	0,20	1,87	2816	43	2836	68	2851	53	99
Zircon DEQ388A B9	0,0007	44	26	56	0,46	19,01	1,21	0,59	1,03	0,85	0,23	0,64	3001	31	3042	37	3070	20	98
Zircon DEQ388A B10	0,0086	9	10	17	0,61	13,05	2,34	0,48	1,66	0,71	0,20	1,66	2547	42	2683	63	2788	46	91
Zircon DEQ388A B11	0,0036	4	2	7	0,26	16,49	2,50	0,56	1,61	0,64	0,21	1,91	2886	47	2905	73	2919	56	99
Zircon DEQ388A C2	0,0039	5	5	11	0,43	17,38	3,79	0,55	3,47	0,92	0,23	1,53	2806	97	2956	112	3060	47	92
Zircon DEQ388A C3	0,0019	12	8	19	0,43	27,14	2,61	0,64	2,49	0,96	0,31	0,77	3196	80	3389	88	3505	27	91
Zircon DEQ388A C4	0,0027	5	3	7	0,44	21,48	3,41	0,62	2,37	0,69	0,25	2,46	3124	74	3160	108	3184	78	98
Zircon DEQ388A C6	0,0096	3	4	7	0,56	16,06	3,65	0,57	2,97	0,81	0,21	2,13	2898	86	2880	105	2868	61	101

Zircon DEQ388A C8	0,0036	13	10	20	0,5	14,98	1,88	0,55	1,39	0,74	0,20	1,26	2843	40	2814	53	2794	35	102
Zircon DEQ388A C12	0,0039	8	9	17	0,52	12,26	2,78	0,47	2,42	0,87	0,19	1,35	2470	60	2624	73	2745	37	90
Zircon DEQ388A C13	0,0004	60	50	85	0,6	18,49	0,74	0,61	0,48	0,64	0,22	0,57	3068	15	3016	22	2981	17	103
Zircon DEQ388A D2	0,0024	41	24	48	0,49	20,10	1,15	0,60	0,99	0,86	0,24	0,58	3045	30	3096	36	3130	18	97
Zircon DEQ388A D5	0,0008	93	101	126	0,8	18,13	1,59	0,57	1,48	0,93	0,23	0,59	2891	43	2997	48	3069	18	94
Zircon DEQ388A D6	0,0003	79	58	104	0,56	17,56	0,87	0,58	0,70	0,81	0,22	0,51	2964	21	2966	26	2967	15	100
Zircon DEQ388A D8	0,0060	3	3	7	0,44	13,14	3,38	0,49	2,37	0,70	0,19	2,41	2576	61	2690	91	2776	67	93
Zircon DEQ388A D9	0,0006	71	73	104	0,71	14,28	0,90	0,51	0,72	0,80	0,20	0,55	2645	19	2768	25	2859	16	93
Zircon DEQ388A D10	0,0055	3	3	5	0,62	17,75	4,35	0,55	2,99	0,69	0,23	3,16	2817	84	2976	130	3086	98	91
Zircon DEQ388A D11	0,0007	44	64	69	0,93	18,67	0,76	0,60	0,54	0,71	0,23	0,54	3016	16	3025	23	3030	16	100
Zircon DEQ388A D13	0,0002	108	189	134	1,41	13,84	0,83	0,53	0,62	0,75	0,19	0,55	2725	17	2739	23	2750	15	99
Zircon DEQ388A E1	0,0073	18	134	43	3,16	11,74	3,24	0,46	3,16	0,97	0,19	0,75	2435	77	2584	84	2703	20	90
Zircon DEQ388A E2	0,0010	95	119	166	0,72	15,06	1,25	0,52	1,13	0,90	0,21	0,54	2680	30	2819	35	2920	16	92
Zircon DEQ388A E4	0,0005	63	37	91	0,41	15,86	0,93	0,54	0,75	0,81	0,21	0,54	2778	21	2869	27	2933	16	95
Zircon DEQ388A E5	0,0008	39	14	57	0,24	15,99	0,84	0,56	0,65	0,77	0,21	0,54	2877	19	2876	24	2875	15	100
Zircon DEQ388A E6	0,0019	50	34	68	0,5	16,90	0,75	0,59	0,45	0,60	0,21	0,60	2994	14	2929	22	2885	17	104
Zircon DEQ388B B2	0,0020	4	22	36	0,62	19,04	2,28	0,61	1,20	0,53	0,23	1,93	3075	37	3044	69	3024	58	102
Zircon DEQ388B B5	0,0029	5	5	13	0,38	18,70	2,04	0,61	1,42	0,70	0,22	1,46	3062	44	3026	62	3003	44	102
Zircon DEQ388B B6	0,0043	4	3	10	0,27	14,69	3,11	0,53	2,58	0,83	0,20	1,74	2728	70	2796	87	2845	49	96
Zircon DEQ388B B7	0,0022	5	4	7	0,51	15,40	2,23	0,55	1,36	0,61	0,20	1,77	2824	39	2840	63	2852	50	99
Zircon DEQ388B B8	0,0031	6	3	10	0,29	22,05	3,05	0,59	2,43	0,80	0,27	1,85	2989	73	3186	97	3313	61	90
Zircon DEQ388B B9	0,0028	5	5	7	0,75	15,31	2,80	0,55	1,79	0,64	0,20	2,15	2833	51	2835	79	2835	61	100
Zircon DEQ388B C2	0,0044	7	12	14	0,86	11,91	3,09	0,49	2,10	0,68	0,18	2,26	2572	54	2597	80	2617	59	98
Zircon DEQ388B C3	0,0006	92	47	121	0,39	20,93	0,77	0,63	0,56	0,73	0,24	0,53	3138	18	3136	24	3134	17	100
Zircon DEQ388B C7	0,0043	68	185	154	1,21	15,43	1,73	0,55	1,59	0,92	0,20	0,69	2827	45	2842	49	2853	20	99
Zircon DEQ388B C8	0,0007	194	106	295	0,36	13,57	2,11	0,52	1,99	0,94	0,19	0,70	2719	54	2720	58	2720	19	100

Zircon DEQ388B C9	0,0018	73	250	105	2,4	14,69	2,12	0,54	1,94	0,92	0,20	0,84	2794	54	2795	59	2796	23	100
Zircon DEQ388B C10	0,0036	127	213	209	1,03	13,95	1,49	0,50	1,28	0,86	0,20	0,75	2615	34	2747	41	2845	21	92
Zircon DEQ388B D2	0,0012	38	203	255	0,8	17,47	0,96	0,58	0,65	0,68	0,22	0,71	2940	19	2961	29	2975	21	99
Zircon DEQ388B D3	0,0021	94	152	153	1	16,13	1,89	0,56	1,74	0,92	0,21	0,75	2874	50	2884	55	2892	22	99
Zircon DEQ388B D5	0,0039	323	1044	829	1,27	12,15	1,03	0,47	0,62	0,60	0,19	0,83	2465	15	2616	27	2734	23	90
Zircon DEQ388B D6	0,0017	109	61	126	0,49	19,44	1,30	0,63	1,14	0,87	0,22	0,63	3162	36	3064	40	3000	19	105
Zircon DEQ388B D7	0,0015	47	47	82	0,57	18,86	1,64	0,60	1,43	0,87	0,23	0,81	3024	43	3035	50	3042	25	99
Zircon DEQ388B D10	0,0006	45	40	61	0,66	16,63	0,83	0,58	0,55	0,66	0,21	0,62	2930	16	2914	24	2903	18	101
Zircon DEQ388B D11	0,0013	118	133	303	0,44	12,34	2,41	0,48	2,30	0,96	0,19	0,70	2514	58	2630	63	2721	19	92
Zircon DEQ388B D12	0,0052	93	177	135	1,32	16,19	1,60	0,57	1,48	0,92	0,21	0,62	2893	43	2888	46	2885	18	100
Zircon DEQ388B E5	0,0006	86	70	142	0,5	17,12	0,84	0,56	0,55	0,65	0,22	0,64	2857	16	2941	25	2999	19	95
Zircon DEQ388B E6	0,0014	67	123	108	1,15	13,95	1,08	0,50	0,80	0,74	0,20	0,72	2609	21	2746	30	2849	21	92
Zircon DEQ388B E7	0,0032	25	149	70	2,14	16,44	3,96	0,54	3,83	0,97	0,22	1,00	2782	107	2903	115	2988	30	93
Zircon DEQ388B E8	0,0019	60	73	104	0,71	15,66	1,02	0,53	0,71	0,69	0,21	0,74	2744	19	2857	29	2937	22	93
Zircon DEQ388B E9	0,0043	75	203	184	1,11	12,45	1,55	0,49	1,32	0,85	0,18	0,81	2577	34	2639	41	2687	22	96
Zircon DEQ388B E10	0,0017	167	399	306	1,31	13,71	1,02	0,49	0,83	0,81	0,20	0,60	2571	21	2730	28	2849	17	90
Zircon DEQ388B E11	0,0035	93	201	148	1,37	12,49	1,81	0,51	1,44	0,79	0,18	1,11	2636	38	2642	48	2646	29	100
Zircon DEQ388B F1	0,0034	52	134	88	1,53	13,11	1,41	0,49	1,18	0,84	0,20	0,77	2556	30	2687	38	2788	22	92
Zircon DEQ388B F2	0,0008	114	149	216	0,69	20,23	1,94	0,59	1,84	0,95	0,25	0,63	2972	55	3103	60	3188	20	93
Zircon DEQ388B F3	0,0013	36	31	59	0,52	17,07	1,37	0,57	0,92	0,67	0,22	1,01	2920	27	2939	40	2952	30	99
Zircon DEQ388B F5	0,0031	54	57	83	0,69	18,29	0,93	0,60	0,58	0,63	0,22	0,72	3025	18	3005	28	2992	22	101
Zircon DEQ388B F7	0,0009	43	36	54	0,68	19,57	1,20	0,61	0,83	0,69	0,23	0,87	3078	26	3070	37	3065	27	100
Zircon DEQ388B F11	0,0016	102	154	160	0,97	15,67	1,78	0,57	1,60	0,90	0,20	0,78	2921	47	2857	51	2811	22	104
Zircon DEQ388B G1	0,0023	104	528	306	1,74	12,50	1,80	0,47	1,63	0,90	0,19	0,77	2498	41	2643	48	2756	21	91
Zircon DEQ388B G2	0,0004	104	47	161	0,29	18,07	0,79	0,61	0,43	0,54	0,22	0,66	3058	13	2994	24	2950	20	104
Zircon DEQ388B G3	0,0100	120	177	166	1,08	14,63	1,50	0,54	1,30	0,87	0,20	0,75	2789	36	2792	42	2794	21	100

Zircon DEQ388B G4	0,0033	167	554	272	2,05	12,87	1,77	0,48	1,60	0,91	0,19	0,75	2525	40	2670	47	2782	21	91
Zircon DEQ388B G6	0,0021	44	40	67	0,6	16,28	1,16	0,58	0,79	0,68	0,20	0,85	2938	23	2893	34	2863	24	103
Zircon DEQ388B G7	0,0033	31	42	46	0,92	17,30	1,63	0,58	1,38	0,84	0,22	0,88	2943	41	2952	48	2958	26	100
Zircon DEQ388B G8	0,0008	147	202	282	0,72	14,53	1,00	0,53	0,67	0,67	0,20	0,73	2722	18	2785	28	2830	21	96
Zircon DEQ388B G10	0,0013	37	25	58	0,44	14,02	1,49	0,50	1,07	0,72	0,20	1,04	2612	28	2751	41	2854	30	92
Zircon DEQ388B G11	0,0010	55	38	92	0,42	16,92	0,86	0,57	0,58	0,67	0,21	0,64	2913	17	2930	25	2942	19	99
Zircon DEQ388B H3	0,0029	63	69	148	0,47	17,40	2,26	0,58	2,12	0,94	0,22	0,78	2966	63	2957	67	2952	23	101
Zircon DEQ388B H5	0,0012	38	59	59	1	15,45	1,15	0,56	0,72	0,63	0,20	0,89	2873	21	2843	33	2823	25	102

[a] Fraction of the non-radiogenic ^{206}Pb in the analyzed zircon spot, where $f_{206}=[^{206}Pb/^{204}Pb]c/[^{206}Pb/^{204}Pb]s$ (c=common; s=sample)

[b] Th/U ratios and amount of Pb, Th and U (in ppm) are calculated relative to GJ-1 reference zircon

[c] Corrected for background and within-run Pb/U fractionation and normalized to reference zircon GJ-1 (ID-TIMS values/measured value); $^{207}Pb/^{235}U$ calculated using $(^{207}Pb/^{206}Pb)*(^{206}Pb/^{238}U)*(137.88)$

[d] Rho is the error correlation defined as the quotient of the propagated errors of the $^{206}Pb/^{238}U$ and the $^{207}/^{235}U$ ratio

[e] Corrected for mass-bias by normalizing to GJ-1 reference zircon and common Pb using the model Pb composition of Stacey and Kramers (1975)

[f] Degree of concordance, 6/8-7/6= ($^{206}Pb/^{238}U$ age * 100) / ($^{207}Pb/^{206}Pb$ age), according to Horstwood et al., 2016.

* Analysis with high common Pb or with >10% of discordance.

Sample DEO-066	Pb rad.[a] (ppm)	U (ppm)	Th/U	Pb comum total (%)	Isotope ratios						Rho[b]	Ages (Ma)						Conc.[c] (%)
					$^{207}Pb/^{206}U$	2σ (%)	$^{207}Pb/^{235}U$	2σ (%)	$^{206}Pb/^{238}U$	2σ (%)		$^{207}Pb/^{206}U$	2σ (Ma)	$^{207}Pb/^{235}U$	2σ (Ma)	$^{206}Pb/^{238}U$	2σ (Ma)	
Zircon DEO-066 12	50	59	0,07	0	0,24802	0,4	23,347	0,5	0,68269	0,3	0,62	3172	7	3241	5	3355	9	106
Zircon DEO-066 13	30	32	0,14	0	0,24536	0,6	23,399	1	0,69167	0,8	0,82	3155	9	3244	10	3389	22	107
Zircon DEO-066 16	22	27	0,10	0	0,24864	0,4	21,45	1	0,62568	0,9	0,9	3176	7	3159	10	3132	22	99
Zircon DEO-066 17	26	30	0,10	0	0,24177	0,4	22,295	0,9	0,6688	0,8	0,87	3132	7	3197	8	3301	19	105
Zircon DEO-066 18	24	32	0,05	0	0,23504	0,4	20,67	0,8	0,63783	0,7	0,87	3087	7	3123	8	3180	18	103
Zircon DEO-066 19	6	8	0,07	0	0,23361	0,4	19,798	1	0,61463	0,9	0,89	3077	7	3082	10	3089	22	100
Zircon DEO-066 20	11	12	0,10	0	0,24285	0,4	22,389	1,2	0,66866	1,1	0,93	3139	7	3201	12	3301	29	105
Zircon DEO-066 22	7	10	0,05	0,7	0,23365	0,5	19,86	1	0,61646	0,9	0,88	3077	8	3085	10	3096	23	101

Zircon DEO-066 23	17	21	0,06	0	0,24129	0,4	22,21	1	0,66756	0,9	0,91	3129	7	3193	10	3296	23	105
Zircon DEO-066 24	9	10	0,11	0	0,24254	0,5	21,908	1,1	0,6551	1	0,91	3137	7	3180	11	3248	26	104
Zircon DEO-066 25	9	9	0,10	0	0,28928	0,4	29,605	1,2	0,74223	1,1	0,93	3414	7	3474	12	3579	30	105
Zircon DEO-066 31	35	42	0,11	0	0,24024	0,4	21,209	1	0,64031	0,9	0,89	3122	7	3148	9	3190	22	102
Zircon DEO-066 32	29	34	0,11	0	0,24418	0,4	21,947	1	0,65187	0,8	0,88	3147	7	3181	9	3236	22	103
Zircon DEO-066 33	21	27	0,03	0	0,24425	0,5	22,199	1	0,65915	0,9	0,88	3148	7	3192	10	3264	22	104
Zircon DEO-066 34	55	64	0,10	0	0,24793	0,4	22,768	0,9	0,66604	0,7	0,87	3172	7	3217	8	3291	19	104
Zircon DEO-066 35	53	70	0,04	0	0,24694	0,4	22,133	0,9	0,65006	0,8	0,88	3165	7	3190	9	3228	20	102
Zircon DEO-066 36	39	47	0,10	0	0,24562	0,4	21,751	1	0,64228	0,9	0,9	3157	7	3173	10	3198	23	101
Zircon DEO-066 37	95	126	0,07	0	0,24032	0,4	20,375	1,2	0,61491	1,1	0,93	3122	7	3109	11	3090	27	99
Zircon DEO-066 38	29	35	0,08	0	0,25054	0,4	23,146	0,9	0,67003	0,8	0,89	3188	7	3233	9	3306	22	104
Zircon DEO-066 39	88	105	0,09	0	0,24657	0,4	22,481	1,1	0,66127	1	0,92	3163	7	3205	10	3272	25	103
Zircon DEO-066 41	120	161	0,07	0	0,23228	0,4	19,819	0,9	0,61883	0,8	0,89	3068	7	3083	9	3105	20	101
Zircon DEO-066 42	37	41	0,10	0	0,25966	0,5	24,934	1,1	0,69644	1,1	0,92	3245	7	3306	11	3407	28	105
Zircon DEO-066 43	55	70	0,05	0	0,23991	0,4	21,79	1,6	0,65875	1,5	0,96	3119	7	3174	15	3262	39	105
Zircon DEO-066 44	27	35	0,10	0	0,24022	0,5	19,845	1,5	0,59914	1,4	0,95	3121	7	3084	14	3026	34	97
Zircon DEO-066 51	12	15	0,09	0	0,24299	0,5	21,806	1,2	0,65086	1,1	0,91	3140	8	3175	11	3232	27	103
Zircon DEO-066 52	23	27	0,09	0	0,2486	0,5	22,697	1	0,66216	0,8	0,88	3176	7	3214	9	3276	22	103
Zircon DEO-066 53	49	57	0,12	0	0,2437	0,4	21,377	0,9	0,63621	0,8	0,89	3144	7	3156	9	3174	21	101
Zircon DEO-066 55	19	24	0,10	0	0,22628	0,4	19,168	1,1	0,61437	1	0,92	3026	7	3050	11	3087	24	102
Zircon DEO-066 56	124	139	0,07	0	0,27452	0,4	26,3	2,4	0,69483	2,4	0,98	3332	7	3358	24	3401	63	102
Zircon DEO-066 57	41	53	0,05	0	0,24572	0,4	21,77	1	0,64256	1	0,91	3157	7	3174	10	3199	24	101
Zircon DEO-066 58	41	49	0,14	0	0,23798	0,5	20,159	1,2	0,61438	1,1	0,93	3107	7	3099	12	3087	28	99
Zircon DEO-066 59	40	64	0,09	0	0,17528	0,4	12,433	0,9	0,51445	0,8	0,88	2609	7	2638	9	2676	18	103
Zircon DEO-066 60	57	67	0,10	0	0,24236	0,4	21,714	1,2	0,64978	1,1	0,94	3136	7	3171	12	3227	29	103
Zircon DEO-066 61	51	77	0,05	0	0,21604	0,4	17,039	1,2	0,57202	1,1	0,93	2951	7	2937	11	2916	26	99
Zircon DEO-066 62	94	117	0,07	0	0,24208	0,4	22,133	1	0,6631	0,9	0,9	3134	7	3190	9	3279	22	105
Zircon DEO-066 63	37	43	0,14	0	0,23807	0,4	20,778	1	0,633	0,9	0,9	3107	7	3128	10	3161	23	102
Zircon DEO-066 64	58	77	0,08	0	0,22121	0,4	18,431	0,9	0,60429	0,8	0,89	2990	7	3013	9	3047	20	102
Zircon DEO-066 65	30	39	0,04	0	0,24534	0,4	22,288	1	0,65887	0,9	0,91	3155	7	3196	10	3263	24	103

Zircon DEO-066 71	53	65	0,07	0	0,24091	0,4	21,754	1	0,6549	0,9	0,9	3126	7	3173	10	3247	23	104
Zircon DEO-066 72	35	40	0,09	0	0,25268	0,4	23,591	0,9	0,67712	0,8	0,88	3202	7	3252	9	3333	21	104
Zircon DEO-066 74	30	36	0,11	0	0,24871	0,5	21,816	1	0,63619	0,9	0,89	3177	7	3176	10	3174	23	100
Zircon DEO-066 75	52	64	0,08	0	0,24586	0,4	21,417	0,9	0,6318	0,8	0,88	3158	7	3158	9	3157	20	100
Zircon DEO-066 76	41	56	0,10	0	0,22659	0,4	17,577	0,9	0,56261	0,8	0,89	3028	7	2967	9	2877	19	95
Zircon DEO-066 77	57	65	0,17	0	0,22889	0,4	19,19	1	0,60804	0,9	0,9	3044	7	3051	9	3062	21	101
Zircon DEO-066 78	22	26	0,10	0	0,24056	0,5	21,703	1	0,65433	0,9	0,88	3124	8	3171	10	3245	23	104
Zircon DEO-066 79	47	52	0,11	0	0,24237	0,4	23,038	1,4	0,6894	1,3	0,95	3136	7	3229	14	3380	35	108
Zircon DEO-066 80	51	65	0,08	0	0,24198	0,4	20,481	1,4	0,61387	1,3	0,95	3133	7	3114	13	3085	32	98
Zircon DEO-066 81	116	142	0,09	0	0,23742	0,4	20,95	1	0,63998	0,9	0,91	3103	6	3136	9	3189	22	103
Zircon DEO-066 82	63	72	0,16	0	0,23878	0,4	20,348	1,2	0,61804	1,1	0,93	3112	7	3108	11	3102	27	100
Zircon DEO-066 83	25	30	0,09	0	0,24742	0,4	22,524	1,1	0,66024	1	0,92	3168	7	3207	11	3268	27	103
Zircon DEO-066 84	23	30	0,11	0	0,22007	0,4	18,52	1	0,61033	0,9	0,91	2981	7	3017	10	3071	23	103

a = Values of radiogenic Pb; b = correlation coefficient; c = Concordance (age $^{206}Pb/^{238}U$ / age $^{207}Pb/^{206}Pb$)x100

						Isotope ratios[c]							Ages (Ma)						
Reference zircon	f_{206}[a]	**Pb (ppm)**	**Th (ppm)**	**U (ppm)**	**Th/U[b]**	$^{207}Pb/^{235}U$	**1σ (%)**	$^{206}Pb/^{238}U$	**1σ (%)**	**Rho[d]**	$^{207}Pb/^{206}Pb$[e]	**1σ (%)**	$^{206}Pb/^{238}U$	**1σ (abs)**	$^{207}Pb/^{235}U$	**1σ (abs)**	$^{207}Pb/^{206}Pb$	**1σ (abs)**	**Conc.[f] (%) 6/8-7/6**
91500 01	0,0028	6	8	29	0,27	1,87	2,96	0,18	2,21	0,75	0,07	1,96	1073	24	1071	32	1068	21	100
91500 02	0,0019	17	25	89	0,29	1,85	2,53	0,18	1,41	0,56	0,07	2,10	1065	15	1064	27	1062	22	100
91500 03	0,0018	23	32	122	0,27	1,86	2,33	0,18	1,33	0,57	0,07	1,92	1071	14	1069	25	1063	20	101
91500 04	0,0013	23	29	116	0,25	1,85	2,72	0,18	1,56	0,57	0,07	2,22	1062	17	1063	29	1066	24	100
91500 05	0,0021	15	24	78	0,31	1,88	2,28	0,18	1,25	0,55	0,07	1,90	1082	14	1074	24	1058	20	102
91500 06	0,0017	16	20	78	0,26	1,88	1,83	0,18	1,02	0,56	0,07	1,51	1079	11	1074	20	1063	16	102
91500 07	0,0002	5	7	25	0,29	1,84	2,93	0,18	2,54	0,87	0,07	1,46	1057	27	1059	31	1063	16	99
91500 08	0,0015	17	19	85	0,22	1,86	1,83	0,18	1,09	0,60	0,07	1,47	1071	12	1068	20	1063	16	101
91500 09	0,0039	16	18	82	0,22	1,85	2,74	0,18	1,43	0,52	0,07	2,34	1068	15	1064	29	1054	25	101

91500 10	0,0016	18	21	89	0,23	1,87	2,46	0,18	1,35	0,55	0,08	2,06	1069	14	1069	26	1071	22	100
91500 11	0,0020	18	19	91	0,21	1,86	2,61	0,18	1,27	0,49	0,07	2,28	1066	14	1066	28	1064	24	100
91500 12	0,0016	18	18	88	0,21	1,86	2,48	0,18	1,25	0,51	0,07	2,14	1069	13	1068	27	1068	23	100
91500 13	0,0058	19	19	93	0,21	1,88	2,86	0,18	1,51	0,53	0,07	2,43	1076	16	1072	31	1065	26	101
91500 14	0,0020	15	16	78	0,21	1,85	2,45	0,18	1,25	0,51	0,07	2,11	1065	13	1063	26	1059	22	101
91500 15	0,0012	27	31	136	0,23	1,88	1,65	0,18	0,80	0,48	0,08	1,45	1075	9	1073	18	1069	15	101
91500 16	0,0013	33	41	169	0,24	1,89	1,74	0,18	1,00	0,57	0,07	1,43	1082	11	1076	19	1065	15	102
91500 17	0,0010	28	34	145	0,24	1,86	1,91	0,18	1,05	0,55	0,07	1,60	1066	11	1066	20	1067	17	100
91500 18	0,0022	24	30	126	0,24	1,86	1,67	0,18	0,88	0,53	0,07	1,42	1065	9	1066	18	1067	15	100
91500 19	0,0011	28	34	145	0,23	1,86	1,58	0,18	0,76	0,49	0,07	1,38	1066	8	1066	17	1067	15	100
91500 20	0,0014	18	23	91	0,26	1,85	1,77	0,18	1,05	0,60	0,07	1,42	1061	11	1062	19	1065	15	100
91500 21	0,0017	19	26	97	0,27	1,86	2,10	0,18	1,25	0,60	0,07	1,68	1065	13	1066	22	1067	18	100
91500 22	0,0015	19	23	95	0,24	1,85	2,60	0,18	1,57	0,60	0,07	2,07	1062	17	1064	28	1068	22	99
91500 23	0,0016	15	18	77	0,24	1,85	2,71	0,18	1,65	0,61	0,07	2,14	1063	18	1063	29	1063	23	100
91500 24	0,0017	18	18	88	0,20	1,85	2,57	0,18	1,64	0,64	0,07	1,98	1061	17	1063	27	1067	21	99
BB 01	0,0060	25	58	240	0,24	0,74	3,81	0,09	2,13	0,56	0,06	3,15	562	12	562	21	562	18	100
BB 02	0,0029	20	50	207	0,24	0,74	3,08	0,09	1,95	0,63	0,06	2,38	560	11	561	17	562	13	100
BB 03	0,0022	22	56	222	0,26	0,74	2,98	0,09	2,20	0,74	0,06	2,02	560	12	561	17	563	11	100

[a] Fraction of the non-radiogenic ^{206}Pb in the analyzed zircon spot, where f_{206}=[$^{206}Pb/^{204}Pb$]c/[$^{206}Pb/^{204}Pb$]s (c=common; s=sample)

[b] Th/U ratios and amount of Pb, Th and U (in ppm) are calculated relative to GJ-1 reference zircon

[c] Corrected for background and within-run Pb/U fractionation and normalized to reference zircon GJ-1 (ID-TIMS values/measured value); $^{207}Pb/^{235}U$ calculated using ($^{207}Pb/^{206}Pb$)*($^{206}Pb/^{238}U$)*(137.88)

[d] Rho is the error correlation defined as the quotient of the propagated errors of the $^{206}Pb/^{238}U$ and the $^{207}/^{235}U$ ratio

[e] Corrected for mass-bias by normalizing to GJ-1 reference zircon and common Pb using the model Pb composition of Stacey and Kramers (1975)

[f] Degree of concordance, 6/8-7/6= ($^{206}Pb/^{238}U$ age * 100) / ($^{207}Pb/^{206}Pb$ age), according to Horstwood et al., 2016.

Table S-3: Summary of results of U-Pb dating of zircon by SHRIMP.

DEQ-581

Spot	204Pb /206Pb	±%	207Pb /206Pb	±%	208Pb /206Pb	±%	206Pb /238U	±%	% $206Pb_c$	ppm U	ppm Th	4-corr ppm $206Pb^*$	4-corr ppm $208Pb^*$	232Th /238U	±%	(1) 206Pb /238U Age		(2) 206Pb /238U Age		(3) 206Pb /238U Age		(1) 207Pb /206Pb Age	
DEQ581-13.1	2,5E-4	23	0,210	0,46	0,163	1,1	1,94	0,7	0,33	67	40	32	5,1	0,61	0,47	2874	±28	2869	±42	2885	±30	2884	±9
DEQ581-10.1	9,9E-5	18	0,209	0,28	0,126	0,8	1,66	2,7	0,13	186	83	91	11,3	0,46	0,31	2901	±32	2907	±48	2903	±33	2889	±5
DEQ581-9.1	3,3E-4	12	0,209	0,32	0,106	2,5	1,06	3,9	0,43	284	87	140	13,5	0,32	0,93	2921	±50	2947	±78	2911	±52	2871	±6
DEQ581-3.1	1,2E-4	21	0,208	0,36	0,290	0,7	1,97	0,5	0,16	114	122	55	15,9	1,10	0,30	2868	±24	2863	±36	2881	±28	2876	±6
DEQ581-12.1	4,4E-4	16	0,206	0,46	0,256	1,3	2,05	1,4	0,57	72	61	37	9,0	0,87	0,38	3004	±28	3106	±50	2997	±31	2831	±10
DEQ581-11.1	3,5E-4	18	0,220	0,50	0,129	1,4	1,95	1,7	0,46	51	23	25	3,0	0,46	0,58	2920	±30	2904	±46	2927	±32	2949	±10
DEQ581-5.1	1,3E-4	29	0,217	0,28	0,094	0,9	1,98	1,0	0,18	175	57	87	7,9	0,34	0,37	2940	±23	2939	±35	2942	±23	2943	±6
DEQ581-15.1	7,6E-5	36	0,221	0,26	0,153	0,7	1,86	2,2	0,10	226	124	111	17,0	0,57	0,29	2928	±22	2900	±33	2931	±23	2978	±5
DEQ581-1.1	2,4E-4	21	0,222	0,50	0,126	1,4	1,98	0,7	0,31	55	25	28	3,3	0,47	0,58	2945	±31	2929	±47	2953	±32	2975	±9
DEQ581-14.1	3,1E-4	20	0,223	0,53	0,137	1,4	1,95	0,8	0,40	48	23	24	3,1	0,49	0,60	2955	±32	2943	±50	2960	±34	2975	±10
DEQ581-16.1	3,0E-4	35	0,225	0,48	0,201	1,1	1,94	1,9	0,39	57	42	29	5,5	0,75	0,46	2945	±30	2919	±46	2957	±33	2993	±12
DEQ581-6.1	7,7E-5	22	0,225	0,46	0,191	0,7	2,04	0,5	0,10	146	103	75	14,3	0,73	0,30	3033	±24	3049	±40	3042	±26	3007	±8
DEQ581-7.1	1,3E-4	22	0,231	0,29	0,121	0,8	1,91	1,4	0,17	164	70	79	9,3	0,44	0,36	2871	±23	2782	±32	2875	±24	3045	±5

DEQ-581 (continuação)

(1) 208Pb /232Th Age		(2) 208Pb /232Th Age		(3) 207Pb /206Pb Age		% Dis-cor-dant	7corr $208Pb^*$ /232Th	±%	(1) 238U /$206Pb^*$	±%	(1) $207Pb^*$ /$206Pb^*$	±%	(1) $207Pb^*$ /235U	±%	(1) $206Pb^*$ /238U	±%	err corr	(3) 238U /$206Pb^*$	±%	(3) $207Pb^*$ /$206Pb^*$	±%	(3) $207Pb^*$ /235U	±%	(3) $206Pb^*$ /238U	±%	err. corr.
2695	±53	2606	±259	2916	±10	+0	0,138	10,6	1,78	1,2	0,207	0,56	16,1	1,3	0,562	1,2	0,9	1,77	1,3	0,211	0,60	16,5	1,3	0,564	1,3	0,9
2854	±44	2996	±396	2895	±6	-1	0,160	14,2	1,76	1,4	0,208	0,30	16,3	1,4	0,568	1,4	1,0	1,76	1,4	0,209	0,39	16,4	1,3	0,569	1,4	1,0
3223	±108	4067	±939	2843	±11	-2	0,223	25,5	1,74	2,1	0,206	0,40	16,2	2,2	0,573	2,1	1,0	1,75	2,2	0,202	0,65	15,9	2,1	0,571	2,2	1,0
2753	±34	2712	±125	2915	±10	+0	0,144	4,9	1,79	1,1	0,206	0,39	15,9	1,1	0,560	1,1	0,9	1,77	1,2	0,211	0,61	16,4	1,2	0,563	1,2	0,9
3085	±58	4324	±273	2809	±14	-8	0,239	7,0	1,68	1,2	0,201	0,64	16,4	1,3	0,594	1,2	0,9	1,69	1,3	0,198	0,84	16,2	1,3	0,592	1,3	0,8
2761	±68	2391	±397	2969	±10	+1	0,126	17,6	1,75	1,3	0,216	0,61	17,0	1,4	0,573	1,3	0,9	1,74	1,4	0,218	0,61	17,3	1,4	0,575	1,4	0,9
2894	±53	2839	±412	2948	±5	+0	0,151	15,5	1,73	1,0	0,215	0,35	17,1	1,0	0,578	1,0	0,9	1,73	1,0	0,216	0,33	17,2	1,0	0,578	1,0	0,9

2873	±35	2348	±224	2987	±6	+2	0,123	10,1	1,74	0,9	0,220	0,30	17,4	1,0	0,575	0,9	1,0	1,74	1,0	0,221	0,35	17,5	0,9	0,576	1,0	0,9
2767	±64	2387	±418	2996	±10	+1	0,125	18,6	1,73	1,3	0,219	0,57	17,5	1,4	0,579	1,3	0,9	1,72	1,4	0,222	0,61	17,8	1,4	0,581	1,4	0,9
2844	±69	2590	±422	2989	±11	+1	0,137	17,4	1,72	1,4	0,219	0,63	17,6	1,5	0,581	1,4	0,9	1,72	1,4	0,221	0,65	17,8	1,4	0,583	1,4	0,9
2779	±65	2396	±248	3026	±11	+2	0,126	11,0	1,73	1,3	0,222	0,74	17,7	1,5	0,579	1,3	0,9	1,72	1,4	0,226	0,66	18,2	1,3	0,582	1,4	0,9
2906	±35	3151	±255	3031	±9	-1	0,169	8,8	1,66	1,0	0,224	0,47	18,5	1,1	0,601	1,0	0,9	1,66	1,1	0,227	0,54	18,9	1,1	0,603	1,1	0,9
2787	±41	541	±264	3055	±6	+7	0,027	49,5	1,78	1,0	0,229	0,33	17,7	1,0	0,561	1,0	0,9	1,78	1,0	0,230	0,37	17,9	1,0	0,562	1,0	0,9

Errors are 1-sigma; Pb_c and Pb^* indicate the common and radiogenic portions, respectively.

Error in Standard calibration was 0.22% (not included in above errors but required when comparing data from different mounts).

(1) Common Pb corrected using measured 204Pb.

(2) Common Pb corrected by assuming 206Pb/238U-207Pb/235U age-concordance

(3) Common Pb corrected by assuming 206Pb/238U-208Pb/232Th age-concordance

DEQ-582

Spot	204Pb /206Pb	±%	207Pb /206Pb	±%	208Pb /206Pb	±%	206Pb /238U	±%	% $206Pb_c$	ppm U	ppm Th	4-corr ppm $206Pb^*$	4-corr ppm $208Pb^*$	232Th /238U	±%	(1) 206Pb /238U Age		(2) 206Pb /238U Age		(3) 206Pb /238U Age		(1) 207Pb /206Pb Age	
DEQ582-6.1	2,6E-5	20	0,202	0,16	0,164	0,37	1,68	0,22	0,05	664	425	284	46,9	0,66	0,16	2605	±22	2479	±30	2626	±24	2837	±3
DEQ582-2.1	3,3E-4	19	0,207	0,81	0,174	1,11	1,80	0,62	0,61	66	40	32	5,2	0,63	0,46	2867	±31	2878	±59	2876	±33	2854	±15
DEQ582-12.1	1,8E-4	19	0,206	0,37	0,197	0,81	1,66	0,46	0,34	128	89	60	11,5	0,72	1,02	2804	±27	2765	±45	2811	±30	2857	±7
DEQ582-1.1	1,2E-4	19	0,200	0,29	0,310	0,51	1,62	0,76	0,23	199	215	93	28,9	1,12	0,50	2808	±25	2804	±45	2806	±30	2813	±5
DEQ582-7.1	4,2E-4	19	0,218	0,59	0,198	2,97	1,86	0,80	0,79	38	27	19	3,5	0,72	0,56	2926	±35	2926	±70	2943	±39	2927	±12
DEQ582-4.1	8,5E-5	21	0,214	0,26	0,178	0,60	1,89	0,74	0,16	201	125	100	17,6	0,64	0,54	2936	±27	2944	±55	2936	±29	2928	±4
DEQ582-10.1	1,7E-4	19	0,218	0,31	0,322	0,93	1,99	0,43	0,31	132	149	66	21,0	1,17	0,69	2953	±40	2957	±82	2953	±47	2948	±6
DEQ582-5.1	1,0E-4	24	0,218	0,39	0,172	0,90	1,81	0,87	0,20	98	62	49	8,4	0,65	0,59	2968	±29	2977	±62	2978	±31	2959	±7
DEQ582-8.1	1,1E-4	18	0,219	0,26	0,125	0,72	1,94	0,36	0,21	205	91	103	12,6	0,46	0,31	2962	±27	2959	±55	2965	±28	2966	±5
DEQ582-11.1	2,6E-4	33	0,223	0,35	0,112	2,27	1,67	1,45	0,49	123	41	60	6,3	0,34	0,45	2907	±28	2839	±50	2896	±29	2981	±9
DEQ582-13.1	6,0E-4	19	0,223	1,24	0,137	3,54	1,77	0,93	1,13	33	14	16	1,9	0,43	0,82	2956	±39	2960	±83	2956	±42	2952	±23
DEQ582-14.1	9,1E-5	19	0,216	0,25	0,145	0,63	1,88	0,33	0,17	256	135	125	18,0	0,55	0,27	2909	±26	2876	±48	2916	±28	2943	±4
DEQ582-15.1	1,1E-4	18	0,221	0,27	0,247	0,54	1,62	0,75	0,20	232	207	117	28,7	0,92	0,23	2976	±26	2973	±56	2983	±30	2978	±5
DEQ582-9.1	1,9E-4	18	0,211	0,39	0,160	1,69	1,87	0,51	0,36	95	53	46	7,1	0,58	0,39	2869	±29	2849	±52	2874	±31	2892	±7

DEQ-582 (continuação)

(1) 208Pb /232Th Age		(2) 208Pb /232Th Age		(3) 207Pb /206Pb Age		% Dis-cor-dant	7corr 208Pb* /232Th	±%	(1) 238U /206Pb*	±%	(1) 207Pb* /206Pb*	±%	(1) 207Pb* /235U	±%	(1) 206Pb* /238U	±%	err corr	(3) 238U /206Pb*	±%	(3) 207Pb* /206Pb*	±%	(3) 207Pb* /235U	±%	(3) 206Pb* /238U	±%	err. corr.
2346	±25	650	±129	2888	±5	+10	0,033	20,1	2,01	1,0	0,201	0,16	13,8	1,1	0,50	1,0	0,99	1,99	1,1	0,208	0,28	14,4	1,0	0,50	1,1	1,0
2740	±60	2895	±435	2875	±15	-1	0,154	16,1	1,79	1,3	0,203	0,91	15,7	1,6	0,56	1,3	0,82	1,78	1,4	0,206	0,90	16,0	1,5	0,56	1,4	0,8
2732	±48	2247	±249	2871	±10	+2	0,118	11,7	1,83	1,2	0,204	0,42	15,3	1,3	0,55	1,2	0,94	1,83	1,3	0,206	0,60	15,5	1,3	0,55	1,3	0,9
2816	±36	2785	±162	2810	±10	+0	0,148	6,2	1,83	1,1	0,198	0,32	14,9	1,2	0,55	1,1	0,96	1,83	1,3	0,198	0,61	14,9	1,2	0,55	1,3	0,9
2745	±97	2734	±483	2959	±16	+0	0,145	18,9	1,74	1,5	0,213	0,76	16,9	1,7	0,57	1,5	0,89	1,73	1,7	0,217	0,99	17,3	1,7	0,58	1,7	0,8
2940	±40	3052	±406	2928	±7	-0	0,163	14,3	1,73	1,1	0,213	0,27	16,9	1,2	0,58	1,1	0,97	1,73	1,2	0,213	0,41	16,9	1,1	0,58	1,2	0,9
2949	±57	2982	±362	2950	±14	-0	0,159	13,0	1,72	1,7	0,216	0,36	17,3	1,7	0,58	1,7	0,98	1,72	2,0	0,216	0,87	17,3	1,9	0,58	2,0	0,9
2840	±46	2971	±487	2978	±9	-0	0,158	17,6	1,71	1,2	0,217	0,42	17,5	1,3	0,58	1,2	0,95	1,70	1,3	0,220	0,53	17,8	1,2	0,59	1,3	0,9
2909	±41	2837	±593	2971	±6	+0	0,151	22,4	1,71	1,1	0,218	0,28	17,5	1,2	0,58	1,1	0,97	1,71	1,2	0,219	0,35	17,6	1,1	0,58	1,2	1,0
3189	±124	1387	±651	2958	±8	+3	0,071	48,6	1,75	1,2	0,220	0,58	17,3	1,3	0,57	1,2	0,90	1,76	1,3	0,217	0,52	17,0	1,2	0,57	1,3	0,9
2943	±153	3036	±1045	2953	±22	-0	0,162	37,1	1,72	1,6	0,216	1,43	17,3	2,2	0,58	1,6	0,75	1,72	1,8	0,216	1,37	17,3	2,1	0,58	1,8	0,8
2790	±36	2259	±397	2958	±6	+1	0,118	18,6	1,75	1,1	0,215	0,26	16,9	1,1	0,57	1,1	0,97	1,75	1,2	0,217	0,35	17,1	1,1	0,57	1,2	1,0
2910	±35	2887	±308	2992	±7	+0	0,154	11,4	1,70	1,1	0,220	0,29	17,8	1,1	0,59	1,1	0,97	1,70	1,2	0,222	0,46	18,0	1,1	0,59	1,2	0,9
2804	±60	2495	±391	2902	±10	+1	0,131	16,7	1,78	1,2	0,208	0,44	16,1	1,3	0,56	1,2	0,94	1,78	1,3	0,210	0,60	16,2	1,3	0,56	1,3	0,9

Errors are 1-sigma; Pb_c and Pb^* indicate the common and radiogenic portions, respectively.

Error in Standard calibration was 0.21% (not included in above errors but required when comparing data from different mounts).

(1) Common Pb corrected using measured 204Pb.

(2) Common Pb corrected by assuming 206Pb/238U-207Pb/235U age-concordance

(3) Common Pb corrected by assuming 206Pb/238U-208Pb/232Th age-concordance

DEQ-583

Spot	204Pb /206Pb	±%	207Pb /206Pb	±%	208Pb /206Pb	±%	206Pb /238U	±%	% $206Pb_c$	ppm U	ppm Th	4-corr ppm $206Pb^*$	4-corr ppm $208Pb^*$	232Th /238U	±%	(1) 206Pb /238U Age		(2) 206Pb /238U Age		(3) 206Pb /238U Age		(1) 207Pb /206Pb Age	
DEQ583-20.1	2,8E-4	18	0,208	0,47	0,396	0,75	1,77	0,61	0,52	68	98	33	12,9	1,48	0,33	2859	±30	2853	±56	2880	±37	2866	±9
DEQ583-19.1	1,6E-4	19	0,207	0,34	0,228	0,70	1,64	0,42	0,30	154	122	73	16,4	0,82	0,29	2847	±27	2827	±48	2848	±30	2870	±6
DEQ583-21.1	2,5E-4	11	0,209	0,55	0,382	1,09	1,93	0,87	0,47	216	268	104	39,3	1,28	0,21	2874	±26	2872	±49	2842	±32	2877	±9
DEQ583-22.1	1,8E-4	16	0,211	0,69	0,258	2,53	1,78	1,41	0,34	137	115	67	17,0	0,86	0,29	2891	±27	2889	±53	2869	±32	2894	±12
DEQ583-7.1	2,4E-4	20	0,209	0,27	0,150	1,5	1,69	1,7	0,31	193	101	94	13,6	0,54	0,50	2901	±22	2912	±33	2905	±23	2880	±6
DEQ583-8.1	5,9E-4	9	0,194	0,19	0,253	2,2	1,84	1,5	0,83	419	113	176	41,6	0,28	0,52	2565	±18	2514	±23	2421	±20	2716	±7
DEQ583-1.1	2,8E-4	19	0,219	0,49	0,150	1,4	2,10	1,2	0,36	51	28	25	3,6	0,58	0,53	2945	±31	2944	±48	2960	±33	2947	±9
DEQ583-15.1	1,6E-4	29	0,229	0,26	0,124	0,8	1,79	1,9	0,21	228	95	115	13,8	0,43	0,32	2978	±22	2946	±34	2976	±23	3033	±6
DEQ583-4.1	2,3E-4	17	0,234	0,35	0,122	1,8	2,01	1,4	0,30	98	40	49	5,7	0,43	0,44	2956	±26	2897	±38	2956	±27	3058	±6
DEQ583-5.1	1,3E-4	18	0,217	0,32	0,363	0,5	1,97	1,1	0,17	127	172	62	22,6	1,40	0,26	2908	±24	2887	±35	2929	±28	2949	±6
DEQ583-23.1	1,4E-4	20	0,213	0,31	0,251	0,62	1,76	0,88	0,26	144	132	70	17,5	0,95	0,27	2902	±27	2888	±51	2916	±30	2917	±6
DEQ583-3.1	2,2E-4	20	0,218	0,41	0,182	1,8	1,85	0,6	0,29	79	53	37	6,5	0,69	0,40	2783	±26	2708	±35	2794	±28	2948	±8
DEQ583-6.1	3,9E-4	15	0,216	0,41	0,178	1,0	1,88	1,6	0,52	78	43	38	6,3	0,57	0,43	2880	±26	2861	±39	2870	±28	2918	±9
DEQ583-16.1	2,0E-4	27	0,212	0,32	0,026	4,6	1,85	1,2	0,27	154	11	74	1,4	0,08	0,81	2850	±23	2826	±33	2851	±23	2900	±7

DEQ-583 (continuação)

(1) 208Pb /232Th Age		(2) 208Pb /232Th Age		(3) 207Pb /206Pb Age		% Dis-cor-dant	7corr $208Pb^*$ /232Th	±%	(1) 238U /$206Pb^*$	±%	(1) $207Pb^*$ /$206Pb^*$	±%	(1) $207Pb^*$ /235U	±%	(1) $206Pb^*$ /238U	±%	err corr	(3) 238U /$206Pb^*$	±%	(3) $207Pb^*$ /$206Pb^*$	±%	(3) $207Pb^*$ /235U	±%	(3) $206Pb^*$ /238U	±%	err. corr.
2755	±42	2720	±168	2911	±18	+0	0,144	6,6	1,79	1,3	0,205	0,56	15,8	1,4	0,56	1,3	0,92	1,78	1,6	0,211	1,09	16,4	2,0	0,56	1,6	0,8
2836	±39	2628	±245	2873	±9	+1	0,139	9,9	1,80	1,2	0,205	0,38	15,7	1,2	0,56	1,2	0,95	1,80	1,3	0,206	0,53	15,8	1,2	0,56	1,3	0,9
3063	±46	3046	±175	2805	±22	+0	0,163	6,2	1,78	1,1	0,206	0,58	16,0	1,3	0,56	1,1	0,89	1,81	1,4	0,197	1,37	15,1	2,0	0,55	1,4	0,7
3091	±81	3067	±293	2847	±19	+0	0,164	10,3	1,77	1,2	0,208	0,72	16,3	1,4	0,57	1,2	0,85	1,78	1,4	0,203	1,16	15,7	1,7	0,56	1,4	0,7
2829	±56	3043	±238	2891	±8	-1	0,162	8,4	1,76	0,9	0,207	0,39	16,2	1,0	0,568	0,9	0,9	1,76	1,0	0,208	0,49	16,3	1,0	0,569	1,0	0,9

6953	±148	5465	±206	2014	±15	+7	0,310	4,3	2,05	0,8	0,187	0,41	12,6	0,9	0,489	0,8	0,9	2,19	1,0	0,124	0,85	7,8	0,9	0,456	1,0	0,6
2671	±58	2651	±341	2989	±10	+0	0,140	13,7	1,73	1,3	0,215	0,57	17,2	1,4	0,579	1,3	0,9	1,72	1,4	0,221	0,63	17,8	1,3	0,583	1,4	0,9
3026	±50	2206	±325	3028	±5	+2	0,115	15,6	1,70	0,9	0,227	0,34	18,4	1,0	0,587	0,9	0,9	1,70	1,0	0,227	0,33	18,3	0,9	0,587	1,0	0,9
2943	±67	1415	±366	3060	±8	+4	0,072	26,8	1,72	1,1	0,231	0,41	18,5	1,2	0,582	1,1	0,9	1,72	1,1	0,231	0,51	18,5	1,1	0,582	1,1	0,9
2771	±31	2605	±100	3006	±11	+2	0,138	4,1	1,75	1,0	0,216	0,34	17,0	1,1	0,570	1,0	0,9	1,74	1,2	0,224	0,66	17,7	1,3	0,575	1,2	0,9
2787	±37	2655	±246	2945	±8	+1	0,140	9,9	1,76	1,2	0,212	0,35	16,6	1,2	0,57	1,2	0,96	1,75	1,3	0,215	0,51	17,0	1,2	0,57	1,3	0,9
2619	±57	1458	±170	2981	±11	+7	0,075	12,1	1,85	1,1	0,216	0,48	16,0	1,2	0,540	1,1	0,9	1,84	1,2	0,220	0,68	16,5	1,2	0,543	1,2	0,8
3055	±55	2701	±253	2888	±9	+2	0,143	10,0	1,78	1,1	0,212	0,53	16,4	1,3	0,563	1,1	0,9	1,78	1,2	0,208	0,57	16,1	1,2	0,561	1,2	0,9
2657	±266	-1036	±1796	2904	±6	+2	-0,050	-168,9	1,80	1,0	0,209	0,45	16,0	1,1	0,556	1,0	0,9	1,80	1,0	0,210	0,37	16,1	1,0	0,556	1,0	0,9

Errors are 1-sigma; Pb_c and Pb^* indicate the common and radiogenic portions, respectively.

Error in Standard calibration was 0.22% (not included in above errors but required when comparing data from different mounts).

(1) Common Pb corrected using measured 204Pb.

(2) Common Pb corrected by assuming 206Pb/238U-207Pb/235U age-concordance

(3) Common Pb corrected by assuming 206Pb/238U-208Pb/232Th age-concordance

UNIVERSIDADE FEDERAL DO PARÁ
INSTITUTO DE GEOCIÊNCIAS
PROGRAMA DE PÓS-GRADUAÇÃO EM GEOLOGIA E GEOQUÍMICA

PARECER

Sobre a Defesa Pública da Tese de Doutorado de RAPHAEL NETO ARAÚJO

A banca examinadora da Tese de Doutorado de **RAPHAEL NETO ARAÚJO** orientando do Prof. Dr. Afonso Cesar Rodrigues Nogueira (UFPA) e composta pelos professores doutores Ricardo Ivan Ferreira da Trindade (Membro-USP), Lucieth Cruz Vieira (Membro-UnB), Jean Michel Lafon (Membro-UFPA), e Joelson Lima Soares (Membro-UFPA), após apresentação da sua tese intitulada **"ESTRATIGRAFIA E EVENTOS NA TRANSIÇÃO NEOARQUEANO-PALEOPROTEROZOICO DA BACIA DE CARAJÁS, SUDESTE DO CRÁTON AMAZÔNICO"**, emite o seguinte parecer:

O candidato realizou sua apresentação de forma clara, bem organizada e segura no tempo estipulado. Na arguição mostrou domínio da temática abordada e respondeu às perguntas formuladas pela banca. O trabalho escrito foi apresentado na forma de três artigos, sendo um já publicado, um submetido, ambos em periódicos internacionais, e o terceiro artigo ainda em elaboração. Consta em anexo um quarto artigo no qual o doutorando é coautor. O conjunto de artigos forma uma unidade coerente, compatível com uma tese de doutorado.

Finalmente, a banca examinadora decidiu por unanimidade aprovar a tese de doutorado.

Belém, 18 de setembro de 2020.

Prof. Dr. Afonso Cesar R. Nogueira (Orientador – UFPA)

Prof. Dr. Ricardo Ivan Ferreira da Trindade (Membro-USP)

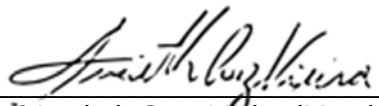

Prof.ª Dr.ª Lucieth Cruz Vieira (Membro-UnB)

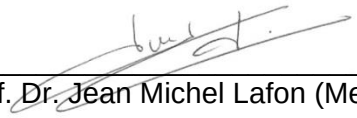

Prof. Dr. Jean Michel Lafon (Membro-UFPA)

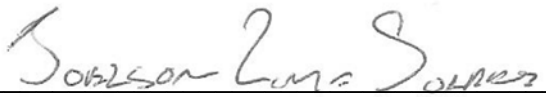

Prof. Dr. Joelson Lima Soares (Membro-UFPA)